TECHNISCHE UNIVERSITÄT MÜNCHEN

FAKULTÄT FÜR MEDIZIN

Analysis of the lineage recruitment from intestinal stem cells in health and in pre-diabetes

Alexandra Aliluev

Vollständiger Abdruck der von der Fakultät für Medizin der Technischen Universität München zur Erlangung des akademischen Grades eines

Doktors der Naturwissenschaften

genehmigten Dissertation.

Vorsitzender: Prof. Dr. Radu Roland Rad

Prüfer der Dissertation:

1. Prof. Dr. Heiko Lickert

2. apl. Prof. Dr. Thomas Floss

Die Dissertation wurde am 11.06.2019 bei der Technischen Universität München eingereicht und

durch die Fakultät für Medizin am 05.11.2019 angenommen.

Contents

1 List of abbreviations

3D	Three-dimensional
5-HT	5-Hydroxytryptamine (serotonin)
Acc	Acetyl-CoA carboxylase
Acot1	Acyl-CoA thioesterase 1
Actb	Beta-actin
AcTub	Acetylated tubulin
Afp	Alpha-fetoprotein
Akt	Serine-threonine kinase AKT (PKB)
Aldob	Fructose-bisphosphate aldolase B
ALI	Air-liquid interface
Arx	Aristaless-related homeobox
Ascl2	Achaete-scute complex homolog 2
Atoh1	Protein atonal homolog 1
Bex1/4	Brain-expressed X-linked protein 1/4
bHGpA	Bovine Growth Hormone polyadenylation signal
Bmi1	B cell-specific Moloney murine leukemia virus integration site 1
BMP	Bone morphogenetic protein
bp	Base pair
BrdU	5-Bromo-2′-deoxyuridine
BSA	Bovine serum albumin
Cck/CCK	Cholecystokinin
Ccnb1/2	Cyclin B1/2
Ccnd1	Cyclin D1
CD	Control diet
Cdk4	Cyclin-dependent kinase 4
Cdkn1a/b/2a	cyclin-dependent kinase inhibitor 1a/b/2A
Cdp	CCAAT-displacement protein
Cdx-2	Caudal type homebox 2
Celsr	Cadherin EGF LAG Seven-Pass G-type Receptor
Cenpa	Centromere protein A
Cfap126	CILIA- AND FLAGELLA-ASSOCIATED PROTEIN 126
ChgA	Chromogranin A
Cplx2	Complexin-2
CreERT2	Tamoxifen-inducible estrogen receptor Cre recombinase
d	Day
DAPI	40, 6-diamidin-2-phenylindol
DIO	Diet-induced obesity
Dll1/4	Delta-like protein 1/4
DMSO	Dimethyl sulfoxide
DNA	Deoxyribonucleic acid

DPP4	Dipeptidylpeptidase 4
Dut	Deoxyuridine Triphosphatase
EC	Enterochromaffin cell
E-Cadh	Epithelial cadherin
ECL	Enhanced chemiluminescence
EdU	5-ethynyl-2'-deoxyuridine
EE	Enteroendocrine
EEC	Enteoendocrine cell
EGF	Epidermal growth factor
eGFP	Enhanced green fluorescence protein
ELISA	Enzyme-linked immunosorbent assay
EP	Enterocyte progenitor
EpCAM	Epithelial cell adhesion molecule
Erk1/2	Extracellular signal-regulated kinase or p44/42 MAPK
ES	embryonic stem (cells)
ESC	Embryonic stem cell
FA	Fatty acid
Fabp1/2	Fatty acid-binding protein 1
FACS	Fluorescence-activated cell sorting
Fasn	Fatty acid synthase
Fltp	Flattop, Cfap126
FoxA2	Forkhead box transcription factor A2
FoxJ1	Forkhead box J1
FSC	Forward Scatter
Fuz	Fuzzy
FVF	Foxa2-Venus fusion
FVR	Fltp-H2B-Venus reporter
fwd	forward
Fzd3/6	Frizzled 3/6
Gast	Gastrin
Gata4-6	GATA binding protein 4-6
Gcg	Glucagon
Gfi1	Growth factor independent 1
GFP	Green fluorescent protein
Ghrl	Ghrelin
GI	Gastrointestinal
GIP	Gastrointestinal inhibitory polypeptide
Glp-1/GLP-1	Gluagon-like peptide 1
Gnas	Guanine Nucleotide binding protein, Alpha Stimulating
GO	Gene Ontology
GP	Goblet cell progenitor
Gsk3β	Glycogen synthase kinase 3β

H&E	Hematoxylin and Eosin staining
H2B	Histone 2B
Hes1	Hairy and enhancer of split-1
HET	Heterozygous
HFD	High-fat diet
Hmgcs2	3-Hydroxy-3-methylglutaryl-CoA synthase 2
Hmgn3	High mobility group nucleosome-binding domain 3
Hnf1a/b	Hepatocyte nuclear factor 1a/1b
HOM	Homozygous
HOMA-IR	Homeostatic model assessment of insulin resistance
HOMA-β	Homeostatic model assessment of β-cell function
Hopx	Homeodomain-only protein
Hprt	Hypoxanthine-guanine phosphoribosyltransferase
HSC	Hematopoietic stem cell
Hsp90	Heat shock protein 90
i.p.	Intraperitoneal
IF	Immunofluorescence
Igf1/IGF-1	insulin-like growth factor 1
Igf1r	insulin-like growth factor 1 receptor
IHC	Immunohistochemistry
IL-6	Interleukin 6
Ins1	Insulin
Insm1	Insulinoma-associated 1
IP	Immunoprecipitation
Ir	Insulin receptor
ISC	Intestinal stem cell
Isl1	Gene of nsulin gene enhancer protein Isl-1
IST	Insulin secretion test
kb	Kilobase
kDa	Kilodalton
Khk	Ketohexokinase
Ki67	Proliferation-related Ki67 antigen
Klf4	Kruppel-like factor 4
KO	Knock-out
LacZ	Gene of β-galactosidase
Lgr5	Leucine-Rich Repeat Containing G- Protein Coupled Receptor 5
LIF	Leukemia inhibitory factor
LPS	Lipopolysaccharide
LRC	Label-retaining cell
Lrig1	Leucine-rich repeats and immunoglobulin-like domains protein 1
LSM	Laser scanning microscopy
Lyz	Lyzosyme

MALDI-MSI	Matrix-assisted laser desorption/ionization mass spectrometry imaging
Mapk	Mitogen-activated protein kinase
MEF	Murine embryonic fibroblast
mG	Membrane-GFP
Mgam	Maltase-glucoamylase
MODY	Maturity Onset Diabetes of Young
mRNA	Messenger RNA
mT	Membrane-Tomato
mTEC	Mouse tracheal epithelial cells
mTERT	Mouse telomerase reverse transcriptase
mTmG	Membrane-GFP and membrane-Tomato
mTor	Mammalian target of rapamycin
Muc2	Mucin 2
nEGFP	Nuclear GFP
Neo or neo	Neomycin
NeuroD1	Neuronal differentiation 1
Neurog3/Ngn3	Neurogenin 3
Nkx2.2	NK2 homeobox 2
NLS	Nuclear localization signal
NMR	Nuclear magnetic resonance spectroscopy
NSC	Neural stem cell
OCT	Optimal cutting temperature
(o)GTT	(oral) Glucose tolerance test
Olfm4	Olfactomedin 4
Onecut2	One Cut Homeobox 2
ORF	Open reading frame
OxPhos	Oxidative phosphorylation
PAGA	Partitioned graph abstraction
Pax4/6	Paired box homeotic gene 4/6
pBKS	pBluescriptKS
PCP	Planar Cell Polarity
PCR	Polymerase Chain Reaction
Pdx1	Pancreatic and duodenal homeobox 1
Pericent	Pericentrin
PFA	Paraformaldehyde
PGK	Phospho-glucerate kinase
PhD	Philosophiae doctor
PI3K	Phosphoinositide 3-kinase
PKB	Protein kinase B (AKT)
Ppar	Peroxisome proliferator-activated receptor
Pyy/PYY	Peptide YY
qRT-PCR	Real-time quantitative PCR

Reg4	Regenerating islet-derived protein 4
rev	reverse
Rfx3/6	Regulatory factor X 3/6
RNA	Ribonucleic acid
RT	Room temperature
RYGB	Roux-en-Y Gastric Bypass
SCAP	Srebp cleavage-activating protein
Scarb1	Scavenger receptor class B type 1
Scd1/2	Stearoyl-CoA desaturase 1/2
scRNAseq	Single-cell RNA sequencing
Sct	Secretin
SEM	Standard error of the mean
Ser	Serin
SI	Small intestinal
Sis	Sucrase-isomaltase
Slc2a2	Solute carrier family 2 member 2
Slc5a1	Sodium-dependent glucose-galactose transporter
Slc18a2	Solute carrier family 18 member A2
Smc2	Structural maintenance of chromosomes protein 2
Sox4/9	SRY-Box 4/9
Spdef1	SAM pointed domain ETS factor 1
Srebf1	Gene of Srebp1 protein
Srebp1/2	Sterol regulatory element-binding protein 1/2
SSC	Side scatter
SSC (buffer)	Saline-sodium citrate
Sst	Somatostatin
T2D	Type 2 diabetes
TA	Transit-amplifying
Tgfβ	Transforming growth factor β
TNFα	Tumour necrosis factor α
Tph1/2	Tryptophan hydroxylase 1
Trp63	Transformation-related protein 63
Tyr	Tyrosin
Ucn3	Urocortin 3
UMAP	Uniform Manifold Approximation and Projection
UTR	Untranslated region
vs.	versus
WHO	World Health Organization
Wnt	Wingless and Int-1
WT	Wildtype

2 Abstract

The gut is the largest endocrine organ and regulates food intake, nutrient absorption and systemic energy metabolism. Intestinal tissue homeostasis is maintained by a tight balance between self-renewal and differentiation of intestinal stem cells (ISCs) into secretory and absorptive progenitors. It has been shown that dietary changes can impact ISC function and cell fate decisions. A deregulation of the ISC homeostasis induced by a high-fat diet (HFD) has been implicated in the pathogenesis of the metabolic syndrome and co-morbidities such as gastro-intestinal cancers. Additionally, alterations in gut hormone levels and signalling, as well as changes in numbers of enteroendocrine cells (EECs) have been associated with severe obesity and type 2 diabetes (T2D). However, the underlying mechanisms remain poorly understood.

The aim of this thesis was to elucidate HFD-induced changes in the ISCs homeostasis and lineage recruitment to identify novel potential targets for non-invasive therapies for obesity and T2D. We used a model of HFD-induced obesity and pre-diabetes to study molecular mechanisms of the early pathogenesis of the associated intestinal disorder. To dissect cell-type specific responses of ISCs, progenitors and mature small intestinal (SI) cells to HFD, we performed a single-cell survey of 27,687 SI crypt cells.

Single-cell RNA-sequencing (scRNAseq) revealed HFD-induced alterations in lineage allocation from ISCs, including enhanced formation of the absorptive and goblet cell lineage, particularly, in the proximal intestine. The increase in numbers of enterocytes and proximal goblet cells was furthermore attributable to the hyperproliferation of their respective progenitors. Strikingly, enhanced ISC turnover on HFD, did not result in an increased ISC pool. On the contrary, we recorded reduced numbers of ISCs combined with diminished Wnt/β-catenin signalling, indicating impaired ISC self-renewal and increased ISC differentiation on HFD.

Further, to obtain a fine-resolved map of the EEC lineage in homeostasis and in metabolic disorder, we utilised the Foxa2-Venus fusion (FVF) reporter mouse line generated in our lab, which allowed us to enrich for EECs. We identified novel differentiation routes via Pax4$^+$ or Arx$^+$/Isl1$^+$ EE progenitors to mature EEC subsets. HFD altered numbers of EE progenitors and mature EEC subsets, including a significant decrease in numbers of a novel subset of enterochromaffin cells, expressing *Reg4*, and reduced plasma serotonin levels.

Finally, combined scRNAseq data, metabolite profiling and protein expression studies on SI crypt cells revealed upregulated fatty acid biosynthesis and Pparα/γ signalling in ISCs and progenitors on HFD. Our preliminary findings indicated that these pathways may link altered energy metabolism to hyperproliferation and cell fate changes in ISCs and progenitors.

Together, our results provide a better understanding of the molecular mechanisms underlying diet-induced disturbances in the ISC homeostasis and early pathogenesis of the EE disorder and T2D.

Further, Fltp was identified as a novel Wnt/PCP effector gene and has been shown to mediate ciliogenesis in the airway epithelia. Wnt/PCP-activated *Fltp*$^+$ ISCs directly allocate to the Paneth cell and the EEC lineage, and in the pancreas, expression of the Fltp-H2B-Venus reporter segregates mature and proliferation-competent β-cells. However, the knowledge about the cellular localisation of Fltp and its exact function in the intestine and pancreas is so far limited. In this thesis, I generated the Fltp-Venus fusion reporter mouse line to address these questions. Due to the transient and low-level expression of Fltp in the pancreas and intestine, it was technically not possible to detect Fltp in these tissues so far. On the other hand, I confirmed that the Fltp-Venus fusion mouse line is as a reliable reporter of the ciliated cell lineage in the airway epithelia and a valuable tool to study PCP-mediated ciliogenesis *in vitro* and *in vivo*.

3 Introduction

3.1 Obesity and type 2 diabetes: focus on the gut

Increased energy intake due to consumption of calorie-rich foods and sedentary lifestyle leads to obesity (Swinburn, Sacks, & Ravussin, 2009). Diet-induced obesity is a major risk factor for developing T2D. These two metabolic diseases have reached epidemic proportions worldwide, whereby the prevalence of obesity have nearly tripled for adults and has risen even more dramatically for children over the last 40 years ("WHO | *Global report on diabetes*," 2017; WHO fact sheet 2017: Obesity and overweight). According to the World Health Organization (WHO) report in 2017, the estimated number of adults with obesity accounted 650 million, and the number of people with diabetes had risen to 422 million in 2014 with an alarmingly increasing prevalence. T2D is becoming the most expensive and urgent health condition worldwide when faced with the number of deaths, directly caused by diabetes (estimated 1.6 million in 2015) or due to related complications, such as cardiovascular diseases, kidney failure, and certain types of cancer, predominantly GI cancer (Finucane et al., 2011; Makary et al., 2010; Y. C. Wang, McPherson, Marsh, Gortmaker, & Brown, 2011; "WHO | *Global report on diabetes*," 2017).

Among all diagnosed diabetes incidents, T2D is the most common form and accounts for around 90 % of all cases (Sanyal, 2013; "WHO | Definition and diagnosis of diabetes mellitus and intermediate hyperglycaemia," 2013). It is a multifactorial chronic metabolic disease characterised by a reduction in glucose-stimulated insulin secretion and insulin resistance resulting in hyperglycaemia (Alberti & Zimmet, 1998; "WHO | Definition and diagnosis of diabetes mellitus and intermediate hyperglycaemia," 2013). The metabolic symptoms may vary in dependence on the level of peripheral insulin resistance and affected tissues, but it is the progressive β-cell dysfunction that determines the rate of disease progression. Even though the susceptibility to impaired β-cell function is to a large extent attributable to genetic and/or epigenetic predisposition (Poulsen et al., 2005), the development and progression of the disease often go aong with the sedentary lifestyle and chronic overeating are often indispensable for (reviewed in Defronzo, 2009).

In the last two decades, T2D has been increasingly considered as an intestinal disease (Sanyal, 2013). Several factors support this view. First, the gut is the site of nutrient sensing and absorption, and obesity-induced adaptation of intestinal morphology and function has been reported (Dailey, 2014). Second, gut microbiota can influence not only intestinal homeostasis, but moreover the organismal metabolic balance (Sommer & Bäckhed, 2013). Interestingly, it has been shown that diet-associated alterations in the gut microbiome can predict and contribute to the development of the metabolic syndrome (Bäckhed, Manchester, Semenkovich, & Gordon, 2007; Sommer & Bäckhed, 2013; Turnbaugh et al., 2006). Finally, the intestinal endocrine system has a major role in the organismal energy control, in particular in blood glucose homeostasis (Gribble & Reimann, 2016). Moreover, gastrointestinal (GI) tract surgery (bariatric surgery) remains the only effective treatment option for severe obesity and T2D and achieves its effects due to the immense adaptation of the EE axis (Sanyal, 2013).

The intestine is the largest endocrine organ in our body (Gribble & Reimann, 2016). Secreted gut hormones, in particular incretins, are crucial regulators of the glucose and energy homeostasis (Drucker, 2007; Gribble & Reimann, 2016; Steinert et al., 2017). The two major incretins, glucagon-like peptide-1 (GLP-1) and glucose-dependent insulinotropic polypeptide (or gastric inhibitory polypeptide) (GIP), are secreted from specialised enteroendocrine L- or K-cells, respectively, and are responsible for the so called incretin effect. The incretin effect describes an enhanced insulin secretion in response to an oral glucose load compared to an equimolar intravenous glucose bolus, and accounts for up to 70 % of postprandial insulin release (Ahrén, 2013; W. Kim & Egan, 2008). The enteroendocrine (EE) dysfunction has been strongly linked to the pathogenesis and progression of T2D (Defronzo, 2009; Sanyal, 2013). Patients with severe obesity exhibit impaired secretion of gut hormones GLP-1, peptide YY (PYY) and cholecystokinin (CCK), and abnormal fasting and postprandial levels of ghrelin (Holst, 2013; Wölnerhanssen et al., 2017). In diabetic patients, the incretin axis is disturbed manifesting in incretin deficiency and incretin resistance (Ahrén, 2013; Defronzo, 2009; Drucker & Nauck, 2006; Meier & Nauck,

2006). Unlike GIP, GLP-1 retains its regulatory function on blood glucose homeostasis in subjects with T2D (W. Kim & Egan, 2008). This finding provided the basis for the development of incretin-based therapies over the last decade. To date, two types of incretin-based agents are successfully applied for T2D treatment, mostly in combination with other antidiabetic drugs (Nauck & Meier, 2016; Vilsbøll, Christensen, Junker, Knop, & Gluud, 2012). These include long-acting GLP-1 analogues, which activate the GLP-1 receptors and stimulate insulin secretion from pancreas, and dipeptidyl peptidase-4 (DPP-4) inhibitors, which block DPP-4, an enzyme responsible for the degradation of GIP and GLP-1, thus stabilising the incretins at physiologic levels. However, neither of these novel incretin-related therapies nor other available pharmacologic treatment options for T2D can achieve full remission or sustainable reduction in T2D-associated mortality at present (Nauck & Meier, 2016). Therefore, it is of urgent interest to understand the molecular mechanisms of the EE dysfunction to provide novel targets and non-invasive therapeutic strategies to combat the metabolic disorder.

3.2 Type 2 diabetes mellitus – an operable intestinal disease

Evidence collected over recent years shows that T2D is an operable intestinal disease (Mingrone et al., 2015; Rubino, Schauer, Kaplan, & Cummings, 2010; Schauer et al., 2017; Seeley, Chambers, & Sandoval, 2015). Bariatric (also metabolic) surgery is recognised as the most effective treatment for severe obesity and T2D (Adams et al., 2012, 2007; Seeley et al., 2015). An incomparable benefit of the bariatric surgery over the conventional pharmacological therapies is, besides the substantial body weight reduction, a striking remission rate of up to 80 % with long-term resolution of T2D (Finucane et al., 2011; K.-S. Kim, Seeley, & Sandoval, 2018; Mingrone et al., 2015; Purnell et al., 2016; Schauer et al., 2017; Singh, Singh, & Kota, 2015). Evidence collected from surveys indicates that the improvement of the glycaemic control, β-cell function and insulin sensitivity is, in fact, weight loss-independent (Bradley et al., 2012; Laferrere et al., 2011; Rubino & Marescaux, 2004; Rubino et al., 2010). Even though this effect was described more than 30 years ago (Ackerman, 1981), the underlying mechanisms are not yet fully understood and are still focus of intense research. The success of the bariatric surgery was originally attributed to the mechanical restriction and malabsorption (Jackness et al., 2013; Plourde et al., 2014). However, increasing body of evidence suggests that alterations in bile acid levels, their composition and signalling, as well as changes in the gut microbiome and a neuro-hormonal adaptation contribute to the normalisation of energy homeostasis after surgery (summarised in Figure 1) (Grenier-Larouche, Carreau, & Carpentier, 2017; Holst, 2013; Hutch & Sandoval, 2017; K.-S. Kim et al., 2018; Seeley et al., 2015). Modifications of the EE axis involve greater postprandial peptide YY (PYY) and cholecystokinin (CCK) secretion, reduced ghrelin signalling and according changes in the numbers of EECs secreting these hormones (Hutch & Sandoval, 2017; Jacobsen et al., 2012; Peterli et al., 2012; Seeley et al., 2015; Tsoli, Chronaiou, Kehagias, Kalfarentzos, & Alexandrides, 2013). The major role for the normalisation of the glycaemic control and weight loss, however, has been attributed to the substantial increase in postprandial GLP-1 secretion (5 to 10-fold), which precedes weight loss (Jørgensen et al., 2013; Martinussen et al., 2015; Seeley et al., 2015). It is clear, yet, that GLP-1 can be not uniquely responsible for the whole range of beneficial effects after surgery, but the combination of the physiologic changes determines the success of the metabolic surgery (Seeley et al., 2015). This understanding has led to the development of combined therapies with dual or even triple receptor agonists (GIP, GLP-1, glucagon) to mimic surgery-induced EE changes and achieve a better therapy effectiveness (K.-S. Kim et al., 2018).

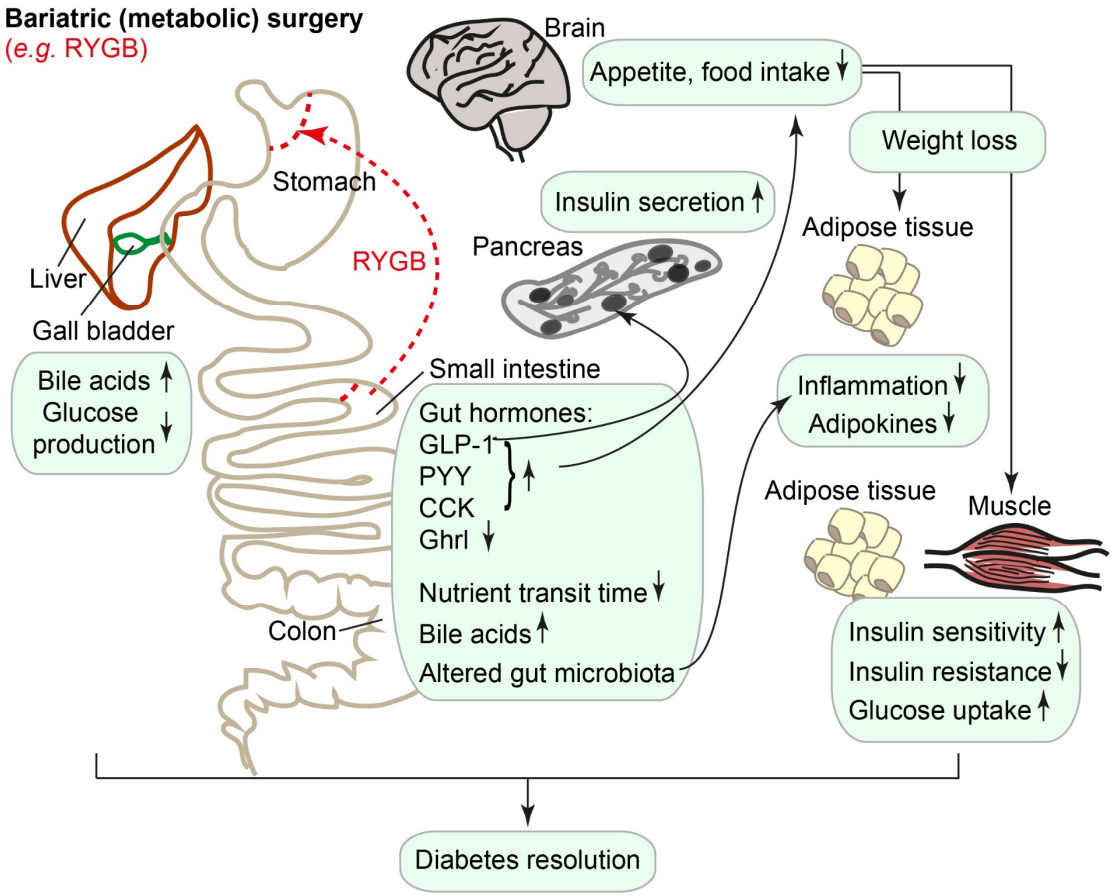

Figure 1: Mechanisms underlying diabetes resolution after bariatric surgery using the example of RYGB

Schematic depicts physiologic changes and crosstalk between these effects contributing to long-term weight loss and diabetes resolution after bariatric surgery. Involved mechanisms include intestinal anatomical changes leading to a more rapid nutrient transit, altered gut hormone levels and signalling, reduced food intake, appetite and adiposity. A remarkable increase in GLP-1 levels contributes to improved insulin secretion from the pancreas. Moreover, changes in gut microbiota composition and availability of bile acids occur. Both, improved glucose disposal and insulin sensitivity in the peripheral organs, such as muscle and adipose tissue, and reduced glucose production in the liver, contribute to improved glycaemic control after surgery. The intercaction of these effects leads to long-term weight loss and diabetes resolution in the majority of patients.
RYGB: Roux-en-Y Gastric Bypass; GLP-1: glucagon-like peptide1; PYY: peptide YY; CCK: cholecystokinin; Ghrl: ghrelin.

3.3 Obesity and risk of cancer

A growing body of evidence suggests that obesity is a common risk factor for diabetes and several types of cancer, such as pancreatic, breast, endometrium, gall bladder, oesophageal cancer and several others (Arnold et al., 2015; Font-Burgada, Sun, & Karin, 2016; Stone, McPherson, & Gail Darlington, 2018). In particular, colon cancer has shown the most clear relationship with BMI and consumption of Western-style diet, which is characterised by processed foods and high contents of fat, sugars and protein from red meat (Calle & Kaaks, 2004; Dermadi et al., 2017; Stone et al., 2018). Based on the previous literature studies, an altered endocrine milieu, involving an abnormal insulin/IGF-1[1] axis, dysregulated adipokine (leptin, adiponectin) signalling, as well as changes in fatty acid metabolism and chronic low-grade inflammation, or a combination of these, are listed among the factors involved in obesity-associated

[1] IGF: insulin-like growth factor

carcinogenesis (Calle & Kaaks, 2004; Font-Burgada et al., 2016; Klil-Drori, Azoulay, & Pollak, 2017; Stone et al., 2018). However, the precise molecular mechanisms linking obesity and cancer remain poorly understood and are area of intense research.

Furthermore, elevated levels of pro-inflammatory cytokines, such as TNFα and IL-6[2], derived from obese adipose tissue, have been shown to promote systemic chronic low-grade inflammation typically associated with obesity and diabetes (Font-Burgada et al., 2016). These cytokines are potent inducers of tumour proliferation and has been correlated with increased prevalence of colorectal adenomas (Font-Burgada et al., 2016; Stone et al., 2018).

Interestingly, evidence from studies in mice suggests that the chronic inflammation may have its origin in the gut (Cani & Jordan, 2018; Font-Burgada et al., 2016; Schwabe & Jobin, 2013). Diet-induced obesity (DIO) induces a shift in the microbiome composition (dysbiosis) in the colon. Many reports have shown that dysbiosis is linked to a higher epithelial permeability to microbial components such as *lipopolysaccharide (*LPS). LPS reaches the circulation and stimulate production of TNFα and IL-6, thus, enhancing systemic inflammation (Cani et al., 2007; Cani & Jordan, 2018; Font-Burgada et al., 2016). A clear evidence links DIO-specific microbiota to colorectal cancer development (Cani & Jordan, 2018; Schwabe & Jobin, 2013). Notably, a recent study has suggested that the pro-tumorigenic effect of HFD on the intestinal cancer is not related to obesity *per se*, but is mainly due to the dysbiosis (Schulz et al., 2014). Moreover, studies indicate that also the metabolic products of the altered gut microbiome can contribute to the progression of colon and liver cancer (Cani & Jordan, 2018).

As mentioned above, chronically elevated insulin levels have also been associated with the progression of different types of cancer and, in particular, colon cancer (Calle & Kaaks, 2004; Renehan, Frystyk, & Flyvbjerg, 2006; Stone et al., 2018). These effects can be mediated by two mechanisms, an increase in expression of insulin receptors on tumour cells and/or by insulin-dependent increase in systemic IGF-1 availability which favours tumour formation.

3.4 Intestinal physiology, architecture and cellular organisation

3.4.1 Intestinal physiology and architecture

The intestine is an endoderm-derived organ and is anatomically subdivided into small and large intestine (Figure 2A) (Chin, Hill, Aurora, & Spence, 2017; de Santa Barbara, van den Brink, & Roberts, 2003). Whereas water re-absorption and mucus secretion take place mainly in the large intestine (colon), the main function of the small intestine is nutrient digestion and absorption as well as antimicrobial defence (Brugmann & Wells, 2013; Hitz, Wurst, & Kuhn, 2007). The small intestine is further subdivided into three segments along the proximal-distal axis, duodenum, jejunum and ileum, which exhibit differences in morphology, cell type composition and gene expression programmes, establishing specialised functions (Figure 2A) (Anderle et al., 2005; Bates et al., 2002; Comelli et al., 2009; Gribble & Reimann, 2016; Haber et al., 2017; Middendorp et al., 2014). Thereby, the main function of the duodenum and jejunum is digestion, absorption of nutrients, minerals (*e.g.* iron and calcium) and water-soluble vitamins, whereas ileum takes up residual nutrients, vitamin B12 and re-absorbs bile acids.

To maximise the absorptive area, the surface of the small intestine is enlarged by millions of protrusions of the single-layered epithelium, called villi, as well as by invaginations into the submucosa, called crypts of Lieberkühn (Figure 2B, C) (Beumer & Clevers, 2017; H. Clevers, 2013). The crypts mainly harbour stem cells and progenitors and constitute the proliferative compartment, whereas villi contain differentiated absorptive and secretory cells.

Due to the constant chemical and mechanical stress, cells at the top of the villi are shed into the lumen and have to be replaced on a daily basis (Marshman, Booth, & Potten, 2002). Thus, the intestinal

[2] IL-6: interleukin 6; TNFα: tumour necrosis factor α

epithelium is characterised by an immense self-renewal rate of three to seven days in mammals (Barker et al., 2007; Cheng & Leblond, 1974; Potten, Kovacs, & Hamilton, 1974).

Four major signalling pathways regulate intestinal epithelial homeostasis, including Wnt, epidermal growth factor (EGF) and Notch signalling, all being active in the crypt compartment, and the bone morphogenetic protein (BMP) signalling, which is active in the villus (H. Clevers, 2013). Moreover, gut homeostasis depends on a complex interplay between intestinal epithelial cells, the gut microbiota and immune cells (Duerkop, Vaishnava, & Hooper, 2009; McCole & Barrett, 2007; Sommer & Bäckhed, 2013). Remarkably, the intestine harbours the biggest microbial community of the body, comprising around 10^{14} bacteria. Commensal microbiota are important for many physiological functions, such as metabolic homeostasis, immunity, and behaviour, and bacterial imbalance has been implicated in a number of diseases (Backhed, Ley, Sonnenburg, Peterson, & Gordon, 2005; Sommer & Bäckhed, 2013).

Moreover, the intestine is the largest endocrine organ of the body, harbouring the greatest variety of endocrine cell types and hormones (Sternini, Anselmi, & Rozengurt, 2008). Gut hormones secreted from specialised EECs are involved in systemic regulation of satiety and appetite, digestion, blood glucose levels and long-term energy homeostasis (Moran, Leslie, Levison, Worthington, & McLaughlin, 2008).

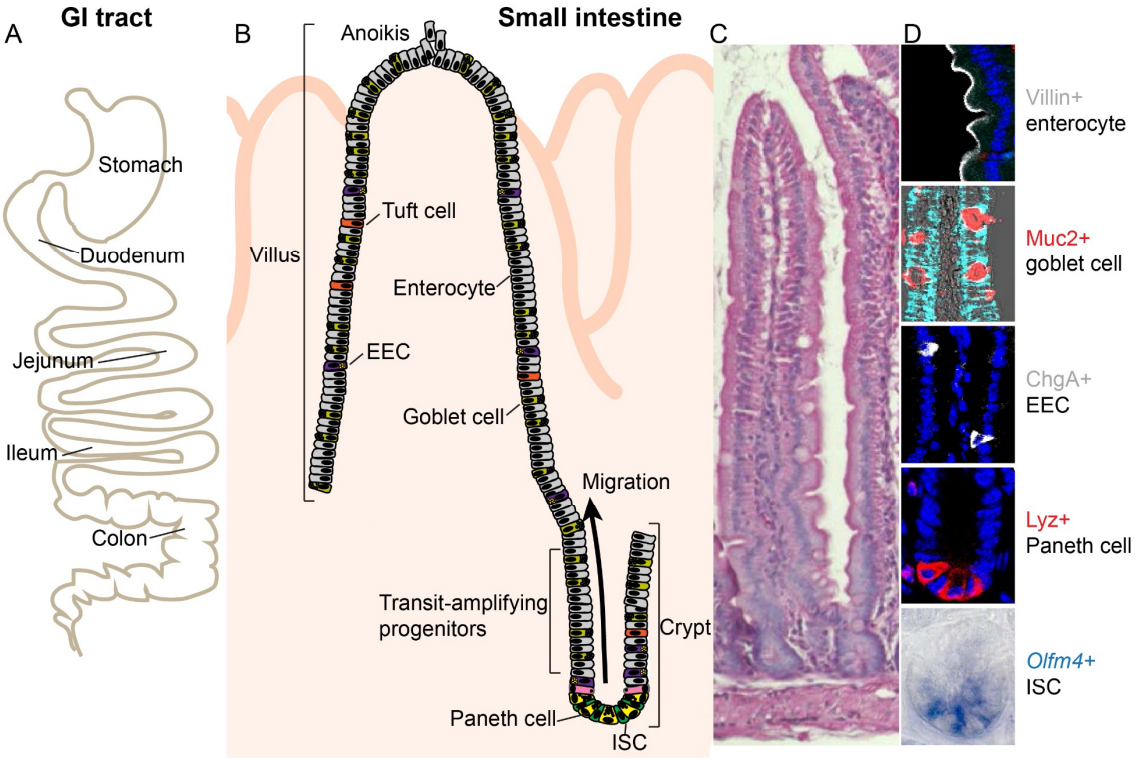

Figure 2: Scheme of intestinal epithelial structure and cell types

(A) Simplified drawing of the structure of the gastrointestinal (GI) tract.
(B) Cartoon depicts structural organisation of the small intestinal epithelium into villi and crypts. ISCs reside at the crypt bottom, intercalated with Paneth cells, and continously produce rapidly proliferating transit-amplifying cells. The latter differentiate, while moving upwards into the villus, thus constantly replacing cells lost via anoikis at the villus tip.
(C) Haematoxylin and eosin (H&E) staining of a duodenal tissue section showing villi and crypt structures.
(D) SI epithelial cell types are depicted as visualised by immunofluorescence stainings. Mature cells, found in villi and crypts, comprise villin+ enterocytes, Muc2+ goblet cells, ChgA+ EECs, Lyz+ Paneth cells and tuft cells (not shown). ISCs, marked by *Olfm4* expression, are found at the crypt bottom.
Muc2: mucin 2; ChgA: chromogranin A; Lyz: lyzosyme; Olfm4: olfactomedin 4; ISC: intestinal stem cell; EEC: eneteroendocrine cell.

3.4.2 Cellular organisation of the small intestine

The cellular organisation of the small intestinal epithelium follows its functional compartmentalisation into villi and crypts. Mature and specialised cells are mostly found in the villi, whereas mainly undifferentiated stem cells and progenitor populations constitute the proliferative crypt domain (Figure 2B, D). The six functional cell types of the intestinal epithelium comprise enterocytes, goblet, enteroendocrine (EE), Tuft, Paneth and microfold (M) cells (Figure 2D) (Cheng & Leblond, 1974; H. Clevers, 2013). M cells are found in the specialised epithelium associated with ileal Peyer's patches and promote an efficient induction of mucosal immune responses to specific antigens (Cheng & Leblond, 1974; Mabbott, Donaldson, Ohno, Williams, & Mahajan, 2013; Noah, Donahue, & Shroyer, 2011). Enterocytes are the most abundant cell type of the villi, and EECs, goblet and Tuft cells are found in both, villi and crypts. The main function of enterocytes, as the most abundant cell type in the entire intestinal epithelium, is nutrient absorption and basal transport (van der Flier & Clevers, 2009). Goblet cells are the most frequent intestinal secretory cell type, and produce mucins to maintain a protective mucus barrier (Noah et al., 2011). EECs are found scattered throughout the gut and comprise only about 1 % of all intestinal epithelial cells, but collectively constitute the largest endocrine system in humans (Gribble & Reimann, 2016; Sternini et al., 2008). EECs sense luminal contents, including nutrients and microbial metabolites, and secrete hormones involved in regulation of pancreatic insulin secretion, appetite and satiety, gastrointestinal (GI) functions and release of digestive enzymes from the gall bladder and pancreas, among other things (Furness, Rivera, Cho, Bravo, & Callaghan, 2013; Gribble & Reimann, 2016; Moran et al., 2008). Paneth cells are long-lived (6-8 weeks) secretory cells and the only type of terminally differentiated cells that are exclusively found at the crypt bottom (Figure 2D) (Ireland, Houghton, Howard, & Winton, 2005; Sato et al., 2011). They secrete antimicrobial peptides, such as lysozymes and α-defensins (cryptdins), and regulate the maintenance of normal gut microbiome (Salzman et al., 2010). Moreover, Paneth cells provide niche support to stem cells through several ligands such as Wnt3, EGF, TGF-β and Notch ligands, Dll1 and Dll4[3] (H. C. Clevers & Bevins, 2013; Farin, Van Es, & Clevers, 2012; Sato et al., 2011). The classification of the poorly studied Tuft cells as secretory lineage is, however, controversial (Bjerknes et al., 2012; François Gerbe et al., 2011). Similar to EECs, they also express taste-chemosensory receptors, but, on the other hand, mediate parasite-induced immune response in the gut (Haber et al., 2017; Middelhoff et al., 2017; Noah et al., 2011).

The crypts of Lieberkühn are mainly populated by proliferative stem cells, rapidly cycling undifferentiated progenitors (also called transit-amplifying (TA) cells) and terminally differentiated Paneth cells (Figure 2B) (H. Clevers, 2013). A small intestinal (SI) crypt harbours 12-16 stem cells (up to 10% of the crypt cell mass) and around 10 Paneth cells (Barker et al., 2007; H. Clevers, 2013; Snippert et al., 2010). Adult ISCs reside at the crypt bottom interspersed between the Paneth cells and are characterised by self-renewal and multipotent differentiation potential (Barker et al., 2007). ISCs, first described as so called crypt base columnar cells (CBCs) by Cheng and Leblond, are marked by the expression of the leucine-rich repeat-containing G-protein-coupled receptor 5 *(Lgr5)* gene and divide every 24 hours to maintain tissue homeostasis (Barker et al., 2007; Cheng & Leblond, 1974). Typically, one stem cell per crypt establishes its predominance, thus, generating monoclonal crypts over time (A. M. Klein & Simons, 2011; Lopez-Garcia, Klein, Simons, & Winton, 2010; Snippert et al., 2010). The villi, however, remain polyclonal as they receive cellular input from multiple crypts.

ISC maintenance is supported by niche signals from Paneth and surrounding mesenchymal cells (H. Clevers, 2013; Farin et al., 2012; Valenta et al., 2016). As niche space in the crypt base is limited, half of the newly generated ISC daughters are pushed upward and lose stemness, while either going through several rounds of division in the TA zone or directly differentiating into distinct progenitors (Andersson-Rolf, Zilbauer, Koo, & Clevers, 2017; H. Clevers, 2013; Boettcher et al., in revision). Lineage-restricted TA cells undergo four to five rounds of rapid cell divisions before they exit the crypt space

[3] TGF-β: transforming growth factor β; Dll1 and Dll4: Delta-like 1 and 4.

and terminally differentiate into functional cell types of the villi (Andersson-Rolf et al., 2017; Cheng & Leblond, 1974; Heath, 1996; Stange & Clevers, 2013).

3.5 Intestinal lineage allocation and signalling determinants

3.5.1 ISC heterogeneity and signalling determinants for ISC homeostasis

The SI epithelium is a tissue with the fastest proliferation rate in mammals and has served as an excellent model system to study stem cell biology and lineage formation (Stange & Clevers, 2013). ISC self-renewal and differentiation is controlled by Wnt, Notch, EGF, TGF-β/BMP and phosphatidyl inositol (3,4,5) kinase (PI3K) signalling (Figure 3A) (Biteau & Jasper, 2011; Farin et al., 2012; Kosinski et al., 2007; Pellegrinet et al., 2011; Valenta et al., 2016). Notch ligands, Dll1 and Dll4, from neighbouring Paneth cells maintain ISCs by blocking the differentiation toward the secretory fate (Pellegrinet et al., 2011; Riccio et al., 2008). EGF receptor signalling upholds the mitogenic programme in the ISCs (Biteau & Jasper, 2011). Mesenchymal-derived BMP signals are active in the villus, and expression of BMP inhibitors (noggin, chordin, ghremlin1/2) in the crypt is required to protect ISCs from cell cycle exit and differentiation (Kosinski et al., 2007).

Canonical Wnt signalling is essential for ISC homeostasis (Fevr, Robine, Louvard, & Huelsken, 2007; V Korinek et al., 1998; D. Pinto, Gregorieff, Begthel, & Clevers, 2003). Wnt gradient along the crypt axis plays a crucial role in the control of stemness, proliferation and differentiation (Vladimir Korinek et al., 1998; Reya & Clevers, 2005; van der Flier & Clevers, 2009). The strongest Wnt signals are present at the crypt base, and exposure to less Wnt and other growth factors upwards along the crypt axis drives cell cycle exit and differentiation (Figure 3A) (Farin et al., 2016). Paneth cells are exception to this concept as their differentiation and maturation are Wnt-dependent (Gregorieff et al., 2005; van der Flier & Clevers, 2009; Johan H van Es, Jay, et al., 2005). R-spondins are potent Lgr-dependent Wnt agonists secreted from the stromal niche (Figure 3A) (de Lau, Peng, Gros, & Clevers, 2014; Kabiri et al., 2014). Whereas Wnt ligands provide the basal competency, but cannot alone maintain the stem cell niche, R-spondins are crucial for Wnt signalling amplification and emerged to be indispensable for ISC self-renewal (Yan, Janda, et al., 2017).

Lgr5 is a well described marker of cycling ISCs and is itself a Wnt target gene (Barker et al., 2007; van der Flier & Clevers, 2009). However, not all ISCs are Wnt-dependent and actively cycling as suggested by numerous studies. Evidence for functional heterogeneity, possible hierarchy and high level of plasticity within the ISC population based on expression of specific markers, position in the crypt, cell cycle activity and lineage potential, has been provided by several reports and is still subject of controversial debate (Buczacki et al., 2013; Montgomery et al., 2011; Powell et al., 2014; Ritsma et al., 2014; Takeda et al., 2011; Johan H van Es et al., 2012; Yan et al., 2012; Boettcher et al., in revision).

First, position within the crypt matters: Lgr5$^+$ ISCs close to the crypt bottom are more likely to remain in the stem cell zone and produce bigger clones than stem cells in the periphery (Ritsma et al., 2014). Apart from the positional heterogeneity, long-term lineage tracing studies identified long-lived label-retaining cells (LRCs) cells, which meet the criteria defining a stem cell (summarised in Figure 3B). These slow-cycling or quiescent stem cells are characterised by a distinct localisation in the crypt, mainly, at the +4 position, (Hughes et al., 2012; Potten et al., 1974), expression of specific markers, such as *Bmi1*, *Hopx*, *mTERT* or *Lrig1*[4] and/or by the co-expression of mature secretory lineage markers (Montgomery et al., 2011; Powell et al., 2014; Sangiorgi & Capecchi, 2008; Takeda et al., 2011) and differential response to Wnt pathway activation (N. Li, Nakauka-Ddamba, Tobias, Jensen, & Lengner, 2016; J. H. van Es et al., 2012; Yan et al., 2012). Upon depletion of actively cycling Lgr5$^+$ cells, quiescent Bmi1$^+$ cells, as well

[4] Bmi1: B cell-specific Moloney murine leukemia virus integration site 1; Hopx: Homeodomain-only protein; mTERT: Mouse telomerase reverse transcriptase; Lrig1: Leucine-rich repeats and immunoglobulin-like domains protein 1

as other mentioned proposed ISC identities, were able to maintain intestinal homeostasis (Montgomery et al., 2011; Powell et al., 2014; Sangiorgi & Capecchi, 2008; Takeda et al., 2011). Though the recent single-cell transcriptomics-based study by Li et al., 2014 comparing the conventional stem cell proxy reporters targeted into *Lgr5*, *Bmi1* and *Hopx* loci supports the functional divergence of reserve *versus* cycling Lgr5⁺ ISCs (N. Li et al., 2016, 2014), conflicting reports on the validity of the *Bmi1-* and *Hopx-Cre* reporters for reserve ISCs exist in the literature. Two groups reported that markers of the quiescent ISCs, discussed above, are expressed more broadly in the crypt and are co-expressed in Lgr5⁺ ISCs (Itzkovitz et al., 2012; Muñoz et al., 2012).

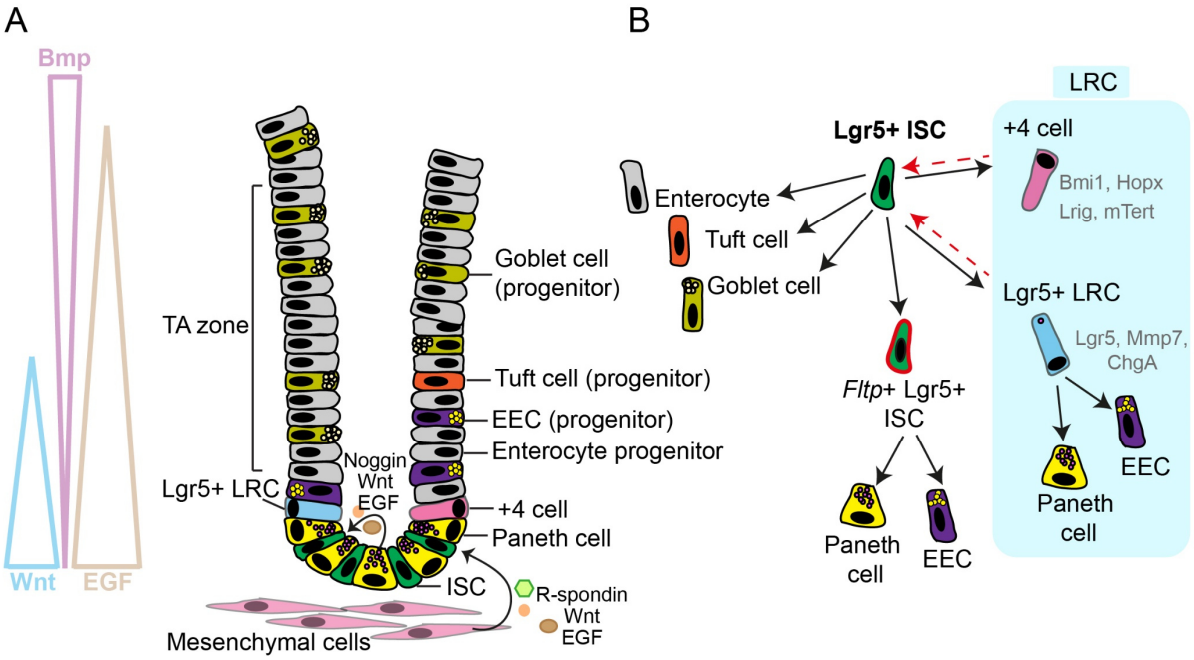

Figure 3: Models of ISC heterogeneity and signalling determinants for ISC maintenance

(A) Scheme of the SI crypt niche depicting epithelial cell types and signalling cues. Spatial gradients of Wnt, EGF and BMP signals exist along the crypt axis. Wnt and EGF signalling is highly active, whereas Bmp signals are low at the crypt bottom. ISCs receive signals from Paneth and mesenchymal cells (Wnt, EGF, R-spondin, Noggin), which are essential to maintain stemnes and ISC proliferation

(B) Simplified scheme of proposed models for ISC identities and lineage relations. Actively cycling Lgr5⁺ ISCs give rise to absorptive, goblet and tuft cells, whereas recently identified Fltp⁺ Lgr5⁺ ISCs directly allocate into Paneth cells and EECs (Boettcher et al., in revision). Other stem cell identities have been described, including the +4 reserve stem cell and Lgr5⁺ LRC. The +4 cell (often found at the fourth position from the crypt bottom) is marked by the expression of Bmi1, Hopx, Lrig1 or Hopx. The Lgr5⁺ label-retaining cell (LRC) co-expresses Lgr5 and secretory cell markers and gives rise to Paneth cells and EECs. Both described LRC stem cells can restore Lgr5⁺ ISCs and crypt compartment following injury. Hierarchical relations between these ISC identities are not yet fully clear.

Another level of complexity was added to the ISC heterogeneity by independent studies showing that also secretory progenitors can acquire multi-lineage potential and maintain intestinal homeostasis upon injury (Figure 3B) (Buczacki et al., 2013; Johan H van Es et al., 2012). Buczacki et al. reported that LRCs are secretory progenitors under homeostatic conditions which co-express *Lgr5* and markers of EECs and Paneth cells. Additionally, van Es and colleagues revealed that the proliferative population of Lgr5-negative Dll1⁺ secretory progenitors can adopt characteristics of ISCs (J. H. van Es et al., 2012). Both, secretory LRCs and Dll1⁺ secretory progenitors, have the ability to restore intestinal homeostasis after radiation injury (Buczacki et al., 2013; Johan H van Es et al., 2012). Furthermore, Sox9-EGFP^{High} cells were suggested to be injury-inducible reserve ISCs co-expressing EE hormones (Van Landeghem et al., 2012).

Taken together, these findings show that the stem cell compartment is heterogeneous and highly plastic. Additionally, not only committed secretory LRCs, but, moreover, enterocyte progenitors have been shown to revert to functional Lgr5$^+$ ISCs upon depletion of resident ISCs (Buczacki et al., 2013; Tetteh et al., 2016; Johan H van Es et al., 2012). This is not surprising when considering that the epigenetic status of the ISCs remains almost unchanged upon differentiation (T.-H. Kim et al., 2014). Thus, the plasticity within the stem cell and progenitor system is allowed by the permissive chromatin and is rather defined by environmental cues (T.-H. Kim et al., 2014).

3.5.2 Signalling determinants for the secretory and absorptive lineage in the intestine

The established model of lineage segregation from the Lgr5$^+$ ISCs describes secretory *versus* absorptive lineage commitment as a binary fate decision through Notch/Delta-mediated lateral inhibition in the immediate stem cell daughter (Fre et al., 2005; Riccio et al., 2008; Q. Yang, Bermingham, Finegold, & Zoghbi, 2001). Proliferative cells in the crypt compartment express Notch1 and Notch2 receptors (Riccio et al., 2008), which can be activated by their ligands Dll1 and Dll4 (Pellegrinet et al., 2011). Paneth cells express Notch ligands, thus activating Notch receptors and expression of Notch target gene hairy and enhancer of split-1 (*Hes1*) on adjacent stem cells (Jensen et al., 2000; Sato et al., 2011). Van Es and colleagues described *Dll1*-expressing cells positioned above the ISC/Paneth cell zone, which can activate Notch receptors on the cells in the TA zone (Johan H van Es et al., 2012). Kim et al., on the other hand, provided evidence for the existence of so-called ISC-derived bipotent progenitors, which are characterised by reduced levels of ISC markers and co-expression of absorptive and secretory markers (T.-H. Kim et al., 2016). It was suggested that lineage priming by lateral inhibition occurs exactly in these cells (T.-H. Kim et al., 2016).

Protein atonal homolog 1 (Atoh1) and Hes1 are the two downstream transcription factors that mediate the differentiation into secretory cells or enterocytes, respectively, whereby Hes1 represses Atoh1 (Jensen et al., 2000; Shroyer et al., 2007; Johan H van Es, de Geest, van de Born, Clevers, & Hassan, 2010; Johan H van Es, van Gijn, et al., 2005; Q. Yang et al., 2001). Loss of Atoh1 results in loss of Paneth, goblet cells and EECs (Q. Yang et al., 2001). Hes1 is critical for the commitment to the absorptive cell lineage (Jensen et al., 2000), and inhibition of intestinal Notch signalling converts proliferating crypt progenitors into goblet cells (Milano et al., 2004; Johan H van Es, van Gijn, et al., 2005).

The potency of secretory progenitors and the mechanisms that regulate further specification into goblet, Paneth, EECs and Tuft cells, are controversial and not yet fully understood (Bjerknes & Cheng, 2010; Buczacki et al., 2013; Grün et al., 2015, 2016; Heuberger et al., 2014; T.-H. Kim et al., 2016; N. Li et al., 2016; Noah, Kazanjian, Whitsett, & Shroyer, 2010; Shroyer, Wallis, Venken, Bellen, & Zoghbi, 2005; Johan H van Es et al., 2012). A direct commitment of ISCs or lineage specification via multi- or bipotent secretory progenitors have been proposed so far and can be summarised as follows.

1) Multipotent secretory progenitor:

   a) A *Dll1*$^+$ multipotent secretory progenitor can give rise to all four secretory cell types (Johan H van Es et al., 2012);

   b) A multipotent enterocyte/secretory progenitor has been proposed, which co-expresses markers of absorptive and secretory lineage and is susceptible to Notch/Delta lateral inhibition (T.-H. Kim et al., 2016).

2) Bipotent goblet/Paneth cell progenitor:

   a) Single-cell transcriptional study by Grün et al. suggests a differentiation route into goblet and Paneth cells via a bipotent progenitor (Grün et al., 2015, 2016);

   b) Gfi1[5] controls EEC *versus* goblet/Paneth cell type allocation from Atoh1$^+$ secretory progenitor through repression of Neurogenin3 (Neurog3) (Bjerknes & Cheng, 2010; Shroyer et al., 2005);

[5] Gfi1: Growth factor independent 1

c) Shp2/MAPK[6] signalling controls goblet *versus* Paneth cell fate choice from a common progenitor (Heuberger et al., 2014);

d) Spdef1[7] is suggested to regulate maturation of Paneth and goblet cells from a common progenitor pool (Gregorieff et al., 2009; Noah et al., 2010);

d) Loss of Sox9 results in reduction of Paneth and goblet cell numbers (Bastide et al., 2007).

3) Direct differentiation route from ISCs to Paneth cells

a) Buczacki and colleagues proposed a direct allocation of Paneth cells and EECs from a common Lgr5$^+$ LRC as a secretory progenitor (Buczacki et al., 2013);

b) Depleted Paneth cells directly mature from Lgr5$^+$ ISCs after damage (Sawada, Takahashi, Sawada, & Midorikawa, 1991).

c) Using single-cell transcriptomics, our lab has identified a subset of Lgr5$^+$ ISCs marked by *Fltp* expression, a Wnt/planar cell polarity (PCP) reporter and effector gene (Figure 3B) (Böttcher et al., in revision). Lineage tracing and functional analyses confirmed that Wnt/PCP-primed *Fltp*$^+$ ISCs directly allocate to the Paneth cell and EE lineage (Böttcher et al., in revision). Moreover, canonical Wnt-dependent Lgr5$^+$ ISCs and *Fltp*$^+$ Wnt/PCP-primed ISCs are otherwise indistinguishable by their transcriptomes with regard to ISC or secretory marker expression (Böttcher et al., in revision). This suggests that Wnt/PCP-mediated priming towards Paneth and EE cell fates precedes the Notch/Delta-mediated lateral inhibition.

Specification of goblet cells from secretory progenitors has been considered as a default fate within the secretory lineage, since all proliferative cells convert into goblet cells upon Notch inhibition (Milano et al., 2004; Johan H van Es, van Gijn, et al., 2005). Transcription factors Spdef1 and Gfi1 have been described to be important for the specification of goblet cells from a common Atoh1$^+$ secretory progenitor (Gregorieff et al., 2009; Noah et al., 2010). The zinc-finger transcriptional repressor Gfi1 is hereby important for the stable repression of the EEC fate-defining transcription factor Neurog3 (Shroyer et al., 2005). Interestingly, apart from its role in the secretory lineage specification, Notch activity is important for goblet cell maturation (Vooijs et al., 2007; Zecchini, Domaschenz, Winton, & Jones, 2005). Kruppel-like factor 4 (Klf4), a transcription factor regulated by Notch pathway was also reported to regulate goblet cell differentiation (Ghaleb, McConnell, Kaestner, & Yang, 2011; Katz et al., 2002).

Furthermore, Tuft cell allocation is still poorly understood. However, a study from Gerbe and colleagues has reported that Tuft cells require expression of Pou domain, class 2, transcription factor 3 (Pou2f3) (F Gerbe & Jay, 2016; François Gerbe et al., 2011).

Finally, enterocyte lineage specification is known to require Hes activity. Deletion of *Hes1* leads to decreased numbers of enterocytes, and the effect is more pronounced upon deletion of Hes1, Hes3, and Hes5 (Jensen et al., 2000; Ueo et al., 2012). On the other hand, differentiation into absorptive lineage has been also considered a default commitment upon exposure to lower levels of Wnt signals above the ISC zone (Fevr et al., 2007). Moreover, new factors have been associated with fate commitment to absorptive lineage, such as Foxm1, Batf2 and Mdx3 (Haber et al., 2017).

3.5.3 Subtype specification of enteroendocrine cells

EECs are chemosensory cells and involved in the regulation of food intake, GI functions, such as motility and digestion, and in maintaining long-term energy homeostasis through a variety of secreted hormones (Cummings & Overduin, 2007; Drucker, 2007; Gribble & Reimann, 2016). Up to 20 different multi-hormonal cell types have been reported to date (Beumer et al., 2018; Grün et al., 2015; Haber et

[6] Shp2: Src homology region 2 domain-containing phosphatase-2; MAPK: Mitogen-activated protein kinase
[7] Spdef1: SAM pointed domain ETS factor 1

al., 2017; Habib et al., 2012). Historically, EECs were considered mainly mono-hormonal cells and were subdivided according to the main hormone they secrete in S-cells (sectretin, Sct), L-cells (GLP-1), K-cells (GIP), D-cells (somatostatin, Sst), I-cells (Cck), A-cells (ghrelin, Ghrl), enterochromaffin cells (serotonin or 5-hydroxy-tryptamine, 5-HT) *etc*. (Engelstoft, Egerod, Lund, & Schwartz, 2013; Gribble & Reimann, 2016). However, recent studies suggest more complex patterns of gut hormone co-localisation, that depend on the regional distribution of the EEC subsets in the intestine (Beumer et al., 2018; Gribble & Reimann, 2016; Grün et al., 2015; Haber et al., 2017; Habib et al., 2012; Steinert et al., 2017; Svendsen et al., 2015; Worthington, Reimann, & Gribble, 2018). For example, ghrelin, CCK and GIP are secreted from EECs in the proximal intestine, whereas GLP-1 and PYY are co-secreted predominantly from L-cells in the distal intestine, and some hormones, such as serotonin are produced along the whole length of the gut.

The specification of the EEC lineage requires transient expression of the transcription factor Neurog3 (Jenny et al., 2002; C. S. Lee, Perreault, Brestelli, & Kaestner, 2002). Downstream of Neurog3, a complex network of overlapping transcription factors has been shown to regulate subset allocation and terminal differentiation of the EECs, but the exact mechanisms are far from being understood (Gribble & Reimann, 2016; Worthington, Reimann, & Gribble, 2018). Transcription factors that have been shown to regulate formation of distinct EEC subsets include Neurod1, Isl1, Pdx1, Pax4, Pax6, Nkx2.2, Insm1, Foxa2, Arx, Rfx3 and Rfx6[8] (Beucher et al., 2012; Desai et al., 2008; Gierl, Karoulias, Wende, Strehle, & Birchmeier, 2006; Gribble & Reimann, 2016; Larsson, St-Onge, Hougaard, Sosa-Pineda, & Gruss, 1998; H. J. Li, Ray, Singh, Johnston, & Leiter, 2011; May & Kaestner, 2010; Naya et al., 1997; Worthington et al., 2018; Ye & Kaestner, 2009). Interestingly, these factors are, in large part, the same that regulate endocrine cell type formation in the pancreas, indicating high degree of similarity between pancreatic and intestinal endocrine cells. In addition, transcription factors Cdx-2, Hnf1a, Hnf1b, Gata4, Gata5, Gata6 and Cdp[9], and Pdx1, which are involved in gut development and are expressed in gradients along the adult gastrointestinal tract (GI) tract, may influence formation and regional distribution of the EEC subsets (Fang, Olds, & Sibley, 2006; Gribble & Reimann, 2016; Haber et al., 2017).

3.6 Impact of dietary changes on the intestinal homeostasis and stem cell function

3.6.1 Rodent models of diet-induced obesity and metabolic disorders

In humans, development of obesity and metabolic syndrome is often attributed to overeating, poor-quality (high-fat, high-sugar, low-fibre *etc*.) diets, and sedentary lifestyle, and may involve years of complex pathophysiologic changes. To circumvent these issues, diets mimicking the composition of the Western-style diet, *e.g*. HFDs with 20–60 % calorie intake from fat, have been commonly used to generate obese rodent models (Buettner, Schölmerich, & Bollheimer, 2007). Such dietary treatments have been shown to induce metabolic disorders in animal models, involving dyslipidaemia, hyperglycaemia, insulin resistance and impaired β-cell function and resembling the human metabolic syndrome (Buettner et al., 2007; C.-Y. Wang & Liao, 2012; Winzell & Ahrén, 2004). However, HFD-induced phenotypes can vary considerably depending on the duration of the dietary intervention, diet composition and genetic background of mice used in the study (Buettner et al., 2007; C.-Y. Wang & Liao, 2012). Due to the differences in the genetic landscape, mouse strains present with distinct degrees of susceptibility or resistance to diet-induced obesity (DIO) and associated metabolic disorders, with a higher responsiveness of the DBA/2J and C57BL/6J mice and resistance of the Balb/cJ mouse model

[8] Neurod1: Neurogenic differentiation 1, insulin gene enhancer protein 1; Pdx1: Pancreatic and duodenal homeobox 1; Pax4/6: paired box 4/6; Nkx2-2: NK2 Homeobox 2; Insm1: insulinoma-associated 1; Foxa1/2: Forkhead box A1/A2; Arx: Aristaless related homeobox; Rfx3/6: Regulatory factor X3.

[9] Cdx-2: Caudal type homebox 2; Hnf1a/b: Hepatocyte nuclear factor 1a/1b; Gata4-6: GATA binding protein 4-6; Cdp: CCAAT-displacement protein

(Buettner et al., 2007; Clee & Attie, 2007; Rossmeisl, Rim, Koza, & Kozak, 2003). At present, C57BL/6J mice are best characterized and most closely resemble disease progression in humans, and, therefore, have been widely used for DIO and diabetes studies (Kondo et al., 2006; Roche, Phillips, & Gibney, 2005; Winzell & Ahrén, 2004). Additionally, gender plays an important role. Since oestrogen, the main female sex hormone, has been suggested to be protective against obesity-related complications, including T2D, primarily male mice have been used for metabolic studies (Pettersson, Waldén, Carlsson, Jansson, & Phillipson, 2012; Shi & Clegg, 2009; Tiano & Mauvais-Jarvis, 2012). In addition, several genetic mouse models are available to study obesity and metabolic disorders, such as, for example, the hyperphagic leptin-deficient *ob*/*ob* mouse model or the leptin receptor-deficient *db*/*db* mouse (Robinson, Dinulescu, & Cone, 2000; Schwartz, Woods, Porte, Seeley, & Baskin, 2000).

3.6.2 Intestinal adaptation to dietary changes

Due to its immense self-renewal ability, mammalian intestine exhibits a remarkable capacity to rapidly adapt its morphology and function to the nutritional status (Dailey, 2014; Mihaylova, Sabatini, & Yilmaz, 2014). Increasing evidence suggests that dietary cues can alter ISC self-renewal, function and differentiation. However, the exact mechanisms leading to a diet-induced dysregulation of the intestinal homeostasis and, eventually, to severe intestinal pathologies, including cancer, is not yet clear.

Changes in intestinal weight and length, nutrient absorption and digestion, hormone secretion, crypt and villus morphology, proliferation and function of ISCs have been demonstrated in mouse and human intestine (Baldassano, Amato, Cappello, Rappa, & Mulè, 2013; Beyaz et al., 2016; Dailey, 2014; Mihaylova et al., 2018, 2014; Richards et al., 2016; Yilmaz et al., 2012). In general, intestinal maintenance and growth is driven by the amount of available nutrients, however, also the type of nutrient can affect intestinal epithelial adaptive responses (Dailey, 2014).

Fasting and caloric restriction have been shown to decrease cell proliferation, villus length and intestinal weight, which may eventually lead to the atrophy of the intestinal epithelium, depending on the severity and duration of dietary restriction (Chappell et al., 2003; Dunel-Erb et al., 2001; Richmond et al., 2015; Steinbach, Heymsfield, Olansen, Tighe, & Holt, 1994). By contrast, refeeding, as shown in *Drosophila*, leads to increased proliferation and organ growth (O'Brien, Soliman, Li, & Bilder, 2011).

Evidence of intestinal adaptation to increased nutrient availability comes from studies in human obesity and in HFD mouse models. The length of the intestine and the absorptive cell mass is increased in obese humans (Dailey, 2014). Though, contradictory reports exist regarding the effects of chronic overeating or HFD on intestinal morphology and cellular homeostasis, in most cases, excess calorie intake increases cell proliferation rate, enterocyte number, villi length and nutrient absorption (Baldassano et al., 2013; Beyaz et al., 2016; Dailey, 2014; N. J. de Wit et al., 2008; Mao et al., 2013; Van Landeghem et al., 2015).

Additionally, obesity-induced alterations in the abundance of the intestinal secretory lineages have been reported. A number of studies demonstrate that dietary modifications can affect EEC subsets, although the findings are inconsistent and depend on the methods used for the EECs quantification. Thus, increase in EECs (Aranias et al., 2015; Dusaulcy et al., 2016), no change (Beyaz et al., 2016; Van Landeghem et al., 2015) or decrease in their numbers or numbers of specific EEC subsets (Richards et al., 2016; Wölnerhanssen et al., 2017) have been reported recently. Similarly, obesity-induced changes in goblet and Paneth cell numbers have been observed (Beyaz et al., 2016; Van Landeghem et al., 2015; W. Yang, Bancroft, Nicholas, Lozonschi, & Augenlicht, 2003).

Though direct effects of diet on mature intestinal epithelial cells are known (and described above), signals from nutrients proved to be critical regulators of the ISC function and, hence, tissue homeostasis (Mana, Kuo, & Yilmaz, 2017; Mihaylova et al., 2014). To date, relatively few studies have focused on the impact of diet on the adult ISCs and have, moreover, yielded conflicting results with regard to the ISC proliferation, function and signalling alterations.

As a general rule, caloric restriction enhances tissue regeneration and stem cell function (Mana et al., 2017; Mihaylova et al., 2014). Long-term calorie restriction or fasting in mice leads to the enhanced ISC

self-renewal and function, mediated by signalling cues in neighbouring Paneth cells or by altered intrinsic metabolic signalling, respectively (Mihaylova et al., 2018; Yilmaz et al., 2012).

On the other hand, the majority of the studies show that obesity and HFD are associated with increased ISC proliferation (Baldassano et al., 2013; Beyaz et al., 2016; Mao et al., 2013; Van Landeghem et al., 2015). By contrast, influence on ISC function is controversial. For example, whereas Beyaz and colleagues observe enhanced ISC function and tumorigenicity, as a long-lasting ability to from organoids in culture, the study by Mah et al. demonstrates impaired ISC function and acquired dependence on external Igf1/insulin signals (Beyaz et al., 2016; Mah, Van Landeghem, Gavin, Magness, & Lund, 2014).

3.7 Flattop, a novel reporter of Wnt/PCP signalling in β-cell heterogeneity and intestinal lineage formation

Flattop (*Fltp*; *17000009p17Rik*; *Cfap126*) was identified in a microarray-based screen for potential Forkhead box A2 (Foxa2) target and novel organizer genes in Foxa2-mutant embryos (Tamplin et al., 2008). Using the *Fltp*^{ZV} (LacZ/histone 2B (H2B)-Venus) knock-in/knockout reporter mouse line, Gegg et al. demonstrated that *Fltp* is expressed in monociliated tissues such as the node, the sensory organs of the inner ear and the testis (Gegg et al., 2014). Additionally, *Fltp* expression was found in multiciliated cells of the respiratory epithelium and the choroid plexi in the brain (Gegg et al., 2014; Lange et al., 2012). In these tissues, *Fltp* expression is associated with active Wnt/PCP signalling (Gegg et al., 2014). The conserved Wnt/PCP pathway regulates polarisation and orientation of cells and organelles within the plane of an epithelial tissue, thus determining cell fate and function and governing organ formation (Wallingford, 2012; Y. Wang & Nathans, 2007). *Fltp* deletion resembles the phenotypes observed in the PCP mutants (Curtin et al., 2003; Gray et al., 2009; T. J. Klein & Mlodzik, 2005; Park, Mitchell, Abitua, Kintner, & Wallingford, 2008; Yates et al., 2010). In particular, it leads to defects in basal body (BB) docking and ciliogenesis in multiciliated lung cells or affects the positioning of the kinocilium in the monociliated inner ear hair cells (Gegg et al., 2014).

Recently, our lab showed that the Fltp-Venus reporter can distinguish between two populations of β-cells in the *Fltp*^{ZV} mouse model, the Fltp-Venus reporter-positive (FVR^{+}) mature and the FVR^{-} proliferation-competent β-cells (Figure 4A) (Bader et al., 2016). Moreover, this work demonstrated that Wnt/PCP signalling is sufficient to induce β-cell maturation, however, Fltp is not required for the development, proliferation or maturation of β-cells (Bader et al., 2016). In the intestinal epithelium, the FVR^{+} cells comprise FVR^{low} EECs and FVR^{hi} Paneth cells, respectively (Figure 4B) (Boettcher et al., in revision). Additionally, *Fltp* mRNA is transiently expressed in Wnt/PCP-activated ISCs, which leads to cell cycle exit and direct priming towards the EEC or Paneth cell fate (Boettcher et al., in revision). Just as in the pancreas, deletion of *Fltp* does not result in defects in the EEC or Paneth cell formation (Boettcher et al., in revision). Thus, the exact role of Fltp and its cellular localisation in the islets of Langerhans and in the intestinal epithelium remains unclear.

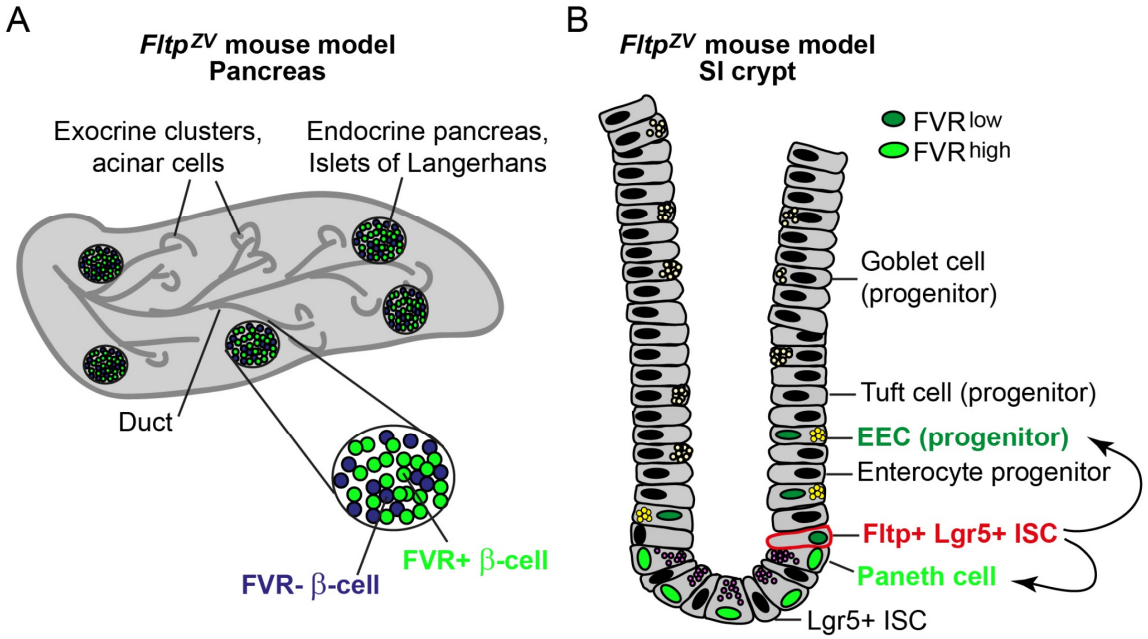

Figure 4: Scheme of FVR expression in SI crypts and islets of Langerhans in the *Fltp*^{ZV} mouse model

(A) In the pancreatic islets, the FVR reporter segregates β-cell populations with proliferative potential (FVR-) and mature FVR+ β-cells (Bader et al., 2016).
(B) In SI crypts, the FVR reporter distinguishes FVR^{low} EECs and FVR^{high} Paneth cells. Red outline highlights a Wnt/PCP pathway-activated Flpt+ Lgr5+ ISC, which directly gives rise to EECs and Paneth cells (Boettcher et al., in revision).

3.8 Aims of the thesis

Recent findings indicate that ISC function and cell fate decisions can rapidly adapt to dietary changes, however, underlying mechanisms are poorly understood (Beyaz et al., 2016; O'Brien et al., 2011; Yilmaz et al., 2012). Moreover, diet-induced deregulation of the ISC homeostasis has been implicated in colorectal cancer and metabolic diseases, such as obesity and T2D. Additionally, changes in the abundance of EECs and alterations in the EE axis have been associated with severe obesity and T2D. However, it is not clear whether the defects directly relate to mature EECs or emerge during the lineage formation. Thus, we aim to investigate diet-induced changes in the ISC homeostasis and lineage allocation using a HFD-fed mouse model of pre-diabetes. Moreover, we aim to dissect HFD-induced alterations in the EE lineage allocation and subtype specification and integrate our findings with approaches for functional validation. A better understanding of molecular mechanisms underlying diet-induced disturbances in the ISC homeostasis and EE disorder may provide novel targets for non-invasive treatment options for the metabolic syndrome.

Furthermore, Wnt/PCP-activated ISCs, which express *Fltp*, are committed to the EEC and Paneth cell fate in the intestine (Böttcher et al., in revision). Fltp was recently identified as a Wnt/PCP effector gene in mono- and multiciliated tissues (Gegg et al., 2014). Further, it has been shown to segregate populations of pancreatic β-cells with distinct functional features (Bader et al., 2016). However, the exact cellular localisation of Fltp and its role in lineage formation and maintenance in the intestine and pancreas is not known. Therefore, we aim to generate a Fltp-Venus fusion reporter mouse model to facilitate the analysis of Fltp function, in particular, in the intestine and pancreas. Specifically, we want to use the Fltp-Venus fusion mouse model as a tool to study quiescent and cycling ISCs as well as lineage recruitment into EECs and Paneth cells in health and under pathologic conditions, in particular, in DIO and diabetes.

4 Results

The results described in chapter 4.1 were obtained in collaboration with the Institute of Computational Biology (Sophie Tritschler), the Institute of Experimental Genetics (Dr. Martin Irmler), the Research Unit of Analytical Pathology (Dr. Na Sun) as well as with the Institute of Diabetes and Regeneration Research (Michael Sterr and Dr. Anika Böttcher) at Helmholtz Zentrum München. Biological experiments were performed by the candidate, and for some experiments, author contributions are indicated. The bioinformatic analyses of the single-cell RNA seuencing data was performed by Sophie Tritschler.

The chapter 4.1 is the basis for the following manuscript in preparation for Nature Metabolism: ***Obesity and pre-diabetes alters intestinal stem cell turnover and lineage allocation***. Alexandra Aliluev*, Sophie Tritschler*, Michael Sterr, Lena Oppenländer, Julia Hinterdobler, Martin Irmler, Johannes Beckers, Na Sun, Axel Walch, Kerstin Stemmer, Matthias H. Tschöp, Fabian J. Theis, Heiko Lickert and Anika Böttcher (status as of 08.03.2020).

(* indicates equal contribution)

4.1 Impact of HFD on ISC homeostasis and intestinal lineage recruitment

Intestinal homeostasis relies on the tight balance between proliferation and differentiation of ISCs into absorptive and secretory progenitors, and its deregulation has been implicated in colorectal cancer and metabolic diseases (Beyaz et al., 2016; H. Clevers, 2013; Mao et al., 2013). Understanding the molecular mechanisms of ISC homeostasis and endocrine lineage recruitment is essential to provide novel targets for non-invasive treatment options of the metabolic syndrome. Importantly, recent findings indicate that ISC function and cell fate decisions can rapidly adapt to meet the metabolic demand (Beyaz et al., 2016; O'Brien et al., 2011; Yilmaz et al., 2012), however, the metabolites and pathways regulating this plasticity are largely unknown. At present, the impact of diet-induced obesity and metabolic syndrome on ISC function and on the homeostasis of distinct intestinal lineages has been insufficiently addressed and remains unclear, also due to contradictory results in HFD animal models.

4.1.1 HFD induces a metabolic disorder and alters small intestinal morphology in FVF mice

HFD is an established model for studying DIO and metabolic disorders in rodents, resembling many features of the metabolic syndrome in humans. However, conflicting results in regard to the effect of HFD on intestinal morphology and cell type composition have been reported (Beyaz et al., 2016; Dailey, 2014; Mah et al., 2014; Mao et al., 2013). To assess the impact of a HFD-feeding on the intestinal homeostasis and lineage recruitment from ISCs, we used the FVF reporter mouse model, previously generated in our laboratory (Burtscher, Barkey, & Lickert, 2013). The differential expression of Foxa2-Venus in SI crypts allows to enrich FVF^{low} ISCs, FVF^{hi} secretory cells and FVF^{neg} enterocytes based on the reporter fluorescence intensity (Sterr et al., in preparation; Boettcher et al., in revision).

A metabolic disorder was induced by maintaining weight-matched three-month-old male FVF mice on a HFD regimen (58 % kcal from fat) for, typically, 12 weeks. Metabolic parameters and SI morphology were assessed with regard to a cohort fed a control diet (CD) (11 % kcal from fat) (Figure 5A). HFD-fed FVF mice developed DIO and dysglycaemia, typical of metabolic syndrome. In particular, HFD-fed mice displayed an average doubling of body weight and fat mass with an over-proportionally high ratio of fat tissue to body weight (Figure 5B-E). Moreover, the HFD impaired the glucose tolerance and induced a fasting hyperglycaemia and a pronounced hyperinsulinemia (Figure 5F, G). Homeostatic model assessment of insulin resistance (HOMA-IR) and HOMA of β-cell function (HOMA-β) calculated from fasting blood glucose and plasma insulin levels indicated a compensatory β-cell hyperfunction and insulin resistance, typical conditions associated with pre-diabetes (Figure 5H, I).

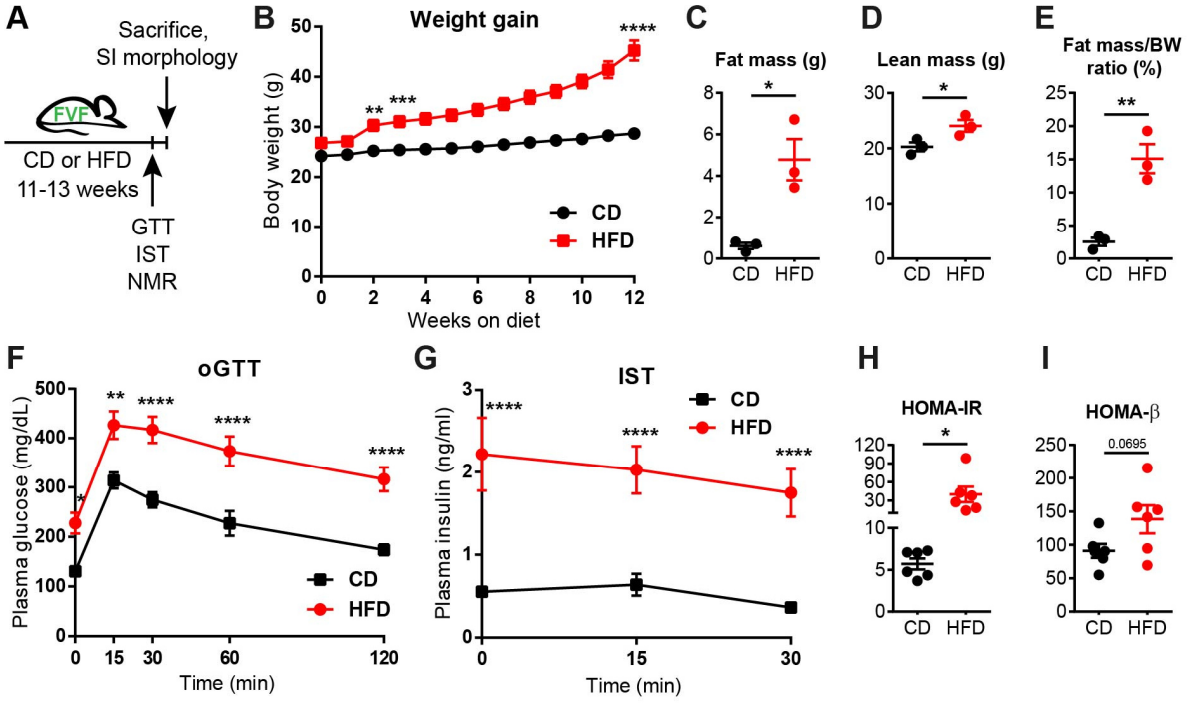

Figure 5: HFD induces obesity and pre-diabetes in the FVF mouse model

(A) Scheme of experimental procedures for the analysis of metabolic parameters and SI morphology in CD- and HFD-fed FVF mice.
(B) Weekly body weight measurement over the time course of the diet regimens. n=8 per group.
(C-E) Fat (C) and lean mass (D) determined by nuclear magnetic resonance (NMR) in FVF mice. HFD-fed mice show an increased ratio of fat mass to body weight as compared to controls after 12 weeks (E). n=3 per group.
(F, G) Assessment of glucose tolerance by oral glucose tolerance test (oGTT) (F, n=8 per group) and plasma insulin levels by insulin secretion test (IST) (G, n=4 *versus* 5 per group) in FVF mice maintained for 12 weeks on CD or HFD. Mice were fasted for 6 hours and basal plasma glucose and insulin were measured. Mice were then given an oral glucose bolus and plasma was collected for measurements of glucose and insulin concentrations at indicated time points.
(H, I) Calculation of insulin resistance (H) or β-cell function (I) by homeostatic model assessment of insulin resistance (HOMA-IR) or HOMA of β-cell function (HOMA-β), respectively. The following conventional formulae were used: HOMA-IR = fasting blood glucose (mg/dl) × fasting insulin (μU/ml) / 405; HOMA-β = fasting insulin (μU/ml) × 360 / fasting glucose (mg/dl) - 63 (Matthews et al., 1985). n=6 per group.
Data (B-I) are shown as mean ± SEM. **P*<0.05, ***P*<0.01, ****P*< 0.001, *****P*< 0.0001 by two-way ANOVA with Sidak's multiple comparison test (B, F, G) or two-tailed Student's *t*-test (C-E and H, I).

Moreover, HFD-feeding led to a significant increase in SI length and weight and to apparent changes in SI tissue morphology (Figure 6A, B). Histological study of the duodenal mucosa revealed rich cellular fat inclusions in the villi of HFD-fed FVF mice (Figure 6C).

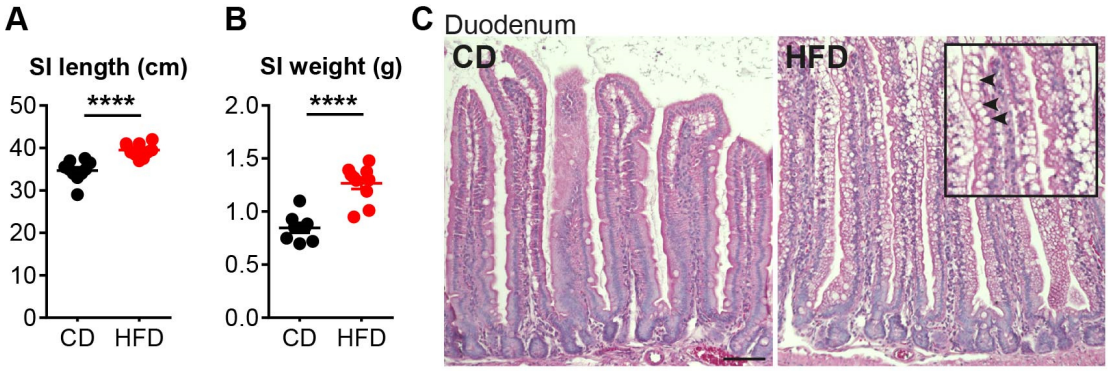

Figure 6: HFD changes SI organ size and tissue histology

(A, B) SI length (B, n=10 per group) and weight (C, n=8 *versus* 10 per group) are increased in HFD-fed FVF animals as compared to controls. Data represent mean ± SEM. ****$P< 0.0001$ by two-tailed Student's *t*-test.
(C) Assessment of SI tissue histology by haematoxylin and eosin staining shows rich fat inclusions in the epithelial lining of the duodenal villi in HFD-fed FVF mice. Black square depicts enlarged segment of the villi. Black arrows indicate fat inclusions in the epithelial cells. Scale bar, 100 µm.

FVF mice maintained on HFD displayed alterations in the villus and crypt morphology characterised by a significant increase in the villus length in both, the proximal and distal parts of the SI, greater duodenal crypt width and a decrease in crypt density (Figure 7A-F). By contrast, there were no changes in the duodenal crypt depth and cell number per crypt (Figure 7G, H). Neither the increased villus length, nor the alterations in crypt morphology were attributable to cellular hypertrophy. Cell sizes, according to the ratio of villus or crypt length to cell number, were comparable between CD and HFD conditions (Figure 7I-K).

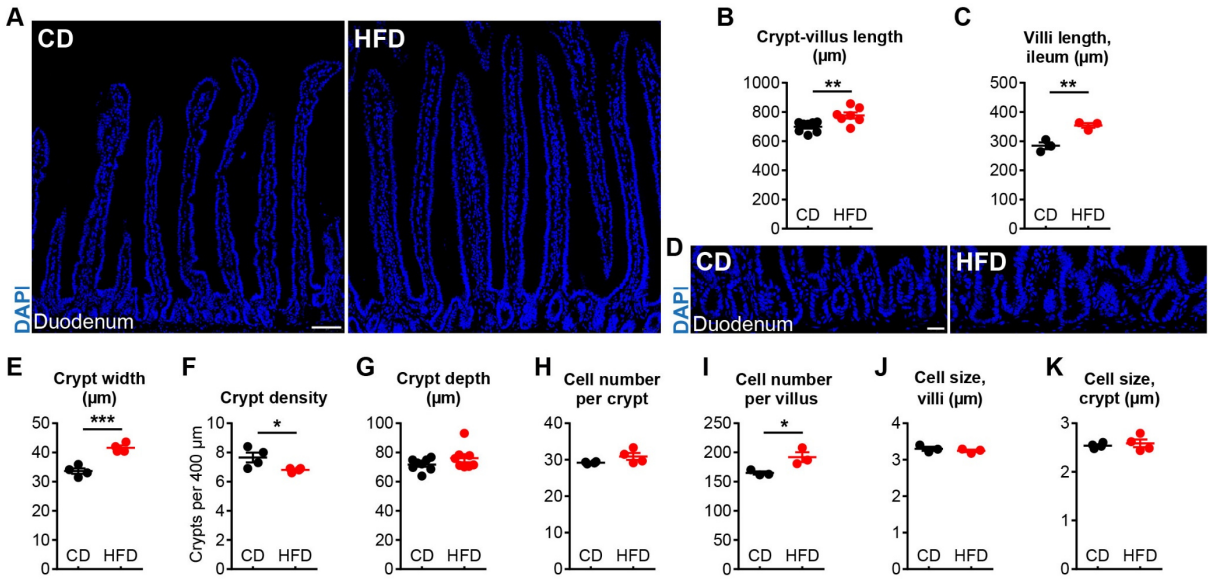

Figure 7: HFD alters small intestinal crypt and villus morphology

(A-C) Representative laser scanning confocal microscopy (LSM) images of duodenal sections from CD- and HFD-fed FVF mice (A) and assessment of crypt-villus unit length in the duodenum (B, n=8 *versus* 7 per group) and ileum (C, n=3 per group).
(D-G) LSM images of duodenal crypt sections from CD- and HFD-fed mice (D) and quantification of crypt width (E), density (F) and depth (G). n=4 per group (E, F), n=8 per group (G).
Data represent mean ± SEM. *P<0.05, **P<0.01, ***P<0.001 by two-tailed Student's *t*-test. Scale bars, 75 µm (A) and 25 µm (D).

Taken together, HFD affected systemic metabolism indicated by obesity and development of a pre-diabetic condition, and induced alterations of SI tissue morphology. However, how changes in intestinal homeostasis relate to obesity and diabetes is still elusive.

4.1.2 Single-cell survey of SI crypt cells reveals altered lineage allocation from ISCs and a shift in regional identities on HFD

ISCs differentiate into absorptive and secretory progenitors in the crypt, which then mature into enterocytes, EECs, goblet, Paneth and tuft cells. These metabolically and functionally distinct cell identities including distinct differentiation states likely react differently to dietary changes (Rodríguez-Colman et al., 2017; Stringari et al., 2012; Yilmaz et al., 2012). Recent single-cell studies revealed considerable phenotypic and functional heterogeneity within cell populations previously considered as homogenous, thus, strongly suggesting that bulk effects may mask crucial molecular mechanisms (Beumer et al., 2018; Haas, Trumpp, & Milsom, 2018; Haber et al., 2017; Povinelli, Rodriguez-Meira, & Mead, 2018; Boettcher et al., in revision). Previous reports addressing HFD effects on ISC function and SI homeostasis utilise bulk cell analyses and, thus, do not provide the necessary resolution to study the distinct progenitor and mature cell types in metabolic disease (Beyaz et al., 2016; Mah et al., 2014; Mao et al., 2013). It is, therefore, increasingly important to exploit single-cell approaches to uncover cell type- and cell stage-specific molecular mechanisms underlying disturbed tissue homeostasis.

4.1.2.1 Single-cell RNA sequencing of SI crypt cells identifies distinct intestinal lineages including mature and progenitor states

To dissect cell-type specific molecular changes in ISCs and discrete intestinal lineages induced by a HFD, we employed massively parallel single-cell RNA sequencing of flow-sorted SI crypt cells from CD- and HFD-fed FVF mice. FVF reporter-based enrichment of SI secretory lineage cells enabled us to study the rare EEC subtypes and, thus, EE lineage allocation in metabolic disorder (Sterr et al., in preparation; Boettcher et al., in revision) (Figure 8A-F). In comparison, proportions of ISCs and enterocyte progenitors (EP) were similar, while enterocytes were less abundant in FVF-derived samples compared to WT samples (Figure 8C-F) (Boettcher et al., in revision). Surprisingly, despite the fact that Paneth cells are labelled by the FVF reporter, they were not enriched in FVF-derived samples, but rather notably underrepresented, which is likely attributable to issues associated with sorting of large cells (~2-2.5% *vs*. 5 % expected (H. C. Clevers & Bevins, 2013; Haber et al., 2017)) (Figure 8D-F).

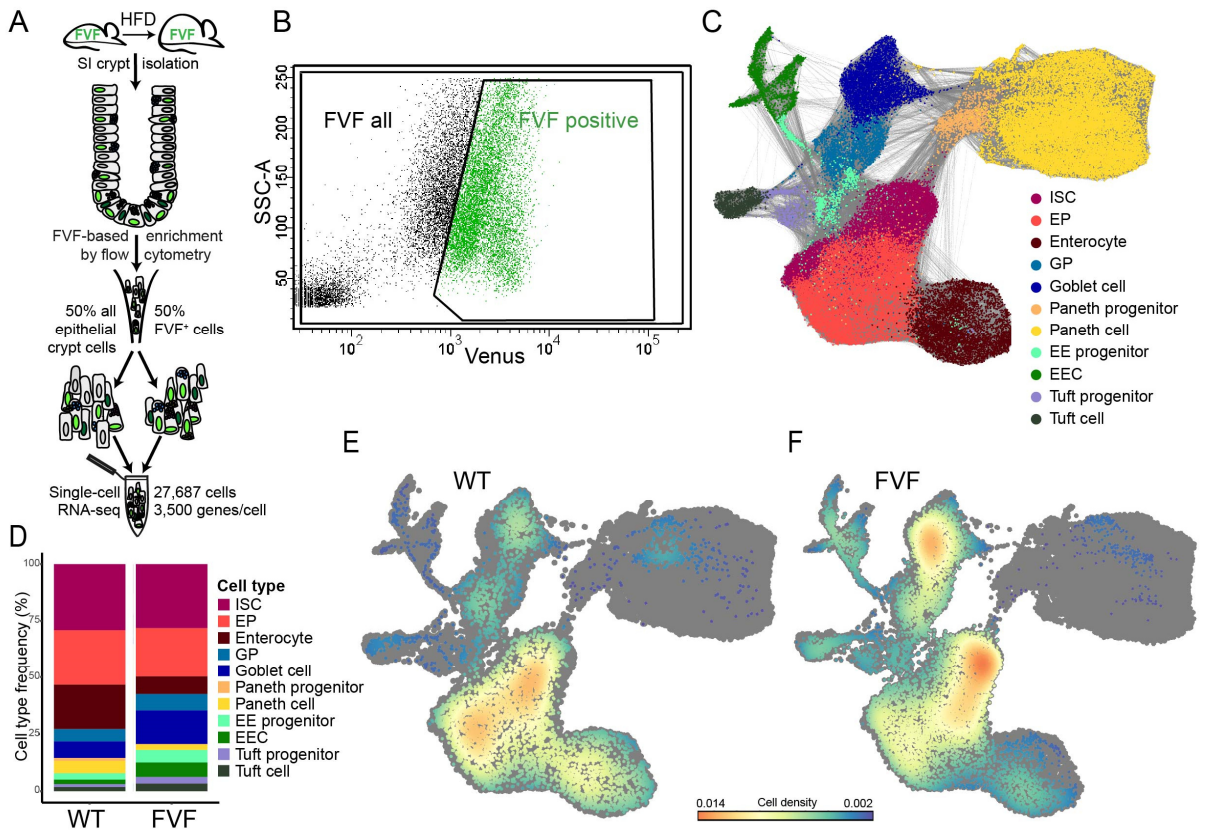

Figure 8: FVF reporter-based enrichment of secretory lineage cells from SI crypts for scRNAseq profiling

(A) Experimental scheme for FVF-based enrichment strategy by flow cytometry and scRNAseq profiling of SI crypt cells from mice under CD and HFD conditions.
(B) Fluorescence-activated cell sorting (FACS) plot depicting gating strategy for flow-sorting of live random crypt cells (FVF all) and FVF+ (FVF positive) cells from SI crypts.
(C) Uniform Manifold Approximation and Projection (UMAP) plot of pooled SI crypt cells derived from *Fltp*^{ZV}, FVF and WT mice with colour-coded cluster annotation. EP: enterocyte progenitor, GP: goblet progenitor, EE: enteroendocrine.
(D-F) Cell type frequencies (D) and cell densities projected onto the two-dimensional UMAP embedding of wild-type (WT) (E) and FVF-derived (F) crypt cells depict an enrichment of secretory lineage cells.
Figures (C-F) are modified from Boettcher et al. (Boettcher et al., in revision).

Table 1: Quality metrics for scRNAseq data

	CD 1	CD 2	CD 3	HFD 1	HFD 2	HFD 3
Number of cells passing quality filters	4637	4575	4154	4345	5083	4893
Median counts per cell	16971	15920	18953	19913	16324	17061
Median detected genes per cell	3532	3400	3788	3839	3225	3499
Mean reads per cell	89994	84867	96805	100616	88070	87093

Bioinformatic analysis shown in this table was done by Sophie Tritschler.

To enrich for EECs, we isolated live FVF+ and whole-crypt cells derived from CD- and HFD-fed FVF mice by flow cytometry at a ratio of 1:1 per sample (Figure 8A, B). In total, we obtained 27,687 epithelial crypt cells from CD- and HFD-fed animals, which passed through quality controls (Methods chapter 7.13.1), and detected on average 3,500 genes per cell (Table 1). Unsupervised graph-based clustering

and cluster annotation using known marker genes identified all groups of mature intestinal cells and discrete progenitor states (Figure 9A, B). One cell cluster could not be annotated due to the absence of a specific marker gene signature (Figure 9A-C, "not annotated"). Transcriptional profiles of mature cell types were clearly distinct while gene expression differences in the progenitor clusters were moderate and could be narrowed down to, *e.g.* a few transcription factors (Figure 9C).

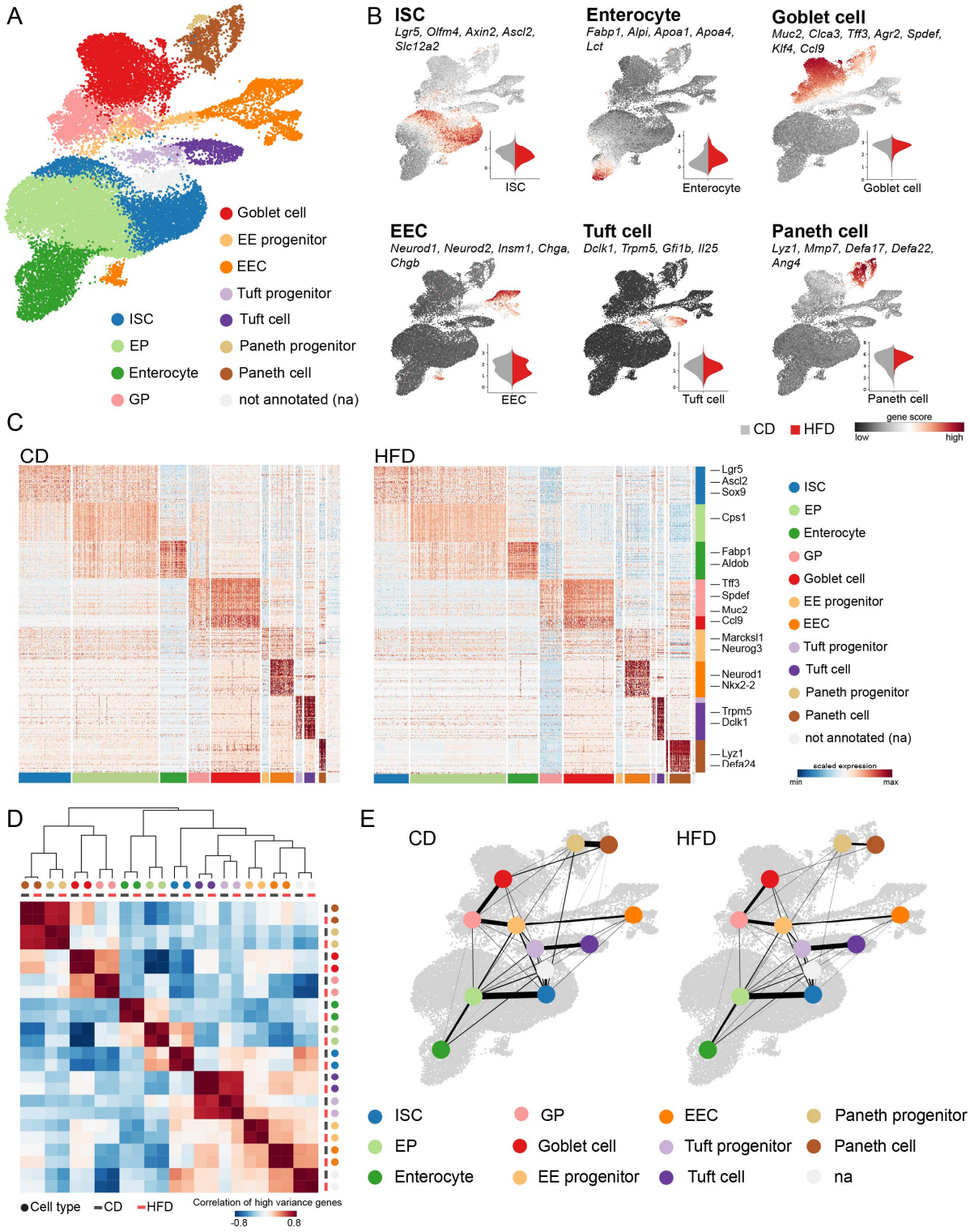

Figure 9: Single-cell transcriptional profiling identifies all SI epithelial lineages in CD- and HFD-derived crypt samples

(A) UMAP plot of 27,687 pooled (n=6) profiled single SI crypt cells from CD- and HFD-derived samples. Colours highlight clusters of intestinal cell types based on expression of known marker genes.
(B) Levels of cell scores calculated based on expression of a set of known indicated marker genes for specific cell types and used for cluster annotation. Violin plots show distribution of score levels in assigned cell types in CD- and HFD-derived samples.
(C) Heatmap depicting scaled expression levels of signature genes (rows) sorted by cell type in single cells (columns) in CD- and HFD-derived samples. Colour bars at the bottom and on the side of the heatmap indicate cell types. Selected known marker genes for every lineage are indicated.
(D) Pearson correlation of average expression values of high variance genes broken down by cell type and diet. Rows and columns are ordered by hierarchical clustering. Clusters and diet conditions are colour-coded along the boundaries.
(E) Lineage tree depicting relationships of CD- and HFD-derived SI crypt cells inferred based on a measure for cluster connectivity using partitioned graph abstraction (PAGA). Edges are weighted by significance, nodes are positioned at the centres of the clusters in UMAP space.
Bioinformatic data analyses for this figure was performed by Sophie Tritschler.

A high Pearson correlation of cell type transcriptomes in CD and HFD conditions indicated their overall broad similarity (Figure 9D). To evaluate lineage relations, we inferred an intestinal lineage tree using partitioned graph abstraction (PAGA) (Wolf, Hamey, et al., 2018). All progenitor clusters, including enterocyte, goblet cell, tuft cell, EEC and Paneth cell progenitors, were rooted to the ISCs in agreement with the previous findings by Boettcher et al. Cluster connectivity was, in total, comparable between CD- and HFD-derived samples (Figure 9E). Together, these findings demonstrate that a HFD did not affect intestinal lineage identities.

4.1.2.2 HFD affects lineage allocation from ISCs and regional identity of distinct intestinal cell types

We next examined whether HFD affected cell-type composition in SI crypts by comparing the relative cell abundances in CD- and HFD-derived samples. Strikingly, relative cell densities of several intestinal lineages were changed in HFD-derived crypt samples (Figure 10A). In particular, the relative abundance of Lgr5^{+} ISCs and tuft lineage cells was decreased, while the proportions of the enterocyte lineage cells and Paneth cell lineage were increased under HFD conditions (Figure 10B). In contrast, the overall abundances of the goblet cell and the EEC clusters was not affected (Figure 10B).

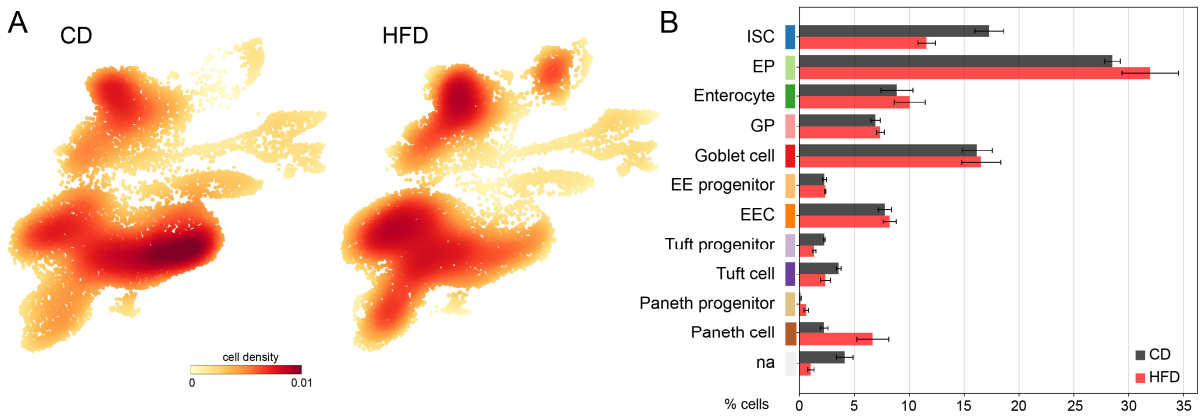

Figure 10: HFD alters relative proportions of SI lineages

(A, B) Compositional differences in CD- and HFD-derived single-cell clusters visualized as cell densities (red, high; yellow, low) projected onto two-dimensional UMAP embedding (A) and quantified as proportions over cell types (B). Cell densities were estimated using Gaussian kernels. Data are mean ± SEM. n=3 per group.
Bioinformatic data analyses for this figure was performed by Sophie Tritschler.

The small intestine is anatomically and functionally compartmentalised along the proximal-distal axis. This involves differences in cell type composition and establishment of selective transcriptional programmes in the duodenum, jejunum and ileum (Anderle et al., 2005; Bates et al., 2002; Comelli et al., 2009; Middendorp et al., 2014). While the main function of the duodenum is absorption and digestion of nutrients, minerals and water-soluble vitamins, *e.g.* vitamin B12, bile acids are absorbed in the ileum.

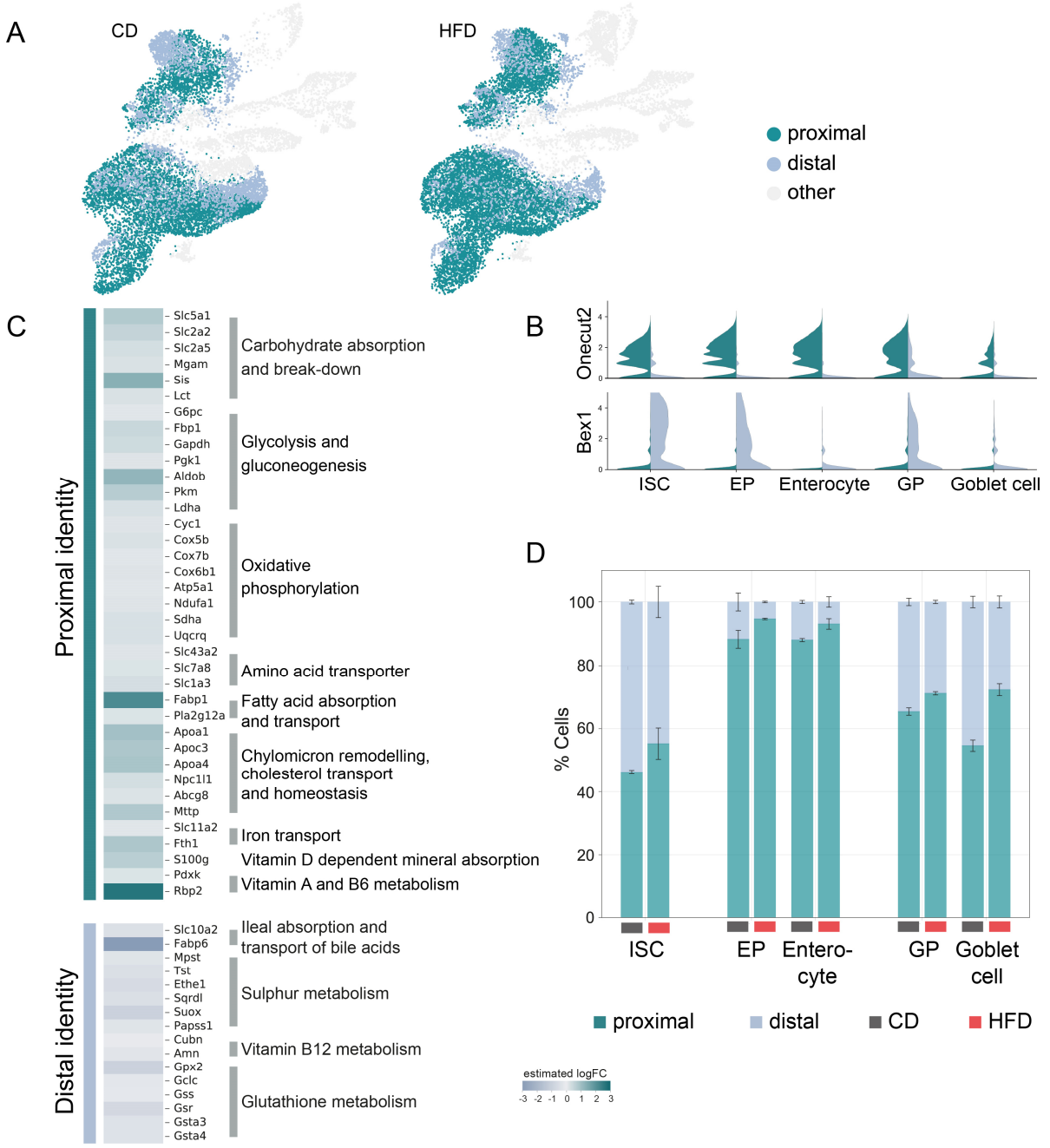

Figure 11: HFD affects regional identity of SI crypt cells

(A, B) Distribution of cells with proximal and distal signatures in ISC, goblet and enterocyte lineage clusters (A). Cells were assigned to a specific regional identity based on the expression of SI regional markers Onecut2 (proximal) and Bex1 (distal) (Haber et al., 2017) (B).
(C) Gene signatures enriched in enterocytes with the proximal or distal identity representing functional identity of enterocytes dependent on SI region. The heatmap shows estimated fold changes in proximal *versus* distal cells from CD-derived samples.

(D) Proportions of cells with proximal or distal identity within CD- and HFD-derived ISCs, enterocyte and goblet lineage clusters. Data are mean ± SEM. n=3 per group.
Bioinformatic data analyses for this figure was performed by Sophie Tritschler.

Transcriptional regulation of regional specification in the GI tract is mediated by Cdx1, Cdx2, Gata4, Gata5, Pdx1 and Hox transcription factors (Beuling et al., 2011; Bosse et al., 2006; Fang et al., 2006; Silberg, Swain, Suh, & Traber, 2000). It has been shown that regional identity is intrinsically programmed in ISCs and enterocytes and involves differential expression of genes, such as *Gkn3*, *Creb3*, *Creb3l3*, *Onecut2* or *Jund*, *Bex1*, *Bex4* and *Osr2* defining the proximal or distal identities for the ISC-enterocyte maturation axis, respectively (Haber et al., 2017; Middendorp et al., 2014; X. Wang et al., 2015). Moreover, Haber et al. suggested regional identities for the distinct EEC subsets and Paneth cells using the single-cell technology. However, it is not known whether dietary alterations have an impact on regional segregation, *i.e*. region-specific transcriptional and functional programmes.

To test whether HFD affected regional heterogeneity of the discrete intestinal lineages, we used the signature genes described by Haber et al. to segregate cell clusters with proximal and distal identities (Figure 11A, B). Most prominent segregation could be detected in the ISC, enterocyte and goblet lineage clusters with differences in the density and distribution of cells with proximal and distal signatures as visualised in Figure 11A. The expression of the regional identity transcription factors *Bex1* and *Onecut2* showed hereby a clear relation to the distal or proximal gene signatures, respectively (Figure 11B). This indicates different metabolic programms of proximal and distal regions contributing to metabolic syndrome. Under normal conditions (CD), transcriptional profiles of proximal enterocytes were enriched for gene signatures related to nutrient absorption (*e.g*. carbohydrate absorption and beak-down, fatty acid absorption and transport, chylomicron remodelling, iron transport, and vitamin metabolism) and nutrient utilisation (*e.g*. glycolysis and gluconeogenesis as well as oxidative phosphorylation) (Figure 11C). In contrast, distal enterocyte signatures included genes related to bile acid absorption and transport, sulphur and glutathione metabolism and vitamin B12 absorption (Figure 11C). Strikingly, a HFD altered relative proportions of cells with proximal and distal identities within several distinct lineage clusters. Thus, in ISCs, enterocyte and goblet lineage clusters, the proportion of cells with proximal identity was increased on HFD (Figure 11D). This indicates, that lineage allocation from ISCs is rapidly adapted to increased metabolic demand, *i.e*. calorie excess, through ectopic upregulation of proximal transcriptional programmes for enhanced nutrient absorption and utilisation. This finding provides novel insights into molecular mechanisms of functional adaptation to altered dietary conditions.

In summary, we identified HFD-induced molecular and compositional alterations in the small intestine associated with pre-diabetes.

4.1.3 Genetic lineage tracing and analysis of the mature lineage relations confirm disturbed lineage allocation from ISCs on HFD

Our scRNAseq data revealed HFD-induced alterations in the composition of SI lineages (see section 4.1.2.2). However, due to the enrichment strategy bias, the relative proportions of SI cell types by single-cell profiling may not reflect the actual cell frequencies in the crypts of CD- and HFD-fed animals, thus, need a thorough verification. Therefore, we employed two experimental approaches to confirm our findings from scRNAseq. First, we assessed lineage formation by short-term genetic lineage tracing of Foxa2-expressing ISCs using the *Foxa2*$^{nEGFP\text{-}CreERT2/+}$;*Gt(ROSA)26*$^{mTmG/+}$ mouse model. Second, to confirm that altered lineage allocation in the crypt translates into the mature compartment, we assessed the frequencies of mature cell types in the intestines of CD- and HFD-fed FVF mice.

4.1.3.1 Short-term genetic lineage tracing of Foxa2-expressing ISCs confirms disturbed lineage relations on HFD

Work by Sterr et al. confirmed that Foxa2 is expressed in ISCs (Sterr et al., in preparation). Using a dual-fluorescent inducible Cre-reporter *Foxa2*$^{nEGFP\text{-}CreERT2/+}$;*Gt(ROSA)26*$^{mTmG/+}$ mouse model, we could show that 30 days after tamoxifen-induced recombination, lineage-labelled cell ribbons containing all lineages were present in the SI epithelium (Imuta, Kiyonari, Jang, Behringer, & Sasaki, 2013; Muzumdar, Tasic, Miyamichi, Li, & Luo, 2007; Sterr at al., in preparation). In this model, all cells ubiquitously express the membrane-targeted Tomato (mT) protein (Figure 12A). Upon induction with tamoxifen, Foxa2-driven Cre recombinase cleaves irreversibly the floxed *mT* sequence resulting in the expression of the membrane-bound GFP (mG) in Foxa2-positive and Foxa2-lineage cells. Yellow cells represent a timely restricted intermediate mT$^+$/mG$^+$ stage.

To verify HFD-induced alterations in lineage allocation from ISCs and to validate the impact on the mature cell type composition, we employed a short-term genetic lineage tracing approach using the *Foxa2*$^{nEGFP\text{-}CreERT2/+}$;*Gt(ROSA)26*$^{mTmG/+}$ mouse model. First, we assessed the recombination efficiency in ISCs 48 hours after a single dose of orally administered tamoxifen (Figure 12B). At this time point, single mG$^+$ cells and small cell patches appeared at the positions typical for ISCs (adjacent to pyramid-shaped Paneth cells) at comparable frequencies in duodenal crypts of CD- and HFD-fed animals (Figure 12C).

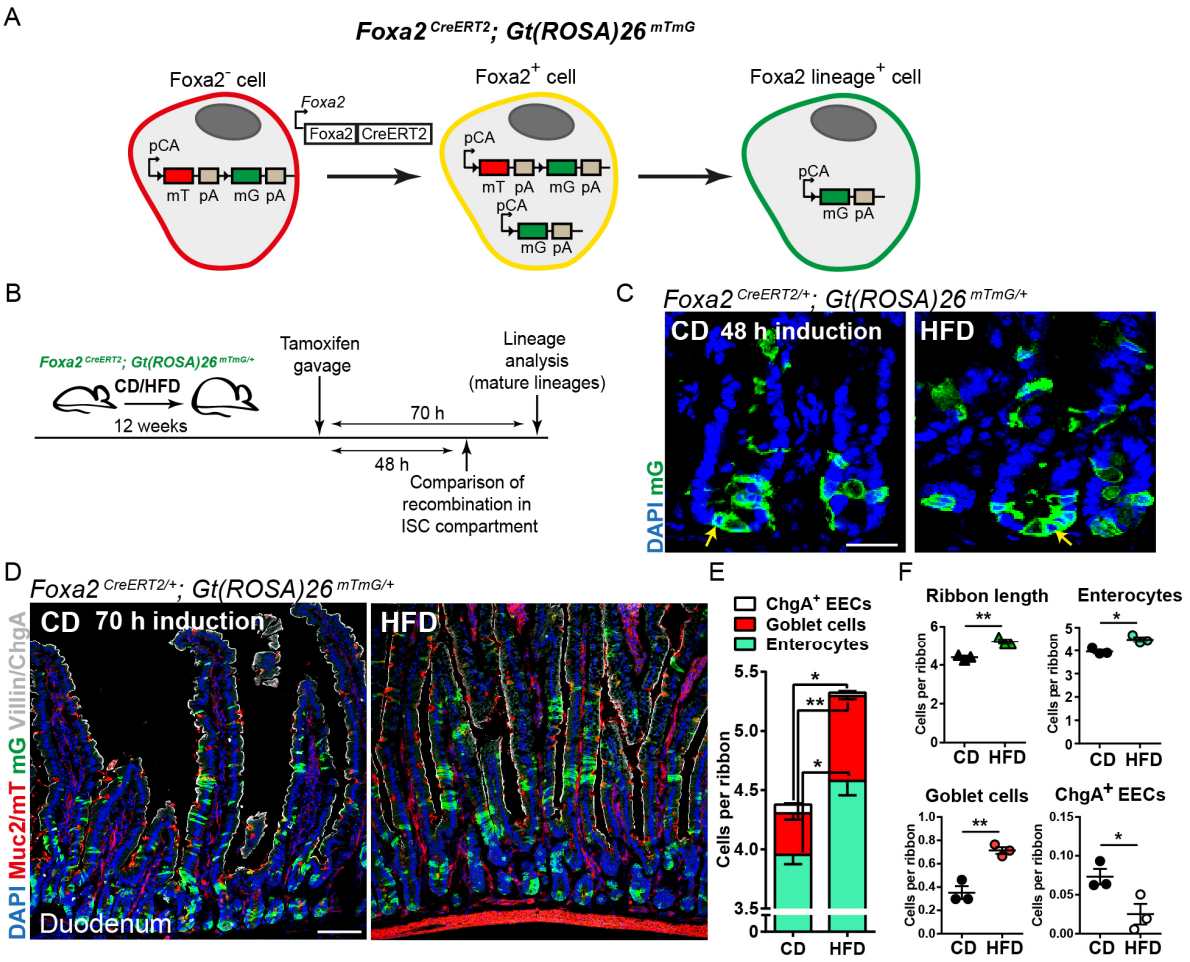

Figure 12: Genetic lineage tracing using *Foxa2*$^{nEGFP\text{-}CreERT2/+}$;*Gt(ROSA)26*$^{mTmG/+}$ mouse confirms altered lineage relations in the mature intestinal compartment on HFD

(A) Scheme illustrating the *Foxa2*$^{nEGFP\text{-}CreERT2/+}$;*Gt(ROSA)26*$^{mTmG/+}$ mouse model. Foxa2-negative cells (mT, red) convert into Foxa2-positive cells (mG, green) upon inducible Foxa2-promoter driven Cre expression via an intermediate (mTmG, yellow) cell state.

(B) Experimental schedule for genetic lineage tracing in CD- and HFD-fed *Foxa2*$^{nEGFP\text{-}CreERT2/+}$;*Gt(ROSA)26*$^{mTmG/+}$ mice. Lineage recombination was induced by oral tamoxifen, and recombination in the ISC compartment or lineage composition in the mature compartment were assessed after 48 hours or 70 hours, respectively.
(C) Recombination in the ISC compartment 48 hours after tamoxifen induction in the duodenal crypts of CD- and HFD-fed *Foxa2*$^{nEGFP\text{-}CreERT2/+}$;*Gt(ROSA)26*$^{mTmG/+}$ animals. Yellow arrows indicate recombined mG$^+$ slender cells at the crypt base next to pyramid-shaped Paneth cells at positions typical for ISCs. Scale bar, 25 μm.
(D) Typical LSM images of the recombination in the duodena of CD- and HFD-fed *Foxa2*$^{nEGFP\text{-}CreERT2/+}$;*Gt(ROSA)26*$^{mTmG/+}$ animals 70 hours after oral tamoxifen. Green cell patches and ribbons in the villi represent Foxa2-lineage. Muc2$^+$ goblet cells (red), ChgA$^+$ EECs (white), villin$^+$ enterocytes (white). Scale bar, 100 μm.
(E) Composition of Foxa2-lineage ribbons induced under CD or HFD conditions. Only coherent mG$^+$ ribbons in the villi were assessed. Right panel: detailed illustration of cell numbers of indicated lineages with regard to the bar plot in the left panel.
(F) Frequencies of coherent mG$^+$ lineage ribbons of different sizes quantified in the villi of *Foxa2*$^{nEGFP\text{-}CreERT2/+}$;*Gt(ROSA)26*$^{mTmG/+}$ mice.
n=3 per group (C-F). Data are mean ± SEM. **P*<0.05, ***P*<0.01 by two-tailed Student's *t*-test.

We next assessed the composition of the Foxa2-lineage ribbons by quantifying the frequencies of ribbon-resident enterocytes, goblet cells and EECs exclusively in the villi of CD- and HFD-fed *Foxa2*$^{nEGFP\text{-}CreERT2/+}$;*Gt(ROSA)26*$^{mTmG/+}$ animals 70 hours after tamoxifen induction (Figure 12B, D). This time period was sufficient to detect recombined coherent mG$^+$ ribbons of mature cells which migrated into the villi. On HFD, lineage ribbons were significantly longer and contained higher numbers of villin$^+$ enterocytes and mucin 2-positive (Muc2$^+$) goblet cells per ribbon, while ribbon-resident chromogranin A-positive (ChgA$^+$) EECs were less abundant (Figure 12D, E). Additionally, the frequency of longer ribbons (≥ 10 cells) was higher, whereas short ribbons (1-5 cells) were less frequent in animals fed a HFD (Figure 12D, F). Together, given that enterocytes were the major constituent of the lineage ribbons, these findings go in line with the scRNAseq data showing increased recruitment of the enterocyte lineage under HFD conditions. By contrast, greater numbers of ribbon-resident goblet cells in the duodena of HFD-fed *Foxa2*$^{nEGFP\text{-}CreERT2/+}$;*Gt(ROSA)26*$^{mTmG/+}$ mice were, at first glance, not congruent with the scRNAseq data, since the overall proportion of goblet cells was not changed in HFD-derived single-cell samples (Figure 12E and Figure 10B). However, the finding that a subset of profiled goblet cells with proximal identity was enriched on HFD (Figure 11D), clearly supports the increase in duodenal (proximal) goblet cells by lineage tracing. This strongly indicates data coherence in both models. Additionally, decreased numbers of lineage ribbon-resident ChgA$^+$ EECs were not congruent with the scRNAseq data showing no change in frequencies of CD- and HFD-derived EECs (Figure 10B). Noteworthy, our analysis showed, however, that *e.g*. only 1/3 of Glp1/2$^+$ EECs were ChgA$^+$ (data not shown), demonstrating that ChgA does not label all EEC subtypes equally (Basak et al., 2017; Beumer et al., 2018; Haber et al., 2017). Thus, changes in numbers of ChgA$^+$ EECs likely represent alterations in specific EEC subtypes.

In summary, using genetic lineage tracing of Foxa2$^+$ ISCs, we could confirm that a HFD induced disturbances in the recruitment of the enterocyte and goblet cell lineages.

4.1.3.2 HFD-induced altered lineage allocation from ISCs in SI crypts translates into mature compartment

Cre-driven genetic labelling of Foxa2$^+$ ISCs confirmed enhanced enterocyte and goblet cell lineage formation in the proximal intestine. Additionally, the results implied that mature lineages inherit, upon differentiation under HFD conditions, region-specific compositional changes as observed by scRNAseq in HFD-derived crypt cells (Figure 11). To validate the impact of HFD on the regional distribution of mature cell types, we first assessed frequencies of goblet cells and ChgA$^+$ EECs in the duodenal and ileal villi of CD- and HFD-fed FVF mice. Consistent with the lower abundance of Foxa2 lineage-labelled ChgA$^+$ EECs, the numbers of both, duodenal and ileal, ChgA$^+$ EECs were diminished in FVF mice fed a HFD (Figure 13D-F). Moreover, the numbers of goblet cells in the duodenum increased 1.5-fold as compared to controls, whereas goblet cells in the ileum were found at slightly lower frequencies in HFD-fed FVF mice (Figure 13A-C). These results are in line with the increase in numbers of lineage-labelled

goblet cells in the duodena of *Foxa2*$^{nEGFP\text{-}CreERT2/+}$;*Gt(ROSA)26*$^{mTmG/+}$ animals as well as with the scRNAseq data (Figure 11D, Figure 12E). Both, an enhanced recruitment of the enterocyte lineage by scRNAseq and a higher abundance of enterocytes and goblet cells by genetic lineage labelling on HFD, (Figure 10B, Figure 12E) coincided with the increase in villi height in FVF mice (Figure 7B), given that enterocytes and goblet cells constitute the main body of the villus. Together, these findings demonstrate a mechanism of adaptation to excess nutrient intake.

Paneth cells are the only differentiated cells permanently located in the crypts and were found at a higher ratio in single-cell samples of HFD-fed FVF mice (Figure 10B). Whereas the scRNAseq data showed a marked increase in Paneth cell numbers (Figure 10B), primarily with proximal identity (Figure 13G-I), the assessed numbers of lysozyme-positive (Lyz$^+$) Paneth cells in duodenal crypts of FVF mice were not changed under HFD conditions (Figure 13J, K). Paneth cells are large cells, thus isolating by flow cytometry likely results in their lower recovery, thus creating a bias (see section 4.1.2.1). Additionally, it is also possible that HFD-derived Paneth cells possess different physical properties (*e.g.* smaller size, different side or forward scatter properties, granularity etc.), which may result in a better recovery compared to controls. Thus, findings independent of isolation bias (*e.g.* assessment of tissue sections or whole-mount crypt stainings) are likely more reliable for Paneth cell quantification.

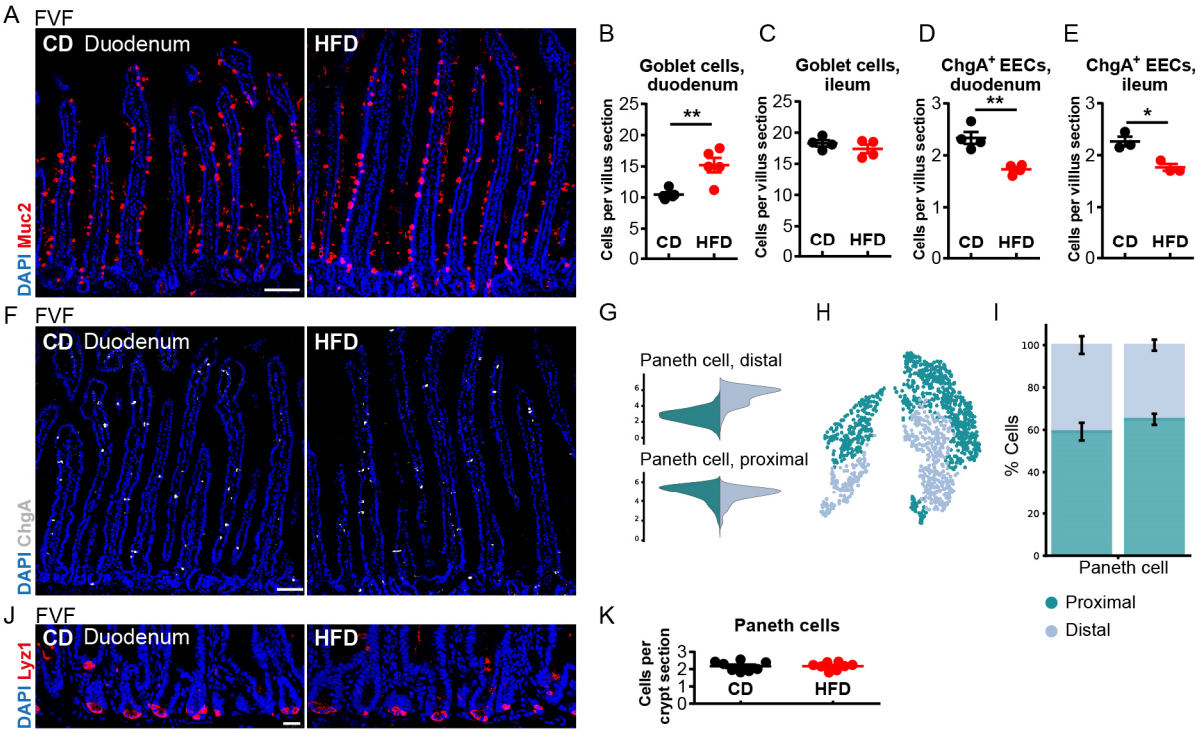

Figure 13: Composition of mature cell lineages is altered in FVF mice under HFD conditions

(A-C) Representative LSM images of a goblet cell staining (Muc2, red) in duodenal sections (A) and quantification of goblet cell numbers in the duodenum (B, n=5 per group; two independent experiments) and ileum (C, n=4 per group) under CD and HFD conditions. Scale bar, 75 µm.
(D-F) Quantification of ChgA$^+$ cell numbers in the duodena (D, n=4 per group) and ilea (E, n=3 per group), and typical LSM images of a ChgA staining in the duodenal sections of CD- and HFD-fed FVF mice. Scale bar, 75 µm.
(G-H) Distribution of Paneth cells with proximal and distal signatures based on regional markers for Paneth cells as recently described (Haber et al., 2017) (G) and presented in UMAP space (H).
(I) Proportions of Paneth cells with proximal and distal identities within CD- and HFD-derived samples. Data are mean ± SEM. n=3 per group.
(J, K) Representative LSM images (J) and quantification (K, n=8 per group) of Paneth cells in duodenal sections of CD- and HFD-fed FVF mice. Scale bar, 25 µm.
In (B-E, K), data are presented as mean ± SEM. **P*<0.05, ***P*<0.01 by two-tailed Student's *t*-test.

Bioinformatic data analyses for (G-I) was performed by Sophie Tritschler.

Additionally, we assessed the numbers of so called label-retaining cells (LRCs), suggested to be putative progenitors for Paneth cells (Buczacki et al., 2013; N. Li et al., 2016; Boettcher et al., in revision). These cells persist for longer than 10 days and are quiescent or slowly cycling. To compare the frequencies of duodenal LRCs between the diet conditions, we administered 5-bromodeoxyuridine (BrdU) to FVF mice, maintained for 11 weeks on a diet, for 14 days (pulse) in drinking water (Figure 14A). Of note, Lyz$^+$ Paneth cells are, in contrast to other intestinal lineages, long-lived cells with a lifespan of around 6-8 weeks and, hence, also label-retaining in this experiment. After a 21-day chase period, the numbers of Lyz$^-$/BrdU$^+$ (non-Paneth cell) LRCs, were slightly lower in the duodena of HFD-fed FVF mice (Figure 14A-D). Thus, the finding that the putative Paneth cell progenitors are reduced in numbers under HFD condition may provide further support for the data from tissue stainings demonstrating that the numbers of Paneth cells are not changed. Nevertheless, additional experiments are required for a definite conclusion.

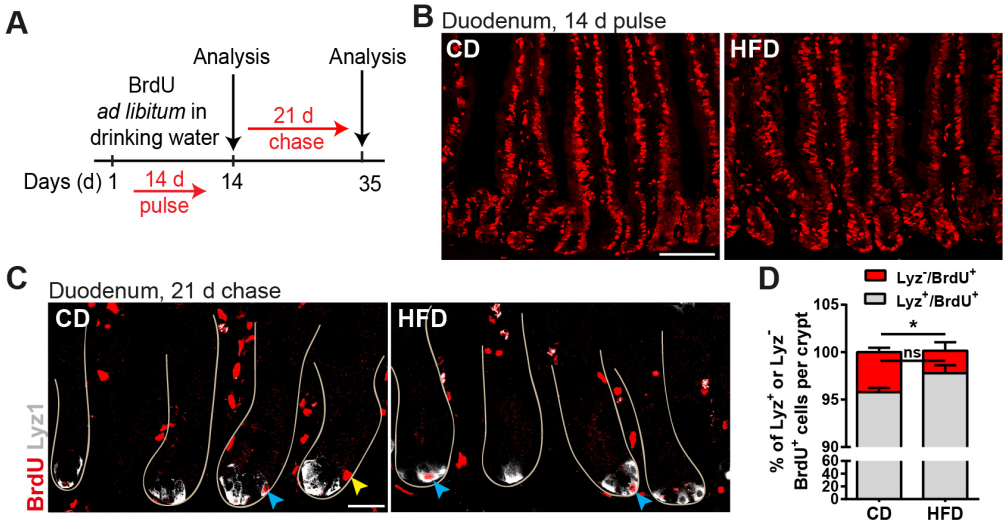

Figure 14: Abundance of label retaining cells (LRCs), as putative progenitors for Paneth cells, is reduced in the duodena of HFD-fed FVF mice

(A) Schedule of 5-bromo-2-deoxyuridine (BrdU) pulse-chase experiment for the analysis of the LRC frequency. To assess BrdU label retention under CD and HFD conditions, FVF mice (after 10 weeks on diet) were given BrdU for 14 days and duodenal sections were analysed after a chase period of 21 days.
(B) Representative LSM images of duodenal sections after 14 days of continuous BrdU pulse in CD- and HFD-fed FVF mice. BrdU-labelled cells are stained in red. Scale bar, 75 µm
(C) Typical LSM images of duodenal crypts of CD- and HFD-fed FVF mice after a chase period of 21 days. Yellow arrowhead highlights a BrdU-labelled/Lyz-negative LRC. Blue arrowheads indicate Lyz/BrdU-double-positive cells. Scale bar, 25 µm.
(D) Percentages of Lyz$^-$ and Lyz$^+$ BrdU-labelled cells of the total number of BrdU-positive cells in duodenal crypts of CD- and HFD-fed mice. n=4 *versus* 5 per group. Data are presented as mean ± SEM. *P<0.05 by two-tailed Student's *t*-test.

Together, these findings demonstrate that HFD-induced disturbances in lineage recruitment and region-dependent distribution of the enterocyte and goblet cell lineages in the crypt translate into the mature compartment. Moreover, reduction of ChgA$^+$ EEC numbers on HFD raises the question as to which explicit EEC subsets are affected.

4.1.4 HFD affects EE progenitor numbers and subset allocation of mature EECs

EECs are important nutrient sensors and regulate systemic energy balance (Cummings & Overduin, 2007; Drucker, 2007; K.-S. Kim et al., 2018). Early endocrine lineage formation from ISCs and EEC subtype allocation are not completely understood. Obesity and diabetes are associated with disturbances in the enteroendocrine axis, however, the cellular and molecular pathomechanisms are still elusive (K.-S. Kim et al., 2018).

EECs are very heterogeneous and rare intestinal epithelial cells and, hence, difficult to study using conventional approaches. Therefore, to examine whether HFD affected EEC lineage formation and EEC subtype allocation, we took advantage of our FVF-based single-cell enrichment strategy for secretory and, in particular, endocrine lineage cells from SI crypts. We profiled in total 2,865 EEC lineage cells to obtain high-resolution data providing a better record of the EEC lineage in homeostasis and in metabolic disorder than available to date (Beumer et al., 2018; Glass et al., 2017; Grün et al., 2015; Haber et al., 2017).

Haber et al suggested a classification of mature EEC types based on single-cell transcriptional signatures comprising mature cell clusters SILA, SILP, SIK, SAKD and two types of enterochromaffin (EC) cells[10] as well as four distinct progenitor clusters (early, middle, late and *ghrelin-* (*Ghrl*) expressing progenitors) (Haber et al., 2017). Hereby, e. g. SILA cells co-express secretin (S), Cck (I), Glp-1 (L) and ghrelin (A).

4.1.4.1 Single-cell transcriptional profiling reveals novel EEC progenitors and differentiation trajectories to mature EEC subsets

To fine-map the EEC lineage, we partitioned the 2,865 CD- and HFD-derived EEC lineage cells from SI crypts into distinct subclusters and annotated them based on known EEC marker gene signatures (Haber et al, 2017). Refined clustering revealed two early (Sox4$^+$, Ngn3$^+$) and three late (Arx$^+$/Isl1$^+$, Pax4$^+$, Ghrl$^+$) EEC progenitor clusters, six mature EEC subsets (SILA, SILP, SAKD, SIK, EC and Reg4$^+$ EC cells) as well as a population of heterogeneous EECs co-expressing hormones and ISC markers (termed Lgr5$^+$ EECs) (Figure 15A-C).

Our CD- and HFD-derived EEC subsets are in large part consistent with the EEC classification by Haber et al., however, we revealed novel late, Arx$^+$/Isl1$^+$ and Pax4$^+$, EE progenitors (Figure 15A-C). To dissect EEC lineage allocation along the differentiation routes to mature subtypes, we used PAGA to estimate cluster connectivity. PAGA robustly predicted differentiation routes along the main branch from the common Ngn3$^+$ progenitor via the Pax4$^+$ progenitor to EC and Reg4$^+$ EC cells or via the Arx$^+$/Isl1$^+$ and Ghrl$^+$ progenitors to SILA, SILP, SIK and SAKD clusters (

Figure 16A). To support this finding, we estimated the RNA velocity, a measure of gene transcription kinetics based on the ratio of unspliced and spliced transcripts and a proxy for cell differentiation state (La Manno et al., 2018). RNA velocity suggested a directed lineage allocation along the main route from the Sox4$^+$ early progenitor via the Pax4$^+$ and Arx$^+$/Isl1$^+$ progenitor states into mature EEC subsets (

Figure 16A). Congruently, *Isl1* and *Pax4* were induced in corresponding EE progenitor clusters indicated by a high RNA velocity (

Figure 16B).

[10] S: Secretin (Sct); A: ghrelin (Ghrl); K: Gastric inhibitory polypeptide (GIP); D: Somatostatin (Sst); I: cholecystokinin (Cck); L: glucagon-like peptide-1 (Glp-1); P: peptide yy (Pyy); EC: serotonin (5-HT)-expressing cells

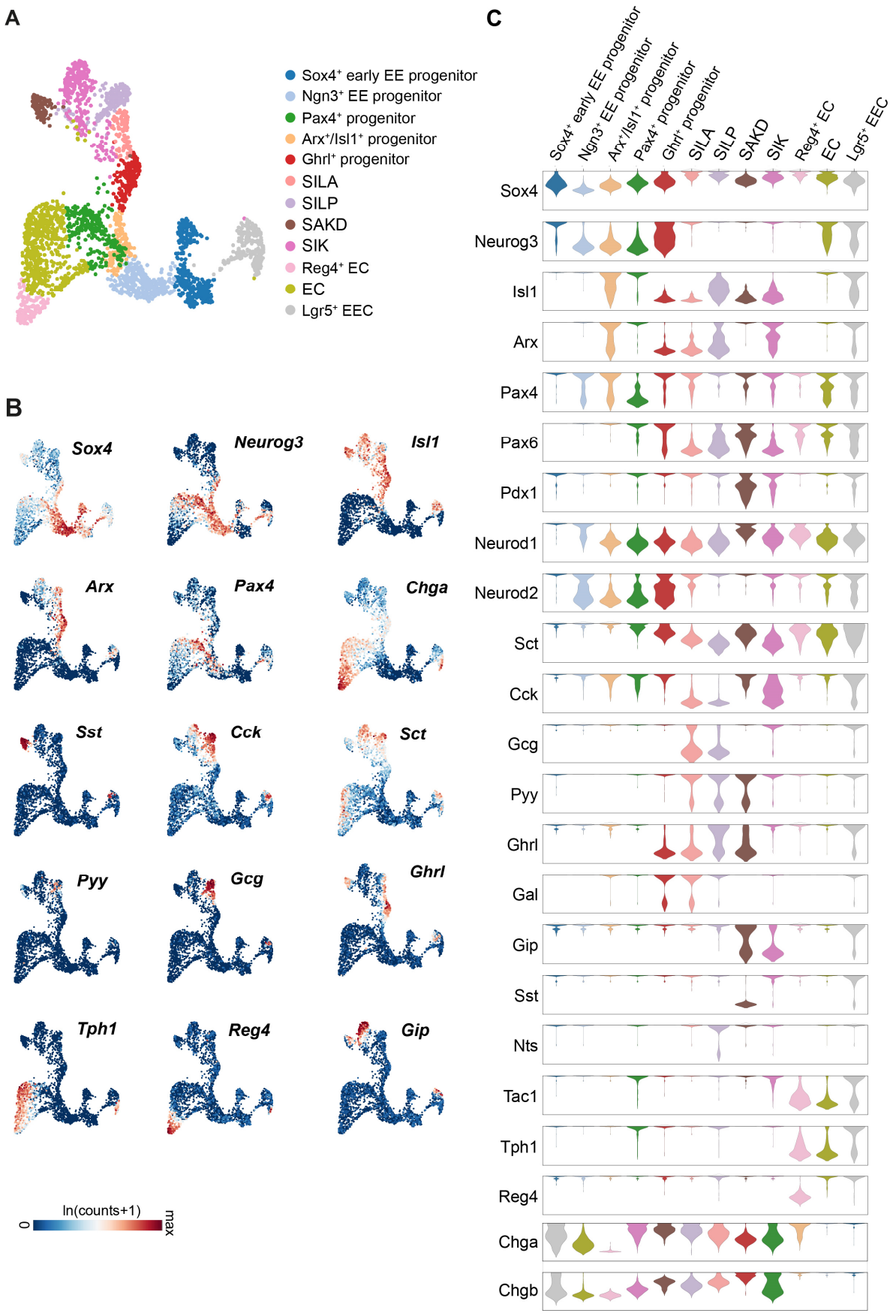

Figure 15: Refined clustering of EEC lineage cells reveals early and novel late EE progenitors and distinct mature EEC subsets

(A) Colour-coded UMAP plot illustrating clusters of 2,865 EEC lineage cells from CD- and HFD-derived samples. Cluster annotation was based on known marker genes. Cluster labelling of mature EEC subtypes as previously described (Haber et al., 2017).
(B) Expression of selected EEC markers (transcription factors, hormones *etc*.) in EEC clusters plotted in UMAP space.
(C) Violin plots illustrating distribution of gene expression levels of selected transcription factors, hormones and important EEC markers in EEC clusters.
Bioinformatic data analyses for this figure was performed by Sophie Tritschler.

Further, we identified transcription programmes specific to the discrete EE progenitors, shared between either the early or the late EE progenitors, or specific for a distinct EEC lineage branch. Thus, *10007H06Rik, Cdc25b* and *Gadd45b* (a gene involved neurogenesis, (D. K. Ma et al., 2009)) were enriched in Sox4$^+$ early progenitor cells, while *e.g*. *Dll1* and *Trit1*[11] marked both, Sox4$^+$ and Ngn3$^+$ early progenitors (

Figure 16C). *Sox4*, *Tox3*[12] and *Marcksl1*[13] marked early and late progenitors while only minimally expressed in mature lineages. Interestingly, a gene set including *Gfra3* (GDNF receptor family member), *Insm1*, *Nkx2.2*, *Trp53*, *Fgd2*[14], *Rph3al*[15], *Vwa5b2*, *Olfm1*, *Neurod1*, *Rfx6,* was expressed throughout all EEC clusters from Nng3$^+$ progenitor on. Genes labelling the late progenitors comprised *e.g*. *Pax4* and *Phip*[16] in the Pax4$^+$ progenitor, *Ooep* in Arx$^+$/Isl1$^+$ progenitor and *Gper*[17] and *Acsl1*[18] in the Ghrl$^+$ progenitor. Some genes marked a lineage branch such as *e.g*. *Mboat4*[19] and *Cd177*, expressed in Ghrl$^+$ progenitor and in *Ghrl*-expressing SILA and SAKD cells.

A considerable heterogeneity within the EEC subtypes including overlapping hormone expression patterns, makes it difficult to study different EEC subsets due to the lack of subtype-specific or panendocrine markers. Thus, we identified gene sets specific to the distinct mature EEC subsets as potential markers for subtype labelling. These included enzymes (*e.g*. *Fars2* and *Cpn1* in SILP, *Arg1* and *Th* in SAKD, and *Prps1* in SIK cells), ion channels (*e.g*. *Kcnk2*, *Asic5* in SAKD, *Trpa1* in Reg4$^+$ EC cells), genes associated with signalling transduction (*e.g. Rgs4* in SAKD, *Pkib* in SIK, *Ptprn* and *Amigo2* in Reg4$^+$ EC cells), receptors (*e.g. Acvrl1* in Reg4$^+$ EC cells), cytoskeletal or vesicular trafficking genes (*e.g. Krt20* and *Scg2* in SILP, *Rab3b* in Reg4$^+$ EC and *Vim* in EC and Reg4$^+$ EC cells) as well as transcription factors (such as *Hhex* in SAKD cells) (Figure 17). The newly described Reg4$^+$ EC cells (Haber et al., 2017) had a highly specific gene signature including *Rpp25*, *Ces3a*, *Psat1*, *Afp, S100a1, Ucn3*[20], *Slc18a2*[21], *Tpbg*[22] and *Reg4*, distinguishing these cells from related EC cells and other subsets (Figure 17).

[11] Mitochondrial tRNA isopentenyltransferase 1; its expression can decrease cell proliferation
[12] TOX High Mobility Group Box Family Member 3: transcriptional coactivator of the p300/CBP-mediated transcription complex; involved in c-FOS transcription activation in neurons
[13] Macrophage Myristoylated Alanine-Rich C Kinase Substrate Like 1: plays a role in cytoskeletal regulation, PKC and calmodulin signalling
[14] FYVE, RhoGEF And PH Domain Containing 2: GEF, controls cytoskeletal membrabe rearrengements, vesicle trafficing
[15] Rabphilin 3A Like: directly regulates calcium-ion-dependent exocytosis in endocrine and exocrine cells; plays a key role in insulin secretion by β-cells
[16] Pleckstrin Homology Domain Interacting Protein: presumable mediator of the insulin and insulin-like growth factor signaling pathways; probable regulator of growth and survival of pancreatic β-cells
[17] G Protein-Coupled Estrogen Receptor 1: binds estrogen and mediates multiple downstream signaling pathways in different cell types
[18] Acyl-CoA Synthetase Long Chain Family Member 1: key enzyme in fatty acid degradation and lipid synthesis
[19] Membrane Bound O-Acyltransferase Domain Containing 4: facilitates the octanoylation of ghrelin at Ser3
[20] Also highly expressed in mouse β-cells
[21] A transporter for monoamines such as serotonin
[22] Antagonist of Wnt/β-Catenin and mediator of Wnt/PCP signalling

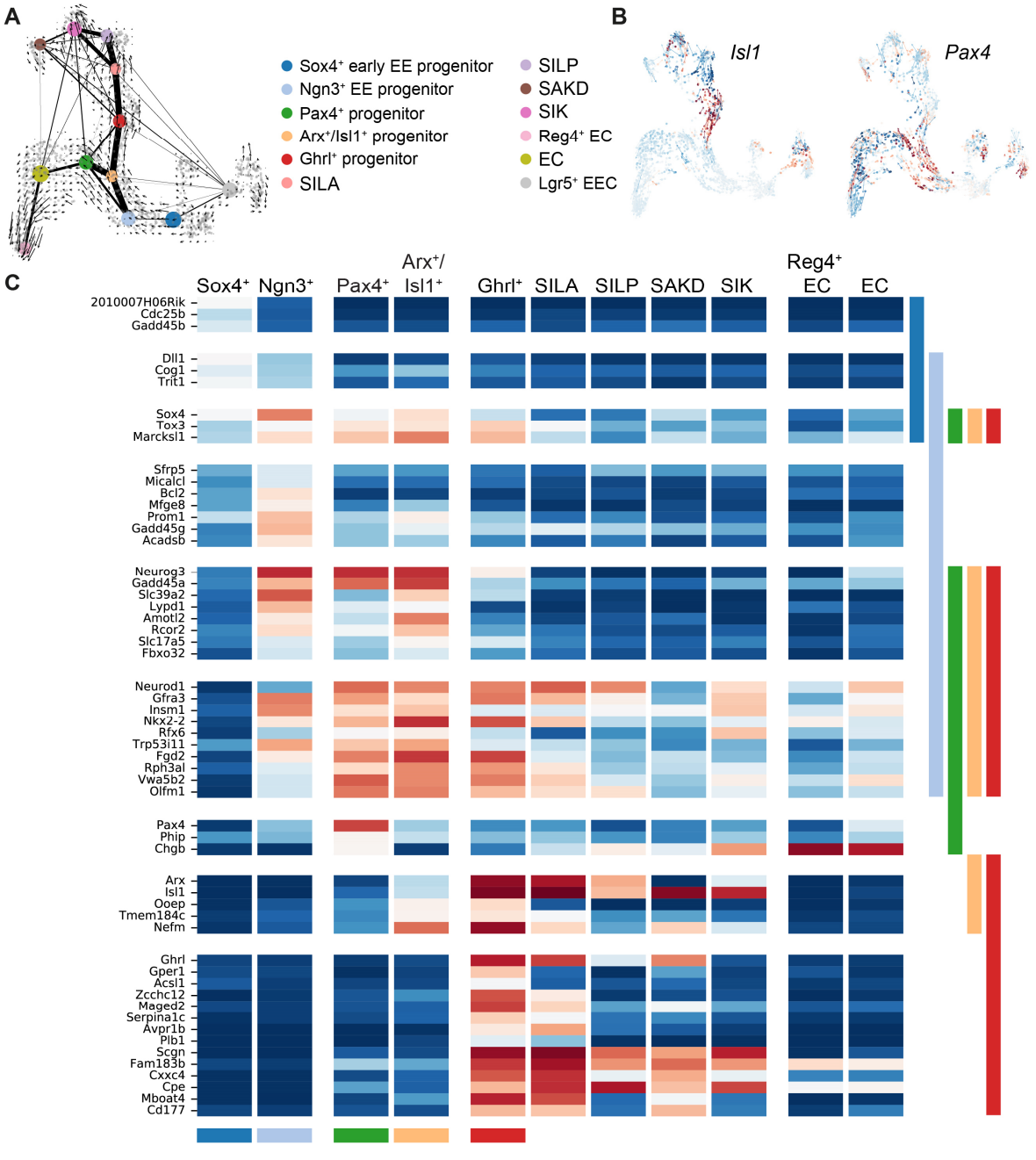

Figure 16: scRNAseq of 2,865 CD- and HFD-derived EEC lineage cells reveals differentiation paths via Pax4⁺ or Arx⁺/Isl1⁺ EEC progenitors

(A) EEC lineage relations presented by PAGA and RNA velocity force field projected into UMAP space. Arrows by RNA velocity indicate average direction of differentiation along the trajectories and estimated future states cells.
(B) RNA velocities of *Isl1* and *Pax4*. High velocities (indicated by red colour) are, correspondingly, found in the late Arx⁺/Isl1⁺ or Pax4⁺ EE progenitors around the branching point of the trajectory and indicate gene induction.
(C) Heatmap of gene signatures specific to EE progenitors or overlapping between progenitors or progenitors and their lineage. Average expression values per cluster are depicted (red, high expression; blue, low). Colour bars at the bottom of the heatmap represent EE progenitor clusters. Colour bars at the right side of the heatmap highlight expression of a gene set across corresponding EE progenitor clusters. Specific EE progenitor markers are distinguished by one coloured line, while overlapping coloured lines highlight gene expression across several progenitor clusters or in the progenitor and its lineage.
Bioinformatic data analysis for this figure was done by Sophie Tritschler.

To summarise, our single-cell data provide a high-resolution map of the EEC lineage in homeostasis and in metabolic disorder. Moreover, we identified novel EEC progenitors and differentiation routes along the EEC lineage tree and proposed potential markers for the segregation of mature EEC subtypes. Interestingly, gene signatures of EEC progenitors and mature EEC subsets resemble transcriptional programmes involved in pancreatic endocrine differentiation and lineage allocation. This may help to better understand the pathomechanisms of the EE dysfunction when learning from known molecular pancreas-related factors associated with T2D pathogenesis.

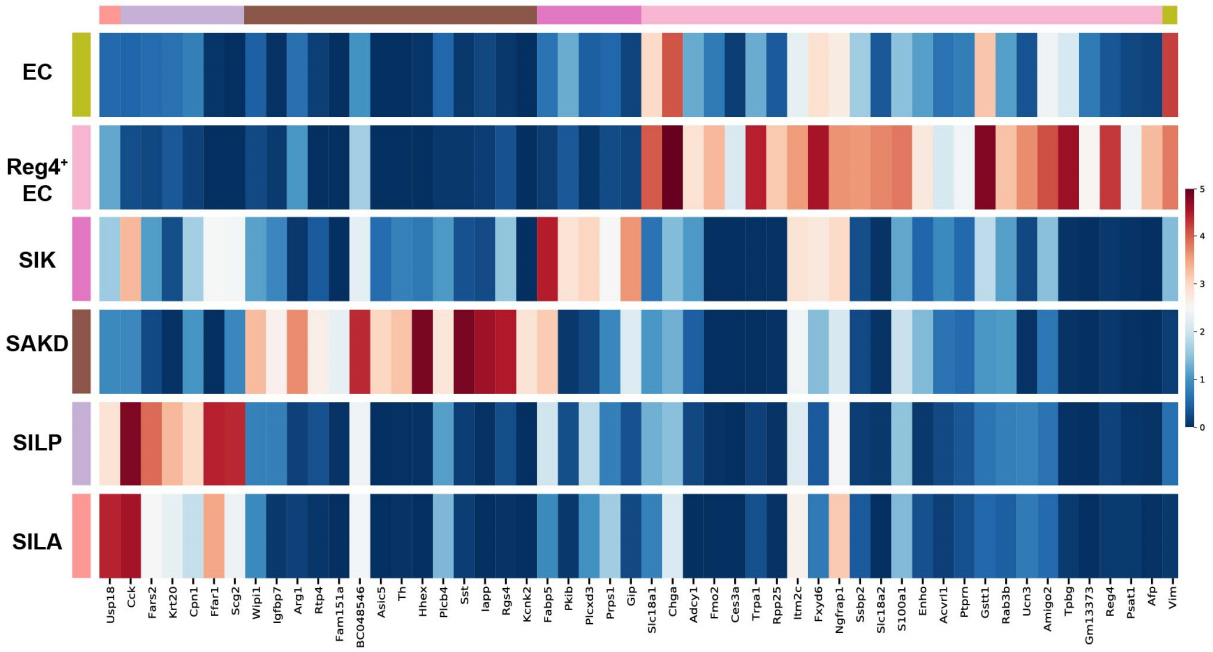

Figure 17: Specific gene signatures of mature EEC subsets as potential candidates for subset labelling

Heatmap depicts average expression levels per cluster of specific known and novel marker genes in mature EEC subtypes.
Bioinformatic data analyses for this figure was performed by Sophie Tritschler.

4.1.4.2 Single-cell profiling reveals disturbances in EEC subset allocation and transcriptional networks on HFD

To test whether HFD affected EEC subset allocation, we compared relative proportions of distinct EEC subclusters between the diet conditions. Cell densities of the early EE progenitors were altered in HFD-derived samples (Figure 18A). Strikingly, the relative abundance of the Ngn3⁺ progenitor cells was increased, while the numbers of Sox4⁺ progenitors were slightly lower and the densities of the late EE progenitors (Arx⁺/Isl1⁺ and Pax4⁺) were not significantly changed under HFD conditions (Figure 18B). Moreover, HFD affected numbers of mature EEC subsets. Thus, the proportion of SILA cells was increased from 2.9 % to 4.3 %, while the relative numbers of not yet functionally characterised Reg4⁺ EC cells decreased by half (from 7 % to 3.5 %) in HFD-derived samples (Figure 18B).

Interestingly, we also observed a marked reduction in the relative proportion of Lgr5⁺ EECs in HFD-fed animals (Figure 18B). These cells represent a highly heterogeneous group of EECs, resembling Bmi1-GFP⁺ EECs described recently that have not been distinctly characterised yet (Yan, Gevaert, et al., 2017).

Together, these findings demonstrate that EEC lineage composition is altered under HFD conditions and that HFD affects EEC subset proportions in different ways.

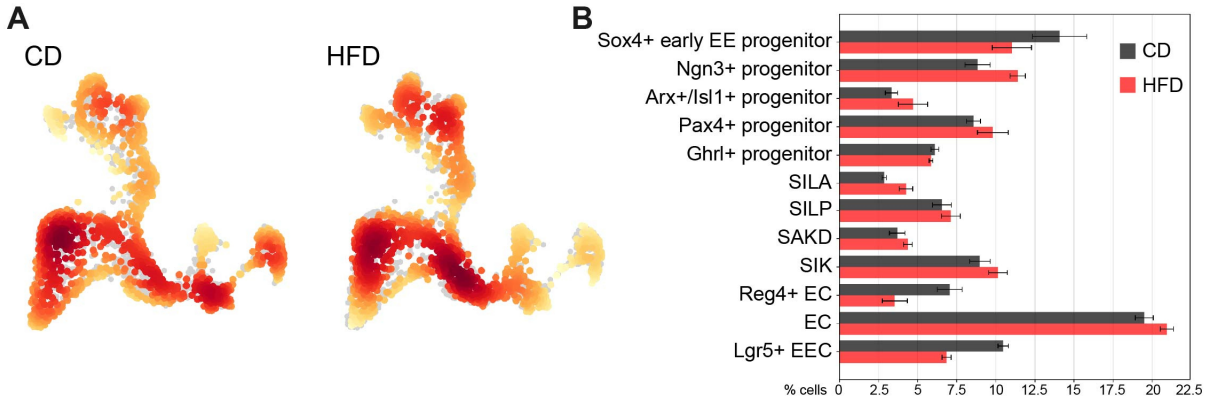

Figure 18: Relative proportions of early EE progenitors and mature EEC subsets are altered on HFD

(A) Densities of EEC lineage cells projected onto the UMAP plot in CD- and HFD-derived samples.
(B) Relative proportions of cells in CD- *versus* HFD-derived EEC clusters. Data are presented as mean ± SEM. n=3 per group.
Bioinformatic data analyses for this figure was done by Sophie Tritschler.

Alterations in the transcriptional network may affect EEC subset formation and function. We therefore analysed gene expression differences in CD- and HFD-derived EEC clusters. Except for the Sox4$^+$ early EE progenitors, transcriptome analysis identified only few differentially expressed transcripts in the EEC clusters of HFD-fed animals. Nonetheless, these included several interesting candidates involved in metabolism (*e.g. Hmgcs2*, *Acot1*, *Scd2* up- or *Sis* downregulated in Sox4$^+$ and Ngn3$^+$ progenitors; *Slc5a1*[23], downregulated, and *Acadl* upregulated in SIK cells; *Scarb1*[24] upregulated in EC cells), vesicular trafficking machinery and secretome (*e.g. Sct* upregulated in SIK cells; reduced levels of *Cplx2*[25] in EC cells), signalling transduction (*Gnas*[26] upregulated in EC cells) and transcription factors (*e.g. Hmgn3*[27] upregulated in EC cells) (Figure 19A-D) (Friocourt & Parnavelas, 2011; Kurahashi, Furusawa, Ueda, & Bustin, 2009; Ueda, Furusawa, Kurahashi, Tessarollo, & Bustin, 2009). Additionally, we found genes, recently associated with diabetes and metabolic syndrome, such as *Serpinb1a* (secreted protein involved in β-cell proliferation and compensation to insulin resistance in diabetic patients), upregulated in EC cells, and *Tmsb4x* (involved in regulation functions, such as proliferation and cytoskeleton modulation, and demonstrated to be upregulated in rat livers after a HFD-feeding), upregulated in the Ngn3$^+$ progenitor cluster (Figure 19B, C) (El Ouaamari et al., 2016; Lan et al., 2015). We, further, specifically compared expression of hormone genes in CD- and HFD-derived EEC clusters in which these are expressed. Only *Gast* (gastrin) transcript abundance was reduced in HFD-derived *Gast*-expressing EECs (Figure 19Figure 20E).

Together, these findings revealed an altered EEC subset allocation including differences in early EE progenitors and several mature EEC subsets. We, moreover, identified a set of differentially expressed transcripts in HFD-derived EEC clusters involved in regulation of cellular functions. However, since the major EE transcription factors and known factors involved in subtype commitment were not changed, observed transcriptional disturbances are unlikely to have impact on the EEC proportions. Further validation is, yet, required to assess the exact effect of these changes on EEC function and how this relates to the pathogenesis of T2D.

[23] Sodium-dependent glucose-galactose transporter
[24] Scavenger receptor for high-density lipoprotein (HDL) that facilitates uptake and transport of cholesterol
[25] Involved in regulation of exocytosis of secretory vesicles
[26] Involved in G protein-coupled receptor (GPCR) signalling, *e.g.* downstream of β-adrenergic receptors
[27] Neuronal Arx-target gene, also expressed in pancreatic α- and β-cells which regulates insulin and glucagon secretion machinery

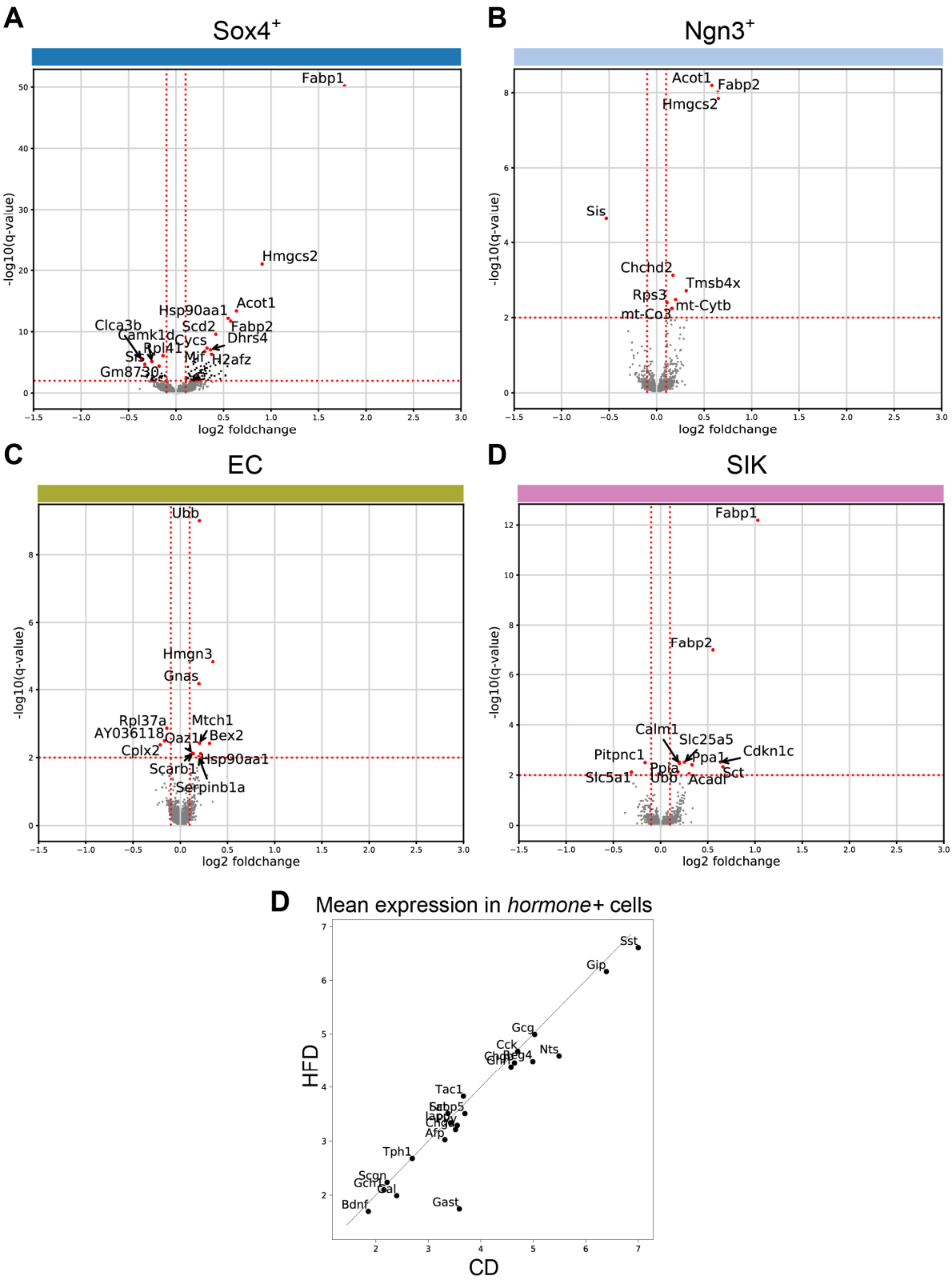

Figure 19: Differential gene expression in CD- and HFD-derived EEC subsets

(A-D) Differentially expressed genes in Sox4+ (A), Ngn3+ (B) EE progenitors and in mature EC (C) and SIK (D) EEC subsets between CD- and HFD-derived clusters. Each dot represents a gene, and regulated genes are highlighted in black. For each gene, estimated logFC is plotted on the x- and adjusted P-value on the y-axis. Thresholds used for significance level and gene expression change are indicated by red lines. The top 10 genes ranked by adjusted P-value are denoted.

(E) Comparison of mean expression levels of hormone genes between the CD- and HFD-derived EECs. EECs with expression levels of indicated genes > 0 were considered for the analysis.
Bioinformatic data analyses for this figure was done by Sophie Tritschler.

4.1.4.3 Validation of the disturbed EEC subset allocation in SI tissue and isolated crypts in FVF mice

To verify changes in EEC subtype proportions identified by scRNAseq, we performed immunofluorescence (IF) stainings of relevant EEC markers on SI tissue sections and in whole-mount SI crypts isolated from FVF mice. As expected, the numbers of Ngn3$^+$ cells more than doubled (from 0,82 ± 0,05 to 1,81 ± 0,12 cells per crypt) in crypts from HFD-fed FVF animals confirming higher proportions of Ngn3$^+$ EE progenitors detected by scRNAseq (Figure 20A, B). Further, the abundance of serotonin- (5-HT) immunoreactive EC cells was significantly reduced under HFD conditions reflecting changes in proportions of EC and Reg4$^+$ EC single-cell clusters (Figure 20B, C). Notably, given that 5-HT$^+$ EECs accounted for over 80 % of ChgA$^+$ cells, also the numbers of ChgA$^+$ EECs were reduced in a similar fashion in HFD-derived SI crypts (Figure 20E, F). These results are in line with the lower frequency of ChgA$^+$ EECs in the villi of FVF mice on HFD as previously shown (Figure 13D-F). To mention here, we obtained similar results in BL/6J mice maintained for 16 weeks on a HFD showing an approximate 25 % reduction in numbers of 5-HT$^+$ and ChgA$^+$ EECs (Figure 20G, H).

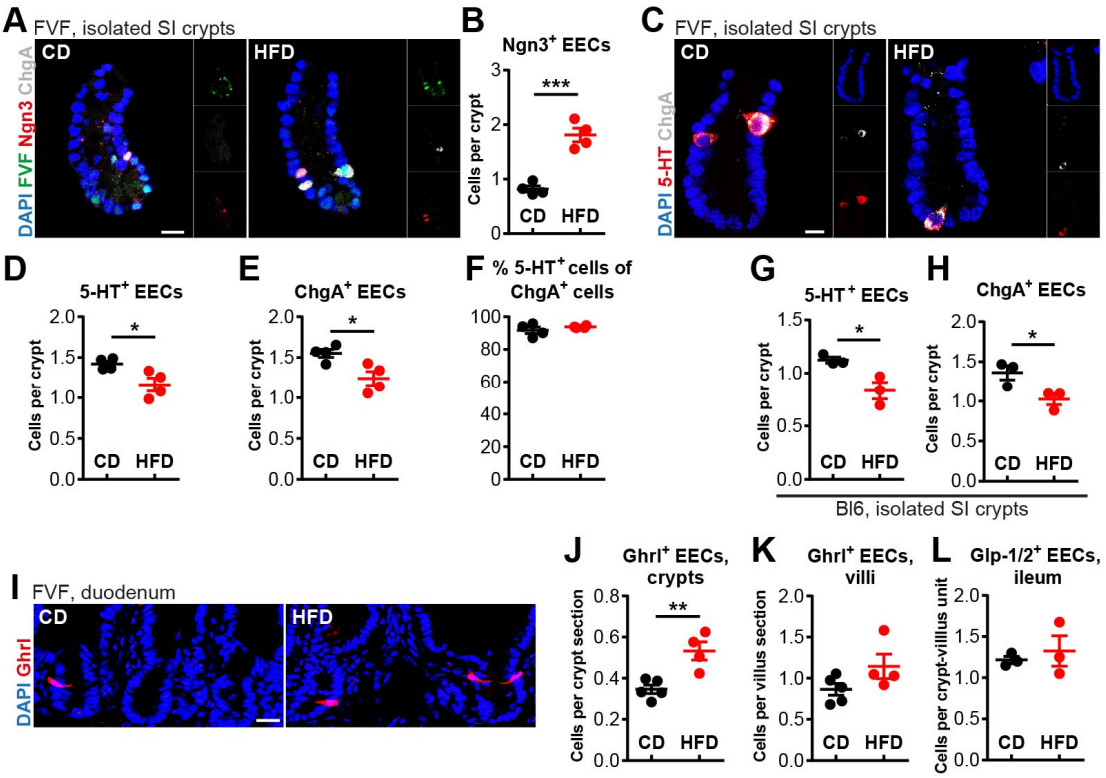

Figure 20: Verification of HFd-induced changes in EEC subset proportions

(A-F) Typical LSM images of Ngn3$^+$ (A), 5-HT$^+$ (D) and ChgA$^+$ cells (E) in whole-mount stainings of isolated SI crypts from CD and HFD-fed FVF mice and quantification (B, D, E). (F) Percentage of 5-HT$^+$ cells of the total number of ChgA$^+$ cells.
(G, H) 5-HT$^+$ (G) and ChgA$^+$ EECs (H) are reduced in SI crypts of BL/6J mice after 16 weeks on HFD.
(I-K) Representative LSM images of duodenal crypt sections (I) and quantification of Ghrl$^+$ EECs in crypts (J) and villi (K) of CD- or HFD-fed FVF mice.
(L) Numbers of Glp-1/2$^+$ EECs in the ilea of CD- and HFD-fed mice.

Data are shown as mean ± SEM. *P<0.05, **P<0.01, ***P<0.001 by two-tailed Student's *t*-test. n=4 per group (B, D-F), n=5 *versus* 4 per group (J, K) and n=3 per group (G, H, L). Scale bars 10 μm (A, C), 25 μm (I).

To validate the increase in numbers of SILA cells, we quantified Ghrl$^+$ cells in crypts and villi in the duodenum, where these EECs are preferentially found in mice (Engelstoft et al., 2013; Gribble & Reimann, 2016). Indeed, HFD-fed animals displayed higher numbers of Ghrl$^+$ EECs in the crypts and a mild increase in the villi (Figure 20I-K).

Gcg is expressed in two EEC subsets in our data, SILA and SILP cells. While the numbers of SILA cells, more abundant in the proximal intestine, were increased, the relative frequency of SILP cells, which are mostly found in the distal part, were not changed (Figure 18B) (Haber et al., 2017). Given that EECs immunoreactive for Glp-1 are most frequent in the distal intestine in mice (Richards et al., 2016), we quantified the abundance of Glp-1/2$^+$ EECs in the ilea of CD- and HFD-fed animals. The frequency of Glp-1/2$^+$ cells in the ileal villi were comparable in both diet groups, a finding possibly correlated with the unchanged proportions of distal SILP cells by scRNAseq (Figure 20L). However, two related questions remain open: whether the Ghrl$^+$ EECs, quantified in the duodena, co-secrete Glp-1/2$^+$ (correspondent with the SILA cells) *in vivo*; and if so, whether the total numbers of Glp-1/2$^+$ EECs are, for that reason, increased.

Moreover, further studies will be required to eliminate the uncertainty of whether the reduced numbers of 5-HT$^+$ cells observed in mouse intestines under HFD conditions directly relate to the changes in Reg4$^+$ EC cells profiled by scRNAseq. In addition, how altered proportions and transcriptional changes identified in single-cell EEC subsets exactly relate to numbers, secretion patterns and regional distribution of EECs *in vivo*, has to be addressed by more thorough studies.

4.1.4.4 HFD-induced disturbances in levels of circulating gut hormones indicate EEC dysfunction

The aetiology of the EE dysfunction in metabolic disorder remains elusive (Defronzo, 2009; Holst, 2013). In addition, how disturbances in circulating hormones correlate with compositional changes or function of EEC subsets is not clear (Gribble & Reimann, 2016; Holst, 2013; Steinert et al., 2017). Our data revealed alterations in both, EEC subtype numbers and gene expression profiles. Disturbances in the transcriptional network, *e.g.* changes in expression of genes related to vesicular trafficking, as detected in a few of EEC subsets, may potentially affect hormone secretion (Figure 19A, B). To test this and to correlate alterations in EEC subset numbers with levels of circulating gut hormones, we measured plasma concentrations of serotonin, ghrelin, Glp-1 and PYY in CD- and HFD-fed FVF mice (Figure 21A).

Over 90 % of body's serotonin is synthesised in the EC cells of the gut (Amireault, Sibon, & Côté, 2013; D. Y. Kim & Camilleri, 2000). In HFD-fed animals, we observed a drastic decrease in relative proportions of Reg4$^+$ EC cells and a reduced abundance of 5-HT$^+$ cells in SI crypts (Figure 18B, Figure 20C, D). Reg4$^+$ EC cells have not been functionally characterised yet, but their transcriptomes strongly indicate a Tph1[28]-dependent serotonin production (Figure 15B, C). To assess whether reduced numbers of 5HT$^+$ EECs are associated with altered levels of serotonin in circulation, we compared basal serotonin concentrations in the plasma of CD- and HFD-fed FVF mice. Plasma serotonin was significantly reduced in mice on HFD (Figure 21B). However, how disturbed serotonin levels relate to obesity and diabetes is still unclear. Several studies have reported, though with conflicting results, that disturbances in the peripheral serotonin levels affect glucose handling by impacting glucose uptake into tissues and insulin secretion from pancreas (Paulmann et al., 2009; Sugimoto et al., 1990; Watanabe et al., 2010; Yamada, Sugimoto, Kimura, Takeuchi, & Horisaka, 1989). Moreover, whether lower serotonin levels in HFD-fed animals are directly attributable to the reduced numbers of Reg4$^+$ EC cells, requires further analyses.

[28] Tph1: Tryptophan hydroxylase 1, a rate-limiting enzyme in the biosynthesis of serotonin (Hasegawa & Nakamura, 2010)

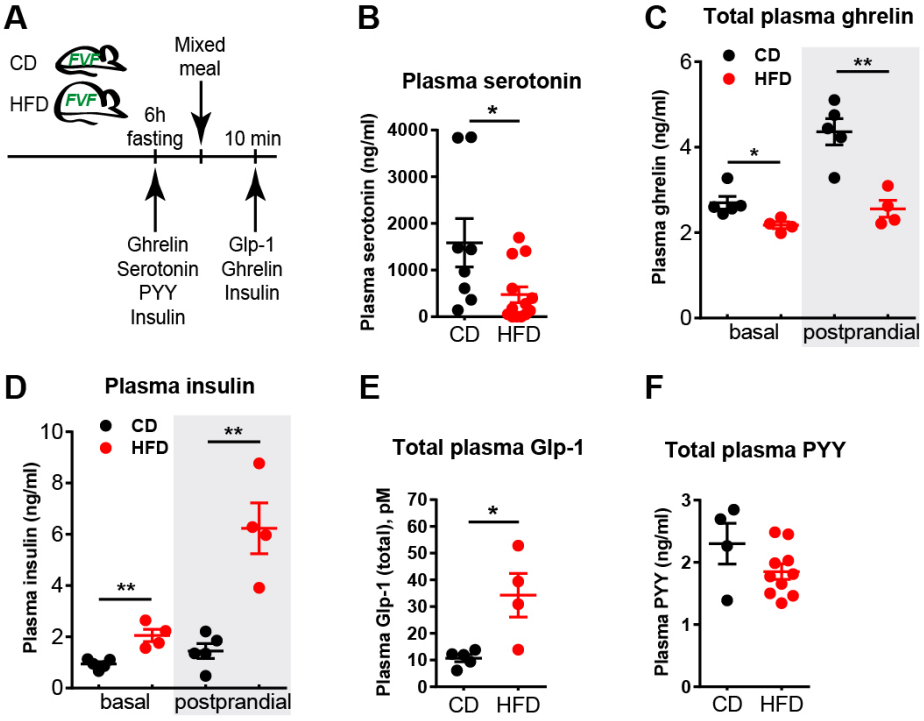

Figure 21: HFD-induced disturbances in gut hormone levels

(A) Experimental scheme for the analysis of basal (after a 6-hour fast) and postprandial (10 min after a mixed meal gavage) plasma levels of indicated gut hormones in FVF mice under CD and HFD conditions.
(B-F) Measurement of basal plasma concentrations of serotonin (B) and PYY (F), basal and postprandial total ghrelin (C) and insulin levels (D) as well as postprandial total Glp-1 (E) concentration in CD- or HFD-fed FVF mice. n=8 *versus* 13 per group (B), n=5 *versus* 4 per group (C-E), n=4 *versus* 10 per group (F).
Data are shown as mean ± SEM. *P<0.05, **P<0.01 by two-tailed Student's *t*-test.

To examine whether increased proportions of *Ghrl*- and *Gcg*-expressing SILA cells, coinciding with the higher abundance of duodenal Ghrl$^+$ EECs in HFD-fed mice, go together with alterations in levels of corresponding hormones, we assessed circulating ghrelin and Glp-1. Strikingly, both, fasted and postprandial, total ghrelin levels were significantly reduced in HFD-fed animals indicating Ghrl$^+$ EEC dysfunction or ghrelin resistance (Figure 21C). In fact, circulating ghrelin has been negatively correlated with fasting insulin concentrations and insulin resistance in obesity (Tschöp et al., 2001; Zhang et al., 2018). Indeed, mice fed a HFD, displayed significantly higher fasting and postprandial insulin levels and were insulin resistant (Figure 21D and section 4.1.1). Ghrelin is, however, also produced by the stomach, thus, we cannot completely exclude that reduced levels of ghrelin may be related to gastric Ghrl-secreting cells (Kojima et al., 1999). In contrast to circulating ghrelin, concentration of postprandial Glp-1 was significantly increased in HFD-fed animals (Figure 21E). However, to correlate the levels of plasma Glp-1 with the frequency of Glp-1$^+$ EECs on HFD, the missing numbers of duodenal Glp-1$^+$ cells have to be added.

We also assessed plasma PYY. Basal PYY levels were lower by tendency in HFD-fed mice despite the unchanged relative proportions of *PYY*-expressing SILP cells or the *PYY* transcript levels in EEC clusters (Figure 21F).

Taken together, our single-cell profiling using the FVF-based enrichment strategy provides a high-resolution data of the EEC lineage in homeostasis and in metabolic disorder at the moment. Altered EEC subset numbers and hormonal disturbances, identified by scRNAseq and *in vivo* data, strongly indicate a dysfunction of the EE system in a HFD-induced pre-diabetic condition. Intriguingly, we identified a significant reduction in numbers of Reg4$^+$ EC cells, a novel functionally uncharacterised

subset of EECs, and lower plasma serotonin levels representing early changes in the pathogenesis of T2D. It is, thus, of great significance to elucidate functional role of these cells in homeostasis and to understand related dysfunction in metabolic disorder.

4.1.5 HFD induces hyperproliferation of ISCs and progenitors

4.1.5.1 Single-cell profiling reveals increased proliferation of ISCs and progenitors on HFD and identifies HFD-associated cell cycle gene signatures

Our analysis revealed enhanced formation of the absorptive and subsets of secretory lineages on HFD, in particular, a marked increase in numbers of enterocyte and Ngn3$^+$ EE progenitors. To unveil, whether a higher turnover rate is responsible for these effects, we identified proliferating cells in CD- and HFD-derived single-cell clusters. Further, cell cycle states (G1, S or G2/M phase) were assigned to each cell, based on cell cycle signature scores (Methods 7.13.3) (Figure 22A). Whereas the total percentage of proliferating cells was not significantly changed (53 % CD *vs.* 55 % HFD), there were distinct shifts in cluster-specific densities and distribution of cycling cells relative to CD-derived samples (Figure 22B). In particular, the HFD treatment increased proportions of cycling ISCs, enterocyte, goblet and EE progenitors (Figure 22C, D). Visualised distribution of cycling cells between the cell cycle stages demonstrated a clear increase in the density of cells in the G2/M phase and higher S phase scores (based on higher expression levels of relevant genes) for HFD-derived ISCs, enterocyte, goblet and EE progenitor clusters (Figure 22E). This coincides with the increased numbers of the Ngn3$^+$ EEC, enterocyte and proximal goblet cell progenitors, as shown previously.

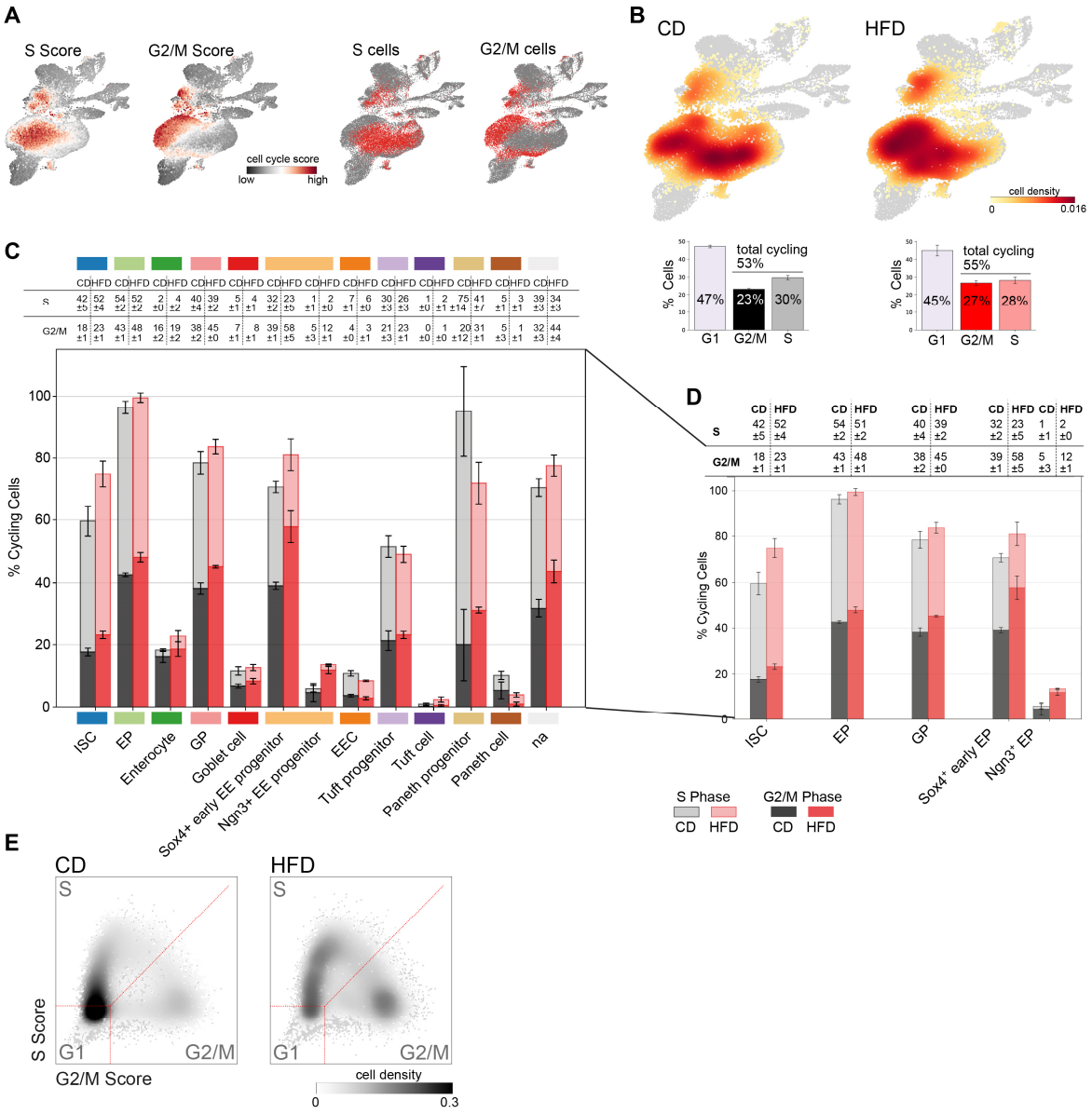

Figure 22: HFD increases proportions of cycling ISCs and progenitors of goblet cell and EEC lineages

(A) UMAP plot depicting cell score levels (left panel) for cell cycle phases S and G2/M. Scores were calculated based on the expression of a gene set related to cell cycle. Right panel: distribution of cells (highlighted in red) assigned to the indicated cell cycle phase (left panel).
(B) Cell density maps of proliferating cells distributed across the CD- and HFD-derived cell clusters projected onto the UMAP (upper panel) and proportions of cells assigned to G1, S and G2/M phases (bar plots).
(C, D) Proportions of cycling cells in S and G2/M phases per cluster (C) and specifically in ISCs and indicated progenitors (D) split by diet. Panels above the bar plot give a detailed overview of exact cell proportions for each cluster and diet.
(E) Scatter plot of S- *versus* G2/M-phase score levels showing distribution (as cell densities) of proliferating ISCs and progenitors of the enterocyte, goblet and EEC lineages over the three cell cycle phases. High score levels correlate with high expression of involved cell cycle genes and *vice versa*. Red lines visualize segregation according to indicated cell cycle phases. Densities were estimated using Gaussian kernels.
Data are mean ± SEM (B-D). n=3 per group.
Bioinformatic data analyses for this figure was done by Sophie Tritschler.

To identify gene signatures associated with the accelerated cell cycle progression, we compared cell cycle signatures in CD- and HFD-derived ISCs and progenitors (Methods 7.13.3). Indeed, a set of

transcripts, including *e.g.* known cell cycle regulators, *Ccnb1*, *Cenpa*, *Dut*, *Pbk* and *Smc2*, was significantly regulated in proliferating ISCs and progenitors under HFD conditions confirming enhanced cell cycle progression (Figure 23).

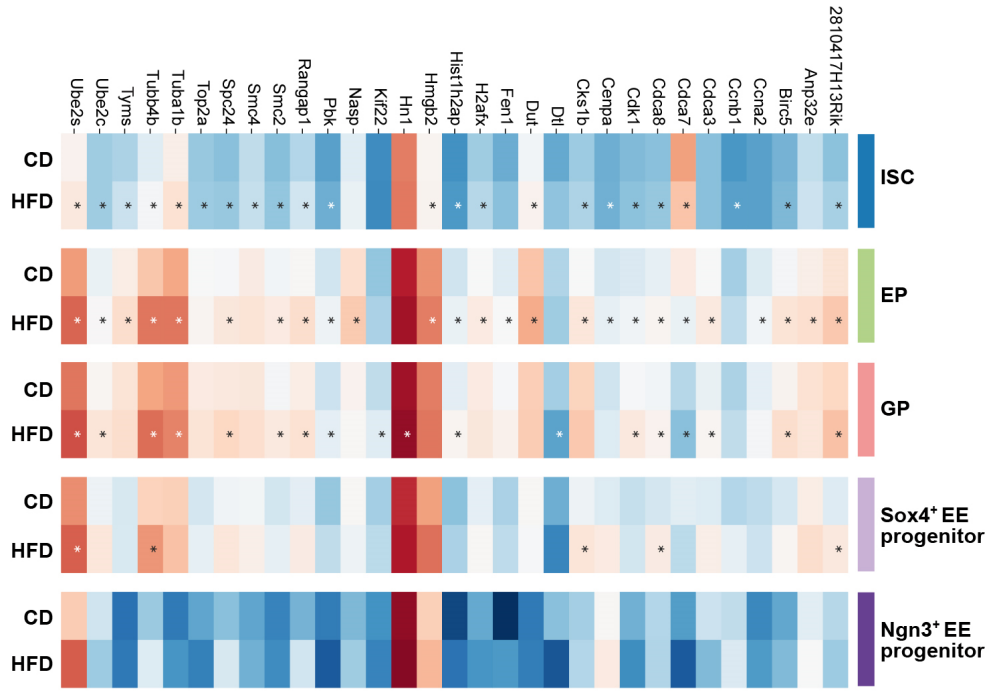

Figure 23: HFD-induced cell cycle gene signatures in ISCs, enterocyte and secretory progenitors

Heatmap shows mean expression values per cluster of differentially expressed genes involved in cell cycle regulation or highly correlating with S and G2/M scores. * indicates differentially expressed genes in CD- *vs.* HFD-derived clusters (limma, adjusted P-value < 0.01, logFC > 0.01).
Bioinformatic data analyses for this figure was done by Sophie Tritschler.

4.1.5.2 Validation of HFD-induced hyperproliferation of SI crypt cells *in vivo*

We used different approaches to confirm a HFD-induced increase in proliferation of profiled SI crypt cells and, in particular, to analyse the proliferative capacity of ISCs and progenitors. This included Ki67 antigen immunoreactivity as another measure of proliferative activity, BrdU labelling to estimate cell migration rate and short-pulse 5-Ethynyl-2-deoxyuridine (EdU) labelling to quantify cycling (S and M phase) cells within the crypts. In HFD-fed animals, Ki67-labelled proliferative domains were significantly longer and extended farther into the villi in contrast to the controls (Figure 24A, B). This strongly indicated that under HFD, early enterocytes in the villi retained the proliferative capacity, which is, under homeostatic conditions, typical of the progenitors in the permissive crypt niche. Interestingly, enhanced proliferation became evident as early as two weeks after the diet start (25 % increase in Ki67 domain length, data not shown). After four weeks on HFD, Ki67 domain length in the duodenum increased by 30 % in HFD-fed FVF mice (Figure 24C). A 24-hour BrdU labelling, 12 weeks after the diet, start revealed higher $BrdU^+$ migration fronts in the small intestines of HFD-fed animals (Figure 24D, E). Subtracting the length of Ki67 domains, which are longer on HFD and may account for a higher BrdU migration front, from the BrdU migration fronts clearly confirmed enhanced intestinal cell turnover in HFD-fed animals (Figure 24F).

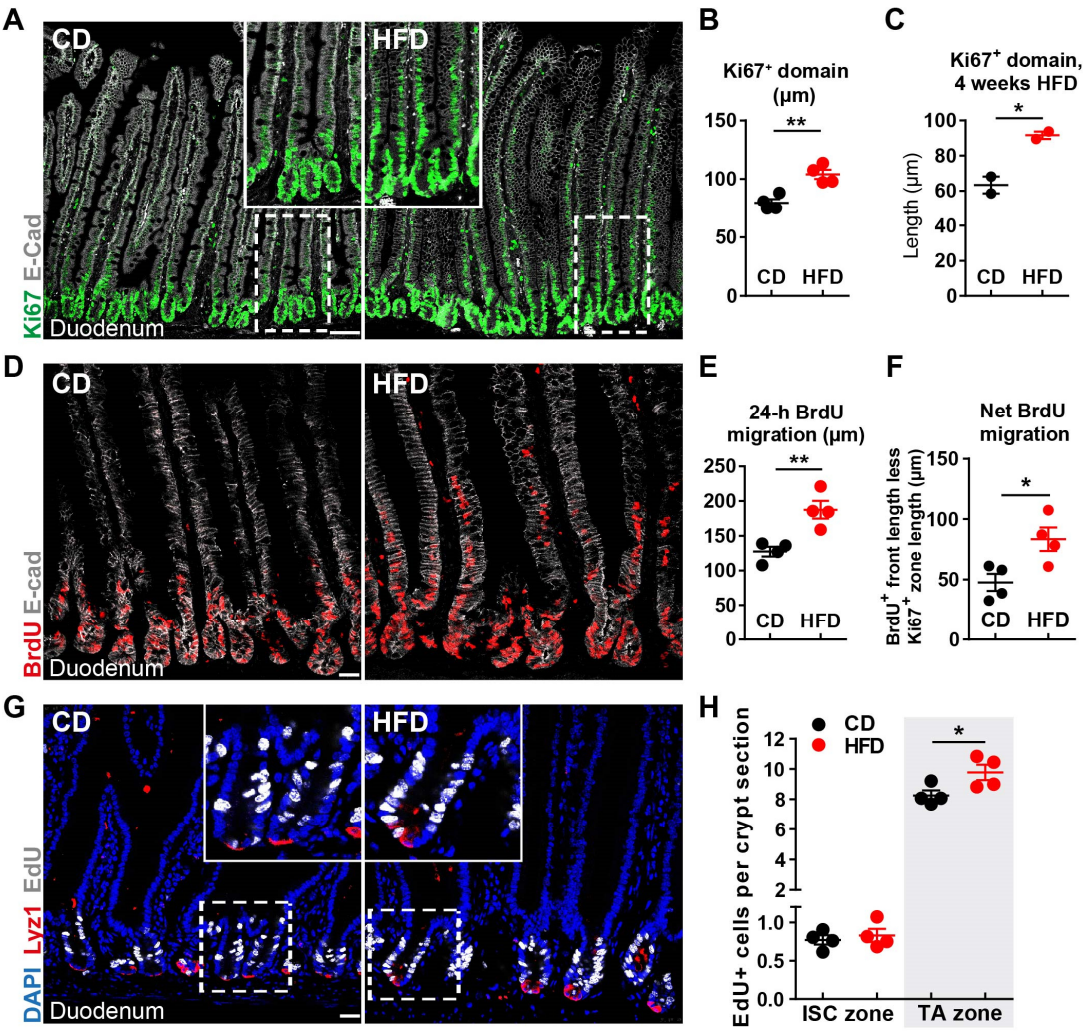

Figure 24: HFD increases proliferation in the crypt compartment of HFD-fed FVF mice

(A-C) Representative LSM images (A) and quantification of Ki67-labelled (Ki67+ nuclei, green) proliferative regions in the duodena of FVF mice after 12 weeks (B, n=4 per group) or after 4 weeks (C, n=2 per group) on a CD and a HFD regimen.
(D-F) Assessment of intestinal turnover by a 24-hour BrdU-labelling. Typical LSM images (D) and quantification (E) of migration fronts of BrdU-labelled cells (red) in the duodena of CD- and HFD-fed mice. For quantification, the distance from the crypt bottom to the highest labelled cell in the villus was measured. (F) Net BrdU migration is calculated as the average distance of BrdU migration front above the length of the average Ki67+ zone. n=4 per group.
(G, H) Representative LSM images (G) and quantification (H) of EdU incorporation after a 2-hour EdU pulse in the ISC zone (crypt base columnar cells) and TA zone (cells above the "ISC zone") in the duodenal sections of CD- and HFD-fed FVF mice.
Scale bars, 75 µm (A) and 25 µm (D, G). Data represent mean ± SEM. *P<0.05, **P<0.01 by two-tailed Student's *t*-test.

Finally, to compare the replication rate of ISCs and progenitors between the diet conditions, we assessed the numbers of EdU-labelled cells in the ISC and transit-amplifying (TA) cell zones after a short pulse of EdU. Due to the lack of appropriate ISC and TA progenitor markers, we quantified the numbers of EdU-labelled crypt base columnar cells (CBCs) (as cells interspersed between the Paneth cells) in the "ISC zone", while the rest of the crypt was referred to as the "TA zone". Indeed, we could ascertain an increase in the frequency of EdU+ cycling progenitors in the TA zone under HFD challenge (Figure 24G, H). Strikingly, the numbers of EdU-labelled cells in the ISC zone were not changed on HFD (Figure 24H). Additionally, we examined ISC abundance in the duodenal sections by *in situ* hybridisation with

the ISC marker *Olfm4* (van der Flier, Haegebarth, Stange, van de Wetering, & Clevers, 2009). Visual assessment of the *Olfm4*-expression patterns did not reveal any obvious changes in the abundance of labelled cells under HFD conditions, supporting our finding by single-cell profiling that, despite the increased proliferation, the overall ISC numbers were not increased on HFD (Figure 25).

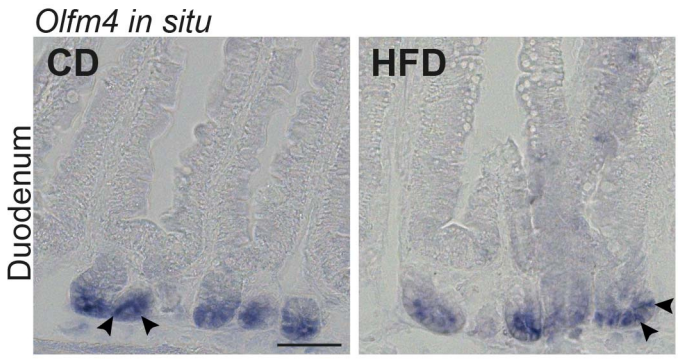

Figure 25: *In situ* hybridisation analysis of the ISC marker *Olfm4* shows similar expression patterns in the duodena of FVF mice fed a CD- or a HFD for 12 weeks

(A) *In situ* hybridisation of duodenal sections with the *Olfm4* probe marks ISCs in the crypts of CD- and HFD-fed animals. Specificity of the *in situ* staining was confirmed by hybridisation with a sense probe (data not shown). Arrowheads indicate *Olfm4*-labelled ISCs. Scale bar, 100 μm.

Of note, when isolated and maintained *in vitro*, HFD-derived SI crypt organoids retained enhanced proliferation capacity after three days in culture, as assessed by visual examination of bright-field micrographs and transcriptional analysis of selected cell cycle genes (*Ccnd1* and *Ccnb2*) (Figure 26A, B). This indicates a possible mechanism of intrinsic memory and a preservation of the HFD-induced proliferation programme independent of extrinsic stimuli for at least 3 days in culture.

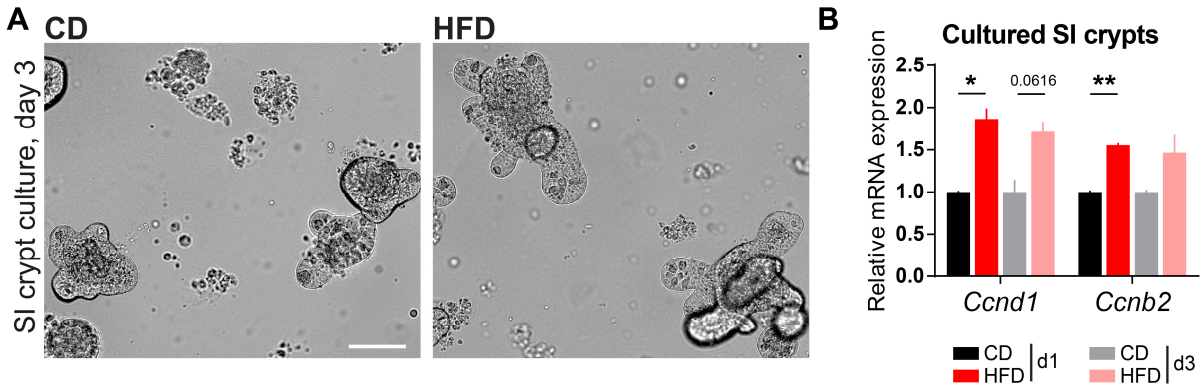

Figure 26: SI crypt organoids derived from HFD-fed mice maintain increased proliferation after 3 days in culture

(A) Typical SI organoids in 3D crypt culture 3 days after isolation from CD- or HFD-fed FVF mice. n=3 per group. Scale bar, 100 μm

(B) Expression analysis by qRT-PCR of proliferation markers, *Ccnd1* and *Ccnb2*, in CD- or HFD-derived SI organoids after 1 or 3 days in culture. n=2 per group. Data are presented as mean ± SEM. **P*<0.05, ***P*<0.01 by two-tailed Student's *t*-test.

In conclusion, our findings revealed that a HFD boosted proliferation of ISCs as well as of absorptive and secretory progenitors. Interestingly, enhanced ISC turnover did not result in the ISC pool expansion as indicated by the reduced proportion of HFD-derived ISCs by scRNAseq (Figure 10B) and by *in vivo*

data (Figure 25). Thus, our findings are highly indicative of a disturbed ISC homeostasis and a HFD-induced shift of the fragile balance in favour of differentiation and progenitor pool expansion on the expense of ISC self-renewal.

4.1.6 Upregulation of Igf1r/Akt signalling combined with induced fatty acid synthesis and PPAR signalling underlie hyperproliferation and disturbed lineage allocation from ISCs on HFD

Metabolic adaptation of stem cell function and mode of division has been described for ISCs in *Drosophila melanogaster* to enable a fast response to altered nutrient availability (O'Brien et al., 2011). Moreover, a central role for metabolic pathways in the regulation of stem cell homeostasis have long been recognised in other stem cell systems including hematopoietic, neural and human pluripotent stem cells (Chandel, Jasper, Ho, & Passegué, 2016). For ISCs, in particular, insulin/Igf1 growth factor signalling and nutrient-sensing Akt/mTor pathways[29], bridging proliferative and metabolic signalling, have been implicated in function and cell fate control (Beyaz et al., 2016; Chandel et al., 2016; Mah et al., 2014; Yilmaz et al., 2012). Moreover, a crosstalk between β-catenin, a key regulator of the ISC maintenance, and metabolic signalling components (including Gsk3β, mTor, Scd1 or Ppar factors[30]) has been demonstrated (Sethi & Vidal-Puig, 2010). Additionally, alterations in basal cellular metabolism, *i.e.* glycolysis or mitochondrial oxidative phosphorylation, can affect stem cell proliferation or even lead to stem cell exhaustion (reviewed in Chandel et al., 2016).

To better understand the molecular cues underlying disturbed ISC homeostasis and alterations in early lineage recruitment induced by HFD, we assessed the activity of signalling pathways bridging proliferation, cellular metabolism and cell fate in SI crypts and single-cell clusters derived from CD- and HFD-fed FVF mice.

4.1.6.1 Igf1r/Akt signalling pathway is deregulated in SI crypts on HFD

FVF mice maintained on a HFD developed obesity and hyperinsulinemia (see section 4.1.1). Elevated systemic levels of insulin are associated with increased levels of free Igf1 in circulation in mice and humans (Cohen & LeRoith, 2012; Mah et al., 2014). Both hormones can mediate cellular proliferation in response to nutrients and energy availability (Calle & Kaaks, 2004; Klil-Drori et al., 2017). Moreover, enterotrophic effects of Igf1 as well as the evidence for Igf1/insulin-mediated ISC hyperproliferation have been reported (Dahly, Guo, & Ney, 2002; Mah et al., 2014). Therefore, we analysed protein expression and activity of the key pathway components of the Ir/Igf1r/Akt[31] signalling cascade in SI crypt lysates from CD- or HFD-fed mice (Figure 27A). Indeed, total levels and phosphorylation of Ir/Igf1r at Tyr1158/Tyr1162/Tyr1163, required for kinase activation, were increased in HFD-derived SI crypts (Figure 27B-D).

The cell context-dependent downstream propagation of Ir/Igf1r signalling is mediated by Akt/mTor or by Ras/mitogen-activated kinase (MAPK) pathway to either induce metabolic functions or to promote cell growth, respectively (Manning & Toker, 2017; Siddle, 2011). In HFD-derived SI crypts, levels of active $pAkt^{Ser473}$ were elevated in line with the increased Ir/Igf1r phosphorylation (Figure 27B, E). Interestingly, activating phosphorylation of p44/42 MAPK (or extracellular signal-regulated kinase (Erk), here Erk1/2) at Thr202/Tyr204 was not significantly altered on HFD (Figure 27B, F), which indicated that Erk1/2, typically, a downstream target of Ir/Igf1r signalling, was not involved in HFD-induced hyperproliferation in the SI crypt compartment. Further, we analysed levels of pmTor (Ser2448), another key mediator of cell growth downstream of Akt. Strikingly, levels of phosphorylated

[29] Igf1: insulin-like growth factor 1; Protein kinase B or Akt: xx; mTor: mammalian target of rapamycin

[30] Gsk3β: glycogen synthase kinase 3 β; Scd1: stearoyl-CoA desaturase 1; Ppar: peroxisome proliferator-activated receptor

[31] Ir/Igf1r: insulin receptor/Igf1 receptor

mTor were significantly reduced in HFD-derived crypt lysates (Figure 27G, H), indicating that the typical crosstalk between mTor and Akt is either uncoupled on HFD or not present in SI crypts.

Akt has various metabolic functions and can mediate proliferation not only via mTor but also via the Gsk3β-dependent crosstalk with β-catenin signalling, which is essential for ISC maintenance and proliferation (Manning & Toker, 2017). Gsk3β, a negative regulator of β-catenin signalling, can typically be targeted by Akt at Ser9 and inhibited, thus integrating metabolic and proliferative cues. pGsk3β^{Ser9} levels were significantly downregulated in HFD-derived SI crypts, strongly indicating increased activity of Gsk3β (Figure 27I, J). Gsk3b activation may in turn facilitate β-catenin degradation, thus preventing its nuclear relocation and target gene expression (Figure 27A).

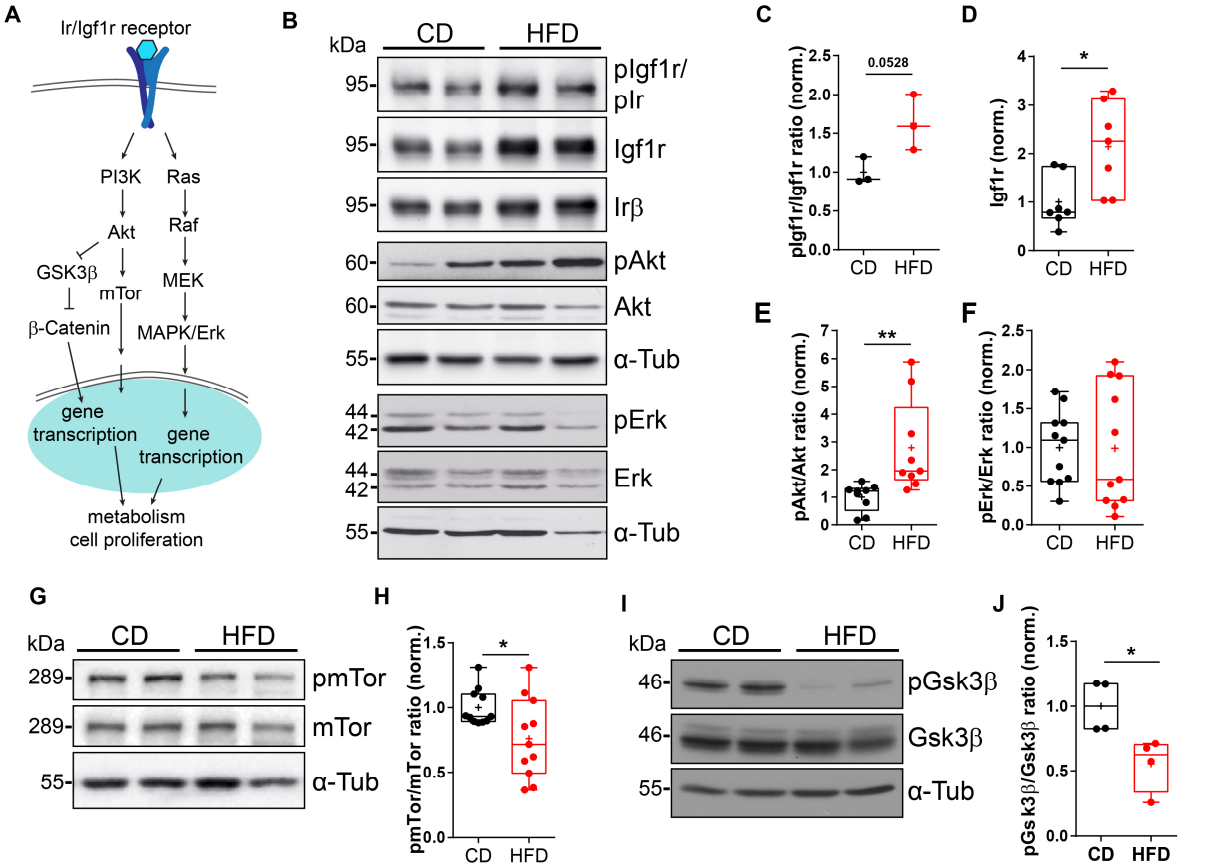

Figure 27: Key pathway components associated with Ir/Igf1r signalling and factors integrating cell proliferation and metabolic cues are deregulated in SI crypts on HFD

(A) Schematic diagram of the downstream mediators of the Ir/Igf1r signalling and integration of metabolic and proliferative cues dependent on cellular context. Ir/Igf1r activates downstream signalling cascades including Ras/MAPK/Erk or PI3K/Akt/mTor pathways. Akt-driven inhibition of Gsk3β facilitates β-catenin nuclear accumulation and target gene expression. Either signalling cascade activates specific expression of metabolic and proliferation genes.

(B-J) Representative immunoblots of p/Igfr1/pIr (Tyr1158/Tyr1162/Tyr1163), Irβ, p/Akt (Ser473) and p/Erk (Thr202/Tyr204) (B), p/mTor (Ser2448) (G) and p/Gsk3β (Ser9) (I) and quantification of the protein levels. Protein expression of relevant pathway components were analysed in whole-cell lysates from SI crypts of CD- and HFD-fed FVF animals. For quantification, signal intensities of all protein bands were normalised to α-tubulin; phosphorylated proteins were additionally normalised to the corresponding non-phosphorylated protein.

n=3 per group (C), n=7 per group, 2 independent experiments (D), n=9 per group, 3 independent experiments (E), n=11 per group, 3 independent experiments (F), n=11 per group, 3 independent experiments (H) and n=4 per group (J). Data are presented using box-and-whisker plots showing minimum to maximum values; the centre line indicates the median, crosses indicate the means. Error bars represent SEM. *P<0.05, **P<0.01 by two-tailed Student's t-test.

Collectively, these data revealed that the Ir/Igf1r signalling was enhanced in SI crypts of HFD-fed animals, however the typical downstream mediators of proliferation, mTor and Erk1/2, were not involved. The exact meaning of these perturbations in metabolic and proliferative signalling in the crypt compartment and which other pathways mediate the HFD-induced hyperproliferation remains to be elucidated. Moreover, not much is known about the role of mTor in the crypt compartment, and, in particular, how metabolic and proliferative cues are integrated in ISCs and progenitors. On the other hand, Gsk3β may be involved in signal integration via β-catenin. Since our results suggested an increased activity of Gsk3β on HFD, we assessed whether β-catenin signalling was affected in SI crypts under HFD conditions.

4.1.6.2 HFD-induced hyperproliferation of ISCs and progenitors is Wnt/β-catenin signalling-independent

Wnt/β-Catenin signalling is a key determinant of the ISC homeostasis and is active in a gradient with the strongest activity at the base of the crypt (Gregorieff et al., 2005; Vladimir Korinek et al., 1998; D. Pinto et al., 2003). Tight regulation of Wnt/β-catenin pathway activity is critical to balance ISC self-renewal and lineage differentiation (van de Wetering et al., 2002; van der Flier & Clevers, 2009). Disturbed Wnt/β-catenin signalling is implicated in the pathogenesis of several GI disorders including cancer and metabolic diseases, such as obesity and diabetes (H. Clevers & Nusse, 2012; Lecarpentier, Claes, Vallée, & Hébert, 2017). Moreover, increased β-catenin activity has been linked to the hyperproliferation of ISCs and progenitors in a number of studies using HFD models (Beyaz et al., 2016; Mah et al., 2014).

Our data showed that the classical effectors downstream of insulin/growth factor proliferative signalling were not active in the crypts of HFD-fed animals (see section 4.1.6.1). Additionally, reduction of Gsk3β phosphorylation could potentially have an effect on β-catenin signalling. To test this, we assessed levels of nuclear β-catenin as well as target gene expression in bulk FVF^{low} enriched ISCs and FVF^{neg} enterocyte progenitors isolated by flow cytometry (Figure 28A). Strikingly, levels of nuclear β-catenin were decreased or not affected in FVF^{low} enriched ISCs or FVF^{neg} progenitors, respectively (Figure 28B, C). Accordingly, the levels of a set of representative β-catenin target genes were downregulated in FVF^{low} ISCs (Figure 28D). Additionally, while the average Wnt signalling score including major Wnt/β-catenin target genes (Methods 7.13.3) was slightly lower in HFD-derived ISCs by scRNAseq, expression levels of the three important ISC markers and Wnt/β-catenin target genes *Lgr5*, *Ascl2* and *Axin2* were markedly decreased (Figure 28E, F).

Together, these results strongly indicate that a HFD-induced hyperproliferation of ISCs and progenitors does not involve increased Wnt/β-catenin signalling. It has been previously reported that an attenuation of Wnt/β-catenin signalling can lead to exhaustion of the ISC numbers as a result of a progressive differentiation into progenitors (Fevr et al., 2007). Thus, reduced Wnt/β-catenin signalling on HFD likely reflects a disturbed ISC homeostasis as suggested above. Moreover, this finding is congruent with the scRNAseq data showing reduced ISC numbers and increased recruitment of absorptive and secretory progenitors under HFD conditions.

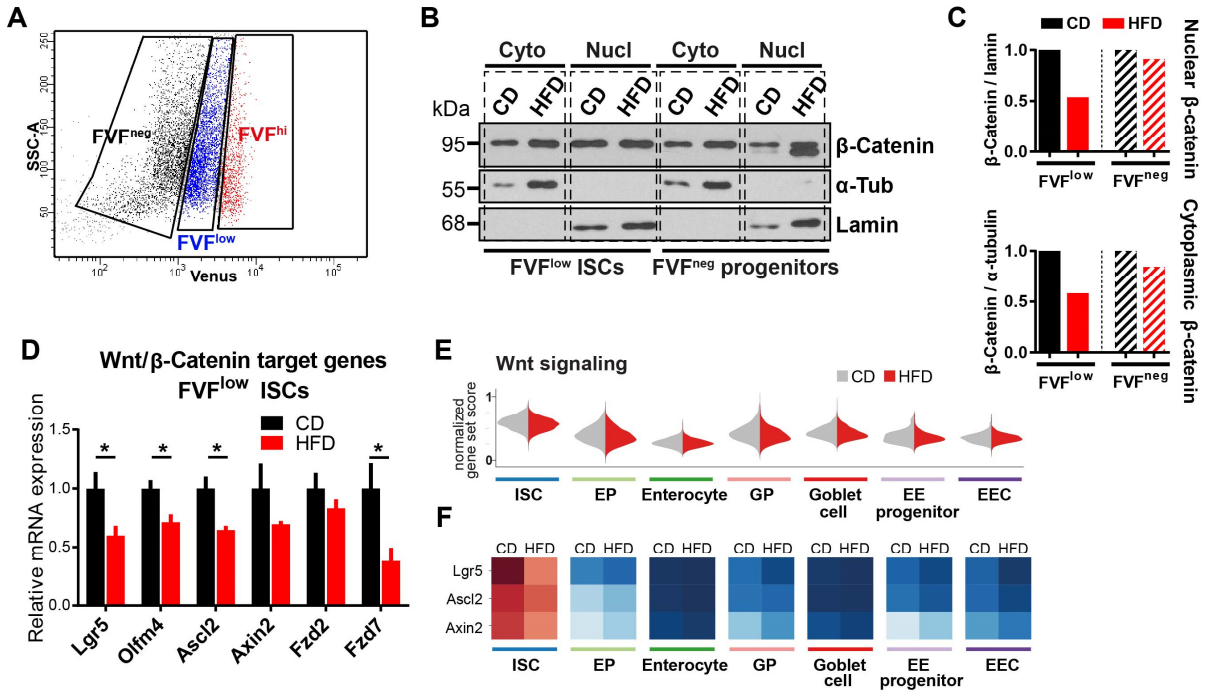

Figure 28: β-Catenin signalling is not involved in hyperproliferation of ISCs and progenitors

(A) FACS gating strategy to isolate FVF^{low}, FVF^{hi} and FVF^{neg} cells from SI crypts of FVF mice following a doublet exclusion and gating for live cells.
(B, C) Western blot analysis (B) and quantification (C) of β-catenin protein levels in cytoplasmic and nuclear lysates from flow-sorted FVF^{low} and FVF^{neg} crypt cells isolated from CD- and HFD-fed FVF mice. β-Catenin expression was normalised to lamin (for nuclear levels) or α-tubulin (for cytoplasmic fraction). One sample per group, each sample represents pooled cells from 4 mice.
(D) qRT-PCR analysis of the gene expression of representative ISC markers and β-catenin target genes in flow-sorted FVF^{low} cells from CD- or HFD-fed animals. Ct values were normalised to the housekeeping genes (*18S*, *Rpl37*) and expressed as means of fold change relative to the control ± SEM. *P<0.05 by two-tailed Student's *t*-test. n=5 *versus* 4 per group from two independent experiments.
(E) Violin plots depicting Wnt signalling score distribution in indicated clusters split by diet. Wnt signalling score was calculated based on the expression of a gene set related to Wnt/β-catenin signalling (Methods 7.13.3).
(F) Average expression levels per cluster of *Lgr5*, *Ascl2* and *Axin2* are reduced in HFD-derived ISCs by scRNAseq. Bioinformatic data analyses for (E, F) was done by Sophie Tritschler.

4.1.6.3 Transcriptional upregulation of the fatty acid synthesis pathway and PPARα/γ signalling in ISCs and progenitors on HFD

To gain more insights into molecular mechanisms underlying enhanced turnover of ISCs and progenitors on HFD and to uncover signalling determinants linking proliferation to cell fate in ISCs, we compared single-cell transcriptomes of CD- and HFD-derived ISCs and progenitors. Differential gene expression and pathway analysis by KEGG revealed gene signatures enriched for Ppar signalling pathway and fatty acid metabolism, in particular, fatty acid (FA) biosynthesis, in HFD-derived clusters. Most prominent increase was detected in the proximal subsets of ISCs and enterocyte lineage clusters (Figure 29A). In contrast, gene signatures related to carbohydrate metabolism (*e.g.* glycolysis, gluconeogenesis, pentose phosphate pathway) were downregulated including genes such as *Mgam*, *Slc5a1*, *Aldob*, *Sis* and *Khk* (Figure 29A-C). The top upregulated genes associated with Ppar signalling and FA synthesis comprised *e.g. Hmgcs2*, *Fabp1/2*, *Creb3l3*, *Acot1*, *Scd2* and *Me1*. Interestingly, the transcripts of the three Ppar isoforms (*Pparα*, *Pparβ/δ* and *Pparγ*) were differentially regulated in single-cell clusters under HFD conditions. While expression of both, *Pparα* and *Pparγ*, was upregulated in

HFD-derived ISCs and absorptive lineage cells, transcript levels of *Pparβ/δ* were reduced (Figure 29C). Pparα and Pparγ are central regulators of lipid and glucose metabolism in a cell-type specific context, but less is known about the Pparβ/δ isoform, most prominently expressed in ISCs and progenitors and involved in Paneth cell differentiation (Varnat et al., 2006). Recently, upregulation of Pparβ/δ pathway activity has been implicated in fasting-activated FAO and in the crypt compartment and in hyperproliferation of ISCs and progenitors in a mouse model of chronic HFD (Beyaz et al., 2016; Mihaylova et al., 2018). Pparα, -β/δ and -γ can all be activated by fatty acids and there is a substantial overlap between their target genes, however, our data do not indicate Pparβ/δ involvement in HFD-dependent ISC and progenitor hyperproliferation.

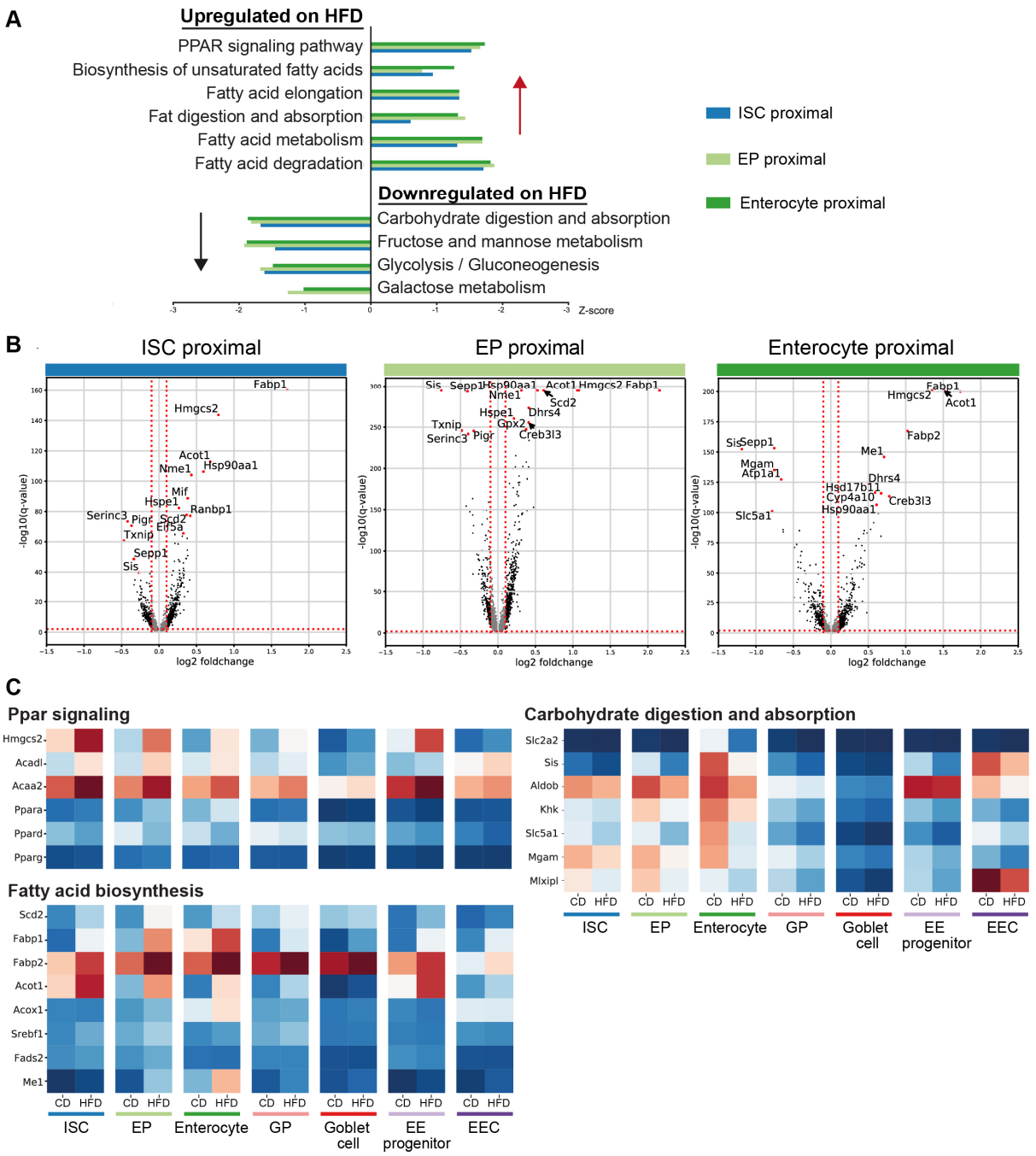

Figure 29: Fatty acid synthesis and Ppar signalling are upregulated in ISCs and progenitors on HFD

(A) Enriched KEGG pathways in genes differentially expressed between CD and HFD conditions in the proximal clusters of ISCs, enterocyte progenitors (EP) and enterocytes.
(B) Differentially expressed genes in the proximal ISCs, EPs and enterocytes under HFD conditions. Each dot represents a gene, and regulated genes are highlighted in black. For each gene, the estimated logFC is plotted on the x- and adjusted P-value on the y-axis. Thresholds used for significance level and gene expression change are indicated by red lines. The top 10 genes ranked by adjusted P-value are denoted.
(C) Average expression values of selected genes related to Ppar signalling, fatty acid biosynthesis and carbohydrate digestion and absorption pathways in indicated clusters under CD and HFD conditions.
Bioinformatic data analyses for this figure was done by Sophie Tritschler.

Stem cells typically engage in basic metabolic programmes, depending on their functional state and modes of division (Chandel et al., 2016; Folmes, Dzeja, Nelson, & Terzic, 2012; Ito & Suda, 2014). Ppar signalling and FA synthesis were strongly upregulated in ISCs and progenitors under HFD conditions (Figure 29). Whereas Ppar activation has been implicated in several metabolic states in intestinal crypt cells, not much is known about the contribution of the FA synthesis. Therefore, we tested whether the FA synthesis was in any degree represented in the transcriptomes of crypt cell clusters under normal conditions. Cell scores for FA synthesis, calculated based on gene sets from GO terms, were less than 0 in the ISCs and progenitors, indicating that FA synthesis was negligible in homeostasis, but a distinguished adopted metabolic programme under HFD conditions (Figure 30A). In fact, also the contributions of FA β-oxidation and glycolysis were relatively low in ISCs and progenitors as compared with oxidative phosphorylation (OxPhos) (Figure 30B-D). In enterocytes, by contrast, glycolysis and OxPhos scores were both higher, reflecting their overall stronger metabolic activity (Figure 30B-D). Moreover, there was a moderate increase in the OxPhos/glycolysis ratio in HFD-derived enterocytes as a result of a decreased glycolysis ratio (Figure 30D).

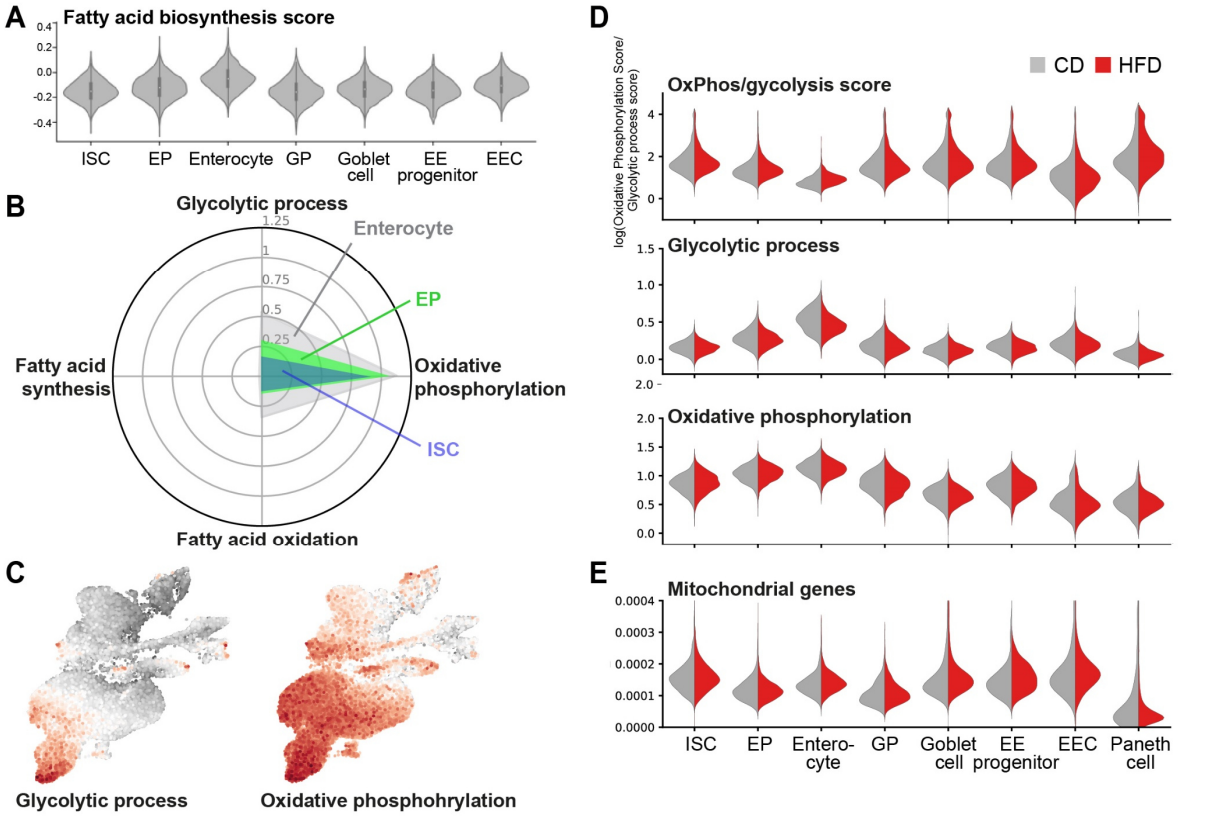

Figure 30: ISCs rely on oxidative phosphorylation and mitochondrial metabolism in homeostasis and under HFD conditions

(A, B) Fatty acid biosynthesis scores are below 0 in ISCs and Eps indicating that FA synthesis does not contribute to the basal metabolism of indicated cell populations. (A) Single-cell distribution of fatty acid biosynthesis scores for indicated cell types under CD conditions. (B) Radar chart depicting cell score levels of basic metabolic pathways in ISCs, EPs and enterocytes under CD conditions.
(C) Cell score levels of gene sets linked to oxidative phosphorylation and glycolysis in single cells of pooled CD- and HFD-derived samples projected into UMAP space.
(D) Violin plots depicting single-cell distribution of cell scores for glycolytic process and oxidative phosphorylation and their ratio in cell clusters under CD and HFD conditions.
(E) Cell score levels of mitochondrial gene expression normalized by total number of gene counts in indicated clusters split by diet. For the mitochondrial signature, genes with an mt-prefix were used.
For metabolic signatures, genes from GO Biological processes were used (fatty acid biosynthesis: GO:0006633, glycolytic process: GO:0006096, fatty acid oxidation: GO:0006635, oxidative phosphorylation: GO:0042776, GO:1903862, GO:0042773; see also Methods 7.13.3).
Bioinformatic data analyses for this figure was done by Sophie Tritschler.

In line with other groups' findings, our data indicated that ISCs exhibited a prominent mitochondrial gene signature and relied on OxPhos under normal conditions as ascertained by the levels of mitochondrial gene scores and by the OxPhos/glycolysis score ratio, respectively (Figure 30D, E) (Rodríguez-Colman et al., 2017). Interestingly, HFD altered neither the mitochondrial score nor the OxPhos/glycolysis ratio, indicating that the major prerequisites determining basal metabolic cell state were not shifted in HFD-derived ISCs (Figure 30D, E). In support, electron microscopy analysis of SI intestinal sections did not reveal any differences in mitochondria numbers or morphology of ISCs from HFD-fed animals (data not shown).

Thus, our transcriptional data indicates that a HFD-dependent upregulation of FA synthesis affected the ISCs' and progenitors' metabolism. To confirm this, we analysed metabolite profiles of SI crypts in CD- and HFD-fed mice (see section 4.1.6.5).

4.1.6.4 Targeted single-cell qRT-PCR analysis confirms transcriptional alterations in ISCs and progenitors on HFD

scRNAseq provides multidimensional data and deep insights into transcriptional programmes of single cells, however data of low-expressed genes can be confounded due to dropout and varying sequencing depth. To validate transcriptional changes induced by a HFD with a more sensitive, independent readout and to confirm the reproducibility of the data, we employed a targeted single-cell qRT-PCR analysis of FVF^{low} ISCs and FVF^{high} secretory cells isolated by flow cytometry from CD- and HFD-fed mice (sorting strategy as described Figure 28A; chapter 4.1.1 and Sterr et al., in preparation). Within the profiled 465 FVF^{low} and FVF^{hi} single cells, we identified clusters of ISCs, early EPs as well as progenitors and mature cells of the goblet, EEC and Paneth cell lineages based on marker gene expression (Figure 31A, B). The relative cell proportions in HFD-derived clusters were changed along the same lines with the scRNAseq profiling (Figure 31C). Accordingly, also the expression of genes associated with FA biosynthesis and Ppar signalling (*Hmgcs2, Fabp1, Scd2, Acaca, Pparα, Pparγ*) was increased while transcripts related to carbohydrate metabolism (*Sis, Slc5a1, Slc2a2, Aldob*) as well as *Pparδ* were less abundant in HFD-derived ISCs and early absorptive progenitors (Figure 31D).

Collectively, using a more sensitive targeted approach, we could confirm a HFD-induced shift in transcriptional programmes of SI crypt cells, in particular in ISCs and absorptive progenitors.

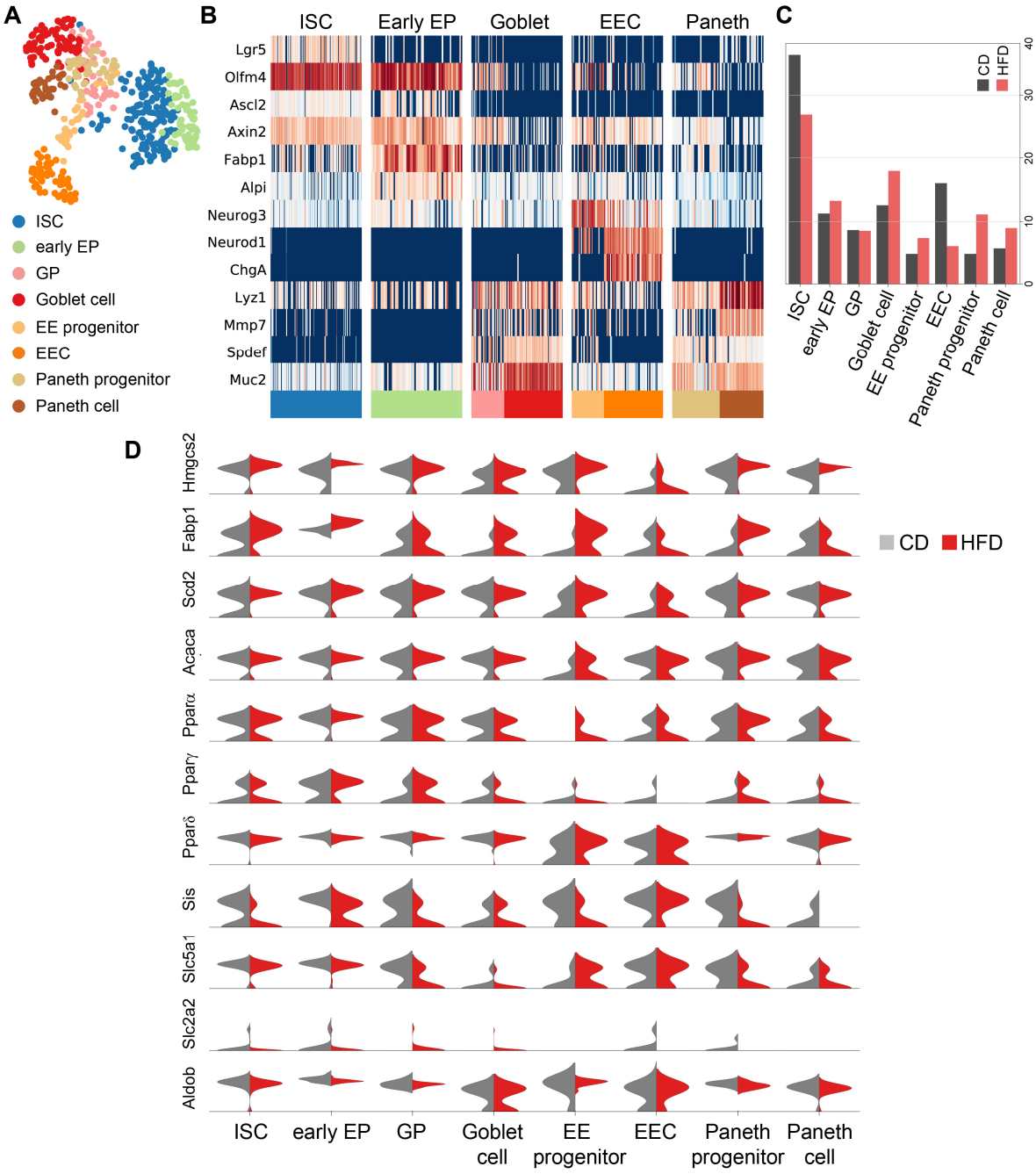

Figure 31: Validation of expression differences in metabolic genes in FVF^{low} ISCs and FVF^{high} secretory cells from CD- and HFD-fed mice using targeted single-cell qRT-PCR

(A, B) UMAP plot of 465 profiled cells coloured by cell type (A). Cluster annotation was based on lineage marker gene expression depicted in the heatmap (B).
(C) Cell type frequencies in CD- and HFD-derived samples.
(D) Violin plots showing expression of selected metabolic genes related to fatty acid synthesis, Ppar signalling and glycolysis in indicated single-cell clusters split by diet.
Bioinformatic data analyses for this figure was done by Sophie Tritschler.

4.1.6.5 Metabolite signatures are altered in ISCs and progenitors on HFD

Changes in single-cell transcriptional networks and in metabolic signalling in SI crypts strongly indicate altered cellular metabolism. To confirm this, we compared metabolite profiles from SI crypts of CD- and

HFD-fed FVF mice using matrix-assisted laser desorption/ionization mass spectrometry imaging (MALDI-MSI) (Aichler & Walch, 2015; Norris & Caprioli, 2013). This technique allows to analyse metabolites directly in tissue sections without isolation bias (Figure 32A). MALDI-MSI identified total 297 discriminative masses ($p \leq 0.05$, fold change ≥ 2) in SI crypts of CD- and HFD-fed animals with 257 (46 annotated) enriched and 40 less abundant (8 annotated) metabolites on HFD (Figure 32B, C). Enrichment analysis of metabolic pathways in annotated metabolites using MetaboAnalyst 3.0 (http://www.metaboanalyst.ca) (Xia & Wishart, 2010) revealed several changes including fatty acid biosynthesis and linoleic acid metabolism signatures upregulated and glucose metabolism-related pathways, such as pentose phosphate pathway and pentose glucuronate interconversions, downregulated on HFD (Figure 32D).

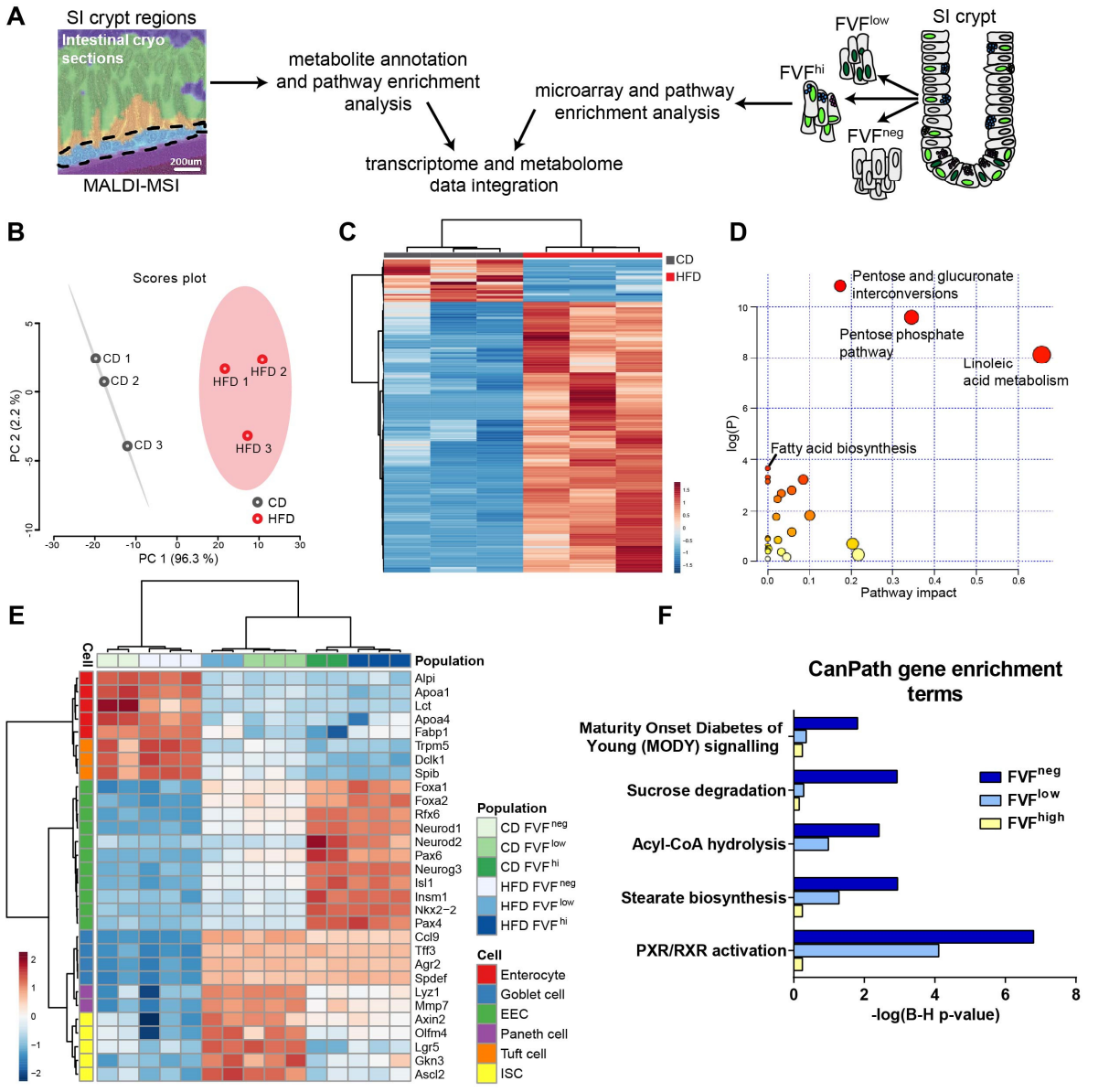

Figure 32: Integrated analysis of SI crypt metabolomes and transcriptomes of FVF^{hi}, FVF^{low} and FVF^{neg} cells reveals overlapping metabolic signatures

(A) Simplified experimental design for the analysis and data integration of SI crypt metabolome and transcriptome data of FVF cell populations.

(B) Principal component (PC) analysis (PC2 vs PC1), presented on a score plot, accurately distinguishes CD- and HFD-derived samples. PCA was performed without data filtering, no data transformation and without scaling. n=3.
(C) Heatmap-based clustering analysis of the 297 discriminative metabolite masses demonstrates clear separation between the CD and HFD groups. Each colored cell on the map corresponds to an intensity value, with samples in rows and features in columns. Euclidean distance and Ward's method were applied for clustering analysis.
(D) Pathway enrichment analysis of deregulated metabolites was performed with MetaboAnalyst 3.0 (http://www.metaboanalyst.ca). Metabolic pathways are represented as circles according to their scores from enrichment (vertical axis) and topology analyses (pathway impact, horizontal axis). Pentose and glucuronate interconversions, pentose phosphate pathway, linoleic acid metabolism and fatty acid biosynthesis were identified as discriminative pathways distinguishing CD- and HFD-conditions.
(E) Heatmap depicting relative expression levels (Z scores, row-wise) of key intestinal lineage marker genes by microarray analysis in biologic replicates of FVF^{hi}, FVF^{low} and FVF^{neg} isolated from SI crypts of CD- (n=2) and HFD-fed (n=3) FVF mice. Normalised expression levels range from blue (low expression) to red (high expression).
(F) Bar plot showing selected terms by Ingenuity pathway analysis for which significant metabolites from MALDI-MSI analysis deregulated on HFD and genes from microarray analysis of FVF^{hi}, FVF^{low} and FVF^{neg} cell populations from CD- and HFD-derived samples show an overlap.

Author contributions to Figure 32: (A-D) was performed in collaboration with the Research Unit Analytical Pathology, Helmholtz Center Munich, and analysed by Dr. Na Sun. Microarray analysis in (E) was performed by Dr. Martin Irmler, the Institute of Experimental Genetics, and computational data analyses was performed by Dr. Martin Irmler and Michael Sterr, Institute of Diabetes and Regeneration Research, Helmholtz Center Munich. Computational analysis for (F) was performed in collaboration with the Institute of Computational Biology, Helmholtz Center Munich.

To account for the limited resolution of the MALDI-MSI technique (~30 μm, crypt regions) and acquisition of metabolite profiles on the whole-crypt level without cellular information, we integrated metabolomics data with the genome-wide mRNA profiling of bulk sorted FVF^{low}, FVF^{hi} and FVF^{neg} ISCs, secretory and absorptive cells, respectively. Indeed, significantly regulated metabolites showed an overlap with regulated genes related to carbohydrate processing (sucrose degradation, Maturity Onset Diabetes of Young (MODY) Signalling), and fatty acid biosynthesis (stearate synthesis, acyl-CoA-hydrolysis) (Figure 32F).

4.1.6.6 HFD-induced upregulation of fatty acid synthesis pathway and PPARα/γ signalling is a potential link to hyperproliferation and disturbed lineage homeostasis in SI crypts on HFD

Our data revealed upregulation of Pparα/γ signalling and fatty acid synthesis pathway on both, transcriptional and metabolic levels, in ISC and progenitors under HFD conditions. Next, we validated whether the protein expression of the related key pathway components was changed in cytoplasmic and nuclear extracts from SI crypts of CD- and HFD-fed animals (Figure 33A). Indeed, the levels of active nuclear sterol regulatory element-binding protein 1 (Srebp1; mature, m-Srebp1), a master transcriptional regulator of the FA synthesis machinery, increased more than fourfold compared to controls (Figure 33B, C). Moreover, the cytoplasmic abundance of the key enzymes of FA biosynthesis, acetyl-CoA carboxylase (Acc) or Scd1, more than doubled or was nearly 25-times higher (while almost absent in controls) in HFD-derived crypts, respectively. The expression of fatty acid synthase (Fasn), a key enzyme in the biosynthesis of saturated FAs, was, however, not changed. Expectedly, nuclear levels of Pparγ increased almost threefold in SI crypts from HFD-fed animals confirming transcriptional differences in single-cell ISC and progenitor clusters.

Taken together, HFD massively affected metabolic and proliferation signalling as well as transcriptional networks and metabolite signatures in ISCs and progenitors.

In other stem cell systems, *e.g.* in hematopoietic stem cells (HSCs) and neural stem cells (NSC), it is well established that changes in metabolic signalling can affect stem cell self-renewal and progenitor differentiation and modulate cell fate (Chandel et al., 2016). Similarly, our findings implied that HFD-induced perturbations in cellular metabolism and signalling precipitated ISC hyperproliferation and disturbed lineage homeostasis. In support, a link between hyperproliferation and *de novo* lipogenesis has been established in various types of cancer (Menendez & Lupu, 2007; Shao & Espenshade, 2012).

To verify our hypothesis, we initiated studies on the inhibition of FA synthesis pathway and Ppar activation in cultured crypt organoids derived from HFD-fed animals. We used a small molecule fatostatin to target Srebp cleavage-activating protein- (SCAP) mediated activation of Srebp1 and Srebp2, hence, to inhibit Srebp-dependent target gene expression (Kamisuki et al., 2009). To target Pparα and Pparγ activation, we used an irreversible PPARγ antagonist, GW9662, combined with Pparα antagonist, GW6471 (Leesnitzer et al., 2002; Xu et al., 2002). Crypt organoid treatment with inhibitors was started upon seeding and maintained over six days (Figure 34A). First preliminary results suggested that inhibition of Sreb1/2 with fatostatin reduced the levels of *Neurog3* and *Hmgcs2* transcripts (Figure 34B, C). Of note, the number of Ngn3$^+$ EE progenitor cells was significantly increased in HFD-derived single-cell clusters and *in vivo*, suggesting that the abundance of *Neurog3* transcript in whole-crypt preparations should be higher under HFD conditions. However, *Neurog3* mRNA was only slightly increased *in vitro* after 6 days in culture (Figure 34B). Nevertheless, reducing *Neurog3* levels may be a promising preliminary result.

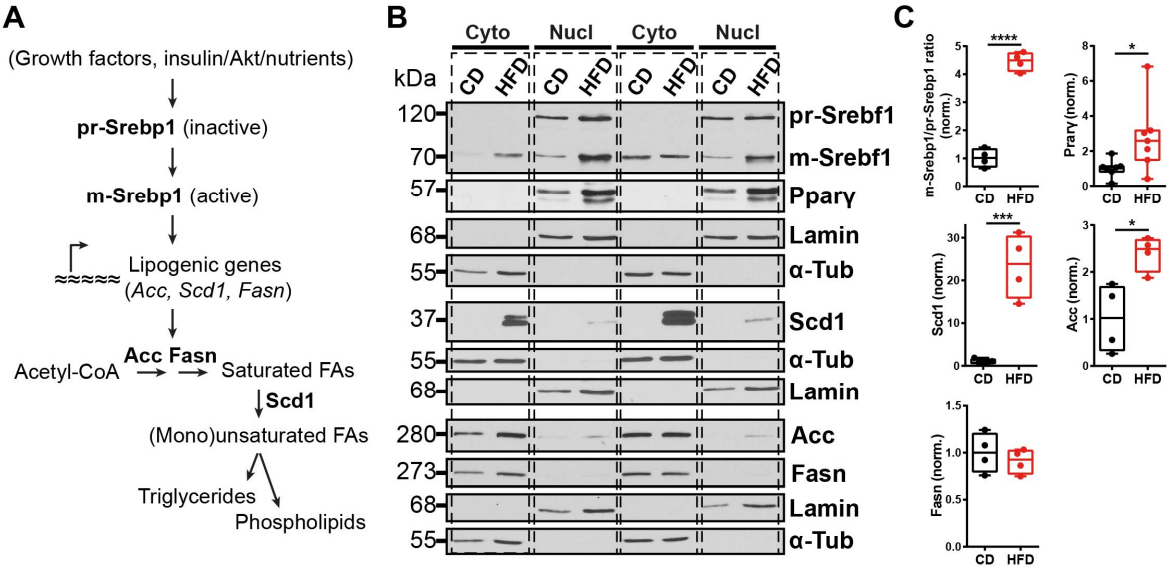

Figure 33: Protein levels of the key components of FA synthesis pathway and Pparγ are upregulated in SI crypts on HFD

(A) Schematic and simplified model of the FA synthesis pathway. Analysed proteins are highlighted in bold.
(B, C) Protein expression analysis by Western blot (A) and relative quantification of band intensity (B) of key transcription regulators (Srebp1) and enzymes (Scd1, Acc, Fasn) of FA synthesis pathway (n=4 per group) and Pparγ (n=7 per group) in cytoplasmic and nuclear extracts from SI crypts of CD- and HFD-fed FVF mice. For the quantification of protein expression levels, signal intensities of bands were normalised with respect to α-tubulin or lamin in cytoplasmic or nuclear protein extracts, respectively. Data are presented using box-and-whisker plots showing minimum to maximum values; the centre line indicates the median. Error bars represent SEM. **P*<0.05, ***P*<0.01, ***P<0.001 by two-tailed Student's *t*-test.

As expected, fatostatin did not affect expression of *Srebf1* (*alias* Srepb1) due to its action on Srebp1/2 transport and proteolytic activation, but not on transcript levels (Figure 34C). However, the expression of *Scd1*, a lipogenic enzyme and Srebp1 target gene, was not changed, in contrast to *Hmgcs2*, indicating

that inhibition of the Srebp2-mediated cholesterol biosynthetic programme (represented by *Hmgcs2*) was stronger than the effect on the Srebp1-mediated lipogenic gene expression (represented by *Scd1*) (Horton, Goldstein, & Brown, 2002). A combined inhibition of Pparα and Pparγ activity, on the other hand, did not affect expression of either of the analysed genes as indicated by the first results (Figure 34D).

Additionally, we did not observe any notable changes in the levels of proliferation markers, *Mki67* or *Ccnb2*, upon fatostatin-mediated inhibition of Srebp1/2 (Figure 34E). This might have several reasons. First of all, the lipogenic programme rather than Srebp2-mediated cholesterol biosynthesis was induced by HFD in SI crypts *in vivo*. However, as indicated by the preliminary data, fatostatin was more potent on Srebp2 *in vitro*, which might attenuate expected effects in regard to proliferation. Thus, a selective inhibition of Srebp1 would be required for further testing. Secondly, fatostatin treatment led to a moderate increase in *Pparα* levels (Figure 34E). To exclude possible negative feedback cues, which could alleviate fatostatin-mediated effects of proliferation (J.-H. Lee et al., 2017), inhibition of both, Pparα (and Pparγ) and Srebp1, should be tested *in vitro*. Moreover, since a HFD-induced phenotype appeared to get reduced upon crypt isolation and cultivation *in vitro*, a further setup optimisation is required for a better *in vivo*-phenotype reproducibility (*i.e.* crypt cell hyperproliferation and effects on EECs). Thus, a parallel longitudinal treatment of cultured organoids with free fatty acids, resembling the HFD-regimen *in vivo*, should be integrated into the setup.

To support our preliminary results, further in-depth studies are required to demonstrate whether the inhibition of HFD-induced lipogenesis and Ppar signalling programmes is sufficient to ameliorate EE disorder and hyperproliferation of ISCs and progenitors and to restore normal intestinal lineage homeostasis.

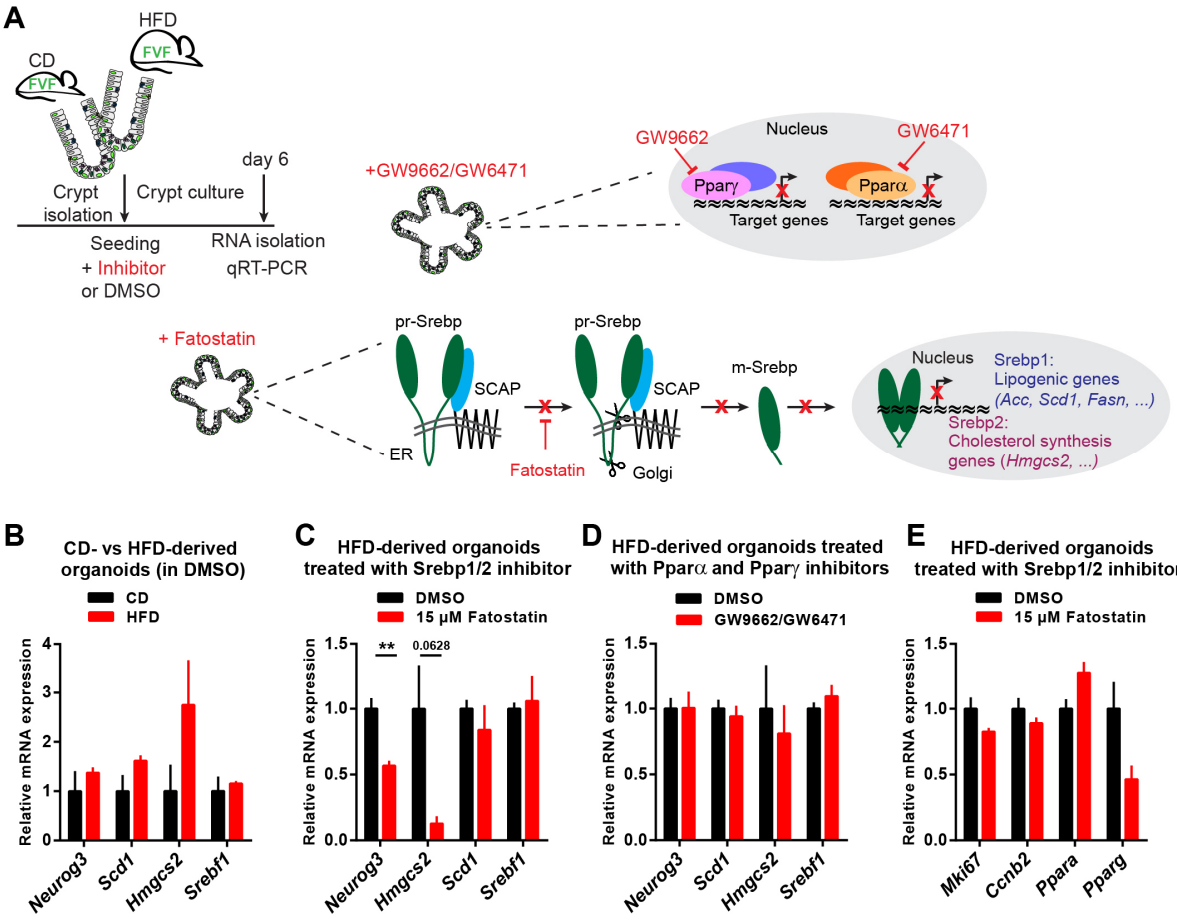

Figure 34: Drug-targeted inhibition of Srebp1/2 or Pparα/Pparγ has a potential effect on EE lineage and proliferation in cultured HFD-derived SI organoids

(A) Experimental scheme of crypt culture and treatment with Srebp1/2 or Pparα/γ inhibitors, fatostatin and GW6471/GW9662, respectively, (left side) and schematic mechanism of the particular inhibitor action (right side).
(B-D) mRNA expression analysis by qRT-PCR of the EE progenitor marker *Neurog3* and selected genes involved in FA synthesis pathway, *Hmgcs2*, *Scd1* and *Srebf1* (*alias* Srebp1) in CD- and HFD-derived SI organoids (B), in HFD-derived crypt organoids treated with 15 µM fatostatin (C) or in HFD-derived crypt organoids treated with 5 µM GW9662/5 µMGW6471 (D) after 6 days in culture.
(E) mRNA expression analysis by qRT-PCR of the proliferation markers, *Mki67* and *Ccnb2*, as well as *Pparα* and *Pparγ* in HFD-derived crypt organoids treated with 15 µM fatostatin after 5 days in culture.
Dimethyl sulfoxide (DMSO) was used as vehicle for inhibitors. Organoids treated with inhibitors were compared with organoid cultures supplemented with the equivalent amount of DMSO (B-E). Inhibitors or DMSO were added to the organoids upon seeding and changed every 2 days.
Gene expression was normalised to housekeeping genes *Hprt* and *Actb*. n=3 per group (B-D), n=4 per group (E). Data are mean ± SEM. ***P*<0.01 by two-tailed Student's *t*-test.

4.2 Generation and characterisation of the Fltp-Venus fusion reporter mouse line

4.2.1 Generation of the Fltp-Venus fusion reporter mouse line

To date, the role of Fltp in the islets of Langerhans and SI intestinal crypts remains elusive, in part due to the lack of appropriate tools (Bader et al., 2016; Gegg et al., 2014; Boettcher et al., in revision). To facilitate the functional analyses and to reveal cellular localisation of Fltp, in particular, in the intestine and pancreas, we generated a Fltp-Venus fusion reporter mouse line. In this mouse model, the Fltp-Venus fusion protein is expressed under the control of the *Fltp* cis-regulatory elements. Moreover, the introduction of the 3xFLAG tag should enable biochemical studies.

The cloning strategy for the Fltp-Venus fusion targeting construct was designed by Dr. Ingo Burtscher (Institute of Diabetes and Regeneration Research, Helmholtz Zentrum München) and is shown in Figure 35A. The experimental cloning and related mouse work was done by me. In brief, the knock-in cassette including the *Venus* reporter gene, was fused in frame to the open reading frame of the *Fltp* gene, followed by a 3xFLAG tag sequence and the *neomycin* (*neo*) resistance gene (Figure 35A). Therefore, the translational stop codon in the exon 6 of the *Fltp* gene was removed. The *neo* cassette, driven by the phospho-glycerate kinase (*PGK*) promoter, was flanked by *loxP* sites allowing for Cre recombinase-mediated excision. A detailed description of the cloning strategy and construct generation is provided in section Methods 7.11.1. The construct integrity was confirmed by sequencing, and the linearized targeting vector, containing the neomycin resistance cassette, was electroporated into the F1 hybrid (129Sv/C57BL/6) mouse ES cells (IDG3.2) (Hitz et al., 2007). Neo-resistant clones were selected using G418 (geneticin), and a homologous recombination at the *Fltp* locus was confirmed by Southern blot analysis of the digested genomic DNA using a probe located upstream of the targeting vector (5′ Southern probe) (Figure 35B). Southern blot analysis revealed a targeting efficiency of 2.88 % at the *Fltp* locus. Given the restriction length polymorphism of the BL/6 and the SV129 alleles (Moritz Gegg, doctoral thesis, https://mediatum.ub.tum.de/doc/1114671/document.pdf; last change 10.11.2014), two respective DNA fragments were observed after *DraIII*-mediated digestion in the wild-type (WT) IGDG3.2 ES cells (Figure 35B). The homologous recombination appeared preferentially on the BL/6 allele due to the design of the targeting vector based on the BL/6 genome (Figure 35B).

Two recombinant ES clones were aggregated with CD1 morulae, successfully producing germline chimeras from both clones (performed by Heide Oller, ISF, Helmholtz Zentrum München). To remove the *loxP*-flanked neomycin selection cassette in the germline, chimeras were intercrossed with the *ROSA26Cre* mouse line (Soriano, 1999). The genotyping PCR was designed as shown in Figure 35C to distinguish the WT, Fltp-Venus-Neo and Fltp-Venus-Δneo alleles ($Fltp^{+/+}$, $Fltp^{+/neo+}$ and $Fltp^{+/\Delta neo}$). To subsequently remove the Cre-allele, mice were backcrossed to C57BL/6J animals. For further analyses, a mouse colony from one $Fltp^{+/\Delta neo}$ clone was propagated, and all subsequent experiments were performed on Fltp-Venus animals with mixed background. Finally, mice with the WT, heterozygous (HET, $Fltp^{V/+}$) and homozygous (HOM, $Fltp^{V/V}$) Fltp-Venus genotypes were distinguished using the PCR strategy shown in Figure 35D. The Fltp-Venus offspring from heterozygous intercrosses showed that $Fltp^{+/+}$, $Fltp^{V/+}$ and $Fltp^{V/V}$ pups were born at Mendelian ratio (data not shown). Moreover, the Fltp-Venus HOM animals were viable, fertile, did not differ from WT animals in weight, behaviour or other basic physiologic functions and had no apparent alterations in tissue morphology of the gut, pancreas, testis, liver and brain upon basic examination (data not shown). This suggests that the Venus fusion protein did not interfere with the normal development.

We confirmed that *Fltp* mRNA levels were comparable in the lungs of WT and $Fltp^{V/V}$ mice by qRT-PCR (Figure 35E). Western blot analysis of adult lung and testis tissues using an anti-Fltp antibody identified both, the endogenous Fltp and the Fltp-Venus fusion proteins in the $Fltp^{V/+}$ animals, whereas an anti-GFP antibody detected exclusively the Venus fusion protein (Figure 35F). Neither the endogenous nor the Fltp-Venus fusion protein were detectable in lysates from SI crypts. In the lung and testis, the level of Fltp synthesised from the WT and that from the targeted allele were comparable (Figure 35F, upper

panel). Likewise, in *Fltp*$^{V/V}$ mice, amount of the Fltp-Venus fusion protein was similar compared to the endogenous Fltp in WT mice (Figure 35G). This suggests that the Fltp-Venus fusion does not interfere with Fltp production, stability and turnover rates, and both, the endogenous and the fusion, proteins are similarly transcribed and translated.

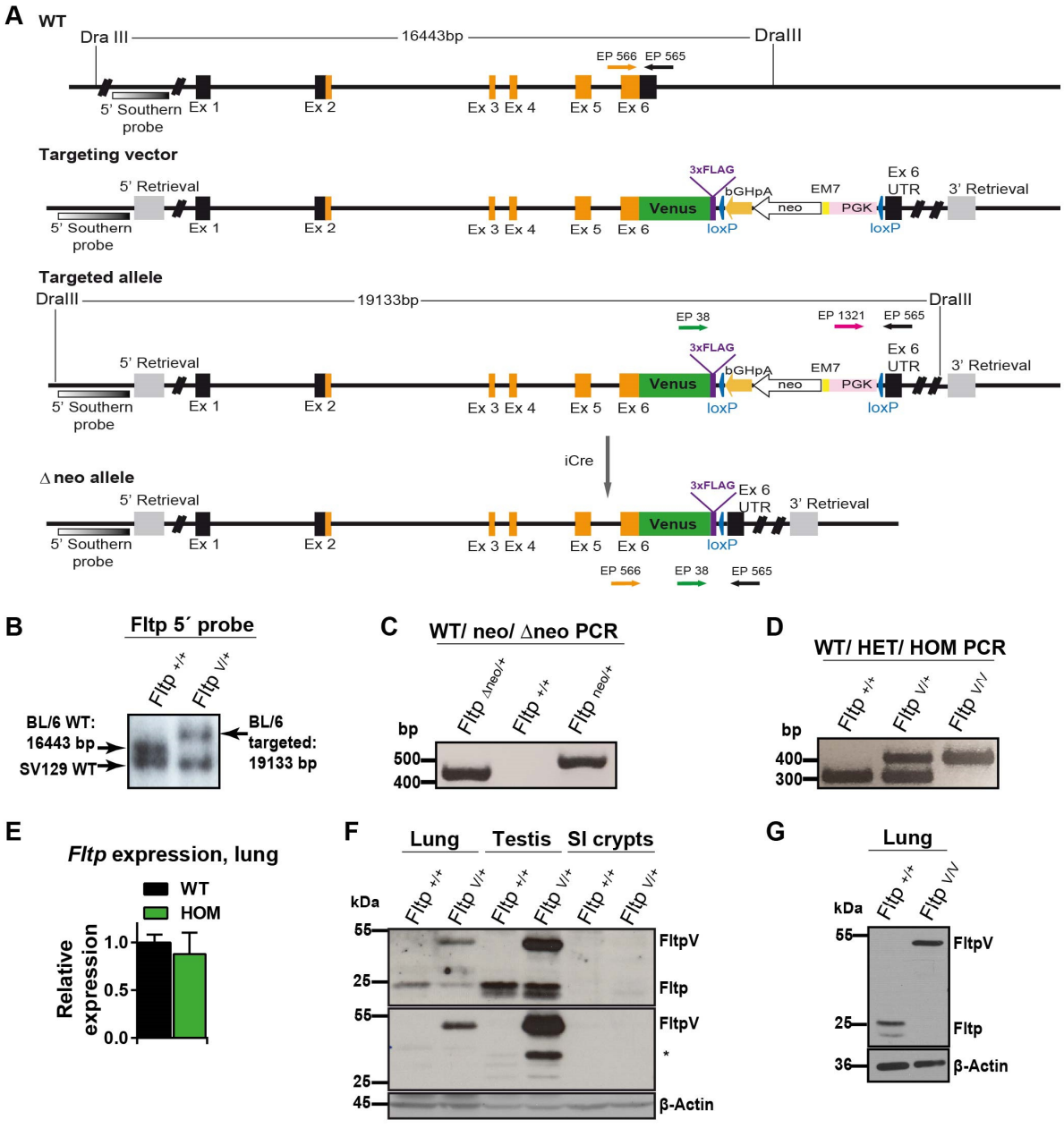

Figure 35: Targeting strategy for the generation of the Fltp-Venus fusion reporter allele and expression in adult tissues

(A) Targeting strategy for the generation of the Fltp-Venus fusion allele. A targeting construct was introduced by homologous recombination in ES cells to fuse the Venus reporter gene (green box) and the 3xFLAG tag (violet box) to the open reading frame (in exon 6) of the *Fltp* gene. Upon germline transmission the *PGK*-driven neomycin resistance cassette (neo, empty arrow) flanked by *loxP* sites (blue triangles) was removed by Cre-mediated excision. The coding region (orange boxes), 5′ and 3′ UTRs (black boxes) and homology regions, indicated as 5′ and 3′ Retrieval (grey boxes), for the generation of the targeting vector are depicted. *DraIII* enzyme restriction sites for and the location of the 5′ Southern probe are shown. Genotyping primers are depicted as coloured arrows (EP 38, EP 1321 and EP 565 for neo vs Δneo PCR; EP 566, EP 38 and EP 565 for the genotyping PCR to distinguish the *Fltp*$^{+/+}$, *Fltp*$^{V/+}$ and *Fltp*$^{V/V}$ animals).

(B) Southern blot analysis of *DraIII*-digested DNA from a WT and a targeted ES cell clone (*Fltp*$^{V/+}$) hybridised with the external 5' Southern probe. Restriction fragments of the SV129 WT, BL/6 WT (calculated size, 16443 bp), and the BL/6 targeted (calculated size, 19133 bp) alleles can be detected.
(C) Genotyping PCR of the mouse DNA to distinguish the *Fltp*$^{+/+}$, *Fltp*$^{neo/+}$ and the *Fltp*$^{\Delta neo/+}$ alleles before or after the removal of the neo cassette. Primers used: EP 38, EP 1321 and EP 565. Δneo allele: 430 bp, neo allele: 520 bp.
(D) Genotyping PCR using primers EP 566, EP 38 and EP 565 to distinguish the *Fltp*$^{+/+}$, *Fltp*$^{V/+}$ and *Fltp*$^{V/V}$ animals. WT band: 317 bp, targeted allele: 430 bp.
(E) qRT-PCR analysis of *Fltp* mRNA expression in the lungs of adult *Fltp*$^{+/+}$ and *Fltp*$^{V/V}$ mice. Expression was normalised to the housekeeping genes *Gapdh*, *Actb* and *18S*. n=3, error bars indicate mean ± SEM.
(F, G) Western blot analysis of the lung, testis and SI crypt lysates (F) or lung lysates (G) from adult mice of indicated genotypes using anti-Fltp antibody (F, upper panel; G) or anti-GFP antibody (F, lower panel) to detect the endogenous Fltp and/or the Fltp-Venus fusion (FltpV) protein. Proteolytic degradation product (*).
Abbreviations: Ex: exon; UTR: untranslated region; PGK: phospho-glycerate kinase; bGHpA = bovine Growth Hormone polyadenylation signal; neo = neomycin resistance cassette.

4.2.2 Analysis of the Fltp-Venus reporter expression in adult tissues

Fltp-Venus was detected by immunofluorescence signal in the adult testis and the respiratory epithelia in *Fltp*$^{V/+}$ and *Fltp*$^{V/V}$ mice (Figure 36A-B'). No Venus signal was observed in tissue sections form WT animals, confirming the specificity of the immunostaining (Figure 36A', B'). In the lung and trachea, Fltp-Venus reporter was found in multiciliated epithelial cells, in agreement with previously published findings (Figure 36B, C) (Gegg et al., 2014). To confirm an accurate spatial activity of the Fltp-Venus reporter, we compared expression and localisation of the Venus fusion and those of the endogenous Fltp protein. Indeed, expression patterns and subcellular localisation of the Fltp-Venus reporter and the endogenous Fltp proteins were overlapping in multiciliated airway cells in tissue sections from *Fltp*$^{V/+}$ mice (Figure 36C). Both Fltp proteins were diffusely distributed in the cytoplasm, but prominently enriched at the apical surface and, in particular, in the cilia (Figure 36C).

Additionally, we confirmed the identical localisation of both proteins *in vitro*. The air-liquid interface (ALI) cultures of isolated mouse tracheal epithelial cells (mTECs) are widely used to model differentiation of airway epithelial cells (You, Richer, Huang, & Brody, 2002). ALI cultures of mTECs from *Fltp*$^{V/+}$ mice comprised multiciliated cells at day 7 after the differentiation start (Figure 36D). Both, the Fltp-Venus reporter and the endogenous Fltp, proteins showed overlapping distribution in the cytoplasm and in the cilia of multiciliated cultured epithelial cells (Figure 36D). These results confirm that the Fltp-Venus fusion reporter expression accurately reflects endogenous Fltp distribution in the murine airway epithelia *in vitro* and *in vivo*.

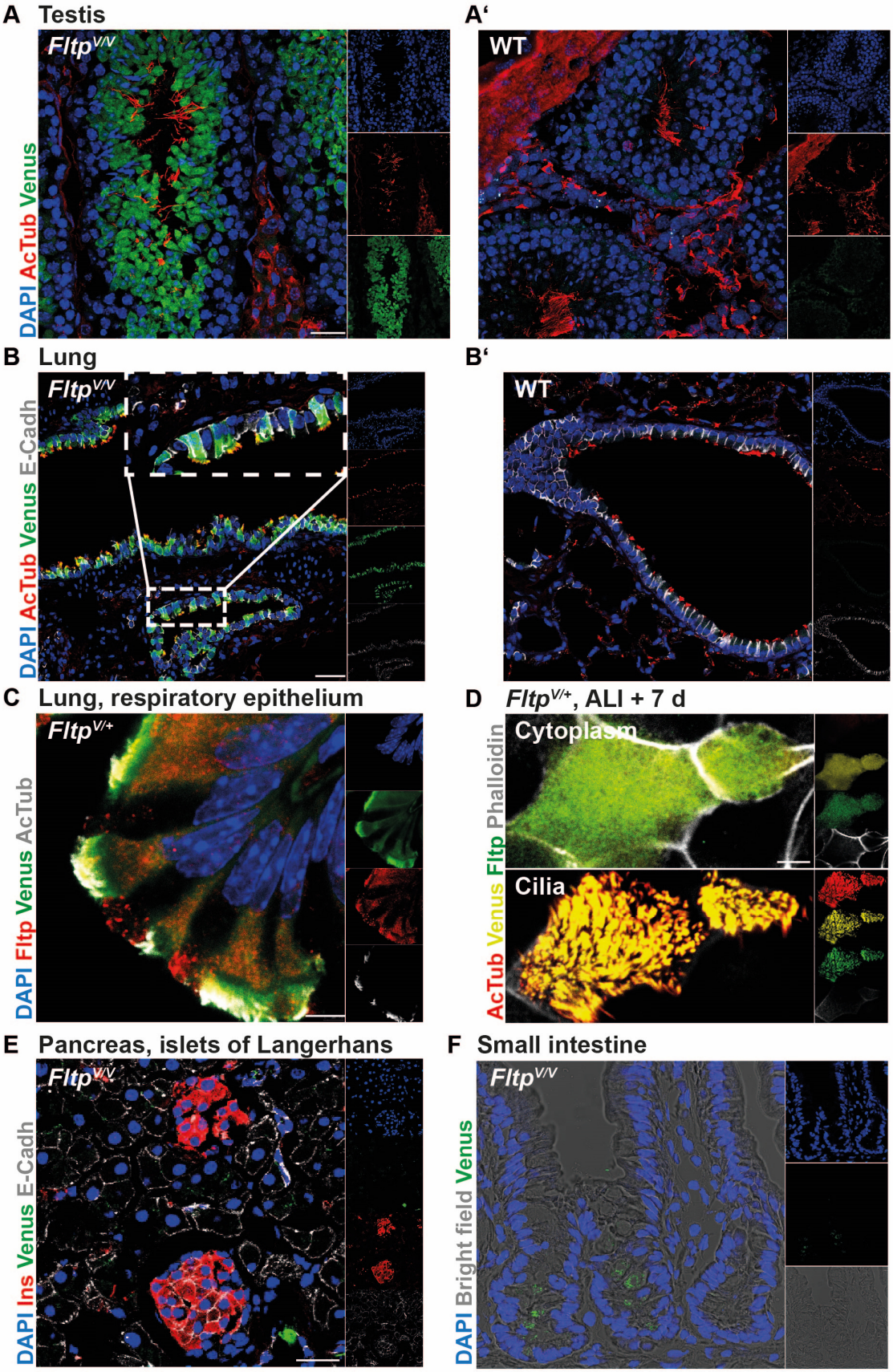

Figure 36: Fltp-Venus fusion protein expression in adult tissues of *Fltp*$^{V/V}$, *Fltp*$^{V/+}$ or WT mice

(A-B') Representative LSM pictures of Fltp-Venus expression in adult testis (A, A') and lung (B, B'). Scale bars, 25 μm.

(C, D) Representative LSM images depicting overlapping expression of the endogenous Fltp and Fltp Venus fusion proteins in multiciliated cells in the lung epithelium (C) or in mTEC cultures 7 days after ALI creation in the cytoplasm (D, upper panel) and at the apical surface (D, lower panel) in *Fltp*$^{V/+}$ mice. Scale bars, 5 μm.
(E, F) Typical LSM images of islets of Langerhans (E) and SI crypts (F) of *Fltp*$^{V/V}$ mice showing absence of specific staining for Fltp Venus fusion protein. Scale bars, 25 μm.

Further, we aimed to specifically characterise Fltp-Venus protein expression in the adult pancreatic islets and in the small intestine. A previous study by Bader et al., using the *Fltp*^{ZV} mouse model, has demonstrated that FVR expression segregates FVR^{+} and FVR^{-} pancreatic β-cells with distinct functional characteristics (Bader et al., 2016). However, we could not detect any specific Fltp-Venus signal, either in the exocrine or in the endocrine part of the pancreas in tissue sections from *Fltp*$^{V/V}$ mice (Figure 36E). Further, we tested different experimental approaches which may perform better in case that the protein expression levels in the tested tissue are very low, and signal intensity is insufficient for the detection with our standard immunofluorescence protocol. Therefore, we used the tyramide signal amplification (TSA) approach in addition to the normal immunostaining procedure, however, did not observe any specific signal either (data not shown). Similarly, isolated live cells derived from pancreatic islets of *Fltp*$^{V/+}$ and *Fltp*$^{V/V}$ mice did not display any specific Venus fluorescent signal when analysed by flow cytometry (data not shown).

In the intestine, FVR expression marks mature Paneth cells, EECs and a subset of Lgr5^{+} ISCs (Boettcher et al., in revision). The *Fltp* mRNA, however, is not expressed in Paneth cells. We analysed Fltp-Venus expression in the small and large intestine of *Fltp*$^{V/+}$ and *Fltp*$^{V/V}$ mice by immunofluorescence or TSA-based staining, however, did not observe any specific staining (Figure 36F and data not shown). Additionally, neither Fltp-Venus fusion reporter was detectable in isolated SI crypts from *Fltp*$^{V/V}$ mice by live cell imaging nor by IF stainings (data not shown). Isolated live SI crypt cells derived from *Fltp*$^{V/V}$ mice did not display any difference in Venus fluorescence signal compared to WT mice upon analysis by flow cytometry (data not shown).

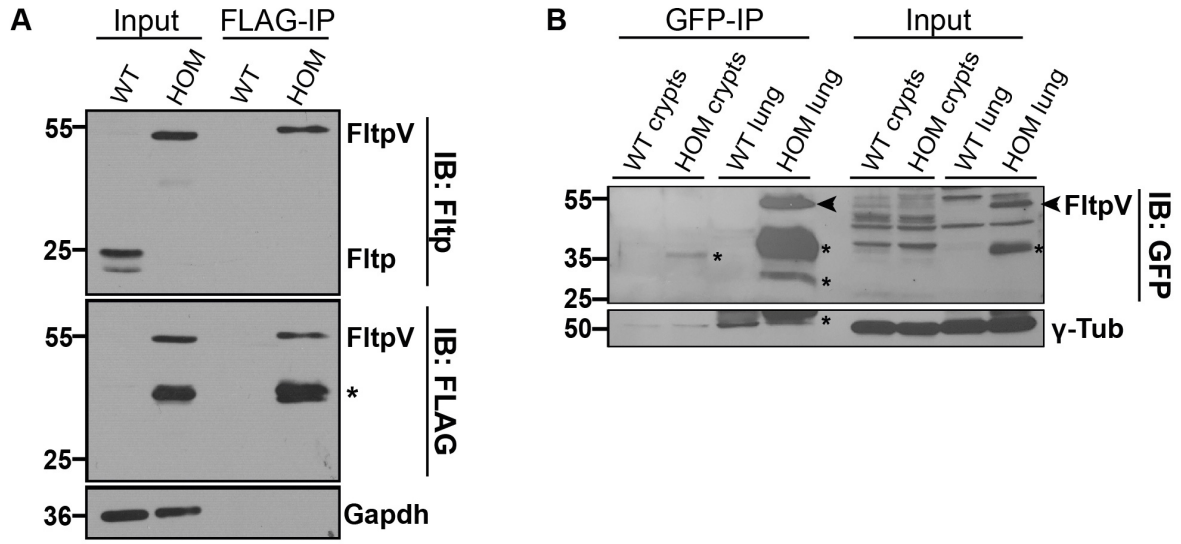

Figure 37: Immunoprecipitation of the Fltp-Venus protein in lung and SI crypt lysates

(A) Immunoblots of total extracts (Input) or immunoprecipitated proteins using anti-FLAG M2 agarose beads (FLAG-IP) from lung lysates of WT or HOM Fltp-Venus animals analysed by anti-Fltp (upper panel) or anti-FLAG (lower panel) antibodies. (*) Unspecific band or degradation product.
(B) Immunoblots of total lysates (Input) or immunoprecipitated proteins using rabbit anti-GFP antibody (GFP-IP) from SI crypt and lung lysates of WT and HOM Fltp-Venus mice analysed by chicken anti-GFP antibody. Arrow heads indicate the Fltp-Venus fusion protein in lung lysates. No specific FltpV bands could be detected in SI crypt lysates. (*) Unspecific bands or degradation product.

To test the functionality of the C-terminal 3xFLAG tag and to analyse whether the intestinal Fltp-Venus fusion protein can be detected by enrichment via an affinity-based pull-down approach, we performed a FLAG immunoprecipitation assay (FLAG-IP) in lung and SI crypt lysates. Western blot analysis using the anti-FLAG and anti-Fltp antibodies identified precipitated Fltp-Venus fusion protein in lung lysates from *Fltp*$^{V/V}$ but not in WT mice (Figure 37A), confirming the functionality of the 3xFLAG tag. However, we were not able, to detect precipitated Venus fusion protein in SI crypt lysates (data not shown). Since the enrichment of the FLAG-tagged protein using the M2 affinity gel was particularly low compared to the protein amount detected in total lysates, we tested a pull-down approach using an anti-GFP antibody against the Venus peptide sequence on lung and crypt lysates from WT and *Fltp*$^{V/V}$ mice. Although the fusion protein was clearly enriched in lung lysates, no signal could be found in SI crypt lysates (Figure 37B).

Taken together, the Fltp-Venus reporter mouse model is a practical tool to study Fltp expression and function in the lung and testis. However, several experimental approaches failed to detect Fltp-Venus reporter in the intestine and islets of Langerhans under homeostatic conditions. The data suggest, that in these tissues, Fltp expression is very low. Thus, studies under conditions that favour Fltp expression may be required.

4.2.3 Fltp-Venus fusion - a reporter of PCP-mediated ciliogenesis in the lung epithelium

Immunofluorescence stainings demonstrated that all multiciliated cells in the lung and tracheal epithelium of *Fltp*$^{V/+}$ and *Fltp*$^{V/V}$ mice were Fltp-Venus-positive (FltpV$^+$) (Figure 36B-C). Ciliogenesis in the lung is a process coordinated by PCP signalling, and Fltp has been implicated in basal body positioning and cilia formation in the airway epithelia (Gegg et al., 2014; Vladar, Bayly, Sangoram, Scott, & Axelrod, 2012). Based on this, we sought to verify whether the Fltp-Venus fusion mouse line can be used as a reliable reporter of/for PCP-mediated ciliogenesis in the airway epithelia.

To confirm that Fltp is enriched or exclusively expressed in multiciliated cells and in cells with active ciliogenesis in the airway tissue, we isolated EpCAM$^+$ epithelial Fltp-Venus$^+$ (FltpV$^+$) and FltpV$^-$ cells from lungs and tracheae of WT, *Fltp*$^{V/+}$ and *Fltp*$^{V/V}$ mice by flow cytometry (Figure 38A). 0.5-1 % of analysed epithelial cells were FltpV$^+$ (Figure 38A). We assessed the ciliation status in FltpV$^+$ and FltpV$^-$ cell populations using cytospin technique and immunofluorescence staining for acetylated tubulin (AcTub), which labels cilia. All FltpV$^+$ cells, captured by cytospin, displayed AcTub$^+$ cilia, whereas FltpV$^-$ cells did not show any basal body-amplification or cilia (Figure 38B).

Furthermore, we compared gene expression of markers of ciliated cells, cell cycle and PCP markers in sorted FltpV$^+$ and FltpV$^-$ cells by qRT-PCR. *FoxJ1*, a master transcriptional regulator of ciliogenesis in multiciliated lung cells (Blatt, Yan, Wuerffel, Hamilos, & Brody, 1999; Brody, Yan, Wuerffel, Song, & Shapiro, 2000; Yu, Ng, Habacher, & Roy, 2008), exhibited a calculated 60,000-times higher expression level in FltpV$^+$ compared to FltpV$^-$ cells (Figure 38C). Similarly, the abundance of *Fltp* mRNA was more than 1,000-times higher in FltpV$^+$ cells. Moreover, gene expression of the three core PCP components, *Celsr1* and *Fzd3*/*6*, as well as of the PCP effector gene Fuzzy (*Fuz*), was highly upregulated in FltpV$^+$ cells (Figure 38D), indicating active PCP signalling. The cell cycle status of FltpV$^+$ cells was, however, not completely clear, since they were enriched in both, cell cycle progression (*Ccnd1*) and cell cycle inhibitor markers (*Cdkn1a*, *Cdkn1b*) (Figure 38E). This finding suggests that FltpV$^+$ cells are likely a heterogeneous population, comprising cells with different cell cycle status. Upon ciliogenesis, cells exit the cell cycle (Goto, Inaba, & Inagaki, 2017; Sánchez & Dynlacht, 2016). Therefore, we presumed the existence of FltpV$^+$ stem cells which may exhibit a certain degree of cell cycle activity and be committed to the ciliated cell-lineage, similar to previously discussed findings on the Wnt/PCP-mediated intestinal lineage priming (Boettcher et al., in revision). Putative lung stem cells are so called basal cells and are marked by expression of transcription factor transformation-related protein 63 (*Trp63*) (Daniely et al., 2004; Rawlins & Hogan, 2006; J. R. Rock et al., 2009). We assessed expression of *Trp63* in FltpV$^+$ cells. The result was ambiguous, though there was a trend toward a higher expression of *Trp63* in FltpV$^+$ cells (Figure 38F). Basal cells are a heterogeneous cell population (Jason R Rock, Randell, & Hogan, 2010) and

may, hypothetically, comprise both, FltpV⁺ and FltpV⁻ cells, similar to the heterogeneity observed in ISCs (Boettcher et al., in revision). However, additional analyses and different experimental approaches are required to address this issue. Moreover, our findings are based on a single experiment, and have to be confirmed for valid conclusions.

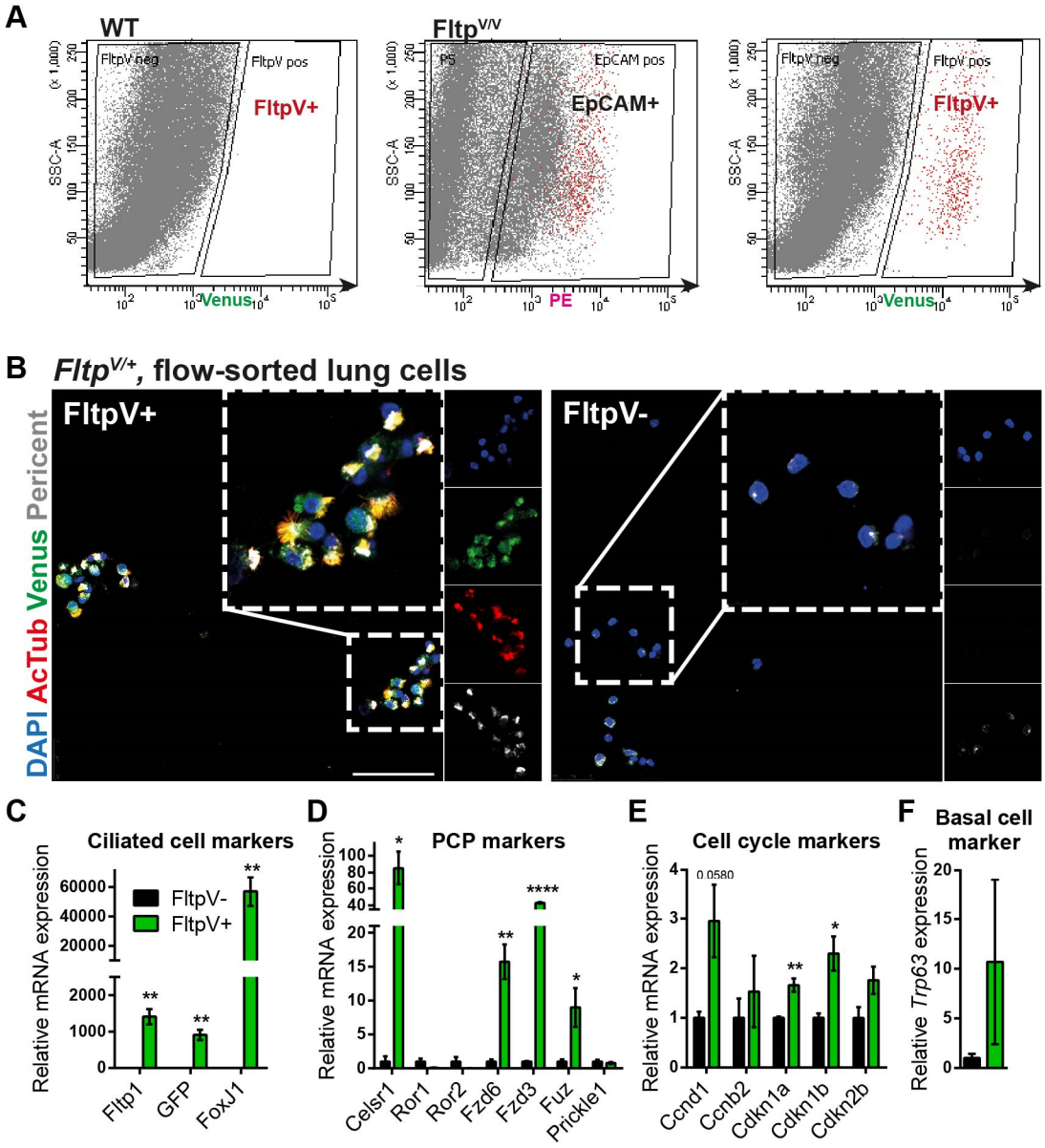

Figure 38: Isolated FltpV⁺ airway epithelial cells are multiciliated and enriched in markers of the PCP pathway

Figure 39: Fltp-Venus is a reporter for ciliogenesis *in vitro*

(A) Typical LSM pictures of ALI cultures of mTECs isolated from *FltpV$^{V/V}$* mice at day 3 post ALI creation as overviews (left side) or enlarged sections (right side). White squares indicate the respective enlarged areas.
A cell layer is depicted at the cytoplasm level (upper panel) or at the apical surface and cilia level (lower panel). A star (*) indicates a multiciliated FltpVhigh cell. Hashes (#) indicate FltpVlow cells with amplified basal bodies (pericentrin+, purple) but no cilia (AcTub+, white) present at the surface yet. The actin cytoskeleton is stained by phalloidin. Pericent = pericentrin, AcTub = acetylated tubulin.
(B) LSM images of day 7 ALI cultures of mTECs from *FltpV$^{V/V}$* mice as an overview (left side) or a zoom-in view – (right side). White squares indicate the enlarged area. FltpVhigh cells are multiciliated. Fltp-Venus fusion protein is localized in the cytoplasm and enriched in the cilia. Maximum projections of z-stacks, 4.53 µm.
Scale bar overview pictures in A and B, 25 µm; scale bar zoom-in views in A und B, 5 µm.

(A) Representative FACS plots depicting the experimental strategy to distinguish EpCAM$^+$ and FltpV$^+$ or negative FltpV$^-$ cells isolated from lungs and tracheae of WT or *Fltp$^{V/V}$* mice.
(B) LSM pictures of flow-sorted and immuno-stained FltpV$^+$ and FltpV$^-$ cells using the FACS strategy from (A). Basal bodies: pericentrin$^+$, white; cilia: acetylated tubulin$^+$ (AcTub), red. Maximum projection of z-stacks, 1.76 μm. Scale bar, 50 μm.
(C-F) qRT-PCR analysis of marker gene sets to for ciliated cells (C), PCP (D), cell cycle markers (E) and a basal cell marker, *Trp63* (F), in flow-sorted FltpV$^+$ and FltpV$^-$ cells. Expression was normalised to the housekeeping genes *Gapdh, Actb and 18S*. n=3, error bars indicate mean ± SEM.

Gegg et al. has demonstrated that the onset of *Fltp* expression correlates with the PCP acquisition in ciliated tissues, in particular, with the onset of airway cilia formation *in vitro* (Gegg et al., 2014). Using ALI cultures of mTECs, Gegg et al. showed that FVR expression is induced when basal bodies are amplified and increases during differentiation into multiciliated cells. Based on this, we sought to verify whether the Fltp-Venus fusion reporter mouse line can be used to study PCP-mediated ciliogenesis as well as Fltp protein dynamics and function. Therefore, we utilised ALI cultures of mTECs, a widely used *in vitro* system which has been demonstrated to reliably model cell differentiation processes in the airway epithelium, including ciliogenesis (Vladar et al., 2012; Vladar & Stearns, 2007; You et al., 2002). Hereby, switching the mTEC culture to ALI conditions induces formation of multiple centrioles and active ciliogenesis in the lung progenitor cells two-three days after ALI creation. Maximal ciliation is achieved at around 14 days after ALI generation. ALI cultures of mTECs isolated from *Fltp$^{V/V}$* mice comprised FltpV$^-$ and FltpV$^+$ cells three days after the switch, whereby FltpV$^+$ cells with low and high FltpV reporter intensity (FltpV^{low} and FltpV^{high} cells) could be distinguished (Figure 39A, upper panel). FltpV^{low} cells exhibited multiple pericentrin$^+$ basal bodies in the cytoplasm and in proximity to the apical cell membrane, indicating onset of ciliogenesis, but no or only one cilium on the apical cell surface. In comparison, FltpV^{high} cells were multiciliated (Figure 38A, lower panel). Additionally, we examined Fltp-Venus fusion protein localisation in differentiated mTECs after seven days of ALI culture. Multiciliated FltpV^{high} cells displayed a spotted Fltp-Venus reporter staining in the cytoplasm and a strong signal in the cilia (Figure 38B). These results are in agreement with the published findings by Gegg et al. (Gegg et al., 2014).

In conclusion, Fltp-Venus fusion reporter mouse model enables to monitor ciliogenesis in multiciliated cells and study localisation and function of Fltp in the airway epithelium *in vitro* and *in vivo*.

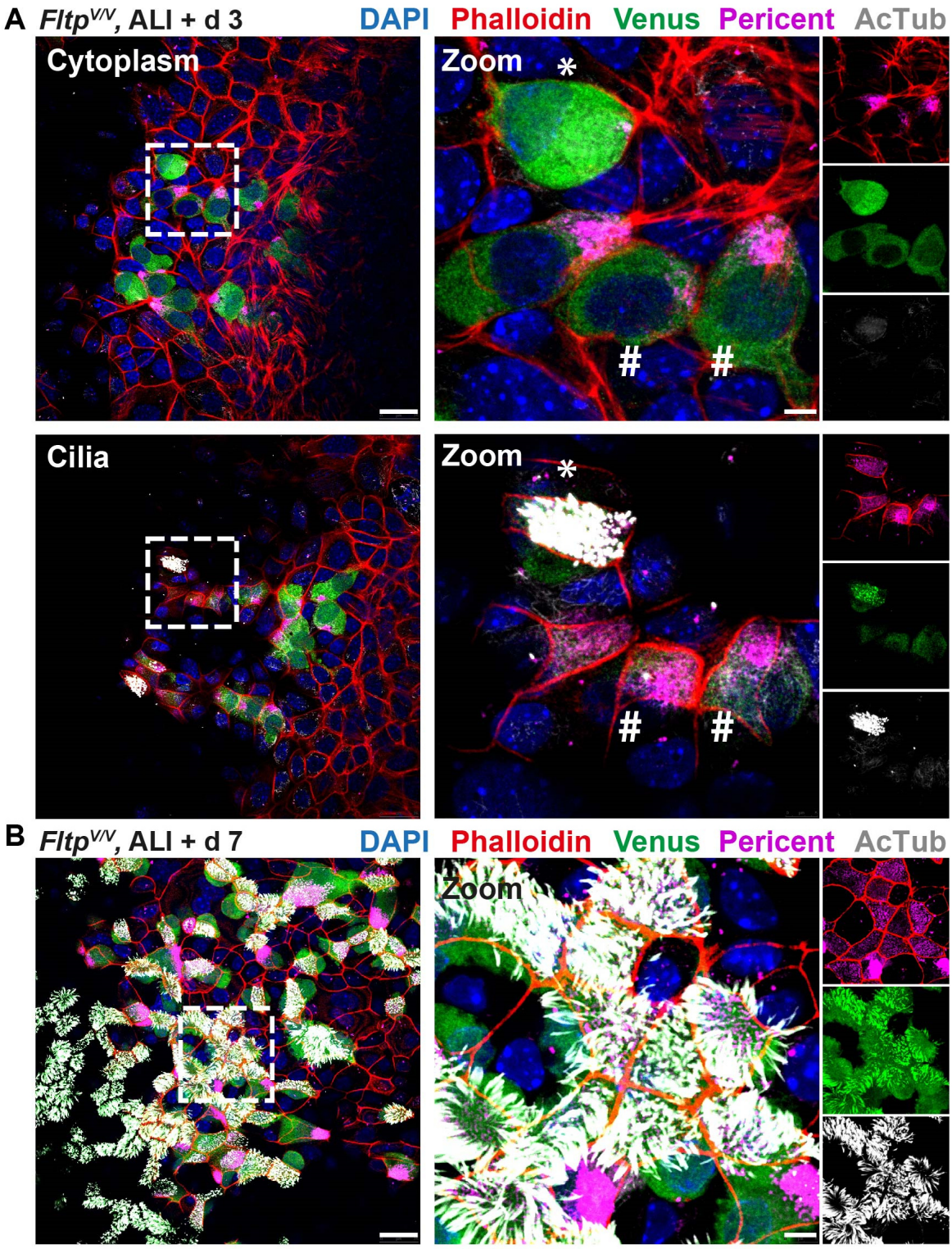

Figure 39: Fltp-Venus is a reporter for ciliogenesis *in vitro*

(A) Typical LSM pictures of ALI cultures of mTECs isolated from *Fltp*$^{V/V}$ mice at day 3 post ALI creation as overviews (left side) or enlarged sections (right side). White squares indicate the respective enlarged areas.
A cell layer is depicted at the cytoplasm level (upper panel) or at the apical surface and cilia level (lower panel). A star (*) indicates a multiciliated FltpV^{high} cell. Hashes (#) indicate FltpV^{low} cells with amplified basal bodies (pericentrin^{+}, purple) but no cilia (AcTub^{+}, white) present at the surface yet. The actin cytoskeleton is stained by phalloidin. Pericent = pericentrin, AcTub = acetylated tubulin.

(B) LSM images of day 7 ALI cultures of mTECs from *Fltp*$^{V/V}$ mice as an overview (left side) or a zoom-in view – (right side). White squares indicate the enlarged area. FltpV^{high} cells are multiciliated. Fltp-Venus fusion protein is localized in the cytoplasm and enriched in the cilia. Maximum projections of z-stacks, 4.53 μm.
Scale bar overview pictures in A and B, 25 μm; scale bar zoom-in views in A und B, 5 μm.

5 Discussion

5.1 Novel insights into HFD-induced intestinal disorder in a mouse model of pre-diabetes

To elucidate changes in the intestinal homeostasis contributing to the development and progression of obesity and T2D, we performed a single-cell survey of 27,687 SI crypt cells in homeostasis and in HFD-fed state and integrated our findings with different approaches for functional validation. Our results demonstrate that HFD promoted ISC and progenitor proliferation and increased recruitment of the absorptive lineage to account for excess nutrient intake. Moreover, we obtained a fine-resolved map of the EE lineage and revealed HFD-induced disturbances in the EE system at the early stage of T2D, including decreased numbers of Reg4$^+$ EC cells and reduced levels of plasma serotonin. We identified upregulated Igf1r/Akt signalling and increased activity of the FA synthesis pathway and Pparα/γ signalling as possible mechanistic links to HFD-induced hyperproliferation of ISCs and progenitors.

5.1.1 Discrepancies in HFD-induced phenotypes between the studies with regard to morphology and cell type composition

We found that mice fed a HFD for 12 weeks develop a metabolic condition equivalent to pre-diabetes and exhibit changes in intestinal tissue morphology, cell type composition and proliferation rate. In particular, the HFD increased intestinal length and weight and villus height, however, did not affect the crypt depth. We could pin down the increased proliferation in the crypt compartment to ISCs and progenitors of the absorptive and goblet cell lineages resulting in a concomitant increase in proportions of the mature enterocytes and proximal goblet cells (Figure 40).

HFD-induced alterations in the intestinal homeostasis, specifically, in crypt-villus morphology, cell type composition and proliferation, have been described across a range of studies using HFD- or genetically induced mouse models of obesity (*e.g*. *ob*/*ob* or *db*/*db* mouse models, Hummel, Dickie, & Coleman, 1966; Ingalls, Dickie, & Snell, 1950; G.-H. Lee et al., 1996). However, considerable discrepancies in phenotypes have been reported. As such, Beyaz et al. observed shorter villi and increased crypt depth on chronic HFD (Beyaz et al., 2016), while other groups found both, increase in villi length solely or together with deeper crypt domains (Baldassano et al., 2013; Beyaz et al., 2016; N. J. de Wit et al., 2008; Mah et al., 2014; Mao et al., 2013).

The appearance of longer SI villi coincided in our study with enhanced recruitment of the absorptive lineage cells. This suggests an adaptation mechanism to surplus nutrient availability consistent with the obesity-induced increase in intestinal absorptive capacity as previously reported (Dailey, 2014). Additionally, we found HFD-induced shifts in cell proportions of the secretory lineages, involving changes in goblet and Paneth cells and distinct EEC subtypes. Altered frequencies of these cell types have been also reported by other groups using HFD mouse models (Aranias et al., 2015; Beyaz et al., 2016; Dusaulcy et al., 2016; Mah et al., 2014; Richards et al., 2016; Wölnerhanssen et al., 2017; Zhou, Davis, Li, Nowak, & Dailey, 2018). However, there are serious inconsistencies between the observations. In studies reported by Beyaz et al. and Mah and colleagues, the numbers of Paneth and goblet cells were decreased and no change in ChgA$^+$ EECs was observed under HFD conditions. Contrastingly, Aranias et al. and Dusaulcy et al. observed an increase in distinct EEC subsets, while Zhou et al., Richards et al. and Wölnerhanssen et al. showed a decrease in numbers of ChgA$^+$ EECs or specific EEC subsets. Collectively, the significant discrepancies between the studies arise most probably due to different types of obesogenic (*e.g*. 60 % HFD (Beyaz et al., 2016; Dusaulcy et al., 2016; Richards et al., 2016), 45 % HFD (Mah et al., 2014)) and reference (low-fat or chow) diets, duration of the dietary intervention (*e.g*. long-term, 9 to 14 months (Beyaz et al., 2016) or around 4 month (Dusaulcy et al., 2016; Mah et al., 2014; Richards et al., 2016)) and/or genetic background of the animal models used. Consequently, based on these variations, animals develop different metabolic conditions, which may range from healthy obesity

to a diabetic mouse model, and lead to different morphologic and molecular alterations. As demonstrated by our results, a 12-week 60 %-HFD regiment results in a pre-diabetic condition in FVF mice. However, comparison of our results with the other studies is difficult due to the lack of basic metabolic phenotyping in most of these studies.

HFD studies on bulk populations collectively lack the necessary resolution to tease apart cell type- and maturation state-specific molecular effects in functionally and metabolically distinct intestinal populations (Rodríguez-Colman et al., 2017; Stringari et al., 2012). Using the single-cell technology, we were able to show that higher numbers of enterocytes and, coincidently, formation of longer villi, were not only attributable to enhanced proliferation (of ISCs and progenitors) as suggested by several studies, but were, moreover, a result of increased absorptive lineage allocation from ISCs. This shows that dietary impact on the lineage decisions, made on the stem cell level, will affect mature lineage composition and tissue homeostasis.

Our single-cell data and validation in tissue sections showed that HFD-induced alterations in cell type proportions vary considerably between the gut regions. Moreover, HFD-induced molecular changes (such as *e.g.* upregulation of FA synthesis pathway and Pparα/γ levels) were more pronounced in the proximal (duodenum/jejunum) intestine. Whereas most of the studies disregard regional heterogeneity, similar findings with respect to regulated genes and region-specific manifestation of transcriptional changes were observed by de Wit and colleagues (N. J. de Wit et al., 2008; N. J. W. de Wit et al., 2011).

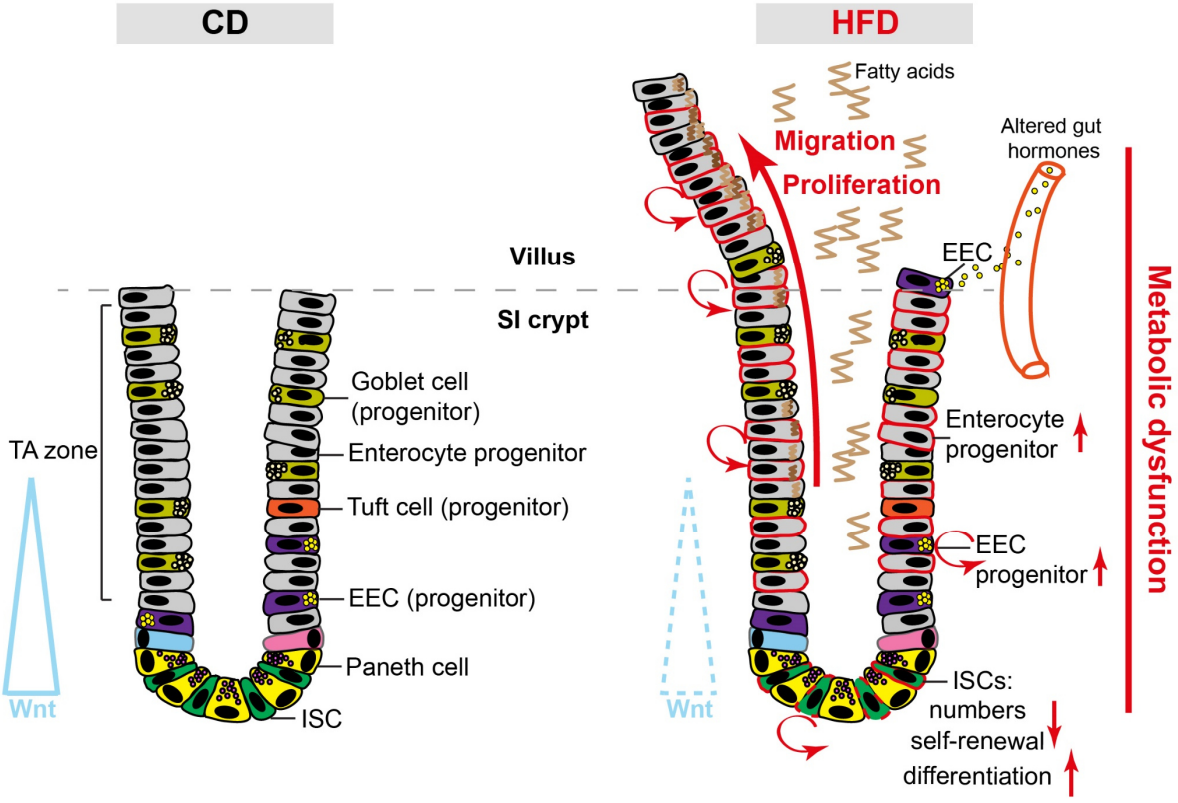

Figure 40: Simplified model of HFD-induced cellular and molecular alterations in the crypt compartment

In the model of DIO and pre-diabetes, HFD induces alterations in the lineage allocation from ISCs and enhances proliferation of ISCs and progenitors. In particular, HFD leads to the increased formation of the absorptive and goblet cell lineages. HFD-induced hyperproliferation of the respective progenitors further contributes to the increase in absorptive and goblet cells. Moreover, HFD leads to a deregulated ISC homeostasis. This is characterised by an enhanced ISC turnover, which is not driven by Wnt/β-catenin signaling. On the contrary, reduced Wnt/β-catenin pathway activation in the crypt leads to an attenuated self-renewal and increased ISC differentiation on HFD. Additionally, HFD induces changes in gut hormone levels and numbers of EECs, including increased EE

progenitor numbers and reduced plasma serotonin levels. On the molecular level, HFD results in an abnormal cellular fatty acid handling and, consequently, in a metabolic dysfunction in the crypt compartment.

Moreover, with regards to the previous reports on changes in the EECs abundance in obesity or under HFD conditions, conclusions from several studies have to be treated with caution. A range of aspects about the EEC lineage heterogeneity have to be taken into account. These include subtype diversity with regard to hormone co-secretion profiles within single cells, differences in regional distribution along the intestine and, not least, plasticity in hormone secretion patterns along the crypt-villus maturation axis (Beumer et al., 2018; Haber et al., 2017; Habib et al., 2012). Of note, our study is in large part consistent with previous reports using single-cell transcriptomics (Beumer et al., 2018; Haber et al., 2017). However, our single-cell sampling approach using the FVF-based enrichment strategy to obtain rare EEC subtypes is a classical bias and so may not reflect the actual compositional conditions in the crypt. While we confirm most of our single-cell data by other experimental approaches, additional analyses are required to address all aspects of the EEC lineage heterogeneity to gain a more profound understanding of diet-associated changes and the EE disorder.

5.1.2 Deregulated metabolic and proliferative signalling on HFD - implications in the development of the metabolic disorder, ISC hyperproliferation and fate control

5.1.2.1 Diminished β-catenin pathway activity - a prerequisite for disturbed ISC homeostasis and increased enterocyte lineage formation

Our single-cell study revealed increased proliferation of ISCs and progenitors under HFD conditions. Strikingly, this was associated with a concomitant decrease in the ISC numbers. When analysing signalling determinants underlying HFD-induced hyperproliferation, we detected diminished nuclear β-catenin levels and reduced Wnt/β-catenin target gene expression in bulk sorted FVF^{low} cells, enriched for ISCs, but no changes in the FVF^{neg} enterocyte progenitors. Likewise, in the single-cell dataset, the three major ISC markers and Wnt/β-catenin target genes, *Lgr5*, *Ascl2* and *Axin2*, were downregulated in HFD-derived ISCs.

As far as proliferation is concerned, our findings are in line with other relevant studies on obese mouse models, however, the signalling determinants for the increased proliferation in the crypt compartment are, for the most part, not clearly characterised or inconsistent (Baldassano et al., 2013; Beyaz et al., 2016; N. J. de Wit et al., 2008; Mah et al., 2014; Mao et al., 2013). As opposed to our findings, studies by Mao et al. and Beyaz et al. provide evidence for the increased β-catenin signalling in the crypt compartment or, specifically, in the ISCs and progenitors, as a mechanistic link to HFD-induced boost in proliferation (Beyaz et al., 2016; Mao et al., 2013). Mao and colleagues show an overactive Gsk3β/β-catenin signalling axis in the crypts of both, HFD-induced and the *db*/*db* mouse model, whereas Beyaz et al. demonstrate a Pparδ/Wnt/β-catenin signalling-based mechanism of hyperproliferation and increased tumorigenicity of ISCs and progenitors under chronic HFD. Neither of these signalling components was directly driving proliferation of ISCs and progenitors in our system, given that Gsk3β activity was upregulated in accordance with the reduced nuclear β-catenin abundance, and *Pparδ* transcript levels were decreased. Similar to our results, Mah et al. also provide evidence for a decreased β-catenin activity in ISCs and an Igf1/insulin signalling-based mechanism of hyperproliferation and impaired ISC function in a long-term HFD mouse model (Mah et al., 2014).

Since Wnt/β-catenin pathway constitutes the master switch between proliferation and differentiation in ISCs and is indispensable for the ISC maintenance, diminished Wnt/β-catenin signalling in ISCs in our model is a strong indicator of a disturbed ISC homeostasis and function on HFD (H. Clevers, 2013). Moreover, reduced β-catenin activation in HFD-derived crypts is clearly in line with the decrease in the ISC numbers. Thus, inhibition of Wnt/β-catenin signalling has been shown to disrupt intestinal homeostasis, thereby forcing terminal differentiation of the ISCs into the absorptive lineage as the default fate (Fevr et al., 2007; Daniel Pinto, Gregorieff, Begthel, & Clevers, 2003). Similarly, reduced β-

catenin pathway activation in our model could be the cause for the increased ISC commitment and differentiation into the enterocyte lineage, and could eventually lead to the ISC pool shrinking despite the increased proliferation Figure 40). In support, comparable mechanisms have been observed in other stem cell systems (J.-M. Lee et al., 2018; Singer et al., 2014; van den Berg et al., 2016). For instance, a HFD impaired hematopoietic stem cell (HSC) function and promoted HSC differentiation leading to altered composition of the HSC compartment and eventual HSC pool exhaustion (van den Berg et al., 2016).

It remains, however, to be answered, which signalling cue is a direct regulator of the ISC hyperproliferation under HFD conditions, if it is not β-catenin and not the classic downstream mediators of the Igf1r/Akt axis, such as Erk or mTor, as described in chapter 4.1.6.1 and 4.1.6.2. We propose that upregulated FA synthesis and Pparα/γ levels or a combination of those with the reduced β-catenin activity may lead to a disturbed ISC homeostasis, involving concomitant increase in the ISC proliferation and differentiation into the absorptive lineage (Figure 41). This is discussed in more detail in chapter 5.1.2.3.

Additionally, whether the reduction in β-catenin activation led to impaired ISC function needs to be further analysed. As shown by Beyaz et al., increased Pparβ/δ/β-catenin signalling boosted ISC function and promoted their independence from the niche signals over a long period of time *in vitro* (Beyaz et al., 2016). By contrast, Mah et al. demonstrated an impaired ISC function *in vitro*, which could be improved through supplement of Igf1 or insulin to the culture media (Mah et al., 2014). Our findings, on the other hand, showed that HFD-derived organoids maintained a higher proliferative capacity than controls independently from external stimuli (such as fatty acids or Igf1/insulin) for 3 days in culture. This indicates increased function of ISCs for this period of time. However, whether a higher proliferation capacity could be sustained over the long term, has to be further studied.

Finally, whether the decrease in β-catenin levels is the cause or the consequence of the reduced ISC pool and what is the upstream signalling trigger has to be clarified by additional experiments.

5.1.2.2 Implications of disturbed Ppar signalling and excessive Srebp1-mediated lipogenesis in the pathogenesis of diabetes and obesity

In the present study, we revealed alterations in metabolic signalling in the crypt compartment under HFD conditions. In particular, we observed a profound upregulation of the Pparα/Pparγ signalling and FA synthesis pathways evidenced by different experimental approaches. Ppar signalling-related terms and FA metabolic pathways, in particular, FA biosynthesis, were highly enriched in the single-cell transcriptomes of HFD-derived ISCs and progenitors. In contrast to increased *Pparα/γ* expression, levels of *Pparδ* were reduced in these cell populations. Moreover, protein expression of the major transcriptional regulators (Srebp1) and enzymes (Scd1, Acc) of FA synthesis as well as Pparγ were upregulated, confirming the single-cell data. Strikingly, these pathways were more prominently regulated in the proximal cell subsets. Furthermore, FA synthesis pathway-derived metabolites were accumulated in the crypt compartments of HFD-fed animals as evidenced by the metabolic profiling.

Srebp and Ppar factors are the main mediators of the whole-body lipid and glucose metabolism, but have also been described to be involved in cell proliferation, inflammation and cardiovascular disease (Han, Shen, Bittner, Kraemer, & Azhar, 2017; Y.-X. Wang, 2010). Disturbances in Ppar signalling and Srebp1-mediated lipogenesis are hallmarks of obesity, dyslipidaemia and T2D (Cimini & Cerù, 2008; Shao & Espenshade, 2012; Tobin & Freedman, 2006). Whereas, these transcription factors have been best studied in the liver, adipose tissue, heart and skeletal muscle, where they are most abundantly expressed, little is known about their function and signalling dysregulation in the small intestine and how this may contribute to the pathogenesis of obesity and diabetes.

In line with our results, de Wit and colleagues provide evidence for the role of deregulated Ppar- and Srebp-mediated pathways in the small intestine in the development of HFD-induced obesity (N. J. de Wit et al., 2008; N. J. W. de Wit et al., 2011). In accordance with our data, they observed overexpression of Pparα target genes and upregulation of the FA synthesis programme, concomitant with a

downregulation of *Pparδ*, most prominently in the proximal and middle parts of the small intestine. Intriguingly, these changes emerged as early as 2 weeks after starting of the diet together with first detectable changes in the intestinal proliferation and weight gain, indicating involvement of these intestine-derived factors in the development of obesity. In our study, the first changes in proliferation and a significant weight gain likewise appeared after 2 weeks on HFD. However, we did not examine whether Ppar and Srebp signalling were already affected at this stage. Hence, this should be addressed in future studies.

With regards to Pparδ, both, its activation and inhibition have been associated with metabolic disorders depending on the tissue context, but mostly in the liver, adipose tissue and muscle (Palomer et al., 2018; Vázquez-Carrera, 2016). Intestinal epithelial cell-specific deletion of Pparδ in mice results in increased abdominal fat accumulation, suggesting a protective role of intestinal Pparδ against diet-induced obesity (Doktorova et al., 2017).

There are no marketed drugs available targeting Pparδ, but antidiabetic effects of Pparδ agonists have been demonstrated in different tissues, such as muscle, pancreas, adipose tissue and liver in animal studies and in humans (Bojic & Huff, 2013; Palomer et al., 2018; Vázquez-Carrera, 2016). In this context, addressing the effect of intestinal Pparδ activation in a HFD mouse model by follow-up studies would be beneficial for the implementation of novel therapeutic agents.

Along the same lines, Srebp factors, as critical transcriptional regulators of cholesterol and FA biosynthesis, have been implicated in the development of diet-related insulin resistance, obesity and diabetes (reviewed in Shao & Espenshade, 2012). Srebp1 and Srebp2 are, extensively studied in the liver, but not much is known about the role of Srebp activity and dysfunction in the intestine. Intriguingly, intestinal epithelial Srebp upregulation did not lead to the increase in systemic triglyceride levels and significant worsening of the systemic metabolic condition in mice in first place (Colin et al., 2008; K. Ma et al., 2014; McFarlane et al., 2015; McFarlane, Liang, & Engelking, 2014). However, an intestine-specific deletion of Insig1/2, proteins required for the feedback inhibition of Srebp, resulted in a dramatic increase of cholesterol synthesis and crypt lipidosis (McFarlane et al., 2014). Whereas the intestinal-derived cholesterol accumulated in the liver and plasma cholesterol levels were increased, the triglyceride levels in the blood were not affected or even decreased (Colin et al., 2008; K. Ma et al., 2014). Interestingly, lipid droplets accumulated mostly in the cells of the crypts but not in the villi, indicating higher activity and critical role of Srebp1 in the crypts. In a follow-up study McFralane et al. demonstrated that Srebp1 activity is essential for crypt proliferation *in vitro*, but they could not specify which cell populations required Srebp1 (McFarlane et al., 2015). Our findings by single-cell profiling showed that *Srebf1* is expressed in ISCs, as well as in some progenitor clusters, indicating its role in ISC proliferation and function. Together, these findings suggest that intestine has a considerable capacity to buffer such an overload of dietary lipids to protect against lipotoxic effects on systemic metabolism. The conclusion made by the authors, that intestinal morphology and ISC function were not majorly affected by Srebp factor upregulation, at least for a period of time, has to be taken with caution since no detailed analyses were provided. Based on published reports and our findings, overactive Srebp in the SI crypt, in particular, in ISCs and progenitors, could mediate significant HFD-induced intestinal side-effects in first place, including hyperproliferation and disturbances in lineage allocation, at least at the early stages of the metabolic disease. In conclusion, since pharmacologic agents inhibiting Srebp activation are being vividly discussed as anti-obesity and anti-diabetes therapeutics, they could have additional beneficial effects on the intestinal pathology and on obesity-induced GI cancers (Shao & Espenshade, 2012; Soyal, Nofziger, Dossena, Paulmichl, & Patsch, 2015).

5.1.2.3 Disturbances in Ppar signalling and upregulation of Srebp1-mediated FA synthesis - possible mechanistic links to hyperproliferation and fate control in ISCs

As mentioned before, we revealed alterations in lipid metabolism-related signalling in the ISCs. As work from our group shows (Boettcher et al. in revision), all lineages are rooted to the ISCs, and progeny identity is determined on the stem cell level. While changes in cell metabolism are well-studied in a

range of other stem cell systems (Chandel et al., 2016; Ito & Suda, 2014; Mihaylova et al., 2014), our understanding of the basic metabolic requirements of the ISCs and the dietary impact on the ISC function and cell fate decisions is very limited (Beyaz et al., 2016; Mah et al., 2014; Mihaylova et al., 2018; Rodríguez-Colman et al., 2017; Stringari et al., 2012; Yilmaz et al., 2012). Our data based on single-cell transcriptional programmes strongly indicate that ISCs rely on mitochondrial metabolism and oxidative phosphorylation (OxPhos) in agreement with the findings by Rodriguez et al. (Rodriguez-Colman, 2016). Interestingly, the basal metabolic flux, indicated by the ratio of glycolysis to OxPhos, was not changed in ISCs under HFD conditions. However, a diet-dependent change in extrinsic substrates, such as lipids, may influence cell proliferation and alter stem cell homeostasis (Mihaylova et al., 2014; Ochocki & Simon, 2013). Our multidimensional analysis demonstrated that ISCs and progenitors upregulate *de novo* FA synthesis in response to a HFD, a metabolic pathway which in adults is mainly restricted to the liver, adipose tissue, kidney and mammary gland under normal conditions and has not been shown/discussed in ISCs before (Weiss et al., 1986). In addition, excessive or even ectopic upregulation of factors most abundant in the liver or adipose tissue and immune system such as Pparα and Pparγ, respectively, in ISCs and progenitors may lead to disturbed stem cell homeostasis as described in other adult stem cell systems (Cimini & Cerù, 2008; Ito & Suda, 2014). Thus, in HSCs for instance, Ppar signalling establishes a link between cell metabolism and HSC self-renewal and fate control, as loss of Pparδ alters HSC division mode and promotes differentiation leading to HSC exhaustion (Ito et al., 2012). In the intestinal compartment, Ppars are more abundant in the villus indicating their primary function in metabolism, but not much is known about Ppar signalling in the ISC fate control (Bünger et al., 2007; H. Yang, Wang, Xiong, & Yin, 2016). In the ISCs, increased Pparδ signalling has been shown to promote stemness and proliferation of ISCs and progenitors (Beyaz et al., 2016). By contrast, we detected, a reduction in Pparδ levels in these populations, but found, likewise, atypical HFD-induced adaptation of progenitor-like features, *i.e*. active proliferation, by the early enterocytes at the villus base, likely caused by other signals.

As mentioned before, our results demonstrated that a HFD induced hyperproliferation of ISC and progenitors. The observed upregulation of Igf1r/Ir/Akt signalling axis activity maybe, at least in part, implicated. However, no canonical mediators downstream of the Igf1r/Ir/Akt factors were found to be upregulated, including Erk, mTor and β-catenin. Thus, we proposed that excessive FA synthesis pathway activation could be directly implicated in the HFD-induced ISC hyperproliferation (Figure 41). This assumption is based on two aspects: Akt is a known strong activator of the lipid biosynthesis (Wong & Sul, 2010; Yecies et al., 2011), and *de novo* lipogenesis has been shown to promote proliferation in other stem cell systems and in cancer (Guo, Bell, Mischel, & Chakravarti, 2014; Menendez & Lupu, 2007; Mounier, Bouraoui, & Rassart, 2014; Shao & Espenshade, 2012).

In neural stem cells, it has been shown that upregulation of *de novo* lipogenesis is required for the active proliferation and deletion of Fasn, a key enzyme in *de novo* lipogenesis, leads to impaired neurogenesis (Knobloch et al., 2013). Further evidence for the role of increased FA synthesis to promote proliferation of ISCs and progenitors is provided by al-Dawairi and colleagues showing that intestinal overexpression of malic enzyme 1 (Me1), enzyme involved in FA and cholesterol synthesis, increases BrdU incorporation in the crypt compartment (Al-Dwairi et al., 2014). In addition, findings by de Wit et al. show an association between the HFD-induced overexpression of the Pparα target gene and FA synthesis-related transcriptional programmes (in a fat-dose dependent manner) and a concomitant increase in crypt cell proliferation after 2 weeks on HFD (N. J. de Wit et al., 2008; N. J. W. de Wit et al., 2011). Moreover, findings by McFarlane et al. revealed that Srebp1 is required for crypt growth and budding *in vitro* (McFarlane et al., 2015). Interestingly, they showed, that hepatocytes, unlike intestinal crypt cells, were able to tolerate loss of Srebp activity, suggesting that Srebp may not be required for maintenance of slowly proliferating cells under normal conditions.

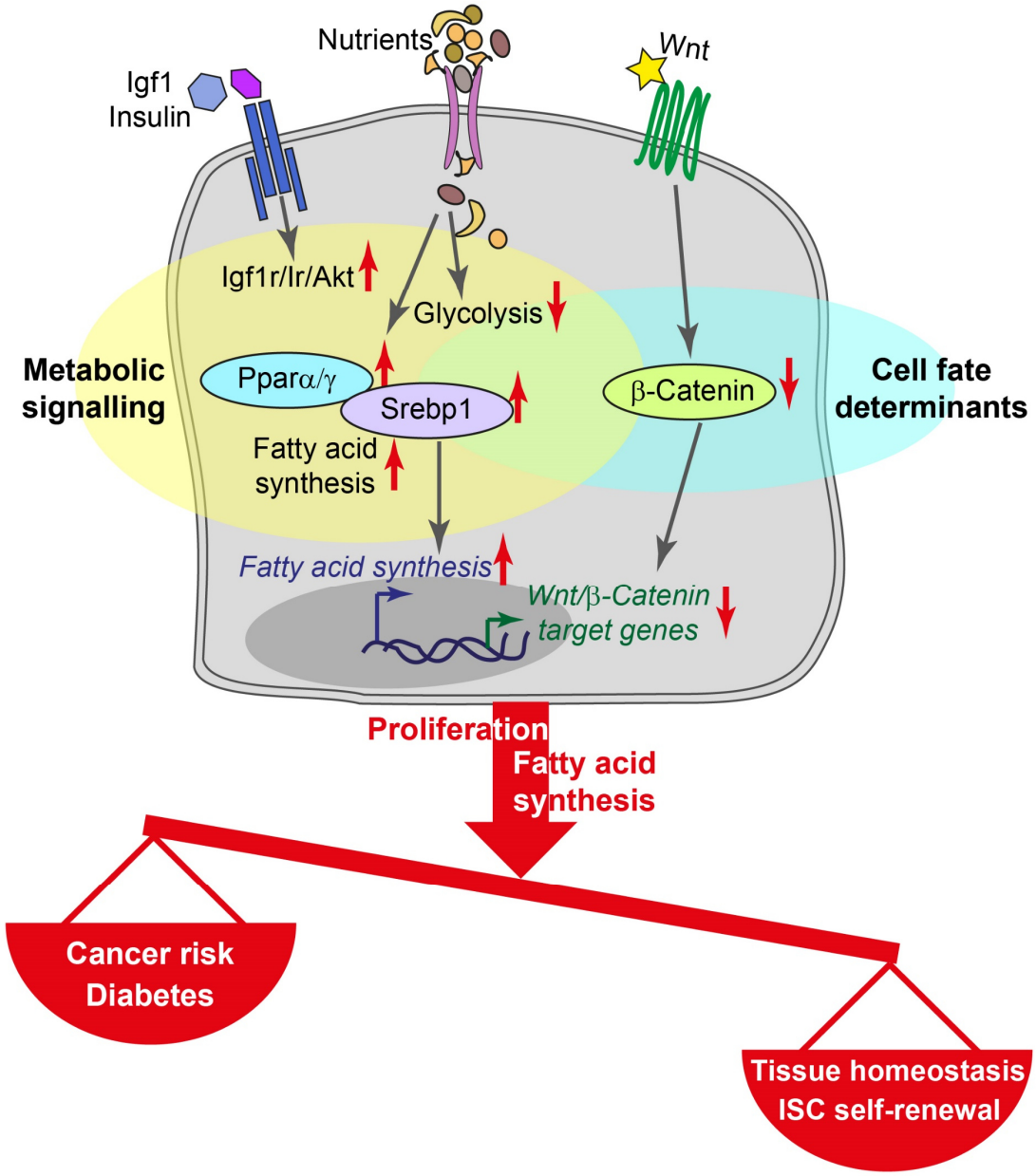

Figure 41: Model of a link between the metabolic and the cell fate determinant signalling in ISCs and progenitors on HFD. A misbalance of the proliferative and metabolic signalling on HFD leads to cancer risk and development of pre-diabetes

As mentioned above, exacerbated lipogenesis due to the overexpression of FA synthesis pathway components Pparγ, Srebp1, Acc, Scd1 or Fasn, has been implicated in tumorigenesis in several types of cancer across different tissues (Guo et al., 2014; Igal, 2010; Jeon & Osborne, 2012; Lecarpentier et al., 2017; Mounier et al., 2014; Müller, 2017; Shao & Espenshade, 2012). Several studies have shown that fatostatin, an inhibitor of Srebp1/2 activation, has antiproliferative properties and can directly affect cell division process in cancer cells (Gholkar et al., 2016; X. Li, Chen, Hu, & Huang, 2014). Moreover, Srebp has been shown to be stabilised during mitosis in a Plk1/Cdk1[32]-dependent manner and required for a proper cell division *in vitro* (Maria T. Bengoechea-Alonso & Ericsson, 2006; Maria Teresa Bengoechea-Alonso & Ericsson, 2016). Several studies demonstrate involvement of Srebp1 in cell cycle regulation.

[32] Plk1, polo-like kinase 1; Cdk1, cyclin-dependent kinase 1

Thus, Motallebipour and colleagues demonstrated that Srebp stimulates expression of key genes involved in cell cycle control (Motallebipour et al., 2009). Another report shows that Srebp promotes cell cycle progression through a novel pathway resulting in transcriptional activation of several cell cycle genes such as *PCNA* and *cyclin A* in kidney cancer (J. H. Lee et al., 2017). Moreover, these reports suggest that Srebp1 regulates lipid metabolism and cell cycle progression in a separate manner/through separate mechanisms, thus serving as a molecular bridge between lipogenesis and proliferation.

While the role of FA synthesis in proliferation is clearer, the function of Ppar factors is controversially discussed. Thus, proliferative and antiproliferative, proapoptotic and antiapoptotic effects have been described for the different Ppar isoforms in different cell types, including intestinal cells (Beyaz et al., 2016; Bünger et al., 2007; Feige, Gelman, Michalik, Desvergne, & Wahli, 2006).

However, to provide a valid mechanistic link between the enhanced Pparα/γ and FA synthesis pathway activation and ISC and progenitor hyperproliferation, inhibitor experiments have to be accomplished in future. These studies will be needed to examine if a combined inhibition of Pparα/γ and FA synthesis pathways will also have beneficial effects on obesity-associated risk of GI cancer and enteroendocrine control.

5.1.3 HFD affects EE lineage formation and function – contribution to the metabolic disorder

Metabolic disorders, such as obesity and T2D, are associated with defects in the EE system, however, underlying mechanisms are not yet fully understood (Gribble & Reimann, 2016; K.-S. Kim et al., 2018). Current therapies for T2D and obesity harness the incretin effect, hence, long-acting GLP-1 analogues and inhibitors of GLP-1 degradation (DPP4 inhibitors) are widely prescribed due to a range of beneficial effects over other conventional antidiabetic agents (Nauck & Meier, 2016). However, bariatric surgery, remains the only effective treatment option to achieve a sustained remission of insulin-dependent diabetes to date (Hutch & Sandoval, 2017; Rubino et al., 2010; Seeley et al., 2015).

EECs are the major sensors of nutrients and critical regulators of the systemic metabolism along the gut-brain-pancreatic axis. The multifaceted heterogeneity of the EEC lineage makes it difficult to study the mechanisms underlying the EE dysfunction and, on the other hand, those of the adaptation after the bariatric surgery. While certain aspects of the EE lineage specification in homeostasis have been revealed, it is still unclear, how extrinsic factors, such as diet, affect EE lineage formation and how this contributes to the development of the metabolic disorder (Gribble & Reimann, 2016; Worthington et al., 2018).

This work is, to our knowledge, the first single-cell study of the EE lineage in a mouse model of HFD-induced pre-diabetes. Novel insights presented here may facilitate the design of new EEC-based therapies, given that already a number of preclinical trials advise co-targeting of multiple gut hormone receptors for improved T2D therapy outcome (Gribble & Reimann, 2017). In summary, to elucidate the impact of HFD on the EE lineage allocation, we used an enrichment strategy based on FVF reporter expression in secretory cells to obtain a high-resolution image of the EEC lineage and to sufficiently cover rare EEC subtypes. We profiled in total 2,865 EE lineage cells providing the most comprehensive record of the EEC lineage in homeostasis and in metabolic disorder to date. We recovered distinct mature EEC subsets, to a large part correspondent with the previously published EEC classification by Haber et al., and identified novel differentiation routes via $Arx^+/Isl1^+$ and $Pax4^+$ EE progenitors to mature EEC subsets (Haber et al., 2017). Our results demonstrate that the HFD alters proportions of specific EEC subsets, including early progenitors and mature cells, accompanied by disturbances in systemic gut hormone levels. Further, we identify marker genes specific to distinct EE progenitors or mature EEC subsets or labelling a lineage branch. However, whether these are also involved in EEC subtype specification, has to be addressed by additional experiments.

5.1.3.1 Thoughts on the development of the L-cell dysfunction and impaired incretin effect in obesity and T2D

The impaired incretin effect and reduced levels of circulating Glp-1 are hallmarks of T2D (Ahrén, 2013; Meier & Nauck, 2006). To date, conflicting findings have been presented on obesity-associated changes in L-cell abundance and Glp-1 secretion in mouse models and humans (Aranias et al., 2015; Baldassano et al., 2013; Richards et al., 2016; Wölnerhanssen et al., 2017). In our scRNAseq dataset, *Gcg*$^+$ cells were found in two EEC clusters, the SILA and SILP cells. While the relative numbers of SILP cells, reported to be more abundant distally, were not changed, the proportion of proximally enriched SILA cells, by contrast, was increased on HFD (Haber et al., 2017). However, when analysing Glp-1$^+$ EEC numbers in the ileum (in tissue sections), their predominant location in the small intestine based on previous reports, we did not find any changes under HFD conditions (Gribble & Reimann, 2016; Haber et al., 2017). It remains open, whether the numbers of duodenal Glp-1$^+$ EECs are affected differently on HFD. It is possible, since proportions of *Gcg*$^+$ SILA cells, more abundant in the proximal (Haber et al., 2017), are higher on HFD, in line with increased numbers of Ghrl$^+$ EECs in tissue sections.

In concordance with our findings, several research groups observed increased basal levels of Glp-1 in HFD-fed, the *ob*/*ob* mice and in severely obese humans (Aranias et al., 2015; Baldassano et al., 2013; Richards et al., 2016). By contrast, findings on the numbers of L-cells are more inconsistent between the studies. Thus, in line with our results, Richards et al. observed no changes in the numbers of SI Glp-1$^+$ cells on HFD, however, detected gene expression disturbances associated with nutrient responsiveness, but not in *Gcg* levels, indicating impaired L-cell function. Moreover, L-cell responsiveness to specific stimuli was impaired *in vitro*. In our HFD-derived SILA and SILP subsets, we detected neither changes in *Gcg* expression, nor any other significant transcriptional alterations, possibly due to the relatively limited sensitivity of the scRNAseq compared to bulk sequencing. By contrast, Aranias and colleagues observed increased numbers of L-cells in the jejunum and ileum, elevated preglucagon expression and increase in Glp-1 secretion in HFD-fed mice and in severely obese subjects (Aranias et al., 2015). Given that no related changes were observed in *ob*/*ob* mice, they postulated that detected disturbances result from a fat-rich diet, and not from obesity *per se*.

Thus, both studies provide evidence for a possible adaptive response to a sustained overstimulation of L-cells by nutrients and an acquired decreased responsiveness to specific stimuli when chronically overeating. This may result in a compensatory Glp-1 overproduction to increase insulin secretion and counteract insulin resistance in a pre-diabetic stage, however, ultimately leading to the exhaustion of both compensatory effects and diabetes. To gain more mechanistic insights and to confirm whether these findings apply to our model, we should combine single-cell transcriptional profiling with more sensitive approaches and functional validation in the future.

5.1.3.2 Reg4$^+$ EC cells - a novel subset of serotonin-producing cells and its relevance for the pathogenesis of diet-induced obesity and diabetes

In concordance with findings by Haber et al., we could allocate two clusters of EC cells, one of them a novel functionally uncharacterised subset expressing high levels of *Reg4*, a largely uncharacterised gene (Haber et al., 2017). *Reg4*$^+$ EECs were first described by Grün et al., however, *Reg4* was presumed to be a general marker for mature EECs (Grün et al., 2015). Intriguingly, given the existence of these two related EC cell clusters, we observed a drastic reduction of cell numbers exclusively in the Reg4$^+$ EC cluster under HFD conditions. Consistently, the frequencies of 5-HT$^+$ EEC in SI crypts were markedly lower and levels of the circulating serotonin were significantly reduced under HFD conditions, constituting early changes in the EE axis in pre-diabetes. As both, the abundance of Reg4$^+$ EC cells and serotonin levels in the blood, were altered after HFD treatment, it is of great importance to understand how these disturbances contribute to the pathogenesis of obesity and T2D.

Reg4$^+$ EC cell cluster seems to be different from the "classical" EC cells, clearly distinguished by a set of specific markers described in our study, such as *Reg4*, *Ucn3*, *Afp*, *Slc18a2 etc*., and a different distribution

along the length of the small intestine (Gribble & Reimann, 2016; Haber et al., 2017). While 5-HT$^+$ EECs are equally dispersed throughout the intestine, Reg4$^+$ cells are significantly enriched in the duodenum, indicating deviant functions or responsiveness to different stimuli (Haber et al., 2017).

While *Reg4* is less well characterised, expression of other hormonal products in Reg4$^+$ EC cells, such as urocortin 3 (*Ucn3*), overlaps with pancreatic β-cells. Alterations in pancreatic Ucn3 have been associated with early pathogenesis of T2D (Weir & Bonner-Weir, 2004). Expression of *Ucn3* has been also observed in colonic EC cells, but it was not shown to be expressed in the small intestine, and its physiological effects are not known (Saruta et al., 2005). Ucn3, a neuropeptide hormone and a marker of functional β- and α-cell maturation, has been suggested to regulate feeding behaviour and insulin secretion in response to blood glucose levels (Benner et al., 2014; Jamieson et al., 2011; Y. Kuperman et al., 2010; Yael Kuperman & Chen, 2008; van der Meulen & Huising, 2014). Patients with T2D exhibit markedly reduced levels of Ucn3 in β-cells emerging at the compensatory stage, prior to the reduction in insulin secretion (Blum et al., 2014; Weir & Bonner-Weir, 2004). This leads to overproduction of insulin to compensate for insulin resistance (Blum et al., 2014). Moreover, a repeated *i.p*. administration of Ucn3 reduced food intake and had anti-obesity effects in a HFD-fed mouse model (Tanaka et al., 2009; Ushikai, Asakawa, Sakoguchi, Tanaka, & Inui, 2011). To draw parallels to our findings, potential reduction in intestinal Ucn3 levels due to decreased numbers of Reg4$^+$ EC cells could also be implicated in T2D pathogenesis.

Further, it remains an open question, how the reduced levels of the peripheral serotonin, observed in HFD-fed mice in our study, contribute to the establishment of the metabolic disorder. Although most of body's serotonin is produced by the intestinal EC cells in a Tph1-dependent manner, its physiological role remains enigmatic, as opposed to the Tph2-derived serotonin in the enteric and central nervous systems (Bornstein, 2012). The belief that serotonin from EC cells is responsible for GI functions such as gastric emptying, intestinal transit and motility, has been disproven due to the evidence from several studies, including the report that *Tph1-/-* mice, in contrast to *Tph2-/-* animals, exhibit normal intestinal function or health (Z. Li et al., 2011). On the other hand, Paulmann et al. demonstrated that *Tph1-/-* mice were diabetic because lack of intracellular serotonin in β-cells led to impaired insulin release (Paulmann et al., 2009). Moreover, they suggested that extracellular serotonin, by contrast, had an inhibitory effect on the insulin secretion. According to these findings, there could be a mechanistic link between the HFD-induced reduction in serotonin secretion from intestinal EC cells, as indicated by our results, and the hypersecretion of insulin during the compensatory pre-diabetic stage. Further studies have shown, though with conflicting results, a relation between the peripheral serotonin levels and changes in glucose handling, *e.g*. due to the role of serotonin in glucose uptake into tissues, hepatic glucose metabolism or insulin secretion from pancreas (Paulmann et al., 2009; Sugimoto et al., 1990; Watanabe et al., 2010; Yamada et al., 1989). Another physiologic role of serotonin has been described by Watanabe and colleagues, who demonstrated that serotonin can promote lipid metabolism through regulation of bile acid levels in the blood.

Altogether, the physiological role of intestinal serotonin from EC cells remains unclear and how reduced levels of peripheral serotonin and reduction in Reg4$^+$ EC cell numbers relate to obesity and diabetes requires further study.

5.1.3.3 Open questions

Altogether, there is a number of open questions left with regard to HFD-induced alterations in the EE system.

Firstly, it is striking, that exclusively the numbers of Reg4$^+$ EC cells were reduced in SI crypts under HFD conditions. Since both EC cell subsets are derived from a common Pax4$^+$ EE progenitor, which is majorly not affected by HFD, and we did not detect relevant significant alterations in gene signatures in the progenitor cluster or in these EEC subsets, the underlying mechanisms remain unclear. Additional analysis is also required to elucidate whether lower serotonin levels in HFD-fed animals are directly attributable to the reduced numbers of Reg4$^+$ EC cells or if they emerge due to different mechanisms.

Secondly, it is intriguing that the HFD-induced increase in Ngn3$^+$ progenitor numbers, based on enhanced proliferation, did not result in the overall rise of the EEC numbers. In contrast, distinct EEC subsets were affected in different ways by HFD such as, *e.g*. the numbers of SILA cells were increased and proportions of Reg4$^+$ EC cell were lower. How is the subset specification regulated in a diet-dependent manner along the maturation axes from different progenitors to the mature EEC subtypes?

Finally, the recent findings by Beumer et al. have revealed additional level of complexity to the EEC lineage, demonstrating that EECs can switch hormone co-expression patterns upon maturation and migration along the crypt-villus axis (Beumer et al., 2018). Thus, it has to be taken into account, that HFD-induced changes observed in the crypt compartment in both, subtype composition and gene expression, may be different in the villus or *vice versa*. For a solid conclusion both compartments should be assessed.

These complex questions require further investigation and could be addressed by follow-up studies.

5.1.4 Conclusion and future directions

Excess calorie intake from fat- and sugar-rich diets leads to obesity often associated with life-threatening conditions such as colorectal cancer and T2D. Diabetes remains an incurable metabolic disease and is poorly controlled in a vast majority.

In this work, we provide novel insights into HFD-induced disturbances of the intestinal homeostasis in the early pathogenesis of T2D in a mouse model. Our findings add to a deeper understanding of the molecular mechanisms underlying the metabolic syndrome and life-threatening co-morbidities, such as GI cancer, and might help to facilitate the development of novel therapeutic approaches and improvements to current options for obesity and T2D treatment. We demonstrate the functional relevance of our single-cell genomics data by combining different experimental approaches, including protein signalling analysis, metabolite profiling, genetic lineage tracing *etc*., and utilise thereby state-of the art techniques. Recent advances in single-cell transcriptomics have provided tools which enable to dissect cell-type specific molecular responses and signalling cues, to distinguish changes in molecular programmes from shifts in cell frequencies and allocate changes in mature populations as opposed to those in distinct differentiation stages of progenitors.

In summary, we reveal a HFD-induced dysbalance in the ISC and progenitor proliferation and ISC lineage commitment. We suggest that altered molecular cues, involving deregulation of expression of Ppar factors and increased activation of the Srebp1-mediated intestinal lipogenesis, are molecular links to HFD-induced hyperproliferation and altered lineage allocation from ISCs. Moreover, we reveal additional metabolic and proliferative signalling pathways deregulated in SI crypts under HFD conditions, including overactive Igf1r/Ir/Akt axis and diminished β-catenin pathway activation. Given the complex cell lineage networks in the crypt compartment, with different metabolic and functional identities, it is very likely that observed signalling alterations ultimately contribute together to the establishment of the intestinal metabolic disorder. And just as important, we find changed EEC subtype allocation, including reduced proportions of Reg4$^+$ EC cells, a novel subtype of serotonin-producing cells, and disturbances in the levels of circulating serotonin and other gut hormones in mice fed a HFD.

This thesis focuses on the impact of HFD on the ISC function and intestinal epithelial lineage homeostasis as well as related mechanistic cues. Accordingly, this work covers only certain aspects of the complex intestinal pathomechanisms associated with obesity and T2D. However, a number of other important factors should be considered as co-actors in the pathomechanistic network, such as *e.g*. gut microbiota and immune system. Both are in close interplay with the intestinal epithelium and have been shown to modulate functions of ISCs and the EE system, thus, ultimately contributing to tissue homeostasis (Biton et al., 2018; Koh, De Vadder, Kovatcheva-Datchary, & Bäckhed, 2016; Neuman, Debelius, Knight, & Koren, 2015). Several reports have demonstrated that diet-induced aberrant gut microbiota influence ISCs promoting intestinal tumour progression (Schulze & Harris, 2012). Moreover, microbiota-derived short-chain fatty acids have been reported to modulate L-cell differentiation and

secretion of Glp-1, PYY, serotonin and, presumably, also of GIP, ghrelin and CCK (Fukui, Xu, & Miwa, 2018; Hildebrandt et al., 2009; Neuman et al., 2015; Tolhurst et al., 2012). Regarding the interactions of ISCs with the immune cells, a recent elegant study by Biton and colleagues showed that T helper cells can modulate ISC self-renewal and commitment to different lineages (Biton et al., 2018).

A number of additional unanswered questions remains.

Firstly, to link the deregulation of Ppar and FA synthesis pathways to the emergence of hyperproliferation and altered lineage allocation from ISCs, it would be beneficial to record the earliest emergence and coincidence of these molecular alterations in SI crypts under HFD conditions. A time-resolved study would substantiate these mechanistic insights.

Second, while it is mostly not known, whether the EE dysfunction in metabolic disorders is, primarily, due to the defects in mature EECs or emerges during the EEC formation, we were able to unveil that at least some aspects can be attributed to the disturbances in early lineage formation. However, we cannot profoundly explain observed disturbances in the EEC subset allocation, such as increase in SILA cell and reduction in Reg4^{+} EC cell proportions, given only minor detected changes in transcriptional programmes of the EECs under HFD conditions. A deeper and more sensitive analysis would be required to explore the pathomechanisms in both, the mature villous cells and undifferentiated progenitors in the crypt, in more detail. Moreover, it is crucial to gain deeper insights into the function of the novel Reg4^{+} EC cells and relate changes in systemic serotonin levels to the pathogenesis of obesity and T2D, to provide potential targets for therapeutic interventions.

And finally, it remains open, whether an inhibition of the excessive activation of Srebp1-mediated lipogenesis and Pparα/γ signalling will achieve significant effects to reduce HFD-induced hyperproliferation in the crypt, restore normal lineage relations and improve the EE control. This is of great significance, because targeting these pathways in the ISCs and intestinal progenitors might be a novel treatment approach for combination therapies with the incretin-based agents and as a non-invasive option to bariatric surgery. Moreover, pharmacologic inhibitors of Srebp activation/pathway are being vividly discussed as anti-obesity and anti-diabetes therapeutics. According to our findings and related scientific reports, it seems that Srebp1 does not only regulate lipogenesis in SI crypts, but, moreover, promotes ISC and progenitor proliferation. Thus, Srebp pathway inhibitors could be beneficial not only for the lipid metabolism-related intestinal pathology and the effects on other organs such as liver, to decrease the steatosis, but could also lower the risk of obesity-associated GI cancers. This is also important, because many agents used in the treatment of diabetes, including insulin glargine, pioglitazone (a selective Pparγ agonist), incretin-based therapies (Glp-1r agonists and DPP4 inhibitors), and sulfonylureas, have been associated with increased cancer risk and clinicians often have to manage patients with both diabetes and cancer (Garg, Maurer, Reed, & Selagamsetty, 2014; Klil-Drori et al., 2017; Wu, Zhu, Prokop, & Murad, 2015).

5.2 Fltp-Venus fusion reporter mouse line - benefits and limitations for studying localisation and function of Fltp

Until now, Fltp function has been addressed in the ciliated cells of the airway epithelium and the inner ear, where Fltp is involved in basal body transport and positioning during PCP acquisition (Gegg et al., 2014). Additionally, Fltp-H2B-Venus reporter (FVR) expression has been found at high levels in the endocrine cells of the pancreas, and in the EECs and Paneth cells in the small intestine of the *Fltp^{ZV}* mouse model (Bader et al., 2016; Boettcher et al., in revision). In the pancreas, FVR acts as a marker subdividing endocrine cells into two subsets, particularly distinguishing two functionally heterogeneous β-cell populations (Bader et al., 2016). In the intestine, *Fltp* expression labels Wnt/PCP-

activated ISCs, which are committed to the EEC or Paneth cell fate (Boettcher et al., in revision). However, the exact function of Fltp in the pancreas and intestine remains elusive, in part, due to the lack of appropriate tools. Specifically, the FVR does not reflect the actual cellular localisation of the endogenous Fltp protein, because Fltp is knocked out and replaced by a nuclear localized fluorescent reporter in the *Fltp^{ZV}* mouse model (Gegg et al., 2014).

To facilitate the analysis of the Fltp function, we generated the Fltp-Venus fusion reporter mouse line. Fltp-Venus fusion reporter accurately reflected the distribution of the endogenous Fltp protein in the airway epithelia *in vivo* and *in vitro*. However, we could not confirm Fltp protein expression in the pancreatic islets and SI crypts under normal conditions using conventional experimental approaches, such as immunostainings, live-cell imaging, analysis by flow cytometry or protein pull-down assays. This is explainable when taking into account several aspects. First, recent results demonstrate that *Fltp* expression in a subset of lineage-primed Lgr5$^+$ ISCs is rather low and transient in the *Fltp^{ZV}* mouse model (Boettcher et al., in revision). Second, whereas *Fltp* mRNA expression is low or absent in ChgA$^+$ EECs or Paneth cells, respectively, the FVR activity reliably labels more than 95 % of all Paneth and ChgA$^+$ EECs (Boettcher et al., in revision). This indicates that the FVR protein is more stable than the *Fltp* transcript, and FVR$^+$ cells rather more accurately represent the lineage of *Fltp*$^+$ cells than the actual *Fltp* expressing cells. In support, H2B-tagged proteins have been shown to exhibit a higher stability compared to endogenous proteins and have been, therefore, used to mark label-retaining cells, *e.g.* in the intestine or the hematopoietic tissue (Foudi et al., 2009; Hughes et al., 2012; N. Li et al., 2016). Finally, in contrast to the Fltp-Venus fusion mouse line, a prefect *Kozak* sequence has been introduced upstream of the H2B-Venus reporter in the *Fltp^{ZV}* targeting construct (Gegg et al., 2014). This enables a more efficient initiation of protein translation (Acevedo, Hoermann, Schlimbach, & Teleman, 2018; Kozak, 1984, 2002), and, assumingly, increases the FVR protein amount and label intensity compared with the actual levels of the endogenous Fltp protein. In conclusion, given the evidence that *Fltp* is expressed transiently and at low levels in a relatively rare population of ISCs and EECs, would require different approaches for the analysis. Thus, conditions which increase the frequency of the rare event of lineage commitment of *Fltp*$^+$ ISCs and/or increasing *Fltp* transcript levels (by *e.g.* specific Wnt ligands or Notch signalling inhibitors, (Boettcher et al., in revision)) could be considered for future analyses. For studying the role of Fltp in the pancreas, specifically, in β-cells, conditions, which enhance β-cell proliferation, such as a HFD-feeding, postnatal β-cell expansion or pregnancy, could be tested. Additionally, introducing a better *Kozak* sequence into the Fltp-Venus fusion targeting vector could be another possibility to test for the generation of a new reporter mouse line.

Despite the current limitations of the Fltp-Venus fusion mouse line for the analysis of the role of Fltp in the intestine and pancreas, it provides major benefits for studying ciliogenesis in the airway epithelium and can serve as a reliable reporter of multiciliated lung cells and, potentially, of their progenitors. Using immunostainings, we confirmed an accurate overlap of the Fltp-Venus reporter and the endogenous Fltp protein distribution patterns in the airway epithelia *in vivo* and *in vitro*. Interestingly, Fltp-Venus fusion reporter expression in ALI cultures of mTECs distinguished cells with high or low reporter intensity, which correlated with early onset of basal body amplification in committed progenitors or with the progressive ciliation in multiciliated cells, respectively. Thus, Fltp-Venus fusion reporter mouse line is a valuable tool enabling isolation and study of different stages of ciliogenesis as well as mature ciliated cells *in vitro*. Whether the same applies *in vivo* has to be analysed in more depth. Our preliminary data, however, provide evidence for the existence of putative FltpV$^+$ airway stem cells expressing the basal cell marker *Trp63*, which may be committed to the ciliated cell-lineage. Moreover, previous work from our group (Moritz Gegg, doctoral thesis, https://mediatum.ub.tum.de/doc/1114671/document.pdf; last change 10.11.2014) identified non-ciliated basal cells in the adult lung, which co-express FVR and the basal cell marker T1α, and may be putative progenitors for FVR$^+$ multiciliated airway cells (Jason R. Rock & Hogan, 2011). These findings resemble the intestinal *Fltp*$^+$ ISCs, which directly allocate to the Paneth cell and EEC lineage (Boettcher et al., in revision). However, whether Fltp$^+$ stem cells in the lung exist and whether they directly give rise to ciliated cells has to be analysed in more depth. So far, stem cell heterogeneity in the lung is controversial

(F. Li, He, Wei, Cho, & Liu, 2015; J. R. Rock et al., 2009; Jason R. Rock & Hogan, 2011). Thus, the Fltp-Venus fusion mouse line may give more insights into this issue.

Together, the Fltp-Venus fusion reporter mouse line is a valuable tool which enables to study ciliogenesis and allows for multiple applications in cilia biology, in particular, in the airway epithelium, *in vitro* and *in vivo*. More effort should be invested to characterise Fltp-Venus fusion reporter expression in the intestinal cells and in the pancreatic islets. This will facilitate analysis of Fltp function in these tissues and shed more light on the mechanisms of the ISC heterogeneity and lineage priming in the intestine as well as mechanisms underlying β-cell heterogeneity in the pancreas.

6 Material

6.1 Equipment

Agarose gel chamber	Midi 450, Neolab, Heidelberg
Agilent 2100 Bioanalyzer	Agilent Technologies
Balances	ScoutTM Pro, OHAUS
Biorep perfusion system	Biorep Technologies, Miami USA
Cell counter	TC20™ Automated cell counter, Biorad, Heidelberg
Cell culture hood	BDK, Luft-und Reinraumtechnik GmbH, Sonnenbühl-Genkingen
Centrifuges	5417R, 5430C, 5804 R, Eppendorf, Hamburg Microcentrifuge, Roth, Karlsruhe, Micro 220, Hettich, Tuttlingen Universal 320R, Hettich, Tuttlingen, 6767, Corning
Chromium controller (scRNAseq)	10x Genomics, Pleasanton, CA, USA
Cryostat	Ag Protect, Leica, Wetzlar
Cytospin equipment	Cyto chambers, filter, rotor, Hettich, Tuttlingen
Developing machine	AGFA Curix 60 developing machine, AGFA HealthCare GmbH, Bonn
Electroporation system	BioRad Gene Pulser Xcell, BioRad Laboratories, München
ELISA reader	PHERAastar FS, BMG Labtech GmbH, Ottenberg Varioskan LUX, Thermo Scientific, Waltham
FAC-sorter	BD FACSAria III, Becton and Dickinson and Company, Franklin Lakes
Film cassettes	Hypercassette, Amersham, Munich
Freezer	-20°C Medline, premium nofrost, Liebherr, Ochsenhausen -80°C, Thermo Scientific, Waltham
Fridge	4°C comfort, Liebherr, Ochsenhausen
Gel documentation system	UVsolo TS Imaging System, Biometra, Goettingen
Glucometer	Freestyle freedom lite, Abbot Diabetes Care Oxon, UK
Incubation systems/ovens	Thermomixer comfort, Thermomixer 5436, Eppendorf, Hamburg Oven, Thermo Scientific, Waltham
Incubators	BBD6220, Thermo Scientific, Waltham Inkubator C16, Labortect, Rosdorf KBF, Binder GmbH, Tuttlingen-Möhringen Shake'n'Stack, ThermoHybaid, Thermo Fisher Scientific Inc., Waltham
Microscopes	Axiovert 200 M, Carl Zeiss AG, Göttingen MS5, MZ75, Leica Microsystems GmbH, Wetzlar TCS SP5 and Cube (heating), Brick (CO_2) (Leica Microsystems GmbH, Wetzlar Zeiss AXIO Scope A1 microscope, Carl Zeiss AG, Germany M80 and Dissection light, Leica, Wetzlar
Microwave	700 W, Severin Elektrogeräte GmbH, Sundern
N_2 tank	Biostore systems, Cryo Anlagenbau GmbH, Wilnsdorf
NMR	EchoMRI LLC, Houston, TX, USA
Odyssey Imaging Systems	LI-COR Biosciences, Lincoln USA
Paraffin embedding station	EG1160, Leica Mikrosysteme Vertrieb GmbH, Wetzlar

PCR machines	Personal Thermocycler, Professional Trio Thermocycler, Biometra, Goettingen PXE0.2 Thermo Cycler, Thermo Fisher Scientific Inc. Waltham
pH meter	FiveEasy™ pH, Mettler-Toledo International Inc., Greifensee, Switzerland
Photometer	NanoDrop 2000c, Thermo Fisher Scientific, Waltham HERAstar FS, BMG LABTECH GmbH, Ortenberg
Pipettboy	Accu-jet® pro, Brand GmbH, Wertheim
Pipettes	1000 µl / 100 µl / 10 µl Eppendorf Research, Eppendorf, Hamburg
Plastic ware	VITLAB GmbH, Großostheim
Polyacrylamid gel chamber	Mini Trans-Blot® Cell, Biorad, Heidelberg
Power supply (agarose gels)	Power Source 300V, VWR International, Darmstadt
Thermocycler:	
ViiA7 Real-time PCR system;	Life technologies, Frankfurt;
Biomark HD and IFC Controller	Fluidigm, CA, USA
Radiation monitor	Berthold LB122, BERTHOLD TECHNOLOGIES GmbH & Co. KG, Bad Wildbach
Roller/Mixer	VSR 23, VWR International, Darmstadt, Shaker DOS-10L, Neolab, Heidelberg, RMS (I), Rocker 247, Everlast
Sonificator	Sonoplus HD2070, Bandelin electronic GmbH&Co.KG, Berlin Elmasonic, UW 2070, Bandelin electronics, Berlin
Sterile hoods	MSC Advantage, Thermo Scientific, Waltham
Stirrer	D-6011, Neolab, Heidelberg
Timer	Roth, Karlsruhe
Tissue Homogenizer	Ultra Turrax T25, IKA
Ultrasonic bath	Ultrasonic cleaner, VWR International, Darmstadt
Vortexer	VWR international GmbH, Darmstadt
Water bath	Memmert SWB25, Thermo Fisher Scientific Inc., Langenselbold
Water purification system	Millipore Q-POD, 0.22 µl filter, Merck Chemicals GmbH, Schwalbach
Western blot semi-dry	Trans-Blot® SD, Semi Dry Transfer cell, Mini-PROTEAN® Tetra Cell, Trans-Blot® Turbo™ Blotting System, Biorad, Heidelberg

6.2 Consumables

50 ml/ 15 ml tubes	Becton and Dickinson and Company, Franklin Lakes
15 cm/ 10 cm/ 6 cm dishes	Nunc, Thermo Scientific Fisher, Waltham
6-well/ 12-well/ 24-well/48-well / 96-well plates	Nunc (flat-bottom/conical), Thermo Scientific Fisher, Waltham
96- and 384-Well plates	Thermo Scientific
10 cm bacterial plates	BD FalconTM, Becton Dickinson GmbH, Franklin Lakes
8-well chambers	Uncoated and coated 8-well imaging plates, Ibidi, Planegg
2 ml/ 1.5 ml / 0.2 ml tubes	Safe-lock reaction tubes, Eppendorf, Hamburg
96.96 Microfluidic chip	Fluidigm
50ml/ 25ml/ 10ml/5ml/ 2ml/ 1ml plastic pipettes	Greiner Bio-One GmbH, Frickenhausen
Adhesive covers	Optical adhesive covers, Life Technologies, Frankfurt

Affymetrix Mouse Gene 1.0 ST arrays	Applied Biosystems
Blotting paper	Whatman paper, GE Healthcare Buchler GmbH & Co. KG, München
Cell scraper	Sarstedt, Nümbrecht
Cell strainer	Nylon cell stainer 70 μm, Falcon, Fisher Scientific, Waltham
Clamp (pancreas)	Bulldog SerrefinE—Straight 35 mm, Fine Science Tools GmbH, Heidelberg
Counting chambers	Neubauer, LO – Laboroptik GmbH, Friedrichsdorf
Cryotubes	Sarstedt, Kleinstadt
Cover slips	VWR International, Darmstadt
Embedding molds	Peel-a-way embedding molds, S-2, Sigma Aldrich, Hamburg
FACS tubes	5 ml polystyrene round bottom tube with cell strainer cap and 5 ml polypropene round bottom tube, Falcon, Fisher Scientific, Waltham
Films	Hyperfilm ECL, GE Healthcare Buchler GmbH & Co. KG, München, CEA, Rö.Blaufilm, RP new, Christiansen und Linhardt GmbH, München
Forceps	Dumount Inox, 11251-, 11252-20, Fine Science Tools GmbH, Heidelberg
Freezing boxes	CoolCell® Alcohol-Free, BioCision LLC, USA, CA Freezing container, Nalgene®, Sigma-Aldrich Chemie Gmbh, München
Glass slides	Menzel Gläser superfrost plus, Thermo Scientific, Waltham
Glassware	Schott-Duran, Schott, Mainz
Hybridisation tubes	Hybridizer HB 100 ThermoHybaid, Thermo Fisher Scientific Inc., Waltham
Needles	Sterican 27G ½ ``, Sterican 30G ½ ``, B.Braun, Puchheim
Nitrocellulose membrane	GE Healthcare Buchler GmbH & Co. KG, München
Nitrocellulose membrane, Hybond-N+	GE Healthcare Buchler GmbH & Co. KG, München
Nylon cell strainer 40 and 70 μm	BD
Optical adhesive covers	Applied Biosystems
Parafilm	Pechiney Plastic Packaging
Phase Lock GelTM, 2 ml tubes	5 PRIME GmbH
PVDF membrane	Biorad, Munich
qPCR 96-well plates	MicroAmp Fast optcal 96-well reaction plate, Life Technologies, Frankfurt
Scalpels	Sterile, B.Braun, Tuttlingen
Scissors	14088-10, Fine Science Tools GmbH, Heidelberg
Spacer	Secure-Sela, 9mm 0.12 mm deep, Life Technologies, Frankfurt
Syringes	Omnifix 30 ml / 3 ml; Omnican 50, B. Braun Melsungen AG, Melsungen 30G1/2-G needle, B. Braun Melsungen AG, Melsungen
Syringe filter	Millex-GP, Filter unit fast flow and low binding 0.22 μm

Pasteur pipettes, plastic	Roth, Karlsruhe
Pasteur pipettes, glass	15cm/23cm, LABOR-BRAND, Gießen; Hirschmann Laborgeräte GmbH & Co. KG, Eberstadt
PCR Tubes	Eppendorf, Hamburg

6.3 Chemicals

Chemicals were purchased from Carl Roth GmbH & Co. KG, Karlsruhe; Merck KGaA, Darmstadt; Sigma-Aldrich GmbH, Hamburg if not otherwise stated.

A	7-AAD (eBioscience, #00-6993-50)
	Acetic acid
	Acrylamide/bisacrylamide (Rotiphorese)
	Agarose (Biozym Scientific)
	Ammoniumpersulfat (APS)
	L-Arginine
B	BCA
	Bradford reagent
	5-bromo-2-deoxyuridine (BrdU)
	Bromophenol blue
C	Calcium chloride
	Chloroform, 99+%
D	DAPI
	Developer G135 A/B (AGFA, Bonn)
	Diethylpyrocarbonate (DEPC), approx. 97%
	Dimethylsulfoxide (DMSO), >99,9%
	Dithiothreitol (DTT)
	Dithizone
	DNAZap (Thermo Fisher Scientific, Waltham)
E	Ethylenediaminetetraacetic acid (EDTA)
	5-Ethynyl-2-deoxyuridine (EdU) (Life Technologies, Frankfurt, #A10044)
	Ethanol, 96%
	Ethidium bromide
F	Ficoll
	Formaldehyde
	Formamide
G	Glucose (D+)
	Glutaraldehyde
	Glycerol
	Glycin
H	Hydrogen chloride (HCl)
I	Isopropanol, 100%
	Igepal
L	LiCl
M	Magnesium chloride
	Methanol, 100%
	Magnesium sulphate (MgSO4)
	Milk powder (Becton Dickinson GmbH, Heidelberg)
	3-(N-morpholino)propanesulfonic acid (MOPS)

N	Natrium citrate
	Nitrogen(l) (Linde AG, München)
	Nonylphenoxypolyethoxyethanol (NP-40)
O	Orange G
P	Paraformaldehyde
	Polyacrylamide
	Polyvinyl-alcohol
	Polyvinylpyrrolidone
	PonceauS
	Potassium chloride (KCl)
	Potassium hydrogenphosphate (KH_2PO_4)
	ProLong Gold antifade reagent (Invitrogen, Carlsbad)
Q	QIAzol lysis reagent (Quiagen GmbH, Hilden, #79306)
R	Rapid fixer G356 (AGFA, Bonn)
	RNaseZAP
S	Sodium chloride (NaCl)
	Sodium deoxycholate ($C_{24}H_{39}O_4Na$)
	Sodium dodecyl sulphate (SDS)
	Sodium hydrogenic phosphate (Na_2HPO_4)
	Sodium hydroxide
	Sodium tetraborate ($Na_2B_4O_7$)
	Superscript II (Fermentas GmbH, St. Leon-Rot)
T	Tamoxifen (Sigma Aldrich, #T5648)
	TEMED
	Tris(hydroxymethyl)aminomethane
	Triton X-100
	Tween-20
X	Xylene

6.4 Kits, mastermixes, reagents for gene expression studies

AccuBlue™ High Sensitivity dsDNA Quantitation Kits (Biotium, Fremont USA)

Agilent RNA 6000 Pico kit (Agilent Technologies)

BCA Protein Assay Kit (Thermo Fisher Scientific, Waltham)

Click-IT EDU Alexa Fluor 647 (#C10340, Life Technologies, Freiburg)

Dynamo Color Flash SYBR Green qPCR kit (Life Technologies, Frankfurt)

ECL Clarity Western ECL substrate kit (Biorad, Munich)

Encore Biotin Module (Nugen)

Fast EvaGreen Supermix with low ROX (Biorad, Munich)

miRneasy Micro Kit (Qiagen Holding, Hilden, #217084)

miRNeasy Mini Kit (50) (Quiagen GmbH, Hilden)

Mouse PYY ELISA kit (#81501, Chrystal Chem, Downers Grove USA)

Mouse total Glp-1 ELISA (#81508, Crystal Chem, USA)

Mouse total Ghrelin ELISA (#EZRGRT-91K, Millipore-Merck)

NE-PER™ Nuclear and Cytoplasmic Extraction Reagents kit (Thermo Fisher Scientific, #78833) Pierce

Ovation® PicoSL WTA SystemV2 (Nugen)

PCR purification kit (Qiagen)

QIAquick PCR Purification Kit (Qiagen Holding, Hilden)

QIAquick Gel Extraction Kit (Qiagen Holding, Hilden)
RNase-Free DNase Set (Qiagen, #79254)
Serotonin ELISA kit (#ADI-900-175, Enzo)
SuperScript Vilo cDNA synthesis kit (Life Technologies, #11754)
SuperSignal West femto maximum sensitivity substrate (Life Technologies, Frankfurt)
TaqMan Fast Advanced Master Mix (Life Technologies, Frankfurt)
TaqMan Fast Advanced Master Mix (Life Technologies, #4444557)
TaqMan Universal Master Mix II, no UNG (Life Technologies, #4440040)
Ultrasensitive mouse insulin ELISA kit (#90080, Crystal chem INC., IL, USA)
5x VILO™ reaction mix and 10x SuperScript (Life Technologies, Frankfurt)

mRNA *in situ* hybridisation reagents

Anti-digoxigenin AP-conjugate, Roche Applied Science - Roche Diagnostics, #11093274910
BM Purple AP Substrate, precipitating, Roche Applied Science - Roche Diagnostics, #11442074001
DIG RNA Labeling Mixture, 10x 40 µl, Roche Applied Science - Roche Diagnostics, #11277073910
RNA Polymerase, T3, 1000 U, Roche Applied Science - Roche Diagnostics, #11031163001

Single-cell qRT-PCR

DNA Binding Dye Sample Loading Reagent, 20x (Fluidigm Corporation, CA, USA)
RNA spikes mix (Fluidigm, #100-5582)
SsoFast EvaGreen Supermix with Low ROX (Bio-Rad Laboratories, #172-5210)
SUPERase-In (Ambion, #AM2694)
TaqMan PreAmp Master Mix (Applied Biosystems, #4391128)
5x VILO reaction mix (Invitrogen, #11754-050)
10x SuperScript enzyme mix (Invitrogen, #11754-050)

Single-cell RNAseq

Chromium™ Single cell 3' library and gel bead kit v2 (10X Genomics, #120237)

6.5 Enzymes, inhibitors, ladders, staining reagents and others

Inhibitors

Aprotinin	Sigma, A-1153
Diprotin A	Abcam, 145599
Fatostatin	Sigma-Aldrich, F8932
GW6471	Sigma-Aldrich, G5045
GW9662	Sigma-Aldrich, M6191
Mitomycin C	Sigma-Aldrich, Y0000378
Proteinase inhibitors	Sigma-Aldrich, P8340
Proteinase inhibitors	Sigma-Aldrich GmbH, Seelze, P5726, P0044
RNAse inhibitors	Fermentas GmbH, St. Leon-Rot

Reagents for staining

Antigen Unmasking Solution, citric acid-based	Vector Laboratories, #H-3300
Bovine serum albumin (BSA)	New England Biolabs GmbH, MA, USA
Donkey serum	Millipore, Schwalbach
Eosin Y solution, aqueous	HT110216, Sigma, Hamburg
Haematoxylin solution (Mayer´s)	MHS1, Sigma, Hamburg
Mowiol	Sigma-Aldrich, Co., MO, USA
OCT medium	Leica Microsystems GmbH, Wetzlar
Phalloidin	Abberior, 2-0205-002-5
Xylene mounting medium	Roti® Histokitt, Carl-Roth GmbH, Karlsruhe

Enzymes

Alkaline (antarctic) phosphatase	NEB GmbH, Frankfurt a. M.; M0289
Collagenase P	Roche, Pensberg, 11 213 865 001/11 213 873 001
DNA-Polymerases:	
DNA Polymerase I, Large (Klenow) Fragment	NEB GmbH, Frankfurt a. M., M0210
Taq DNA Polymerase recombinant	Fermentas GmbH, St. Leon-Rot, EP0402
Taq DNA Polymerase	Qiagen, Hilden, 201203
Pfu DNA Polymerase	Stratagene, La Jolla, M7741
Exonuclease I	New England BioLabs, M0293S
Restriction enzymes	NEB GmbH, Frankfurt a. M.; Fermentas GmbH, St. Leon-Rot
Rnase A	Thermo Fisher Scientific, EN0531
T4 DNA ligase	NEB GmbH, Frankfurt a. M., M0202
T4 Polynucleotide Kinase	NEB GmbH, Frankfurt a. M., M0201

Others

ANTI-FLAG® M2 Affinity Agarose Gel	Sigma-Aldrich, A2220
Big Dye/ Big Dye Buffer	Life Technologies, 4337457
DNA ladder	New England BioLabs GmbH, Frankfurt a.M.
dNTPs	Thermo Scientific, St. Leon-Roth
Genotyping/cloning primer	Eurofins
Nuclease-free water	Promega, P119C
Protein ladder	PageRuler Plus Pre-Stained, Life Technologies, Frankfurt
RNA ladder	New England BioLabs GmbH, Frankfurt a.M.
T4 Gene 32 Protein	New England BioLabs, M0300S
10X Taq Buffer w/o $(NH_4)2SO_4$ - $MgCl_2$	Fermentas
Stripping buffer (Western blot)	ThermoFisher Scientific, 21059

6.6 Solutions and reagents for cell culture

Advanced DMEM/F12	Gibco, Invitrogen, 12634028
Ampicillin	Sigma-Aldrich, 10835242001
Bovine serum albumin (BSA)	New England Biolabs GmbH, MA, USA
BPE	Sigma, P1476
B27 supplement (50x)	Life technologies, 12587-010
Cholera toxin	Sigma, C8052
CULTREX	Trevigen, 3700-100-01
DMEM	Gibco, Invitrogen, 10829-018
EGF	Life technologies, PMG8043
ESGRO® (LIF)	Chemicon, Millipore, Schwalbach
FCS (PAA)	Laboratories Gesellschaft GmbH, Pasching, Österreich
FCS (PAN)	Biotech GmbH, Aidenbach
Fungizone	Gibco, 15290018
2 mM GlutaMax	Gibco, Invitrogen™ Cooperation, Carlsbad, CA
10 mM Hepes	Gibco, Invitrogen™ Cooperation, Carlsbad, CA
Insulin	Sigma, I6634
Kanamycin	Sigma-Aldrich, 60615
Matrigel Matrix Growth Factor Reduced	BD Bioscience, 356231
MEM (non-essential amino acids, 100x)	Gibco, Invitrogen™ Cooperation, Carlsbad, CA
mR-spondin1	R&D sytems, 2474-RS-050
N-acetylcysteine	Sigma-Aldrich, A9165
Neomycin/ G418 (Geneticin	Gibco, Invitrogen™ Cooperation, Carlsbad, CA
Noggin	Peprotech, 250-38
N2 supplement (100x)	Thermo Fisher Scientific, 17502048
Nu-Serum	BD, 355100
1x PBS without Mg^{2+}/Ca^{2+}	Gibco, Invitrogen™ Cooperation, Carlsbad, CA
Penicillin/Streptomycin (100x)	Gibco, Invitrogen, 15140-122
Retinoic acid	Sigma, R2625
ROCK inhibitor (Y-27632)	Sigma, Y0503
Transferrin	Sigma, T0665
TrypLE	Life technologies, 12605
Trypsin-EDTA (0.05% or 0.25% Trypsin, 0.53 mM EDTA4Na)	Gibco, Invitrogen, Carlsbad, CA
β-mercaptoethanol , 50mM	50 mM, Gibco, Invitrogen™ Cooperation, Carlsbad, CA

6.7 Buffers and solutions

FACS buffer	1x PBS, 2 % FCS, 2 mM EDTA

Single-cell RNA sequencing FACS buffer	1x PBS, 1 % FCS, 0.1 mM EDTA

Immunostaining buffers

10x PBS, pH7.4	1.37 M NaCl, 26.8 mM KCl, 0,101 M Na_2HPO_4, 13.8 mM KH_2PO_4
PBST	1x PBS, 0.1 % Tween20, pH7.4
4% PFA	1.3 M PFA in 1x PBS, pH7.2-7.4
Permeabilisation (sections)	0.25 % TritonX-100, 100 mM glycin in dH_2O
Permeabilisation (crypts)	0.5 % TritonX-100, 100 mM glycin in dH_2O
Blocking solution	10 % FCS, 1 % BSA, 3 % donkey serum in PBST
DAPI	5 mg DAPI in 25 ml PBS
Elvanol	0.015 mM Polyvinyl-alcohol, 24 mM Tris pH6.0, 2 g DABCO in 90 ml H_2O and 37.8 ml glycerol
Antigen retrieval (BrdU)	3.3 N HCl in H_2O
10x Tris-Borat-Buffer	10 mM $Na_2B_4O_7$ in dH_2O

DNA/RNA buffers

50x TAE buffer	2 M Tris, 50 mM Glacial acetic acid, 50 mM EDTA
DNA (genomic) lysis buffer	100 mM Tris (pH8.5), 5mM EDTA, 0.2 % SDS, 200 mM sodium chloride, 100 µg/ml proteinase K

Protein biochemistry buffers

IP Lysis buffer	150 mM NaCl, 50 mM TRIS pH7.5, 1 mM EDTA, 1 % NP-40
RIPA buffer	50 mM Tris pH 7.5, 150 mM NaCl, 1 mM EDTA, 1 % Igepal, 0.1 % SDS, 0.5 % sodium-deoxycholate
Ponceau-solution	0.2% PonceauS, 3% TCA
APS	10 % APS (in dH_2O)
4x Tris/SDS	1.5 M Tris, 0.4 % SDS (pH8.8)
4x Tris/SDS	0.5 M Tris, 0.4 % SDS (pH6.8)
10x Tris-Glycine (running)	1.0 % SDS, 0.25 M Tris, 1.92 M glycine
4x SDS-loading buffer	200 mM Tris/HCl, pH6.8, 8 % SDS, 40 % glycerol 0.4 % bromine phenol blue (add freshly 400 mM DTT)
Buffer cathode (KP)	25 mM Tris/HCl, 40 mM glycine, 10 % methanol (adjusted to pH9.4)
Buffer anode I (API)	300 mM Tris/HCl, 10 % methanol (adjusted to pH10.4)
Buffer anode II (APII)	25 mM Tris/HCl, 10 % methanol (adjusted to pH10.4)
10x TBST	100 mM Tris/HCl, 1.5 M NaCl, 2.0 % Tween20 (adjusted to pH7.4)
Blocking solution	5 % Milk powder in 1x TBST

mRNA *in situ* hybridisation

20xSSC	175 g NaCl; 88.2 g sodium citrate per l L DEPC-H_2O. Adjust pH to 4.5 with citric acid
50x Denhardts	5 g Ficoll, 5 g BSA, 5g polyvinylpyrrolidone (for 1L)

Prehyb	50 % formamide; 5x SSC pH 4.5; 1x Denthardt's; 0.1 % Tween-20 (for 1L)
Hyb	Prehyb; 50 µg/ml tRNA; 3 µg/ml probe (for 1 L)
MEMFA	100 mM MOPS; 2 mM EGTA (EDTA); 1 mM MgSO4; 3.7 % formaldehyde

Plasmid preparation

P1 buffer	50 mM Tris HCl, pH 8.0, 10 mM EDTA, 100 µg/ml RNase A
P2 buffer	200 mM Sodium hydroxide, 1 % SDS
P3 buffer	3 M Potassium acetate, pH5.5
TE buffer	10 mM Tris HCl, pH8.0, 0.1 mM EDTA
EB buffer	10 mM Tris HCl, pH8.0

Isolation of genomic DNA

Proteinase K lysis buffer	100 mM Tris, pH8.0-8.5, 5 mM EDTA, pH8.0, 2% SDS, 200 mM sodium chloride

Southern blot

Depurination	1.1 % HCl in H_2O
Denaturation	87.66 g Sodium chloride, 20 g NaOH in 1000 ml H_2O (final volume)
Neutralization	87.66 g Sodium chloride, 60.50 g Tris in 1000 ml H_2O (final volume), pH7.5
Transfer, 20x SSC	88.23 g Tri-sodium-citrate, 175.32 g sodium chloride in 1000 ml H_2O (final volume), pH7-8
Hybridisation buffer	1 M Sodium chloride, 50 mM Tris, pH7.5 (at 37 °C), 10 % dextransulfate, 1 % SDS, 250 µg/ml Salmon Sperm DNA sonicated
Washing buffers	a) 2x SSC/0.5 % SDS b) 1x SSC/0.5 % SDS c) 0.1 % SSC/0.5 % SDS

6.8 Cell and organoid culture media

Bacterial culture

LB Medium (Lysogeny broth; (Bertani, 1951)

LB Agar (Lysogeny broth); (Bertani, 1951)

Cell culture media

ES cells (IDG3.2)

DMEM, supplemented with 2 mM L-glutamine, 15 % FCS (PAN), 0.1 mM β-mercaptoethanol, ESGRO® (LIF) (107 U/ml), 1x MEM, 2 mM HEPES

MEFs

DMEM, supplemented with 2 mM L-glutamine, 15% FCS (PAN), 0.1 mM β-mercaptoethanol, 1x MEM

MTEC and ALI culture

MTEC basic

DMEM/F12 supplemented with 15 mM HEPES, 4 mM L-Glutamin, Penicillin/Streptomycin (100 U/ml and 100 mg/ml), 0.25 mg/ml Fungizone

MTEC Plus

MTEC basic supplemented with 10 µg/ml Insulin, 5 µg/ml Transferrin, 0.1 µg/ml cholera toxin, 25 ng/ml EGF, 30 µg/ml BPE, 5 % FBS (PAA), and 0.01 µM Retinoic acid

MTEC Nu-Serum

MTEC basic including 2 % Nu-Serum and 0.01 µM Retinoic acid

Crypt culture

Crypt basal medium

Advanced DMEM/F12

10 mM Hepes

2 mM GlutaMax

100 U/ml Penicillin/100 µg/ml Streptomycin

ENR (EGF, Noggin, R-spondin) medium

Basal culture medium supplemented with N2 supplement (1×), B27 supplement (1×), 1 mM N-acetylcysteine, 50 ng/ml EGF, 100 ng/ml Noggin, 1 µg/ml mR-spondin1, and 10µM ROCK inhibitor (Y-27632).

6.9 Antibodies

Table 2: List of primary antibodies

Name	Generated in	Company	Cat. No.	Dilution
Acc (Acetyl-CoA Carboxylase) (C83B10)	rabbit	Cell Signaling	3676	WB 1:1000
Akt (pan) (C67E7)	rabbit	Cell signaling	4691	WB 1:5000
Akt(pan) (40D4) Mouse mAb	mouse	Cell Signaling/NEB	2920S	WB 1:5000
Akt-Phospho (Ser473) (D9E)	rabbit	Cell signaling	4060	WB 1:5000
Ampk alpha	rabbit	Cell signaling	2532	WB 1:1000
Ampk-Phospho α (Thr172)	rabbit	Cell signaling	2535	WB 1:1000
β-Actin				
β-Catenin	mouse	BD	610154	IF 1:400, WB 1:5000

Name	Generated in	Company	Cat. No.	Dilution
BrdU	rat	Abcam	ab6326	IF 1:200
Cdk4	mouse	NEB	2906	WB 1:1000
ChgA	rabbit	Abcam	ab15160	IF 1:200
ChgA	goat	Santa Cruz	sc-1488	IF 1:200
E-cadh (extracell. domain)	rabbit	gift from Rolf Kämmer	GP84	IF 1:800
EpCAM (G8.8-c)	rat hybridoma	DSHB hybridoma	4G1	IF 1:400
EpCAM-PE (CD326, clone G8.8)		eBiosciense	12-5791-81	1.25μg/10^{5-8} cells
Fasn (Fatty Acid Synthase) (C20G5)	rabbit	Cell Signaling	3180	WB 1:1000
Fltp116	rabbit	Home made		IF 1:100, WB 1:500
GFP	chicken	Aves Labs	GFP-1020	IF 1:500
GFP	rabbit	Abcam	ab290	IP 1 μl/ 40 μl beads
GSK-3β	rabbit	Cell Signaling	12456	WB 1:5000
GSK-3β Phosho Ser9 (D85E12)	rabbit	Cell Signaling	5558	WB 1:5000
IGF-I Receptor β (D23H3) XP®	rabbit	Cell Signaling	9750	WB: 1:1000
Insulin	guinea pig	Thermo Scientific	10520565	IF 1:1000
Ir/Igf1R (Tyr1158/Tyr1162/Tyr1163)-phospho	rabbit	Millipore	07-841	WB: 1000
Ki67	rabbit	Abcam	ab15580	IF 1:200
Lamin	goat	Santa Cruz	sc-6217	WB 1:20000
Lyz1	rabbit	DAKO	A0099	IF 1:1000
Mapk p44/p42 (Erk1/2) (1367F5)	rabbit	Cell signaling	4695	WB 1:5000
Mapk Phospho-p44/42 (Erk1/2) (Thr202/Tyr204)	rabbit	Cell signaling	4370	WB 1:5000
mTor	rabbit	Cell signaling	2972	WB 1:1000
mTor-Phospho (Ser2448) (D9C2)	rabbit	Cell signaling	5536	WB 1:1000
Muc2	rabbit	Santa Cruz	sc-7314	IF 1:1000
Pericentrin	rabbit	Covance/HISS Diagn.	PRB-432C	IF 1:500
Pparγ (81B8)	rabbit	Cell Signaling	2443	WB 1:1000
S6 Ribosomal Protein (5G10)	rabbit	Cell Signaling	2217S	WB 1:5000
S6 Ribosomal Protein (Ser235/236)- Phospho	rabbit	Cell Signaling	2211S	WB 1:5000
Scd1 (C12H5)	rabbit	Cell Signaling	2794	WB 1:1000
Srebp1 Antibody (2A4)	mouse	Novus Biologicals	NB600-582SS	WB 1:1000
Tubulin-Acetylated	mouse	Sigma	T7451	IF 1:1000
Tubulin-α	mouse	Sigma	T6199	WB 1:40000
Tubulin-α	mouse	Synaptic sytems	302211	WB 1:50000

Table 3: List of secondary antibodies

Name	Company	Cat. No.	Dilution
Donkey anti-chicken Alexa Fluor 488	Dianova	703-225-155	IF 1:800
Donkey anti-mouse Cy5	Dianova	715-175-151	IF 1:800
Donkey anti-goat Alexa Fluor 555	Invitrogen	A21432	IF 1:800
Donkey-anti-goat Alexa Fluor 633	Invitrogen	A21082	IF 1:800
Donkey anti-rabbit Alexa Fluor 488	Invitrogen	A21206	IF 1:800
Donkey anti-rabbit Alexa Fluor 555	Invitrogen	A31572	IF 1:800
Donkey anti-rabbit Alexa Fluor 649	Dianova	711-605-152	IF 1:800
Goat anti-mouse HRP	Dianova	115-036-062	WB 1:20000
Goat anti-rabbit HRP	Dianova	111-036-045	WB 1:20000
Rabbit anti-goat HRP	Dianova	305-035-045	WB 1:20000

6.10 Primers, probes and plasmids

6.10.1 TaqMan probes

Table 4: List of TaqMan probes

Gene	Assay ID (Thermo Fisher)
Actb	Mm00607939_s1
Ascl2	Mm01268891_g1
Axin2	Mm00443610_m1
Ccnb2	Mm01171453_m1
Ccnd1	Mm00432359_m1
Cdkn1a	Mm04205640_g1
Cdkn1b	Mm00438168_m1
Cdkn2b	Mm00483241_m1
Celsr1	Mm00464808_m1
eGFP	Mr04329676_mr
Fltp1	Mm00512620_m1
FoxJ1	Mm01267279_m1
Fuz	Mm01205398_m1
Fzd2	Mm02524776_s1
Fzd3	Mm00445423_m1
Fzd6	Mm00433387_m1
Fzd7	Mm00433409_s1
Gapdh	Mm99999915_g1
Hprt	Mm01545399_m1
Lgr5	Mm00438890_m1
mKi67	Mm01278817_m1
Neurog3	Mm00437606-s1
Olfm4	Mm01320260_m1
Prickle1	Mm01297035_m1
Ror1	Mm00443463_m1
Ror2	Mm00443470_m1

Gene	Assay ID (Thermo Fisher)
Rpl37	Mm00782745_s1
Trp63	Mm00495793_m1
18S	Mm03928990_g1

6.10.2 Single-cell qPCR primers

Table 5: Primers for single-cell qRT-PCR

Gene	Outer primer fwd/rev	Inner primer fwd/rev
Acaca	GATCTATCCGTCGGTGGTCT	GAACGTGCAATCCGATTTGT
	TGGAACATAGTGGTCTGCCA	TTCTGCATTGGCTTTAAGGTCT
Actb	TGTCGAGTCGCGTCCA	CTTCTTTGCAGCTCCTTCGT
	GCTTTGCACATGCCGGAG	CGCAGCGATATCGTCATCCA
Aldob	TGAGGATTGCTGACCAGTGT	TCCAGCCTTGCTATCCAAGAA
	GTCATGGTCTCCGTCAGGAA	AGCCCATTCTGCTGACAGAT
Alpi	TCAGTGATGTACCGTGCCAA	CAGGGAAGTCTGTGGGAGTG
	AGGCATCTCTGCATCTGAGTA	GTTCACCGTGTGTGCGTAG
Ascl2	GTTAGGGGGCTACTGAGCAT	GGTGACTCCTGGTGGACCTA
	AGTCAGCACTTGGCATTTGG	TGCACTAGACAGCATGGGTAA
Axin2	CCGACCTCAAGTGCAAACTC	CCACCGTGGTTGGCTTGT
	ACTGGGTCGCTTCTCTTGAA	TGAATCCGTTTTCAGCTGTTTC
Chga	AACAGCCCCATGACAAAAGG	CAAGGTGATGAAGTGCGTCC
	CTCGTCTCCTTGGAGGGTC	CAGACACTCAGGGCTGACA
Fabp1	ACTTCTCCGGCAAGTACCAA	AGAGCCAGGAGAACTTTGAGC
	ACGATTTCTGACACCCCCTT	ATGTCCTTCCCTTTCTGGATG
Hmgcs2	GCATAGATACCACCAACGCC	GCACAGCCTCCCTCTTCAAT
	TTACCACTCGGGTAGACTGC	TAGCGACCATCCCAGTAGC
Lgr5	CCAGTCTCCTACATCGCCTC	TTACGTCTTGCTGGAAATGCT
	GTCTCAGCTGGTTGTTCTGC	AGCATAAGCACTTTGAGGCTG
Lyz	TCTACAATCGTTGTGAGTTGGC	ATGGCTACCGTGGTGTCAAG
	CGGTTGTAGTTTGTAGCTCGT	CGGTTGTAGTTTGTAGCTCG
Mmp7	ACTCTAGGTCATGCCTTCGC	TAGGCGGAGATGCTCACTTT
	GAGTGGCCAAATTCATGGGT	GCAGCAAACAGGAAGTTCAC
Muc2	GAAGCCAGATCCCGAAACCA	CTGGGGTGACTTCCACTACA
	TGTAGGAGTCTCGGCAGTCA	GCAAAGTTGTAATCACAGAGGC
Neurod1	GGAATTCGCCCACGCAGAAG	CCCGAGGCTCCAGGGTTAT
	CCCGCTCTCGCTGTATGATT	GGTCATGTTTCCACTTCCTGT
Neurog3	GCAATTTACTCCAGGCGAGG	TAGCAGAACTTCAGAGGGAGC
	AGCAGGTCAGTCAGTGACAA	GCAGTGGATAGGGTCAGTGT
Olfm4	CAGAGTGGAGCGCTTAGAGT	CACAGCTCACATCCTTTCTCAG
	CTACTCGGACCGTCAGGTTC	AGCCTCTTCTCATACACACTT
Ppara	GAACCGGAACAAATGCCAGT	TCACAAGTGCCTGTCTGTCG
	TTCAGGTCGTGTTCACAGGT	CTTGGCATTCTTCCAAAGCG
Ppard	GGCAGCCTCAACATGGAATG	TCGGGCTTCCACTACGG
	ATACTCGAGCTTCATGCGGA	TGTCCGGCGGAAGAAGC
Pparg	AGGGCGATCTTGACAGGAAA	ACAAATCACCATTTGTCATCTACGA
	ATTCGGATGGCCACCTCTTT	GGGGGTGATATGTTTGAACTTGA

Gene	Outer primer fwd/rev	Inner primer fwd/rev
Scd2	TAGCTCTCGGGAGAACATCT	GTTTCCATGGGAGCTGTGG
	AGCCATGCAATCGATGAAGA	CTGGCAGAGTAGTCGTAGGG
Sis	CAGCACTGGGGGAATCAGTA	CTGTATGGATACAGCATGGCTA
	GTCCCGAACCAGCAAATGTT	CCGGGTAAGGATGAAGCTT
Sclc2a2	CGGTGTGATCAATGCACCTC	TTCCACTGGATGACCGGAAA
	GCTGGTGTTGTGTATGCTGG	TGTGACTGTAAGTGGGGTGT
Sclc5a1	GAAGTGGTCACTTTGTGGGG	CATGGGTGGCTTTGAATGGA
	CCGGCCTTGATGTAAATCGG	ACAAATATCCAGCCCAGCAC
Spdef	GTTGGCTCTGCCGAGGA	TCTTCTGACAGCAGGCGG
	ATCTGGGAACAGTAGCAGGC	GGGGGACACGTTGCTCA
Uba52	AACTGCCGCAAGAAGAAGTG	GGCCATACCAACAACCTGC
	CAGTGGATGGAAGGGGACTT	GGGGTCACATGCCAGGTA

6.10.3 Genotyping PCR and cloning primers

Cloning primers:

EP 33 5′-GTAAAACGACGGCCAGTG-3′

EP 34 5′-GGAAACAGCTATGACCATG-3′

EP 1228 5′-NNN GCGGCCGC GGTTGGATTCTGAGGCTGACTGGG-3′

EP 1229 5′-NNN TCTAGA CTTGGTGCTCTTACAAGGGCTCGG-3′

EP 1230 5′-NNN GAATTC GTCCTAGTCTAGCTGAGGTCCAGATCTATG-3′

EP 1231 5′-NNN AAGCTT GTGGGAGTCACTGACATTCTTGTTAACC-3′

EP 1126 5′-GCGGCCGCAGCCACCATGTCTAGAATGGTGAGCAAGGGCGAGGAGCTGTTC-3′

EP 1201 5′-NNN ACTAGTTCA CTTGTCATCGTCATCCTTGTAATCGATGTCATGATCTTTATAA-TCACCGTCATGGTCTTTGTAGTCCTTGTACAGCTCGTCCATGCCGAGAGTGATCC-3′

Genotyping PCR primers:

EP 38 5′-CAAGATCCGCCACAACATCG-3′

EP 565 5′-CAGCATGGCATAGATCTGGAC-3′

EP 566 5′-GAGGCTGACTGGGAACAATC-3′

EP 1321 5′-CAGAAAGCGAAGGAGCAAAG-3′

EP 397 5′-CTACTACCAAGGAGTGTACTCC-3′

EP 398 5′-CTGTGGCCCATCTATTTAGGG-3′

EP 981 5′- GGGCTCTACTTCATCGCATTCC-3′

EP 1302 5′-CTCTGCTGCCTCCTGGCTTCT-3′

EP 1303 5′-CGAGGCGGATCACAAGCAATA-3′

EP 1304 5′-TCAATGGGCGGGGGTCGTT-3′

6.10.4 Probes

Southern Blot, *Fltp* 5′ probe, 608 bp (generation described in (Moritz Gegg, doctoral thesis, https://mediatum.ub.tum.de/doc/1114671/document.pdf; last change 10.11.2014).

5′–GAGCCCTTACGCACACTTAAGTATGCCTTTTTCTTTCCCTAGTCTCTCTTTCTCTTAACCTTCT
TGTGTAAAGTTTGTCAGAAGTGTTCTTCAGGAGCCGGAGAGACGGCAAGTACTGGCACTTAAC
CTCCTGAGTACCGGTTTTCATTGTAGGTGTAGATGCCACCTTGTTTAATACAGATTTAAGGACA

AATACTGAAAGATAGAGAGCAGCTTAGGAAAATGCAGGAAACACATTACAAACCTGAGGGT
GGGTACGGATGTCTCAAAAGAGTAAGACCAGACACTTAACTGAAGTCACTGAATAGCTTCCA
GTCATTACCCTTTATTATGCTATTTCTGTGTACTCACTTGAGCAACGTAGCCTATATCTCCTCCT
TGGGAGAAACTGACTAAAGAGGAAATGTCACCGGTTTCATTATACAAGGTGACACACCTTCC
TCTTCATTGTCTTGGGATACACTTAGAACCCACCATCCTGAACATGCTAATTAAAATGCCCTGA
TAGCAAAATAACTAAGTAAAATTCATTTTTTTTAAAAGATATCTTCTGAGAGGCCACACGAGA
CTGCTCCTGCAACCTCAGATAAGATGCAGTTAATGTCCCG–3'

6.10.5 Plasmids

H-24A	(Gegg et al., 2014; Moritz Gegg, doctoral thesis, https://mediatum.ub.tum.de/doc/1114671/document.pdf; last change 10.11.2014)
RP23-333P11	(Gegg et al., 2014)
pBKS-Venus vector	(Nagai et al., 2002)
PL452 vector	(Liu, Jenkins, & Copeland, 2003)

6.11 Cell lines, primary cells and bacteria

Murine cell lines	
Primary MEFs	Primary murine embryonic fibroblasts isolated at E13.5
IDG3.2 murine ES cell line (F1)	Genetic background 129S6/SvEvTac x C57BL/6J (Hitz et al., 2007)
Primary mTECs	Mouse tracheal epithelial cells isolated from tracheae of adult wild-type or Fltp-Venus fusion mice
Bacteria	
E.coli K12 EL250	(E. C. Lee et al., 2001)
E.coli K12 XL-1 Blue endA1 gyrA96(nalR) thi-1 recA1 relA1 lac glnV44 F`[:: Tn10 proAB + laclq (lacZ)M15]hsdR17(rK-mK+)	Stratagene, LaJolla
E.coli K12 DH5α F-.lacl-recA1, endA1, D(lacZY A-argF), U169, F80dlacZDM15, supE44, thi-1, gyrA96, relA1	(Hanahan et al., 1985)

6.12 Mouse lines and animal diet

Table 6: List of mouse models

Mouse model	Background	Source
Foxa2^{FVF} (FVF)	C57BL/6J	(Burtscher, Barkey, & Lickert, 2013)
Fltp^{ZV}	C57BL/6J	(Gegg et al., 2014)
Fltp^{V} (Fltp-Venus)	Mixed C57BL/6J, 129/SvJ, CD1	This thesis
Foxa2$^{nEGFP\text{-}CreERT2}$; *Gt(ROSA)26^{mTmG}*	Mixed C57BL/6J, 129/SvJ, CD1	(Imuta, Kiyonari, Jang, Behringer, & Sasaki, 2013), (Muzumdar, Tasic, Miyamichi, Li, & Luo, 2007)
C57BL/6J	C57BL/6J	Charles River
ROSA26-Cre	C57BL/6J	(Soriano, 1999)

6.12.1.1 Animal research diets

Control and high-fat diets were sterilised by γ–irradiation.

- High-fat diet with sucrose (58 % kcal from fat, 25 % kcal from carbohydrates, 17% kcal from protein) - Research Diets Inc., USA, Cat. No. D12331.
- Control diet: ssniff EF R/M Control, 5 % fat (11 % kcal from fat, 64 % kcal from carbohydrates, 25 % kcal from protein) – ssniff Spezialdiäten GmbH, Cat. No. E15051-047.
- Liquid diet for GTT/IST: Osmolite HiCal - Abbott GmbH & Co, Germany

7 Methods

7.1 General mouse handling and animal experimental procedures

Animal experiments were carried out in compliance with the German Animal Protection Act, guidelines of the Society of Laboratory Animals (GV-SOLAS) and Federation of Laboratory Animal Science Associations (FELASA).

Mice were maintained in groups of two to four animals at 23 ± 1 ^{0}C, with constant humidity and on a 12-h light-dark cycle with free access to water and food unless otherwise indicated.

All experiments were performed using 3-6-month-old mice, unless otherwise stated.

7.1.1 Genotyping of mouse lines

7.1.1.1 Isolation of genomic DNA from tail biopsies

Genomic DNA was isolated from tail biopsies or ear punch samples upon mouse weaning. Samples were lysed in tail clip lysis buffer (section 6.7) supplemented with proteinase K (100 µg/ml) and incubated overnight at 55 °C. Subsequently, the lysates were thoroughly vortexed, centrifuged (14,000 rpm, 10 min) and genomic DNA was precipitated with pure isopropanol. Pellets were then washed with 70 % EtOH, centrifuged (14,000 rpm, 5min, RT), air-dried for 10-15 min and re-suspended in 50-100 µl milli-Q water.

7.1.1.2 Genotyping-PCRs

PCR mix

DNA sample	1 µl
10X Fermentas Taq Buffer w/o $(NH_4)2SO_4$ - $MgCl_2$	2 µL
25mM $MgCl_2$	2 µL
10µM dNTPs	1 µL
10 pmol/µL primer	1 µL each
Taq DNA Polymerase (5 U/µL)	0.25 µL
ddH_20 ad	20 µl

Primer sequences are specified in section 6.10.3.

Fltp-Venus fusion (*Fltp^{V}*)

Neo+ vs Δneo

Primers: EP 565, 1321, 38

Band size: neo+: 520 bp; Δneo: 430 bp; WT: no band

95 °C 4 min → (95 °C 30 sec → 57 °C 45 sec →72 °C 1 min) x35 → 72 °C 10 min

WT, HET, HOM

Primers: EP 565, 566, 38

Band size: WT: 317 bp; Mutant (MUT): 430 bp

95 °C 4 min → (95 °C 30 sec → 58 °C 45 sec →72 °C 1 min) x35 → 72 °C 10 min

Gt(ROSA)26 ^{mTmG}

EP 1302, 1303, 1304

Band size: WT: 330 bp; MUT: 250 bp

94 °C 30 sec → (94 °C 30 sec → 58 °C 40 sec →72 °C 40 sec) x28 → 72 °C 10 min

Foxa2 $^{nEGFP\text{-}CreERT2}$

Primers: EP 397, 398, 981

Band size: WT: 207 bp; MUT: 291 bp

95 °C 5 min → (95 °C 30 sec → 55 °C 45 sec →72 °C 1 min) x35 → 72 °C 10 min

FVF

EP 38, 397, 398

Band size: WT: 207 bp; MUT: 506 bp.

94 °C 4 min → (94 °C 30 sec → 56 °C 45 sec →72 °C 1 min) x35 → 72 °C 10 min

7.1.1.3 Gelelectrophoresis

PCR products were mixed with OrangeG at a ratio 1:4, respectively, and separated on 1-2 % agarose gels in 1x TAE buffer using gelelectrophoresis at 100 V. Agarose gels, supplied with EtBr, were prepared and run using the 1x TAE (Tris-acetate, EDTA). Visualisation of separated PCR products was achieved using a gel documentation system.

7.1.2 Dietary interventions

Three-month old weight-matched male mice were divided into cohorts matched for body weight with similar variance and fed *ad libitum* either a diabetogenic high-fat diet with sucrose (HFD) or a control diet (CD) (see section 6.12.1.1) for a period of 11-13 weeks. Mice were weighed every second or third week.

7.1.3 Induction of Cre recombinase activity

For short-term genetic lineage studies, Cre recombinase activity was induced in *Foxa2* $^{nEGFP\text{-}CreERT2/+}$; *Gt(ROSA)26* $^{mTmG/+}$ mice by a single dose of orally administered tamoxifen at 0.3 mg/g body weight in sunflower oil (Sigma-Aldrich, Germany) after a 3-h fast. Mice were sacrificed 70 hours after tamoxifen gavage.

7.1.4 EdU and BrdU administration

To assess the epithelial replication rate in the small intestine, 5-Ethynyl-2-deoxyuridine (EdU) (Thermo Fisher Scientific, A10044) or 5-bromo-2-deoxyuridine (BrdU) (Sigma, #B5002) was administered as an *i.p*. injection at 100 μg/g body weight or at 50 μg/g body weight, respectively, each from a 10 mg/ml stock and in sterile PBS. Mice were sacrificed 2 h post EdU injection or 24 h post BrdU administration.

To compare BrdU label retention with BrdU pulse-chase experiment under CD and HFD conditions in FVF mice, mice maintained 10 weeks on a diet, were given BrdU in drinking water at 1 mg/ml supplemented with 1 % sucrose for 14 days. BrdU containing drinking water was changed every three days. BrdU was then withdrawn and mice were further maintained on a diet and *ad libitum* drinking water for a chase period of 21 days. A group of mice was sacrificed after 14 days of continuous BrdU labelling or after a 21-day period of chase.

7.1.5 Oral glucose tolerance and insulin secretion tests (oGTT, IST)

Glucose tolerance was assessed in FVF mice fasted for 6 hours at time points 0 min (prior to the glucose gavage), 15, 30, 60 and 120 min after the oral administration of 1.5 g glucose per kg body weight (20 % (wt/v) D-(+)-glucose (Sigma-Aldrich) in PBS). Glucose concentration was measured in blood samples from tail veins using a handheld glucometer (Abbott GmbH & Co. KG, Wiesbaden, Germany). To measure the insulin secretion, small blood samples from tail veins were collected into EDTA-coated microvette tubes (Sarstedt) at time points 0, 15 and 30 min of the glucose tolerance test and plasma was extracted by centrifugation at 3500 rpm for 15 min at 4 °C. Plasma insulin concentration was determined with the Ultra Sensitive Mouse Insulin ELISA Kit (Crystal Chem, Downers Grove, IL) according to the manufacturer's instructions and absorbance was measured using the Varioskan LUX microplate reader (Thermo Fisher Scientific Inc., Waltham, MA, USA) at 450 and 630 nm.

7.1.6 Plasma hormone measurements

Concentrations of circulating gut hormones were measured in FVF mice maintained 13 weeks on a CD or a HFD. Basal levels of total ghrelin, serotonin and PYY were assessed in plasma after a 6-hour fast. Therefore, tail vein blood was collected into EDTA-coated microvette tubes (Sarstedt) and plasma extracted by centrifugation at 13,000 rpm for 2 min at 4°C. To measure postprandial hormone levels of ghrelin and Glp-1, mice were gavaged with 250 μl of mixed meal containing liquid diet (Osmolite HiCal, Abbott GmbH & Co, Germany) supplemented with dextrose at 20 % (wt/v) (Sigma-Aldrich). 10 min after the mixed meal bolus, blood was sampled either from vena cava, under terminal anaesthesia with isoflurane, or from the tail vein. To avoid the rapid Glp-1 degradation, blood samples were immediately mixed with 500 KIU/ml aprotinin (Sigma, A-1153) and 0.1 mM Diprotin A (Abcam, 145599). Hormone concentrations were measured according to the manufacturer's instruction using ELISA kits listed in section 6.4**Fehler! Verweisquelle konnte nicht gefunden werden.**.

7.1.7 NMR spectroscopy

Lean and fat mass of mice was determined by a nuclear magnetic resonance (NMR) technology using EchoMRI (Houston, TX, USA).

7.2 Crypt isolation, crypt culture and single cell preparation for flow cytometry

Small intestines were dissected and the mesenteric tissue was removed in ice-cold PBS. Intestinal tube was then cut open longitudinally, the villi were scraped off using a cover slip and the remaining tissue was cut into 2 cm pieces. After several washes in ice-cold PBS, tissue fragments were incubated in 2 mM EDTA in ice-cold PBS for 35 min at 4 °C on a benchtop roller. Finally, crypt fractions were collected in

fresh PBS by rigorous shaking (three to four fractions). Isolated crypts were passed through a 70-µm cell strainer to remove residual villous contamination and pelleted at 300xg for 5 min at 4 °C. For protein biochemistry, crypt pellets were lysed immediately in RIPA buffer after this step or stored at -80 °C. For crypt culture, crypts were washed with ice-cold basal medium (advanced Dulbecco's modified Eagle medium (DMEM)/F-12 supplemented with 100 U/ml penicillin/streptomycin, 10 mM HEPES, 2 mM GlutaMax) and centrifuged at low speed (250xg for 2-3 min at 4 °C) to remove single cells. At latest after this step, the quality of isolated crypts was examined under the microscope and the number of crypts was calculated. Crypts were plated in warm 24-well plates at a density of 400 crypts per well in 50 µl growth factor-reduced Matrigel (basal medium : Matrigel as 30:70), and incubated at 37 °C in the incubator to allow the Matrigel to polymerise for 10 min. Afterwards, crypts were overlaid with 500 µl ENR medium containing N2 supplement (1×), B27 supplement (1×), 1 mM N-acetylcysteine, 50 ng/ml EGF (Life technologies PMG8043), 100 ng/ml mNoggin (Peprotech, #250-38), 1 µg/ml mR-spondin1 (R&D sytems, #2474-RS-050) (ENR) in the presence of 10 µM Rock-Inhibitor (Sigma, Y0503) in Advanced DMEM/F-12 and cultured in an incubator (5 % CO2, 37 °C). Every two to three days the medium was changed. Bright-field images were acquired using a Zeiss microscope. When indicated, Fatostatin (15 µM in DMSO, Sigma-Aldrich, F8932), Pparα and Pparγ inhibitors (GW6471, Sigma-Aldrich, G5045, and GW9662 Sigma-Aldrich, M6191, both 5 µM in DMSO,) or DMSO as control were added directly upon crypt seeding in the crypt culture media. Medium was changed every 2-3 days. For gene expression studies, cultured crypts were washed several times with warm PBS. Matrigel was dissolved with CULTREX (Trevigen, 3700-100-01) and crypts were lysed in QIAzol (Qiagen, 79306). Bright-field images of cultured organoids were acquired using a Zeiss microscope.

For single cell preparation and flow cytometry, isolated crypts were incubated with 1-2 ml TrypLE (Life technologies, #12605) for 5 min on ice and subsequently for 5 min at 37 °C in a water bath. 5-7 ml of crypt complete medium (basal medium supplemented with 10 % FCS) supplemented with 10 µg/ml DNase I were added and cells were incubated 5 min at 37 °C in a water bath to digest released DNA. Cells were then re-suspended 20 times, pelleted at 300x g for 5 min at 4 °C, and washed with ice-cold FACS buffer. The cell pellet was re-suspended in 1-2 ml FACS buffer supplemented with 10 µM Rock-inhibitor (Sigma, Y0503), and solution was passed through a 40-µm cell strainer cap of FACS tubes. For single-cell RNA sequencing, isolated single cells were re-suspended in the modified FACS buffer, containing 1x PBS, 1 % FCS, 0.1 mM EDTA.

7.3 Single cell preparation from lung and trachea for flow cytometry

Lungs and tracheae were dissected, cleared from connective, rinsed in PBS and minced with scalpel. Tissue pieces were washed with fresh PBS, pelleted and digested with collagenase P (2 mg/ml in PBS) at 37 °C for 1 h. Afterwards, clumps were disaggregated using a 21 G needle and filtered first through a 100 µm and 40 µm cell strainer. Cells were pelleted at 7000 rpm for 5 min at 4 °C and red blood cells were removed by incubation with the red blood cell lysis buffer (RBC lysis buffer, eBioscience) for 4 min on ice. The reaction was stopped by adding an excess of PBS, cells were pelleted and washed with FACS buffer. If necessary, cells were stained with fluorescently labelled antibodies as described in section 7.4.

7.4 Cell analysis by flow cytometry and fluorescence-activated cell sorting

Prepared solutions of small intestinal or lung and tracheal single cells were sorted using FACS-Aria III (BD Bioscience). For all experiments, population of interest was identified based on size and granularity upon gating according to their forward *vs side scatter area* (FSC-A *vs* SSC-A), doublets were excluded by gating, and dead cells by labelling with 7-AAD (eBioscience, #00-6993-50).

FVF- or Fltp-Venus-labelled cells were sorted according to the Venus reporter fluorescence signal. For bulk gene expression analyses (microarray, qRT-PCR), cells were sorted directly into QIAzol reagent

using the 80-µm nozzle. For single-cell transcriptomics and Western blot, cell suspensions were sorted using the 100 µm nozzle.

To obtain FVF-enriched SI crypt cell samples for single-cell RNA sequencing, 30,000 FVF^{+} cells, comprising FVF^{low} and FVF^{hi} cells, were sorted based on Venus fluorescence and then combined with 30,000 sorted live crypt cells in one sample. For single-cell qRT-PCR, isolated small intestinal crypt cells from two mice were pooled per sample prior to sorting, and FVF^{low} and FVF^{hi} cells were sorted directly into 96-well plates containing pre-amplification and lysis reagents as described in section 7.6.1.

To distinguish epithelial cells by cell surface staining with CD326 (EpCAM-PE, eBiosciense, section 6.9), isolated single cells were incubated with the fluorescently labelled antibody or the isotype control (rat IgG2a K isotype control, eBioscience, #12-4321-42). Therefore, 10 Mio cells were stained with 1.25 µg antibody in 100µl volume of FACS buffer for 20 min on ice, then washed and filtered as described above. Fluorescence compensation was applied when required. Data analysis was performed using the FACS Diva software.

7.5 RNA biochemistry

7.5.1 RNA isolation from sorted cells, cultured crypts and tissue

7.5.1.1 RNA isolation from sorted cells and cultured crypts

For gene expression studies of bulk-sorted cells, cells were sorted directly in QIAzol lysis reagent, then thoroughly vortexed and total RNA was extracted using the miRNeasy Mini (Qiagen, #217004) or miRNeasy Micro (Qiagen, #217084) Kit according to the kit manual. Briefly, RNA was extracted upon incubation of the sample with chloroform (ratio QIAzol:chloroform 5:1) and by collecting the RNA-containing aqueous phase with the help of Phase Lock Gel™ tubes. RNA was precipitated with pure EtOH, and bound to the column membrane. To remove genomic DNA contaminations, on-column DNA digestion using DNase I (Qiagen, #79254) was used according to manufacturer's guidelines. Bound RNA was afterwards washed and eluted in RNase-free water and, if required, stored at -80 °C.

7.5.1.2 RNA isolation from cultured crypts

To isolate RNA from cultured SI crypts, culture media were discarded, and crypt organoids were washed once with cold PBS. To dissolve the Matrigel, 1ml of ice-cold CULTREX solution was added to each well (for cultures in 24-well format) and incubated for 30 min on ice. Afterwards, crypts were gently re-suspended, pelleted at 300x g, 4 min, 4 °C, and washed five times with cold PBS. Pellets were then lysed with QIAzol lysis reagent, and mRNA was extracted using the miRNeasy Mini Kit as described above.

7.5.1.3 RNA isolation from tissue

Dissected tissue was disrupted by grinding in liquid nitrogen using mortar and pestle and homogenized by pipetting several times through a 21-27 G needle. Total RNA was extracted using xxx (Qiagen, #xxx) kit according to the manufacturer's protocol (see also REFER to chapter above).

7.5.1.4 RNA concentration and quality measurement

RNA concentration was measured by the absorbance at 260 nm using the NanoDrop, and quality was assessed by the ratio of the absorbance at 260 and 280 nm ($A_{260/280}$).

For gene profiling using Affymetrix Mouse Gene 1.0 ST arrays, RNA concentration and integrity was analysed using the Agilent 2100 Bioanalyzer and Agilent RNA 6000 Pico Kit according to the manufacturer's instructions.

7.5.2 Reverse transcription for cDNA synthesis and RNA amplification

Reverse transcription of mRNA was carried out using the SuperScript VILO cDNA synthesis kit (Invitrogen) according to the manufacturer's instructions. Up to 2 µg RNA was transcribed into complementary DNA (cDNA) upon incubating the reaction mix 10 min at 25 °C and 2 h at 42 °C and the reaction was stopped by incubation at 85 °C for 5 min. cDNA was stored at -20 °C. In case the RNA content was low or for the Affymetrix Mouse Gene array, RNA amplification and reverse transcription were carried out using the Ovation® PicoSL WTA SystemV2 (Nugen) according to the manufacturer's instructions. Amplified cDNA was purified using the PCR purification kit (Qiagen).

7.5.3 Quantitative real-time PCR (qRT-PCR)

For gene expression analysis, quantitative real-time RT-PCR (qRT-PCR) was performed using TaqMan™ probes (Life Technologies) and the ViiA 7 Real-Time PCR System (Applied Biosystems or Thermo Fisher Scientific now). The following reaction mix was prepared per reaction (total volume 10 µl): 10 – 25 ng cDNA (1-3 µl), 5 µl TaqMan Fast Advanced Master Mix (Applied Biosystems, #4444557) or TaqMan Universal Master Mix II (Applied Biosystems, #4440040) for amplified cDNA, 0.5 µl TaqMan probe in nuclease-free H_2O. Target gene expression was normalised to the reference (housekeeping) genes. Gene expression was analysed using the comparative Ct method. Ct values were transformed to normalised relative quantities (NRQs) using multiple (f) reference genes (Hellemans, Mortier, De Paepe, Speleman, & Vandesompele, 2007).

$$NRQ = \frac{2^{\Delta Ct\,(gene\ of\ interest)}}{\sqrt[f]{\prod_{p=1}^{f} 2^{\Delta Ct\,(reference\ gene)_p}}}$$

7.5.4 mRNA profiling using Affymetrics gene chips

mRNA preparation for bulk transcriptional profiling, microarray staining, scanning and statistical analyses were performed by Dr. Martin Irmler (IEG, Helmholtz Zentrum München). For mRNA profiling, total RNA from flow-sorted FVF^{hi}, FVF^{low} and FVF^{neg} cells was amplified using the Ovation PicoSL WTA System V2 in combination with the Encore Biotin Module (Nugen). Amplified cDNA was hybridized on Affymetrix Mouse Gene 1.0 ST. Staining (Fluidics script FS450_0007) and scanning of the microarray was performed according to the Affymetrix expression protocol including minor modifications as suggested in the Encore Biotin Kit protocol. The Expression Console (v.1.3.0.187, Affymetrix) was used for quality control and annotation of the normalized RMA (robust microarray analysis) gene-level data and standard settings including median polish and sketch-quantile normalisation were employed.

7.5.5 mRNA *in situ* hybridisation

7.5.5.1 *Olfm4* probe preparation and digoxigenin-labelling

The construct containing cDNA sequence of *Olfm4* was a kind donation from Prof. Hans Clevers group (Hubrecht institute, Utrecht, Netherlands) (Schuijers, van der Flier, van Es, & Clevers, 2014). Probe sequence was confirmed by sequencing using the M13 primer (EP 33/34). *Olfm4* anti-sense probe (800 bp), which will recognise the sense *Olfm4* mRNA, was generated by an *in vitro* transcription of the *NotI*-linearized plasmid using the T7 polymerase. The sense probe was generated using the T3 polymerase on a *HindIII*-linearised template. The probes were labelled using the digoxigenin-coupled UTPs (10x DIG RNA reaction mix, Boehringer Mannheim) during the *in vitro* transcription for 2 h at 37 °C. DNA

was then digested using DNAseI (15 min at 37 °C). Probes were subsequently precipitated in LiCl/EtOH mix (10 µl 4 M LiCl, 300 µl EtOH in 100 µl DEPC-H_2O) for 15 min on dry ice, centrifuged (10 min, 4 °C), and the pellet was washed twice in 70 % EtOH and air-dried. The probes were re-suspended in DEPC-H_2O, analysed on a 1 % TAE gel and stored at -80°C.

Reaction mix for the probe synthesis and labelling for one slide:

DEPC-H_2O	6µl
10x transcription buffer	1 µl
DNA (500 ng/ml)	1 µl
10x DIG reaction mix	1 µl
RNAse inhibitor	0.5 µl
Polymerase (T7 or T3)	0.5 µl

7.5.5.2 *In situ* hybridisation

To identify intestinal stem cells by the mRNA expression of the validated marker *Olfm4*, *in situ* hybridisation (ISH) was performed using digoxigenin-labelled *Olfm4* RNA probe. In brief, paraffin-embedded tissue is hybridised to the digoxigenin-labelled probe. Digoxigenin is recognized by an antibody that can be visualized by an enzymatic reaction with BM-purple. Hybrids are then detected by the anti-digoxigenin antibody and visualised by enzymatic reaction using BM-purple.

To prevent RNA degradation all solutions were made with DEPC-treated water and staining utensils (glass jars) were sterilised by baking at 200 °C. DEPC-treated water (or 1x PBS) was prepared as follows: 0.1% DEPC was added, incubated overnight on a stirrer, and sterilised by autoclaving.

Intestines were dissected as described and fixed in 4 % PFA at 4 °C overnight. Fixative was removed and tissue was washed in PBS at RT. Samples were then dehydrated in ethanol (1x 40 %, 1x 70 %, 1x 95 %, each step 10 min and 3x 100 % ethanol, 3 min each step) and xylene (replaced three times, each step 3 min) at RT, incubated in paraffin wax (replaced once) overnight in a 55 °C oven and embedded in fresh wax. 7 µm sections were prepared and dried overnight. Samples were then dewaxed in xylene (2x 10 min) and rehydrated through ethanol series (100 %, 95 %, 80 %, 70 %, 50 % ethanol, by quickly dipping the slides into the solution) and rinsed with DEPC-water and then PBS. Slides were then postfixed in 4 % PFA for 20 min and digested with Proteinase K (10 µg/ml) in 0.1 M TRIS pH 7.5 for 10 min at 37 °C. The reaction was stopped with 0.2 % glycine in PBS (10 min, RT). Slides were rinsed in PBS, treated with 0.2 M HCl for 15 min at RT, and 0.25 % acetic anhydride solution in 0.1 M triethanolamine (TEA), (pH 8.0) was added for 10 min at RT. Slides were rinsed in PBS and then in DEPC-H_2O. Sections were then pre-hybridised using pre-hybridisation buffer and incubated in an oven at 70 °C for 2 h. Afterwards, pre-hybridisation solution was removed and sections were treated with the hybridisation solution containing 3 µg/ml of digoxigenin-labelled RNA probe (denatured at 80 °C for 5 min) and tRNA (~240 ng/60 µl) in an oven at 70 °C overnight. Subsequently, sections were washed in Solution I containing 50 % formamide/ 1% SDS in 5xSSC three times for 30 min at 70 °C and in Tris/NaCl/Tween buffer (TNT) three times 5 min at 37 °C. Non-hybridised RNA was digested with 100 µg/ml RNase in TNT for 60 min at 37 °C and slides were rinsed with TNT/Solution II (1:1) for 5 min at RT and then washed with Solution II at 65 °C (3x 30 min), followed by three MAB washes (each 5 min) at RT. Sections were blocked in 10 % sheep serum in MAB/2 % blocking reagent for 2 h at RT and incubated with the anti-digoxigenin antibody (1:1000) in blocking solution at 4 °C overnight. Slides were then extensively washed (3-4 h) in MAB buffer and then in NTM buffer at RT, stained with BM-purple at RT overnight and postfixed in MEMFA for 45 min at RT. Sections were washed in PBS, mounted with Moviol and analysed with a light microscope.

7.6 Single-cell gene expression analyses

7.6.1 Single-cell gene expression analysis by microfluidic qRT-PCR

To assess transcriptional profiles of single FVF^{low} and FVF^{hi} cells, a nested single-cell qPCR design was used. FVF^{low} or FVF^{hi} cells were sorted as described above directly into single wells of 96-well plates containing 5 µl of a pre-amplification solution composed of 1.2 µl 5x VILO reaction mix (Invitrogen, #11754-050), 0.3 µl 20 U/µl SUPERase-In (Ambion, #AM2694), 0.25 µl 10 % NP40 (Thermo Scientific, #28324), 0.25 µl RNA spikes mix (Fluidigm, #100-5582) and 3 µl of nuclease-free water (Promega, #P119C). Cells were lysed by incubation at 65 °C for 90 s, and cDNA transcription from RNA was performed by RT cycling (25 °C for 5 min, 50 °C for 30 min, 55 °C for 25 min, 60 °C for 5 min and 70 °C for 10 min) with 1 µl RT mix solution containing 0.15 µl 10x SuperScript enzyme mix (Invitrogen, #11754-050), 0.12 µl T4 Gene 32 Protein (New England BioLabs, #M0300S) and 0.73 µl nuclease-free water. The efficiency and specificity of outer and inner primer pairs for target-specific cDNA amplification were tested in advance. Primers showing single peaks and single bands by melt curve analysis and by separation of qPCR products on a 2.5 % agarose gel, respectively, were considered specific (Table 5). Primer efficiency was analysed over a range of 10-fold cDNA dilutions (1:1 to 1:100) and primers with 100 ± 15 % efficiency were qualified for further proceedings. Specific Target Amplification was performed with 9 µl reaction mix containing 7.5 µl TaqMan PreAmp Master Mix (Applied Biosystems, #4391128), 0.075 µl 0.5 M EDTA, pH 8.0 (Invitrogen, #Am9260G), 1.5 µl 10x outer primer mix (500 nM) under following cycling conditions: enzyme activation step at 95 °C for 10 min, 20 cycles of denaturation for 5 s at 96 °C, and 4 min annealing/extension at 60 °C. Amplified cDNA samples were then treated with 6 µl of Exonuclease I reaction mix containing 0.6 µl reaction buffer, 1.2 µl Exonuclease I (New England BioLabs, #M0293S) and 4.2 µl nuclease-free water. To increase the target specificity, amplified single-cell cDNA samples were analyzed with gene-specific inner primer pairs (Table 5) and SsoFast EvaGreen Supermix with Low ROX (Bio-Rad Laboratories, #172-5210) using the 96.96 Dynamic Array on the BioMark System (Fluidigm). The BioMark Real-Time PCR Analysis software (Fluidigm) was used to calculate the CT values.

7.6.2 Single-cell RNA sequencing (RNA preparation, library generation, sequencing)

Single-cell solution was prepared as described in 7.2. FVF^{+} cells were enriched by flow cytometry as described in 7.4. Sorted cells were counted and number of dead cells was estimated by trypan blue staining. Cell samples were further processed when dead cells were < 20 %. Single-cell libraries were generated using the Chromium™ Single cell 3' library and gel bead kit v2 (10x Genomics, #120237) according to the manufacturer's instructions. Briefly, to obtain a target cell number of 10.000 cells per sample, 16.000 cells per sample were loaded onto a channel of the 10x chip to generate Gel Bead-in-Emulsions (GEMs). These underwent reverse transcription to barcode RNA before cleanup and cDNA amplification. Afterwards, enzymatic fragmentation and attachment of 5' adaptor and sample index was performed. Libraries were sequenced on the HiSeq4000 (Illumina) with 150 bp paired-end sequencing of read 2.

7.7 MALDI imaging mass spectrometry (MALDI-MSI)

MALDI-MSI and statistical analysis of the data was performed by Dr. Na sun and the Research Unit Analytical Pathology, Helmholtz Center Munich. Fresh-frozen small intestinal tissue pieces were sectioned at 12 µm using a cryo-microtome at -20 °C (Leica CM1950, Leica Microsystems, Germany) and mounted onto precooled conductive indium-tin-oxide (ITO)-coated MALDI target glass slides (Bruker Daltonics, Bremen, Germany). Tissue sections were coated with 9-aminoacridine hydrochloride monohydrate matrix (Sigma-Aldrich, Germany) at 10 mg/ml in water/methanol 30:70 (v/v) using a SunCollect automatic sprayer (Sunchrom, Friedrichsdorf, Germany) and flow rates of 10, 20 and 30, respectively, were applied for the first 3 layers. Matrix application for the residual 5 layers was

performed at 40 µl/min. The MALDI-MSI measurement was performed on a Bruker Solarix 7T FT-ICR-MS (Bruker Daltonics, Bremen, Germany) and the data were obtained over a mass range of m/z 50-1000 in negative ionization mode with 30 µm spatial resolution using 50 laser shots at a frequency of 500 Hz. Subsequently, spectra processing of the acquired data was performed using the FlexImaging v. 4.2 (Bruker Daltonics, Bremen, Germany). To assess tissue histology, the matrix was removed with 70% ethanol and MSI-analysed intestinal sections were stained with haematoxylin and eosin (H&E). Finally, slides were scanned with a MIRAX DESK digital slide-scanning system (Carl Zeiss MicroImaging, Göttingen, Germany).

7.8 Mouse tracheal epithelial cell (MTEC) culture and air liquid interface (ALI) culture

The MTEC culture was based on Vladar, Bayly, Sangoram, Scott, & Axelrod, 2012; Vladar & Stearns, 2007; You, Richer, Huang, & Brody, 2002. To isolate epithelial cells from tracheae, mice were sacrificed and tracheae dissected and cleared from connective tissue. Tracheae were opened longitudinally and digested overnight at 4 °C in DMEM/F-12 medium supplemented with 1.5 mg pronase (protease 14) and antibiotic-fungicide mixture (penicillin/streptomycin (P/S) 1:100, 0.25 mg/ml Fungizone). Next day, digestion medium was supplemented with 10 % FBS, and cells were dislodged by gentle agitation. Tracheae were transferred into a new tube with fresh medium to remove all cells from the tissue. The fractions were pooled and pelleted at 400x g (10 min, 4 °C). The pellet was then treated with DNaseI (0.5 mg/ml DNAseI in DMEM/F12 + P/S and 10 mg/ml BSA) for 5 min on ice and again centrifuged (400x g, 5 min). The cells were re-suspended in MTEC basic medium supplemented with 10 % FBS, plated on the BD Primaria 10 cm plates and incubated for 3-4 h in the incubator at 37 °C to adhere the contaminating mesenchymal cells. Subsequently, the supernatant containing the non-adherent epithelial cells was collected, centrifuged for 5 min at 400x g and re-suspended in MTEC Plus for cell counting. For the MTEC culture, cells were seeded onto Transwell-Clear (Corning) permeable filter supports at 75,000 cells per cm^2 in MTEC Plus medium. Filters were pre-coated with 50 µg/ml rat tail collagen type I (BD) at 37 °C overnight. Medium was changed every two days below and on top of the filter. The switch to the ALI culture was achieved by removal of the medium from the upper side of the filter after the cells became confluent, usually after 7 days of culture, and by feeding MTEC Nu-Serum medium only below the filter. Fresh medium was fed every two days. To reach different stages of differentiation and ciliogenesis, cells were cultured for one to seven days (usually fully ciliated by day seven) and filters were cut out and processed for immunofluorescence and confocal analysis as described in chapter 7.9.1.

7.9 Histology and immunohistochemistry

For all experiments, fluorescent images were taken using a Leica SP5 confocal microscope and image analysis was carried out using the Leica LAS AF software. Cells were counted manually. Images of histological stainings were acquired with the Zeiss AXIO Scope A1 microscope (Carl Zeiss AG, Germany) and processed using Axio Vison 4.8 software.

7.9.1 Immunofluorescence stainings on cryo-preserved tissue sections

7.9.1.1 Immunofluorescence stainings on cryo-preserved tissue sections

Tissue was dissected, rinsed in ice-cold PBS (intestinal lumen was carefully flushed with PBS to remove faecal contents), fixed with 4 % paraformaldehyde (PFA) for 3 h at 4 °C and incubated in a progressive sucrose gradient (1 h in 5 % sucrose/PBS and 1 h in 15 % sucrose/PBS at RT and 30 % sucrose/PBS overnight at 4 °C) for cryo-protection. Prior to embedding with optimal cutting temperature (OCT, Leica) embedding medium, the tissue was incubated in 1:1 of 30 % sucrose/PBS and OCT for 3 h at RT,

placed into embedding molds, frozen on dry ice and stored at -80 °C. Tissue was sectioned on a cryostat (Leica CM 1860) at 10-16 µm. Cryo-sections were dried for 40 min at RT, rehydrated with PBS for 20 min, permeabilised with 0.4 % Triton X-100/PBS for 20 min, washed once in PBST (0.1 % Tween-20/PBS) and blocked in blocking solution containing 10% FCS, 0.1% BSA and 3% serum (donkey or goat)/PBST for 1-2h at RT. Sections were stained with primary antibodies diluted in blocking solution overnight at 4 °C, then washed three times with PBS and secondary antibodies in blocking solution were applied for 1 h at RT. After three washes in PBS, nuclei were stained with DAPI (1:1000) in PBS for 15 min at RT and sections were thoroughly washed and embedded with self-made Elvanol antifade reagent. Sections were dried overnight at RT.

For IF stainings (Ki67) on paraffin-embedded tissue, sections were deparaffinised and rehydrated as described in 7.9.2 and IF staining was carried out as described in this chapter.

7.9.1.2 EdU and BrdU staining in SI intestinal tissue sections

Cryo sections were prepared as described above sectioned at 14µm. Standard antibody staining procedure was carried out and followed by an incubation in 3.3 N HCl for 10 min on ice, 50 min at 37 °C and treatment with borate buffer pH 8.5 twice for 15 min at RT for neutralization of HCl. A staining with rat anti-BrdU (1:200, Abcam, ab6326) antibody was performed over night at 4°C followed by an incubation with the secondary antibody donkey anti-rat DyLight 549 (Dianova, #712-505-153) for 1 hour at RT.

EdU staining was performed following the standard staining procedure for other markers using the Click-IT EdU Alexa Fluor 647 kit according to the manufacturer's instructions.

7.9.1.3 IF staining of cultured organoids

For whole mount staining of cultured organoids, the medium was aspirated, organoids were rinsed in pre-warmed (37 °C) PBS and fixed with warm PFA (4 %) directly in matrigel and in culture plates for 10 min at 37 °C. Afterwards organoids were washed three times with warm PBS, permeabilised at RT with 0.4 % Triton X-100 in PBS for 30 min, washed again in warm PBS and blocked for 2 h at RT. To reduce the unspecific binding of the antibodies to the matrigel components, both primary and secondary antibodies (diluted in blocking solution) were incubated with a solid drop of matrigel for 1 h at 37 °C. The primary antibody in blocking solution was added overnight at 4 °C, the organoids were then washed three times with PBS and secondary antibody (pre-absorbed with matrigel) was added for 2 h at RT. The organoids were washed and DAPI staining (DAPI 1:1000 in PBS) was applied for 15 min at RT. For embedding, 200 µl self-made Elvanol reagent were added on top. The culture plate was then stored, sealed with parafilm, at 4 °C and images taken on a Leica SP5 confocal microscope within three days.

7.9.1.4 Whole-mount IF staining of isolated SI crypts

SI crypts were isolated as described in section 7.2 and fixed in 4 % PFA for 30 min at RT with agitation. Crypts were then washed three times with PBS and pelleted each time at 300 g for 5 min. PBS was replaced by a mixture of PBS/PBST, and crypts were incubated for 10 min on a benchtop roller. Afterwards, cell membranes were pemeabilised using 0.5 % Triton-X 100 with 0.1 M glycin for 30 min at RT. Crypts were then distributed in Epis for blocking and antibody staining. Blocking (donkey block) was performed for 2 h at RT as described above (section 7.9.1.1), followed by incubation with the primary antibody in blocking solution over night at 4 °C on a benchtop roller. Next day, crypts were incubated for an additional hour at RT, followed by three washes with PBS and incubation with secondary antibody for 2 h at RT and then over night at 4 °C. Finally, isolated crypts were washed three times with PBS, and nuclei were stained with DAPI (30 min at RT). After an additional wash, crypts were mixed with 100 µl Elvanol/per slide and embedded on glass coverslips using 0.12 mm spacers.

7.9.1.5 IF staining of sorted cells using cytospin

Single cells from lungs and trachea were flow-sorted into complete medium (chapter 7.3 and 7.4) and samples containing at least 8000 sorted events centrifuged using cytospin devices and the Hettich Cyto System with a benchtop centrifuge onto glass slides (1200 rpm, 6 min, 4 °C). Residual fluid was removed and slides were dried at RT for 2 h. The cells were fixed in 4 % PFA for 10 min, washed with PBS, permeabilised with 0,2 % Triton X-100/PBS for 15 min and further treated as described in 7.9.1.5).

7.9.2 Histochemistry and tissue morphology on paraffin-embedded tissue sections

Tissue was dissected, rinsed in PBS and fixed in 4 % PFA overnight at 4 °C. Tissue was subsequently dehydrated using ethanol (70 % EtOH overnight (4 °C), 1 h 80 % EtOH, 1 h 90 % EtOH, 1 h 100 % EtOH, 1 h fresh 100 % EtOH at RT), then cleared by xylene (up to 3x 10 min, changing used xylene) and finally infiltrated with wax (1h wax I, 1h wax II and wax III overnight, all steps at 65 °C). Tissue was then embedded in wax in embedding cassettes using a paraffin embedding machine and stored at 4 °C.

Tissue was sectioned using a microtome at 6-8 µm. To assess tissue morphology, a standard haematoxylin and eosin (H&E) staining was performed. In brief, sections were deparaffinised (xylene I 3 min, xylene II 3 min) and rehydrated through a graded ethanol series (100 % EtOH 2 min, 96 % EtOH 2 min, 70 % EtOH 2 min, distilled water 1 min), then stained with freshly prepared Mayer´s solution for up to eight minutes, depending on the thickness of the section. Subsequently, a counterstaining with eosin was applied. Sections were rinsed in milli-Q water, dehydrated (70 % EtOH rinse, 96 % EtOH 1 min, 100 % EtOH 3 min, fresh 100 % EtOH 3 min, xylene I 2 min, xylene II 2 min, Roti-Histol 5 min) and mounted with resinous mounting medium. Images were acquired using the Zeiss AXIO Scope A1 microscope (Carl Zeiss AG, Germany).

7.10 Protein biochemistry

7.10.1 Preparation of protein lysates and protein concentration measurement

For Western blot analysis, disrupted and homogenised tissue, whole crypt pellets or pellets of flow sorted crypt cells were lysed in RIPA buffer containing phosphatase and proteinase inhibitors, sonicated at 40 % power (5 x 1min) in case of tissue and crypt lysates, and incubated on ice for 10 min (cells) or 3 h at 4 °C on a roller (tissue and crypts). Lysates were then centrifuged at 13,000 rpm at 4 °C for 10 min and supernatants were collected and stored at -80 °C or further processed.

For protein expression studies on nuclear or cytosolic extracts, whole crypts or flow sorted cells were lysed using NE-PER Nuclear and Cytoplasmic Extraction Reagents kit (Thermo Fisher Scientific, Cat# 78833) according to manufacturer's instructions. In brief, cell or crypt pellets were lysed in cytosolic lysis buffer (CER 1+ II) supplemented with protease and phosphatase inhibitors (P/i, Ph/i), vortexed, incubated on ice for 1min and centrifuged for 5 min at maximum speed on the microcentrifuge (cytosolic fraction in the supernatant). The pellet containing nuclei was re-suspended in the nuclear lysis buffer (NER) supplemented with P/i and Ph/i, vortexed every 10 min for 40 min and centrifuged for 10 min at maximum speed (nuclear fraction in the supernatant).

To determine the protein concentration, the colorimetric detection using Pierce BCA Protein Assay Kit was used according to the manufacturer's instructions. The absorbance was measured at 562 nm and the sample concentration was calculated relative to the standard curve. BSA standards and blanc solutions were prepared with the respective lysis reagents (RIPA- or NE/PER-buffer-based).

7.10.2 Western Blot

Cell lysates were mixed with 4x SDS sample buffer supplemented with DTT and denatured at 95 °C for 5 min. Proteins were resolved by SDS-PAGE based on their size and negative charge supplied by SDS on a denaturing polyacrylamide (PAA) gel with 1x Tris glycine running buffer at 80-100 V. Protein ladder was used to identify the molecular weight of the protein to be detected.

Table 7: Ingredients for two separating (10 % PAA) and two stacking gels (1mm spacer plates)

Acrylamid/bisacrylamide (10 %)	**5 ml**	**Acrylamid**	**650 µl**
4x Tris hCl/SDS buffer pH 8.8	3.75 ml	4xTris/SDS pH 6.8	1.25 ml
H_2O	6.25 ml	H_2O	3.10 ml
TEMED	20 µl	TEMED	10 µl
10 % APS	150 µl	10 % APS	50 µl

After the protein separation, PAA-gels were equilibrated in KP buffer for 20 min. The PVDF membrane was briefly activated in 100 % methanol to pre-wet it for the use with aqueous buffers, then incubated with tap water for 2 min and APII buffer for 10 min. Separated proteins were subsequently transferred onto a PVDF membrane at constant current (0,22 A per gel for 30 min) in a semi-dry blot using the following sandwich order:

Top/cathode → 3x Whatman paper soaked in KP buffer → PAA-gel → PVDF membrane → 1x Whatman paper soaked in APII buffer → 2x Whatman paper soaked in API buffer → anode/bottom.

The membrane was then stained with Ponceau S solution to evaluate the quality of the transfer, washed twice and blocked in 5 % milk in 1x TBST for 1 hour at RT. Subsequently, the membrane was incubated with the primary antibody in blocking solution at 4 °C overnight, washed (3x 10 min) in 1x TBST and incubated with the horseradish peroxidase (HRP)-conjugated secondary antibody in blocking solution for 1 hour at room temperature. If a re-probing on the same blot was required, the membrane was stripped using striping buffer for 15 min at RT, washed, blocked and incubated with new/additional primary and secondary antibody as described above. Protein bands were detected with the enhanced chemoluminiscence (ECL)-solution or SuperSignal™ West Femto Maximum Sensitivity Substrate depending on the expected signal strength by exposure to photographic films and their subsequent development or in the Western Blot imager (UVsolo TS Imaging System, Biometra, Goettingen). Films were scanned, and the intensity values of the detected protein bands were quantified using ImageJ software. Expression of proteins of interest was normalised to the loading controls on the same membrane. Band intensities of phosphorylated proteins were additionally normalised to the corresponding total protein.

7.10.3 FLAG fusion protein immunoprecipitation (FLAG-IP)

FLAG-IP is based on a binding of a FLAG tag fusion protein by a purified anti-FLAG antibody covalently attached to agarose beads. The elution of the bound fusion protein by competition with a 3x FLAG peptide allows its detection in Western Blot.

For FLAG-IP, protein lysates were prepared in RIPA buffer as described in section 7.10.1 and incubated with the washed ANTI-FLAG M2 Affinity Gel according to the manufacturer's instructions. Samples were incubated at 4 °C on a roller shaker overnight. The resin was centrifuged, the supernatant was removed and the resin washed three times with 1x TBS. Subsequently, the FLAG-fusion protein was eluted under native conditions by incubating the resin with the 3x FLAG peptide solution for 30 min at 4 °C. The resin was centrifuged and the supernatant subjected with the 4x SDS sample buffer for Western Blot detection.

7.11 Generation of the Fltp-Venus fusion reporter mouse line

7.11.1 Cloning of the Fltp-Venus fusion targeting vector

The Fltp-Venus fusion targeting construct was designed as shown in Figure 35A.

The cloning of the 5′ and 3′ homology regions (HR) for the *Fltp* gene and production of the *Fltp* retrieval vector is described in (Gegg et al., 2014). For the cloning of the knock-in cassette, the 5′ HR (PCR using primers EP1228, EP 1229) and 3′ HR (PCR using EP 1230, EP 1231) for the knock-in into the ATG of exon2 of *Fltp* were amplified by PCR using the C57BL/6J BAC clone (RP23-333P11) as template (Gegg et al., 2014). These PCR products were subcloned via *NotI*, *XbaI*, *EcoRI*, or *HindIII* into the pBluescript KS (pBKS), respectively, to generate the pBKS-Fltp HR. Restriction digests were carried out according to the optimal conditions for the restriction enzymes provided by the manufacturer. The STOP codon of the 5′ HR was excluded resulting in a fusion construct with introduced downstream sequences. The Venus sequence was amplified from pBKS-Venus vector (Nagai et al., 2002) using primers EP 1126 (containing an *XbaI* recognition site) and EP 1201 (containing a *SpeI* site). Subsequently the *Venus* and the C-terminal 3xFLAG tag sequences were subcloned between the homology regions of the pBKS-Fltp HR vector using *XbaI* and *SpeI*. Next, the phosphoglycerate kinase *(PGK)* promoter-driven *neomycin* (neo) resistance gene flanked by *loxP* sites (loxP-bGHpA-neo-EM7-PGK-loxP) was cloned from the PL452 vector (Liu et al., 2003) via *BamHI*/ *EcoRI* 3′ of the Venus-3xFLAG sequence resulting in the pBKS-Fltp HR-Venus-3xFLAG-Neo vector. Subsequently, the mini-targeting cassette was digested with *NotI* and *HindIII* and introduced into the *Fltp* retrieval vector pL254-Fltp via bacterial homologous recombination in EL350 bacteria resulting in the final targeting construct pL254-Fltp-Venus-3xFLAG-Neo.

The vector sequence was confirmed by sequencing (chapter 7.11.1.5) and the *AscI*-linearized vector was electroporated into the wild-type IDG3.2 ES cells (section 7.11.2.2).

7.11.1.1 Restriction digest, dephosphorylation of linearized DNA and ligation

A typical reaction for a **restriction digest**:

500-1000 ng DNA 5 µl
10x enzyme buffer 2 µl
10x BSA (optional) 2 µl
Enzyme (5,000 U) 0.5 µl
H_2O 10.5 µl → total volume 20 µl

Digests were carried out at optimal conditions for relevant enzyme as suggested by the manufacturer, usually at 37 °C or 25 °C for 1.5 hours.

Linearized plasmid DNA was dephosphorylated to avoid self-ligation using the alkaline phosphatase. A typical reaction for **vector dephosphorylation** contained:

1.0 µg DNA
10x enzyme buffer 1.0 µl
Alkaline phosphatase (1 U/µl) c_{end} = 1 U enzyme/reaction (1 µg DNA) 1.0 µl
H_2O 7.0 µl → total volume 10 µl

For **ligations**, linearized vector DNA was used and enzymatic ligation was performed using the T4 DNA ligase in presence of ATP. The vector and the insert were used in a ratio of 1:3 for ligations with sticky ends or as 1:1 for blunt end ligations.

A typical **ligation reaction** contained:

Vector DNA (quantity (ng) calculated using concentration and size of the vector)	1.0 µl
Insert DNA (quantity (ng) calculated using concentration and size of the insert)	0.5 µl
10x T4 ligation buffer	1.0 µl
T4 ligase (5 U/reaction)	0.5 µl
H_2O	7.0 µl → total volume 10 µl

7.11.1.2 Plasmid DNA preparation

Required amount of plasmid DNA was isolated from bacterial overnight cultures by mini-, midi or maxi-prep using the QIAGEN Mini, Midi or Maxi Kit according to the manufacturer's instructions. Isolated plasmid DNA was re-suspended in 30-50 µl (mini-prep) in 150-300 µl (maxi-prep) Milli Q H_2O or with TE buffer for long-term storage at -20 °C.

7.11.1.3 BAC-DNA preparation

BAC-DNA preparation protocol was adopted from (Warming, Costantino, Court, Jenkins, & Copeland, 2005). For BAC mini-prep, 5 ml of bacterial overnight culture were pelleted at 5,000 rpm for 5 min and the pellet was re-suspended in 250 µl P1 (resuspension) buffer. An equal amount of P2 (lysis) buffer was added for 5 min followed by addition of P3 (neutralisation) buffer (250 µl) and incubation for 5 min on ice. The protein precipitate was collected by centrifugation at 13,500 rpm for 5 min and the supernatant containing the BAC-DNA was again centrifuged to obtain a clean DNA preparation. Subsequently, the DNA was precipitated with isopropanol (10 min on ice) and pelleted at 13,000 rpm for 10 min. The pellet was washed with 70 % EtOH and air-dried for 10 min. Isolated BAC-DNA (typically, 1-1.5 µg) was dissolved in 50 µl TE buffer by incubation at 37 °C for 1 hour.

For the BAC maxi-prep, the NucleoBond BAC Purification Maxi Kit was used according to the manufacturer's protocol.

7.11.1.4 Transformation of bacteria

For the amplification of plasmid DNA in bacterial cultures, bacteria were transformed either by electroporation or by a heat shock.

Transformation of bacteria by electroporation:

Electro-competent bacteria *E.coli* K12 XL-1 Blue endA1 gyrA96(nalR) thi-1 recA1 relA1 lac glnV44 F`[:: Tn10 proAB + laclq (lacZ)M15]hsdR17(rK-mK+) or were generated according to the standard procedure (Moritz Gegg, doctoral thesis, https://mediatum.ub.tum.de/doc/1114671/document.pdf; last change 10.11.2014) and thawed on ice. Plasmid DNA (1-2 µl) was added and the mixture and electroporation was carried out in a pre-cooled electroporation cuvette (0.1 cm) at 2.5 kV. Bacteria were then immediately transferred into 1 ml of LB medium and incubated at 37 °C under agitation (850 rpm) for 1 hour. Finally, transformed bacteria were plated onto LB plates supplemented with the required antibiotic and incubated at 37 °C overnight.

Transformation of bacteria using heat shock:

For this purpose Dh5α cells (section 6.11) were used. Bacteria were thawed on ice, and 4 µl of vector DNA were added followed by an incubation on ice for 30 min. A short heat shock (42 °C, 90 s) was applied to the bacteria. Immediately after that, bacteria were transferred into 1 ml LB medium, briefly incubated on ice and let to regenerate for 1 hour at 37 °C under constant agitation (850 rpm). Bacteria were plated as described above.

7.11.1.5 DNA sequencing

The vector assembly was confirmed by sequencing using the BigDye™ Terminator v3.1 Cycle Sequencing Kit (Life Technologies 4337457).

A typical **sequencing reaction** contained:

Long sequence	Short sequence	
1.0 µl	0.5 µl	Big Dye (containing the polymerase)
1.0 µl	2.0 µl	Big Dye buffer
10 pM	10 pM	Primer (sence or antisense)
Template DNA: (n) bp/ 100 = x ng DNA		
Σ 5.0 µl		

PCR programme:

96°C 1 min → (96°C 10 sec → 50°C 5 sec → 60°C 4 min) x 35 → 16°C ∞.

The amplified DNA was precipitated by incubation with a mixture of EDTA, NaAc in EtOH (0.5 µl 125 mM EDTA, 2.0 µl 3 M NaAC, and 50 µl 100% EtOH) for 15 min at RT. DNA was pelleted at 11,000 rpm at 4 °C for 30 min, then washed with 70 % EtOH and air-dried. The DNA pellet was re-suspended in 25 µl HPLC water and samples were sequenced by the HMGU sequencing service facility.

7.11.2 Cell culture and homologous recombination in ES cells

7.11.2.1 ES cell culture

Mouse embryonic stem (ES) cells IDG3.2 (Hitz et al., 2007) were cultured at 37 °C in 5-7 % CO_2 in a humid incubator on a layer of mouse embryonic fibroblasts (MEF) feeder cells to prevent spontaneous differentiation. ES cell medium containing DMEM (Invitrogen) supplemented with 15 % FCS (PAN), 2 mM L-glutamine (Invitrogen, 200 mM), 1x MEM (nonessential amino acids, 100x ,Invitrogen), 0.1 mM β-mercaptoethanol (Invitrogen, 50 mM), 2 mM HEPES (Invitrogen, 200 mM) and 1500 U/ml LIF was used. Prior to the use for the ES cell culture, MEFs were treated with 1 mg/ml mitomycin C (MMC) in MEF medium (section 6.8) (45 min, 37 °C) to inhibit their growth. ES cells were split for expansion every two days using 0.05 % trypsin-EDTA. Therefore, ES cells were washed with PBS (without Mg^{2+}/Ca^{2+}) and incubated with trypsin-EDTA for 5 min at 37 °C in 5-7 % CO_2 in a humid incubator. Cells were pelleted at 250x g for 4 min, re-suspended in ES cell medium and plated on feeder cells. For long-term storage, ES cells were cryopreserved in liquid nitrogen. For this purpose, cells were trypsinized as described above, pelleted and re-suspended in ES freezing medium containing 4 ml ES cell medium, 5 ml FCS and 1 ml DMSO. Finally, cells were aliquoted into cryovials and transferred into freezing boxes for 12 hours to gradually reach -80 °C before the long-term storage in liquid nitrogen.

Cells were thawed in a 37 °C water bath, immediately transferred into pre-warmed ES cell medium for pelleting (250x g, 4min) and plated in fresh ES cell medium on feeder cells as described before.

7.11.2.2 Homologous recombination in ES cells and picking of neomycin-resistant clones

For one electroporation, ½ 10 cm dish of IDG3.2 ES cells was trypsinized, washed with PBS (without Mg^{2+}/Ca^{2+}) and cell pellet was re-suspended in 1.5 ml of ice-cold PBS. One half of the suspension was mixed with 25 µg (100 µl) of the linearized targeting vector (chapter 7.11.1) and electroporated in a pre-cooled cuvette at 220 V, 500 µF and ∞ resistance (two pulses). Next, the cuvette was incubated on ice for additional 5 min, and the content was plated for culture on feeder cells supplemented with ES cell medium. After 24 hours, neomycin-resistant clones were selected for 6-8 days using 300 µg/ml G418 (Invitrogen). Hereby, the medium was changed daily. After washing with PBS, resistant ES clones, which looked compact and round, were detached and picked under a stereo microscope in 20 µl PBS into a 96-well plate (conical bottom) filled with 60 µl PBS. Afterwards, cells were trypsinized in 30 µl trypsin-EDTA per well for 15 min at 37 °C and split equally onto two 96-well plates, one coated with 0.1 % gelatine for genomic DNA preparation (section 7.11.3), and one with a feeder layer for the freezing of the ES clones. After 2-4 days, ES cells were cryopreserved or used for DNA preparation.

7.11.2.3 Cryopreservation of selected ES clones

For cryopreservation, ES cell clones cultured in 96-well plates, as described above, were washed once with PBS and trypsinized for 5 min at 37 °C. 100 µl of 2x freezing medium containing (4 ml ES cell medium, 4 ml FCS and 2 ml DMSO) was added per well. Plates were sealed with parafilm, wrapped in paper tissue and stored for 6-8 weeks at -80 °C.

7.11.3 Preparation of genomic DNA from ES cells (for Southern Blot analysis)

Confluent ES cell clones, plated on 0.1 % gelatine in 96-well, were washed twice with PBS and lysed using genomic DNA lysis buffer (chapter 6.7) supplemented with 100 µg/ml proteinase K in a sealed plate overnight at 55 °C in a humid chamber. DNA was then precipitated using sodium chloride in ice-cold ethanol (150 µl of 5 M sodium chloride in 10 ml of 100 % EtOH) for 30 min at RT. Precipitated DNA was washed three times with ice-cold 70 % ethanol and dried for 10-15 min at RT. The DNA pellet was re-suspended in TE buffer and incubated at 4 °C overnight in a humid chamber.

7.11.4 Southern blot

Homologous recombination at the *Fltp* locus was ensured by Southern blot analysis using the 5′ Fltp probe (chapter 6.10.4) located outside the targeting vector. Genomic DNA, isolated from ES clones (described in 7.11.3), was digested with the restriction enzyme *DraIII* directly in 96-well plates sealed with parafilm at 4 °C overnight. A typical **DNA digestion reaction** contained:

25.0 µl DNA

0.40 µl 100x BSA (final concentration: 1x BSA)

0.40 µl 100 mM spermidine (final conc.: 1 mM spermidine)

0.25 µl RNase A 1 mg/ml (final amount: 6.25 µg RNase A)

4.00 µl 10x enzyme buffer (final conc.: 1x enzyme buffer)

2.50 µl enzyme (10 U/µl) (final conc.: 25 U enzyme)

7.45 µl H_2O

Digested DNA was separated on a 0.8 % agarose gel in TAE buffer at 30 V overnight. The gel was depurinised, denatured and neutralised (buffer recipes in section 6.7) and blotted onto the Hybond-N+ nitrocellulose membrane in 20x SSC overnight. Membrane was then backed for 30 min at 80 °C to enable a stable DNA binding to the membrane. The membrane was subsequently pre-hybridised with the hybridisation solution at 65°C for 3 hours.

The hybridisation probe was radioactively labelled with (α-^{32}P) dCTP and 5 U Klenow enzyme (3′→ 5′ exo(-) Klenow) included in the Stratagene Kit (#300385) according to the manufacturer's protocol. 1x10^6 counts were used per 1 ml hybridization solution. Prior to the hybridisation, the probe was chemically denatured using 50 µl 10 N NaOH and mixed with 500 µl denatured (boiled for 10 min at 100 °C) salmon sperm DNA (10 mg/ml). For neutralisation, 300 µl 2 M Tris (pH 8.0), and subsequently 475 µl 1 M HCl were drop-wise pipetted into the tube. Subsequently the probe was hybridised onto the membrane at 65 °C overnight. The membrane was then washed in 2x SSC/0,5 % SDS at 65 °C till the radioactivity reached a value of around 35x10^2 counts. Afterwards, the membrane was wrapped in saran wrap and exposed to a film (Kodak, BioMax) using a film cassette at -80°C for 2 days. The film was developed using AGFA Curix 60 developing machine.

7.11.5 Generation of Fltp-Venus chimeras

Three homologous recombined clones were aggregated with CD1 morulae (performed by Heide Oller, ISF, Helmholtz Zentrum München) to generate germline chimeras. The *loxP*-flanked *neo*-selection cassette was subsequently removed by intercrossing the chimeras with the *ROSA26-Cre* mouse line (Soriano, 1999) and excision was confirmed by PCR. To eliminate the *Cre* allele, mice negative for the neo-cassette (genotyping PCR, section 7.1.1.2) were backcrossed to C57BL/6 animals. Further analyses were carried out on Fltp-Venus fusion mice with mixed background. *Fltp^V* mouse genotypes were assessed using the PCR described in section 7.1.1.2.

7.12 Statistical analysis of bulk data

Statistical analyses were performed using the GraphPad Prism 6 Software (GraphPad Software, USA). Two-sided and unpaired Welch-corrected *t*-test was used to compare two independent groups. For statistical comparison of longitudinal data (body weight curves, GTT, IST), two-way ANOVA corrected by Sidak's multiple comparison test was used. P-values of <0.05 % were considered statistically significant. The data are shown as mean ± standard error of the mean (SEM). In Box-and-Whiskers plots, data are represented as minimum and maximum with centre lines indicating the median. For metabolic studies (GTT, IST), sample size was statistically determined, otherwise sample size estimates were not used. All samples represent biological replicates. Studies were not conducted blinded with some exceptions.

7.12.1 Gene expression analysis of bulk sorted cells

This analyses were performed in collaboration with Dr. Martin Irmler, Institue of Experimental Genetics, and Michael Sterr, Institute of Diabetes and Regeneration Research, Helmholtz Center Munich.

Statistical transcriptome analyses were performed using the statistical programming environment R (R Development Core Team: Team, R. D. C., R: A language and environment for statistical computing. 2005) implemented in CARMAweb (Rainer, Sanchez-Cabo, Stocker, Sturn, & Trajanoski, 2006). Gene-wise testing for differential expression was carried out employing the limma t-test and P-values were adjusted by Benjamini-Hochberg multiple testing correction (FDR < 10%), applied due to the low number of replicates. Heatmaps were generated using CARMAweb and cluster dendrograms were drawn with the R script hclust. Pathway enrichment analyses were carried out with Ingenuity pathway software (IPA, QIAGEN Redwood City).

7.12.2 Overlap of transcriptome and metabolome

This analysis was performed in collaboration with the Institue of Computational Biology, Helmholtz Center Munich.

Lists of genes participating in the candidate pathways from the Ingenuity Canonical Pathways analysis were compiled. For each of these genes, information on the reaction it is involved in and the participating metabolites were extracted from the mouse specific BiGG databank (https://www.ncbi.nlm.nih.gov/pmc/articles/PMC2874806/, https://www.ncbi.nlm.nih.gov/pubmed/20959003). If genes and metabolites participating in a reaction were also significant in their analyses, the reaction and its pathway were set to be affected on both the metabolomics and the transcriptomics level.

7.12.3 Bioinformatics and statistical analysis of MALDI-MSI data

These analyses were performed by Dr. Na Sun, Research Unit Analytical Pathology, Helmholtz Center Munich.

MATLAB R2014b (v.7.10.0, Mathworks, Inc., Natick, MA) was used as MALDI spectral pre-processing tool for the bioinformatical and statistical analysis of the MALDI-MSI data. Peak picking was carried out by applying the following parameters and as described in Aichler et al., 2017; Buck et al., 2015; Sun et al., 2014: m/z 0.0005 minimal peak width, signal to noise threshold of 4, and intensity threshold of 0.01 %. Isotopes were automatically identified and excluded. Two-tailed student's t-test was used for statistical comparisons and metabolites with an intensity fold change ≥ 2 and a p-value ≤ 0.05 were considered significant. Annotation of metabolites was carried out by matching accurate mass with databases as previously published (Aichler et al., 2017; Buck et al., 2015; Sun et al., 2014) (mass accuracy ≤ 4ppm, METLIN, http://metlin.scripps.edu/; Human Metabolome Database, http://www.hmdb.ca/ (Wishart et al., 2007); MassTRIX, http://masstrix3.helmholtz-muenchen.de/masstrix3/; METASPACE, http://annotate.metaspace2020.eu/ (Palmer et al., 2017)). Heatmap-based clustering, principal component (PCA) and enrichment analysis of metabolic pathways were performed using MetaboAnalyst 3.0 (http://www.metaboanalyst.ca) (Xia & Wishart, 2010). Lists of peacks with their respective intensities were uploaded to MetaboAnalyst, without data filtering, no data transformation and without scaling.

7.13 Computational analyses of single cell data

Computational analysis of the single-cell RNA sequencing and single-cell RT-qPCR data was performed by Sophie Tritschler, Institute of Computational Biology, Helmholtz Center Munich.

7.13.1 Preprocessing of droplet-based scRNA-seq data

CellRanger analysis pipeline (Version 2.0.0) provided by 10X Genomics was used for demultiplexing of raw base call (BCL) files, alignment, read filtering, barcode and UMI counting. Reads were aligned to the mm10-reference genome as found on the 10X-Website. All further analyses were performed using the python-based Scanpy API (Wolf, Angerer, & Theis, 2018) unless otherwise indicated (for software specifications and code availability see below). High quality cell barcodes were selected using the standard CellRanger cell detection algorithm, which is based solely on the UMI count distribution. Based on our observation of a high variability of RNA content and number of genes expressed per cell (UMI count > 1) among cell types, a further selection step was introduced, and cells with >1000 expressed genes were additionally included. High fraction of counts from mitochondrial genes (10% or more) within a cell is commonly interpreted as a sign for stressed or dying cells. Accordingly, we excluded such cells from further analyses. For all samples, cell by gene count matrices were then concatenated to a single data matrix, and values log transformed (log(count+1)). Further, we excluded genes with expression in <20 cells. To facilitate clustering, batch correction was run using a python

implementation of ComBat ((Johnson, Li, & Rabinovic, 2007), available on https://github.com/brentp/combat.py) with default parameters and defining each sample as one batch. ComBat was recommended by an extensive batch correction method comparison and evaluation (Büttner, Miao, Wolf, Teichmann, & Theis, 2019). An initial round of unsupervised graph-based clustering (louvain) was performed to assess contamination from non-epithelial cells. Based on this, we removed a clearly distinct cluster of cells, highly expressing marker genes of immune cells.

Top 2000 variable genes were selected based on normalized dispersion of genes as previously described, using the pp.filter_genes_dispersion function from the Scanpy API with default parameters. Changing the number of selected top variable genes to 1500 or 3000 did not have a considerable influence on the further analyses (data not shown). This output matrix was used as an input for further analyses. Differential expression testing, where log transformed raw data was used without batch correction, was an exception. Instead, batch was included as covariate (see below).

7.13.2 Low dimensional embedding and clustering for cell type annotation

To compute the single cell neighborhood graph on the 50 first principal components, Scanpy (pp.neighbors) with a local neighborhood size of 25 and a Gaussian kernel for computing connectivities (method=gauss) was used. Uniform Manifold Approximation and Projection (UMAP) was run for visualization as recently established (Becht et al., 2018). Louvain-based clustering at varying resolution in different parts of the data manifold as adopted by Scanpy from louvain-igraph was used to identify cell subtypes (Traag V., 2017, https://github.com/vtraag/louvain-igraph) (‚split-and-merge' approach, for detailed steps of clustering analysis see code – available upon request). All cell subtypes were annotated based on the expression of known marker genes and clusters merged, if only reflecting heterogeneity within a cell type. We used the tl.rank_genes function of Scanpy and the wilcoxon rank-sum test to identify novel marker genes and characteristic gene signatures. To determine marker genes over all lineages, genes associated with the Gene Ontology (GO) term for cell cycle (GO:0007049) were excluded before testing, and the top 50 ranking genes with a score > 5 were then used.

For the characterization of the enteroendocrine cell types and to assess possible lineage relations, we performed for each subpopulations pairwise tests against all other subpopulations (including other lineages, but excluding the Lgr5^{+} EECs due to the overlapping expression of many enteroendocrine subtype markers in this cluster). Hereby, all genes with a score > 5 within top 1200 ranking genes in every test were defined as specific subtype markers. Further, to identify lineage markers, pairwise tests against all other subpopulations, except mature endocrine subtypes and progenitor subtypes of a later stage, were performed. All genes with a score > 5 within top 1200 ranking genes in every test were defined as lineage genes. This approach describes genes which are specifically turned on in a lineage progenitor and then potentially sustained in the derived cell types.

7.13.3 Annotation of cell types and states based on gene sets (cell scores)

To specify a cell score for a given set of genes, an approach as described by Satija et al. and implemented in the tl.score_cells function in Scanpy was used with default parameters (Satija, Farrell, Gennert, Schier, & Regev, 2015). In brief, a score is defined as the average expression of a gene set subtracted with the average expression of a randomly sampled background set with expression values within the same range. To assess the cell cycle genes and distinguish between S and G2/M phase, genes as defined in Tirosh et al. were used with the tl.score_genes_cell_cycle (Tirosh et al., 2016). For cell type scores, gene sets as described in (Haber et al., 2017) were used. Genes from GO Biological processes were used (Glycolytic process: GO:0006096, Oxidative phosphorylation: GO:0042776,GO:1903862,GO:0042773) to specify metabolic signatures. For the mitochondrial gene signature, genes with an mt-prefix were considered. The Wnt signaling gene set was manually curated and included genes *Lgr5, Ascl2, Ccnd1, Ppard, Cd44, Tcf1, Axin2, Myc, Mycn, Bmp4, Jag1, Jag2, Sox9, Ephb4, Mmp7, Fzd2* and *Fzd7*. To specify the

proximal and distal identities, cell types were clustered with increased resolution (tl.louvain) and clusters annotated based on regional markers identified by Haber et al. (Haber et al., 2017).

7.13.4 Reconstruction of lineage relationships and differentiation trajectories

Partition-based graph abstraction (PAGA) was applied to infer lineage relationships between clusters (Wolf, Hamey, et al., 2018) using the tl.paga function of Scanpy with a threshold of 0.001 for the overall cell map and 0.01 for the enteroendocrine lineage. PAGA creates a simple abstracted graph of clusters of the single-cell neighborhood graph. Confidence of connections is represented by edge weights and is quantified by the connectivity of clusters. Paths in the abstracted graph represent potential differentiation trajectories, rooting in the stem cell cluster. To infer directionality of differentiation, a stochastic version of RNA velocity estimation as initially proposed by (La Manno et al., 2018) was applied using the scVelo python package (Bergen V., 2018, https://github.com/theislab/scvelo). Velocyto pipeline (http://velocyto.org) was used to extract splicing information of reads (spliced/unspliced), stored in a loompy file and then read into an AnnData object for downstream analysis with scVelo and Scanpy. Velocities and the RNA force field were assessed according to the recommended steps of scVelo, as follows: preprocessing, computing first- and second-order moments, estimating velocities, and constructing a velocity graph. Genes were first filtered and top 3000 variable genes were selected by dispersion. Spliced and unspliced data layers were normalised to the initial total count per cell and then log transformed. Subsequntly, first- and second-order moments were calculated for each cell across its nearest neighbours of a single-cell neighbourhood-graph in PC space (number of neighbours=15, number of PCs=50). For each gene, estimates for velocities were then calculated by fitting a stochastic model of transcriptional dynamics. At last, a velocity graph was generated from the correlations between potential cell transitions in the neighbourhood graph and the predicted cell state change given by the velocity vector. This graph was the basis for the projection of the estimated velocities into the low dimensional UMAP space.

7.13.5 Correlation of gene signatures

For the correlation of expression profiles between subpopulations, the average of the first 50 PCs over all cells within a subpopulation was used. Based on this, the pairwise Pearson correlation between subpopulations was calculated. Clustering of correlation values was carried out using the seaborn clustermap function with euclidean distance metric and average linkage method (UPGMA algorithm).

7.13.6 Differential expression analysis and GO term enrichment

Differential expression between conditions was analysed using limma-trend (Law, Chen, Shi, & Smyth, 2014) via an rpy2 (2.9.1) interface with batch and scaled cellular detection rate (the fraction of detected genes per cell) as additional covariates. For differential expression analysis in single-cell data, Limma was recommended as one of the top performers in an extensive comparison and performance evaluation of available methods (Soneson & Robinson, 2018) https://paperpile.com/c/PROaZZ/R968. Previously identified ambient genes and genes, expressed in less than 1% of cells in any of the two subsets tested, were excluded. Genes with a p-value < 0.01 and an estimated logFC (output from limma, not the actual logFC, as log transformed data was the input) > 0.1 were used for GO term enrichment. The latter was performed using the gseapy (0.9.3) implementation of EnrichR (Kuleshov et al., 2016), and genes were weighted by their logFC values (for details see code – available upon request).

7.13.7 Identification of free-floating ‚ambient' mRNA

In droplet-based single-cell RNAseq, lysed cells in the single-cell solution release mRNA (free-floating, ambient mRNA). The ambient RNA is included into the droplets with cells and is not distinguishable

from the endogenous mRNA when sequenced. This results in contaminating background reads, especially, from highly expressed genes. For abundantly expressed genes, this effect is expected to be comparable between different samples, given that an approximately same total number of cells is lysed and these genes are not cell-type specific. However, we observed that background expression of highly expressed marker genes of a certain cell type varies between samples. This is most likely due to changes in cell type frequencies, *i.e.* the ambient mRNA is more or less likely to be derived from a specific cell type. Such effects can lead to false positives in cell types with only background expression level when performing the differential expression analysis between samples. To identify such ambient marker genes, we assessed gene expression in empty droplets (1-200 total number of UMI counts), in which all transcripts originate from free-floating RNA. For each sample, genes which were expressed in >1% of the empty droplets were considered. We then concatenated the samples and calculated the log2 fold change of the mean of each gene between the two diet conditions. We argued that any gene showing a high fold change in expression between the conditions in empty droplets would generate false positives in subsequent differential expression analyses. Based on this, we identified *Ifitm3, H2afv, Zfos1, Smim24, Plac8, Oat, Fth1, Aldob, Defa24, Gm15284, Lyz1, Gm14851, Fabp1, Itln1, Defa17, AY761184, Gm14850, Defa20, Clps, Gm7861, Spink4, Ang4, Defa22, Defa26, Defa21, Fabp2, Gm21002, Defa23, Defa-rs1, Gm15308, Defa3, Zg16, Agr2, Tff3, Reg4, Ccl6, Defa5, Mptx2, Fcgbp, Tmsb10* as cell-type specific marker genes with a clear ambient effect (log2 fold change in empty droplets >0.15 or <-0.44). Instead of excluding these genes from differential expression tests, we analysed the distribution of the estimated logFCs (model output) for each gene over all comparisons performed. As expected, for most comparisons the estimated logFCs were similar and within the range of the ambient effect. Outliers in these distributions were set to be significant changes (‚above ambient effects').

7.13.8 Analysis of changes in cell type composition

Dirichlet-Mulitnomial model was used to compare the shifts in cell type proportions between the two conditions. In particular, the detected cell count data was modelled with a Multinominal distribution and a Dirichlet prior on the cell type proportions as described in the following:

$p_c \sim$ Dirichlet (1); $\quad \Delta_{diff} = p_{c1} - p_{c2}$; $\quad y_{c,i} \sim$ Multinomial ($N_{c,i}$, p_c).

Hereby, $y_{c,i} = (y_{c,i,1}, ...y_{c,i,k})$ indicates the vector of cell counts representing the abundances of cell types in condition c, with $y_{c,i,j}$, denoting the frequency of the jth cell type, for j=1,...,k, in the ith replicate, and $N_{c,i}$ being the total number of cell counts of replicate i in condition c. Δ_{diff} indicates the shift in cell type proportions between conditions c_1 and c_2. Parameters were calculated with Hamiltonian Monte Carlo using NUTS (https://arxiv.org/abs/1111.4246) for 20,000 iterations across four chains and a burn-in of 5,000 iterations. Convergence was analysed based on Gelman-Rubin convergence diagnostics (Gelman & Rubin, 1992). Samples were taken from the posterior distribution to calculate the expected mean, standard deviation, and the 95% highest posterior density interval (HPD-region) of the frequency shift for each cell type. A shift was considered credible if the HPD-region did not include 0.

7.13.9 Preprocessing of the single-cell qRT-PCR data

Processing of the single-cell qRT-PCR data was performed in R (http://www.r-project.org/). Ct values were substracted from the assumed limit of detection of the BioMark (LOD=29), which was higher than any of the Ct values which passed quality control. The expression values of the three most robustly expressed housekeeping genes *Uba52, ActB* and *Hsp90* were used as quality control measure for cells. All cells which did not express all three housekeepers were excluded. Since the three synthetic RNAs of different concentrations did not amplify within the detectable range of the BioMark system in all experimental runs, we did not use them as a reference and removed them from further analyses. All

housekeeping genes (*Rn18S, ActB, Hsp90, Uba52*) and *GFP* were detected in the negative control and, therefore, were excluded from further analysis. The remaining genes were expressed in more than 3 cells. 26 missing values (due to technical problems during experimental proceedings) were then imputed with the mice function of the mice package using the Predictive Mean Matching method. Obtained cell x gene matrix of ΔCt values of 83 genes and 465 cells was input for all further analyses.

7.13.10 Single-cell qPCR analysis

The analysis of the single-cell qRT-PCR data was performed using Scanpy following a similar pipeline as for the scRNAseq data described above. The single-cell neighbourhood graph was calculated on the 12 first principal components with a local neighbourhood size of 25 (pp.pca and pp.neighbours). UMAP was then run for visualization (tl.umap). We used Louvain-based clustering at varying resolution for subtype annotation based on the expression of known marker genes (pp.louvain). Subtype annotation and branching trajectories of lineages and were verified in a Diffusion Map representation (not shown, the code is available upon request). PAGA was used to infer lineage relationships as described above (tl.paga).

7.13.11 Software specifications and code and data availability

Python v3.5.4 with the Scanpy v.1.0.4 and anndata v0.5.10 was used for all analysis of the scRNAseq data from UMI count matrices and of single-cell qRT-PCR data from filtered ΔCt matrices. Versions of packages required by Scanpy, which might have influence on numerical results, were numpy v1.14.2, scipy v1.0.1, pandas v0.22.0, scikit-learn v0.19.1, statsmodels v0.8.0, python-igraph v0.7.1, louvain v0.6.1. Cell type frequency shifts were modelled using the pymc3 python package and basic tensor functionality of the theano python package.

matplotlib and seaborn were used to plot all figures, and data was exported to excel-sheets with xlsxwriter v1.0.2. Code and custom scripts for complete analysis are available upon publication of the first-author manuscript based on the results of these PhD thesis or upon request.

8 List of figures and tables

8.1 List of figures

8.2 List of tables

9 References

Acevedo, J. M., Hoermann, B., Schlimbach, T., & Teleman, A. A. (2018). Changes in global translation elongation or initiation rates shape the proteome via the Kozak sequence. *Scientific Reports*, *8*(1), 4018. https://doi.org/10.1038/s41598-018-22330-9

Ackerman, N. B. (1981). Observations on the improvements in carbohydrate metabolism in diabetic and other morbidly obese patients after jejunoileal bypass. *Surgery, Gynecology & Obstetrics*, *152*(5), 581–586. Retrieved from http://www.ncbi.nlm.nih.gov/pubmed/7013122

Adams, T. D., Davidson, L. E., Litwin, S. E., Kolotkin, R. L., LaMonte, M. J., Pendleton, R. C., … Hunt, S. C. (2012). Health Benefits of Gastric Bypass Surgery After 6 Years. *JAMA*, *308*(11), 1122. https://doi.org/10.1001/2012.jama.11164

Adams, T. D., Gress, R. E., Smith, S. C., Halverson, R. C., Simper, S. C., Rosamond, W. D., … Hunt, S. C. (2007). Long-Term Mortality after Gastric Bypass Surgery. *New England Journal of Medicine*, *357*(8), 753–761. https://doi.org/10.1056/NEJMoa066603

Ahrén, B. (2013). Incretin dysfunction in type 2 diabetes: Clinical impact and future perspectives. *Diabetes & Metabolism*, *39*(3), 195–201. https://doi.org/10.1016/J.DIABET.2013.03.001

Aichler, M., Borgmann, D., Krumsiek, J., Buck, A., MacDonald, P. E., Fox, J. E. M., … Walch, A. (2017). N-acyl Taurines and Acylcarnitines Cause an Imbalance in Insulin Synthesis and Secretion Provoking β Cell Dysfunction in Type 2 Diabetes. *Cell Metabolism*, *25*(6), 1334–1347.e4. https://doi.org/10.1016/j.cmet.2017.04.012

Aichler, M., & Walch, A. (2015). MALDI Imaging mass spectrometry: current frontiers and perspectives in pathology research and practice. *Laboratory Investigation*, *95*(4), 422–431. https://doi.org/10.1038/labinvest.2014.156

Al-Dwairi, A., Brown, A. R., Pabona, J. M. P., Van, T. H., Hamdan, H., Mercado, C. P., … Simmen, F. A. (2014). Enhanced Gastrointestinal Expression of Cytosolic Malic Enzyme (ME1) Induces Intestinal and Liver Lipogenic Gene Expression and Intestinal Cell Proliferation in Mice. *PLoS ONE*, *9*(11), e113058. https://doi.org/10.1371/journal.pone.0113058

Alberti, K. G. M. M., & Zimmet, P. Z. (1998). Definition, diagnosis and classification of diabetes mellitus and its complications. Part 1: diagnosis and classification of diabetes mellitus. Provisional report of a WHO Consultation. *Diabetic Medicine*, *15*(7), 539–553. https://doi.org/10.1002/(SICI)1096-9136(199807)15:7<539::AID-DIA668>3.0.CO;2-S

Amireault, P., Sibon, D., & Côté, F. (2013). Life without Peripheral Serotonin: Insights from Tryptophan Hydroxylase 1 Knockout Mice Reveal the Existence of Paracrine/Autocrine Serotonergic Networks. *ACS Chemical Neuroscience*, *4*(1), 64–71. https://doi.org/10.1021/cn300154j

Anderle, P., Sengstag, T., Mutch, D. M., Rumbo, M., Praz, V., Mansourian, R., … Roberts, M.-A. (2005). Changes in the transcriptional profile of transporters in the intestine along the anterior-posterior and crypt-villus axes. *BMC Genomics*, *6*(1), 69. https://doi.org/10.1186/1471-2164-6-69

Andersson-Rolf, A., Zilbauer, M., Koo, B.-K., & Clevers, H. (2017). Stem Cells in Repair of Gastrointestinal Epithelia. *Physiology*, *32*(4), 278–289. https://doi.org/10.1152/physiol.00005.2017

Aranias, T., Grosfeld, A., Poitou, C., Omar, A. A., Le Gall, M., Miquel, S., … Serradas, P. (2015). Lipid-rich diet enhances L-cell density in obese subjects and in mice through improved L-cell differentiation. *Journal of Nutritional Science*, *4*, e22. https://doi.org/10.1017/jns.2015.11

Arnold, M., Pandeya, N., Byrnes, G., Renehan, P. A. G., Stevens, G. A., Ezzati, P. M., … Soerjomataram, I. (2015). Global burden of cancer attributable to high body-mass index in 2012: a population-based study. *The Lancet. Oncology*, *16*(1), 36–46. https://doi.org/10.1016/S1470-2045(14)71123-4

Backhed, F., Ley, R. E., Sonnenburg, J. L., Peterson, D. A., & Gordon, J. I. (2005). Host-Bacterial Mutualism in the Human Intestine. *Science*, *307*(5717), 1915–1920. https://doi.org/10.1126/science.1104816

Bäckhed, F., Manchester, J. K., Semenkovich, C. F., & Gordon, J. I. (2007). Mechanisms underlying the resistance to diet-induced obesity in germ-free mice. *Proceedings of the National Academy of Sciences*, *104*(3), 979–984. https://doi.org/10.1073/pnas.0605374104

Bader, E., Migliorini, A., Gegg, M., Moruzzi, N., Gerdes, J., Roscioni, S. S., … Lickert, H. (2016). Identification of proliferative and mature β-cells in the islets of Langerhans. *Nature*, *535*(7612), 430–434. https://doi.org/10.1038/nature18624

Baldassano, S., Amato, A., Cappello, F., Rappa, F., & Mulè, F. (2013). Glucagon-like peptide-2 and mouse intestinal adaptation to a high-fat diet. *Journal of Endocrinology*, *217*(1), 11–20. https://doi.org/10.1530/JOE-12-0500

Barker, N., van Es, J. H., Kuipers, J., Kujala, P., van den Born, M., Cozijnsen, M., … Clevers, H. (2007). Identification of stem cells in small intestine and colon by marker gene Lgr5. *Nature*, *449*(7165), 1003–1007. https://doi.org/10.1038/nature06196

Basak, O., Beumer, J., Wiebrands, K., Seno, H., van Oudenaarden, A., & Clevers, H. (2017). Induced Quiescence of Lgr5+ Stem Cells in Intestinal Organoids Enables Differentiation of Hormone-Producing Enteroendocrine Cells. *Cell Stem Cell*, *20*(2), 177–190.e4. https://doi.org/10.1016/J.STEM.2016.11.001

Bastide, P., Darido, C., Pannequin, J., Kist, R., Robine, S., Marty-Double, C., … Jay, P. (2007). Sox9 regulates cell proliferation and is required for Paneth cell differentiation in the intestinal epithelium. *The Journal of Cell Biology*, *178*(4), 635–648. https://doi.org/10.1083/jcb.200704152

Bates, M. D., Erwin, C. R., Sanford, L. P., Wiginton, D., Bezerra, J. A., Schatzman, L. C., … Aronow, B. J. (2002). Novel genes and functional relationships in the adult mouse gastrointestinal tract identified by microarray analysis. *Gastroenterology*, *122*(5), 1467–1482. https://doi.org/10.1053/gast.2002.32975

Becht, E., McInnes, L., Healy, J., Dutertre, C.-A., Kwok, I. W. H., Ng, L. G., … Newell, E. W. (2018). Dimensionality reduction for visualizing single-cell data using UMAP. *Nature Biotechnology*, *37*(1), 38–44. https://doi.org/10.1038/nbt.4314

Bengoechea-Alonso, M. T., & Ericsson, J. (2006). Cdk1/Cyclin B-Mediated Phosphorylation Stabilizes SREBP1 During Mitosis. *Cell Cycle*, *5*(15), 1708–1718. https://doi.org/10.4161/cc.5.15.3131

Bengoechea-Alonso, M. T., & Ericsson, J. (2016). The phosphorylation-dependent regulation of nuclear SREBP1 during mitosis links lipid metabolism and cell growth. *Cell Cycle (Georgetown, Tex.)*, *15*(20), 2753–2765. https://doi.org/10.1080/15384101.2016.1220456

Benner, C., van der Meulen, T., Cacéres, E., Tigyi, K., Donaldson, C. J., & Huising, M. O. (2014). The transcriptional landscape of mouse beta cells compared to human beta cells reveals notable species differences in long non-coding RNA and protein-coding gene expression. *BMC Genomics*, *15*(1), 620. https://doi.org/10.1186/1471-2164-15-620

Beucher, A., Gjernes, E., Collin, C., Courtney, M., Meunier, A., Collombat, P., & Gradwohl, G. (2012). The Homeodomain-Containing Transcription Factors Arx and Pax4 Control Enteroendocrine Subtype Specification in Mice. *PLoS ONE*, *7*(5), e36449. https://doi.org/10.1371/journal.pone.0036449

Beuling, E., Baffour–Awuah, N. Y. A., Stapleton, K. A., Aronson, B. E., Noah, T. K., Shroyer, N. F., … Krasinski, S. D. (2011). GATA Factors Regulate Proliferation, Differentiation, and Gene Expression in Small Intestine of Mature Mice. *Gastroenterology*, *140*(4), 1219–1229.e2. https://doi.org/10.1053/j.gastro.2011.01.033

Beumer, J., Artegiani, B., Post, Y., Reimann, F., Gribble, F., Nguyen, T. N., … Clevers, H. (2018). Enteroendocrine cells switch hormone expression along the crypt-to-villus BMP signalling gradient. *Nature Cell Biology*, *20*(8), 909–916. https://doi.org/10.1038/s41556-018-0143-y

Beumer, J., & Clevers, H. (2017). How the Gut Feels, Smells, and Talks. *Cell*, *170*(1), 10–11. https://doi.org/10.1016/J.CELL.2017.06.023

References

Beyaz, S., Mana, M. D., Roper, J., Kedrin, D., Saadatpour, A., Hong, S.-J., … Yilmaz, Ö. H. (2016). High-fat diet enhances stemness and tumorigenicity of intestinal progenitors. *Nature*, *531*(7592), 53–58. https://doi.org/10.1038/nature17173

Biteau, B., & Jasper, H. (2011). EGF signaling regulates the proliferation of intestinal stem cells in Drosophila. *Development (Cambridge, England)*, *138*(6), 1045–1055. https://doi.org/10.1242/dev.056671

Biton, M., Haber, A. L., Rogel, N., Burgin, G., Beyaz, S., Schnell, A., … Xavier, R. J. (2018). T Helper Cell Cytokines Modulate Intestinal Stem Cell Renewal and Differentiation. *Cell*, *175*(5), 1307–1320.e22. https://doi.org/10.1016/J.CELL.2018.10.008

Bjerknes, M., & Cheng, H. (2010). Cell Lineage metastability in Gfi1-deficient mouse intestinal epithelium. *Developmental Biology*, *345*(1), 49–63. https://doi.org/10.1016/j.ydbio.2010.06.021

Bjerknes, M., Khandanpour, C., Möröy, T., Fujiyama, T., Hoshino, M., Klisch, T. J., … Cheng, H. (2012). Origin of the brush cell lineage in the mouse intestinal epithelium. *Developmental Biology*, *362*(2), 194–218. https://doi.org/10.1016/j.ydbio.2011.12.009

Blatt, E. N., Yan, X. H., Wuerffel, M. K., Hamilos, D. L., & Brody, S. L. (1999). Forkhead Transcription Factor HFH-4 Expression Is Temporally Related to Ciliogenesis. *American Journal of Respiratory Cell and Molecular Biology*, *21*(2), 168–176. https://doi.org/10.1165/ajrcmb.21.2.3691

Blum, B., Roose, A. N., Barrandon, O., Maehr, R., Arvanites, A. C., Davidow, L. S., … Melton, D. A. (2014). Reversal of β cell de-differentiation by a small molecule inhibitor of the TGFβ pathway. *ELife*, *3*, e02809. https://doi.org/10.7554/eLife.02809

Bojic, L. A., & Huff, M. W. (2013). Peroxisome proliferator-activated receptor δ. *Current Opinion in Lipidology*, *24*(2), 171–177. https://doi.org/10.1097/MOL.0b013e32835cc949

Bornstein, J. C. (2012). Serotonin in the Gut: What Does It Do? *Frontiers in Neuroscience*, *6*, 16. https://doi.org/10.3389/fnins.2012.00016

Bosse, T., Piaseckyj, C. M., Burghard, E., Fialkovich, J. J., Rajagopal, S., Pu, W. T., & Krasinski, S. D. (2006). Gata4 is essential for the maintenance of jejunal-ileal identities in the adult mouse small intestine. *Molecular and Cellular Biology*, *26*(23), 9060–9070. https://doi.org/10.1128/MCB.00124-06

Bradley, D., Conte, C., Mittendorfer, B., Eagon, J. C., Varela, J. E., Fabbrini, E., … Klein, S. (2012). Gastric bypass and banding equally improve insulin sensitivity and β cell function. *The Journal of Clinical Investigation*, *122*(12), 4667–4674. https://doi.org/10.1172/JCI64895

Brody, S. L., Yan, X. H., Wuerffel, M. K., Song, S.-K., & Shapiro, S. D. (2000). Ciliogenesis and Left–Right Axis Defects in Forkhead Factor HFH-4–Null Mice. *American Journal of Respiratory Cell and Molecular Biology*, *23*(1), 45–51. https://doi.org/10.1165/ajrcmb.23.1.4070

Brugmann, S. A., & Wells, J. M. (2013). Building additional complexity to in vitro-derived intestinal tissues. *Stem Cell Research & Therapy*, *4*(Suppl 1), S1. https://doi.org/10.1186/scrt362

Buck, A., Ly, A., Balluff, B., Sun, N., Gorzolka, K., Feuchtinger, A., … Walch, A. (2015). High-resolution MALDI-FT-ICR MS imaging for the analysis of metabolites from formalin-fixed, paraffin-embedded clinical tissue samples. *The Journal of Pathology*, *237*(1), 123–132. https://doi.org/10.1002/path.4560

Buczacki, S. J. A., Zecchini, H. I., Nicholson, A. M., Russell, R., Vermeulen, L., Kemp, R., & Winton, D. J. (2013). Intestinal label-retaining cells are secretory precursors expressing Lgr5. *Nature*, *495*(7439), 65–69. https://doi.org/10.1038/nature11965

Buettner, R., Schölmerich, J., & Bollheimer, L. C. (2007). High-fat Diets: Modeling the Metabolic Disorders of Human Obesity in Rodents*. *Obesity*, *15*(4), 798–808. https://doi.org/10.1038/oby.2007.608

Bünger, M., van den Bosch, H. M., van der Meijde, J., Kersten, S., Hooiveld, G. J. E. J., & Müller, M. (2007). Genome-wide analysis of PPARα activation in murine small intestine. *Physiological Genomics*, *30*(2), 192–204. https://doi.org/10.1152/physiolgenomics.00198.2006

Burtscher, I., Barkey, W., & Lickert, H. (2013). Foxa2-venus fusion reporter mouse line allows live-cell analysis of endoderm-derived organ formation. *Genesis*, *51*(8), 596–604. https://doi.org/10.1002/dvg.22404

Büttner, M., Miao, Z., Wolf, F. A., Teichmann, S. A., & Theis, F. J. (2019). A test metric for assessing single-cell RNA-seq batch correction. *Nature Methods*, *16*(1), 43–49. https://doi.org/10.1038/s41592-018-0254-1

Calle, E. E., & Kaaks, R. (2004). Overweight, obesity and cancer: epidemiological evidence and proposed mechanisms. *Nature Reviews Cancer*, *4*(8), 579–591. https://doi.org/10.1038/nrc1408

Cani, P. D., Amar, J., Iglesias, M. A., Poggi, M., Knauf, C., Bastelica, D., … Burcelin, R. (2007). Metabolic Endotoxemia Initiates Obesity and Insulin Resistance. *Diabetes*, *56*(7), 1761–1772. https://doi.org/10.2337/DB06-1491

Cani, P. D., & Jordan, B. F. (2018). Gut microbiota-mediated inflammation in obesity: a link with gastrointestinal cancer. *Nature Reviews Gastroenterology & Hepatology*, 1. https://doi.org/10.1038/s41575-018-0025-6

Chandel, N. S., Jasper, H., Ho, T. T., & Passegué, E. (2016). Metabolic regulation of stem cell function in tissue homeostasis and organismal ageing. *Nature Cell Biology*, *18*(8), 823–832. https://doi.org/10.1038/ncb3385

Chappell, V. L., Thompson, M. D., Jeschke, M. G., Chung, D. H., Thompson, J. C., & Wolf, S. E. (2003). Effects of incremental starvation on gut mucosa. *Digestive Diseases and Sciences*, *48*(4), 765–769. Retrieved from http://www.ncbi.nlm.nih.gov/pubmed/12741469

Cheng, H., & Leblond, C. P. (1974). Origin, differentiation and renewal of the four main epithelial cell types in the mouse small intestine I. Columnar cell. *American Journal of Anatomy*, *141*(4), 461–479. https://doi.org/10.1002/aja.1001410403

Chin, A. M., Hill, D. R., Aurora, M., & Spence, J. R. (2017). Morphogenesis and maturation of the embryonic and postnatal intestine. *Seminars in Cell & Developmental Biology*, *66*, 81–93. https://doi.org/10.1016/J.SEMCDB.2017.01.011

Cimini, A., & Cerù, M. P. (2008). Emerging Roles of Peroxisome Proliferator-Activated Receptors (PPARs) in the Regulation of Neural Stem Cells Proliferation and Differentiation. *Stem Cell Reviews*, *4*(4), 293–303. https://doi.org/10.1007/s12015-008-9024-2

Clee, S. M., & Attie, A. D. (2007). The Genetic Landscape of Type 2 Diabetes in Mice. *Endocrine Reviews*, *28*(1), 48–83. https://doi.org/10.1210/er.2006-0035

Clevers, H. (2013). The Intestinal Crypt, A Prototype Stem Cell Compartment. *Cell*, *154*(2), 274–284. https://doi.org/10.1016/J.CELL.2013.07.004

Clevers, H. C., & Bevins, C. L. (2013). Paneth cells: maestros of the small intestinal crypts. *Annual Review of Physiology*, *75*(1), 289–311. https://doi.org/10.1146/annurev-physiol-030212-183744

Clevers, H., & Nusse, R. (2012). Wnt/β-Catenin Signaling and Disease. *Cell*, *149*(6), 1192–1205. https://doi.org/10.1016/J.CELL.2012.05.012

Cohen, D. H., & LeRoith, D. (2012). Obesity, type 2 diabetes, and cancer: the insulin and IGF connection. *Endocrine-Related Cancer*, *19*(5), F27–F45. https://doi.org/10.1530/ERC-11-0374

Colin, S., Bourguignon, E., Boullay, A.-B., Tousaint, J.-J., Huet, S., Caira, F., … Delerive, P. (2008). Intestine-Specific Regulation of PPARα Gene Transcription by Liver X Receptors. *Endocrinology*, *149*(10), 5128–5135. https://doi.org/10.1210/en.2008-0637

Comelli, E. M., Lariani, S., Zwahlen, M.-C., Fotopoulos, G., Holzwarth, J. A., Cherbut, C., … Grigorov, M. (2009). Biomarkers of human gastrointestinal tract regions. *Mammalian Genome*, *20*(8), 516–527. https://doi.org/10.1007/s00335-009-9212-7

Cummings, D. E., & Overduin, J. (2007). Gastrointestinal regulation of food intake. *Journal of Clinical Investigation*, *117*(1), 13–23. https://doi.org/10.1172/JCI30227

Curtin, J. A., Quint, E., Tsipouri, V., Arkell, R. M., Cattanach, B., Copp, A. J., … Murdoch, J. N. (2003).

Mutation of Celsr1 disrupts planar polarity of inner ear hair cells and causes severe neural tube defects in the mouse. *Current Biology : CB*, *13*(13), 1129–1133. Retrieved from http://www.ncbi.nlm.nih.gov/pubmed/12842012

Dahly, E. M., Guo, Z., & Ney, D. M. (2002). Alterations in Enterocyte Proliferation and Apoptosis Accompany TPN-Induced Mucosal Hypoplasia and IGF-I-Induced Hyperplasia in Rats. *The Journal of Nutrition*, *132*(7), 2010–2014. https://doi.org/10.1093/jn/132.7.2010

Dailey, M. J. (2014). Nutrient-induced intestinal adaption and its effect in obesity. *Physiology & Behavior*, *136*, 74–78. https://doi.org/10.1016/j.physbeh.2014.03.026

Daniely, Y., Liao, G., Dixon, D., Linnoila, R. I., Lori, A., Randell, S. H., … Jetten, A. M. (2004). Critical role of p63 in the development of a normal esophageal and tracheobronchial epithelium. *American Journal of Physiology-Cell Physiology*, *287*(1), C171–C181. https://doi.org/10.1152/ajpcell.00226.2003

de Lau, W., Peng, W. C., Gros, P., & Clevers, H. (2014). The R-spondin/Lgr5/Rnf43 module: regulator of Wnt signal strength. *Genes & Development*, *28*(4), 305–316. https://doi.org/10.1101/gad.235473.113

de Santa Barbara, P., van den Brink, G. R., & Roberts, D. J. (2003). Development and differentiation of the intestinal epithelium. *Cellular and Molecular Life Sciences (CMLS)*, *60*(7), 1322–1332. https://doi.org/10.1007/s00018-003-2289-3

de Wit, N. J., Bosch-Vermeulen, H., de Groot, P. J., Hooiveld, G. J., Bromhaar, M. M. G., Jansen, J., … van der Meer, R. (2008). The role of the small intestine in the development of dietary fat-induced obesity and insulin resistance in C57BL/6J mice. *BMC Medical Genomics*, *1*, 14. https://doi.org/10.1186/1755-8794-1-14

de Wit, N. J. W., Boekschoten, M. V, Bachmair, E.-M., Hooiveld, G. J. E. J., de Groot, P. J., Rubio-Aliaga, I., … Müller, M. (2011). Dose-dependent effects of dietary fat on development of obesity in relation to intestinal differential gene expression in C57BL/6J mice. *PloS One*, *6*(4), e19145. https://doi.org/10.1371/journal.pone.0019145

Defronzo, R. A. (2009). Banting Lecture. From the triumvirate to the ominous octet: a new paradigm for the treatment of type 2 diabetes mellitus. *Diabetes*, *58*(4), 773–795. https://doi.org/10.2337/db09-9028

Dermadi, D., Valo, S., Ollila, S., Soliymani, R., Sipari, N., Pussila, M., … Nyström, M. (2017). Western Diet Deregulates Bile Acid Homeostasis, Cell Proliferation, and Tumorigenesis in Colon. *Cancer Research*, *77*(12), 3352–3363. https://doi.org/10.1158/0008-5472.CAN-16-2860

Desai, S., Loomis, Z., Pugh-Bernard, A., Schrunk, J., Doyle, M. J., Minic, A., … Sussel, L. (2008). Nkx2.2 regulates cell fate choice in the enteroendocrine cell lineages of the intestine. *Developmental Biology*, *313*(1), 58–66. https://doi.org/10.1016/j.ydbio.2007.09.047

Doktorova, M., Zwarts, I., Zutphen, T. van, Dijk, T. H. van, Bloks, V. W., Harkema, L., … Jonker, J. W. (2017). Intestinal PPARδ protects against diet-induced obesity, insulin resistance and dyslipidemia. *Scientific Reports*, *7*(1), 846. https://doi.org/10.1038/s41598-017-00889-z

Drucker, D. J. (2007). The role of gut hormones in glucose homeostasis. *Journal of Clinical Investigation*, *117*(1), 24–32. https://doi.org/10.1172/JCI30076

Drucker, D. J., & Nauck, M. A. (2006). The incretin system: glucagon-like peptide-1 receptor agonists and dipeptidyl peptidase-4 inhibitors in type 2 diabetes. *The Lancet*, *368*(9548), 1696–1705. https://doi.org/10.1016/S0140-6736(06)69705-5

Duerkop, B. A., Vaishnava, S., & Hooper, L. V. (2009). Immune Responses to the Microbiota at the Intestinal Mucosal Surface. *Immunity*, *31*(3), 368–376. https://doi.org/10.1016/j.immuni.2009.08.009

Dunel-Erb, S., Chevalier, C., Laurent, P., Bach, A., Decrock, F., & Le Maho, Y. (2001). Restoration of the jejunal mucosa in rats refed after prolonged fasting. *Comparative Biochemistry and Physiology. Part A, Molecular & Integrative Physiology*, *129*(4), 933–947. Retrieved from http://www.ncbi.nlm.nih.gov/pubmed/11440878

Dusaulcy, R., Handgraaf, S., Skarupelova, S., Visentin, F., Vesin, C., Heddad-Masson, M., … Gosmain,

Y. (2016). Functional and Molecular Adaptations of Enteroendocrine L-Cells in Male Obese Mice Are Associated With Preservation of Pancreatic α-Cell Function and Prevention of Hyperglycemia. *Endocrinology*, *157*(10), 3832–3843. https://doi.org/10.1210/en.2016-1433

El Ouaamari, A., Dirice, E., Gedeon, N., Hu, J., Zhou, J.-Y., Shirakawa, J., … Kulkarni, R. N. (2016). SerpinB1 Promotes Pancreatic β Cell Proliferation. *Cell Metabolism*, *23*(1), 194–205. https://doi.org/10.1016/j.cmet.2015.12.001

Engelstoft, M. S., Egerod, K. L., Lund, M. L., & Schwartz, T. W. (2013). Enteroendocrine cell types revisited. *Current Opinion in Pharmacology*, *13*(6), 912–921. https://doi.org/10.1016/j.coph.2013.09.018

Fang, R., Olds, L. C., & Sibley, E. (2006). Spatio-temporal patterns of intestine-specific transcription factor expression during postnatal mouse gut development. *Gene Expression Patterns : GEP*, *6*(4), 426–432. https://doi.org/10.1016/j.modgep.2005.09.003

Farin, H. F., Jordens, I., Mosa, M. H., Basak, O., Korving, J., Tauriello, D. V. F., … Clevers, H. (2016). Visualization of a short-range Wnt gradient in the intestinal stem-cell niche. *Nature*, *530*(7590), 340–343. https://doi.org/10.1038/nature16937

Farin, H. F., Van Es, J. H., & Clevers, H. (2012). Redundant Sources of Wnt Regulate Intestinal Stem Cells and Promote Formation of Paneth Cells. *Gastroenterology*, *143*(6), 1518–1529.e7. https://doi.org/10.1053/j.gastro.2012.08.031

Feige, J. N., Gelman, L., Michalik, L., Desvergne, B., & Wahli, W. (2006). From molecular action to physiological outputs: Peroxisome proliferator-activated receptors are nuclear receptors at the crossroads of key cellular functions. *Progress in Lipid Research*, *45*(2), 120–159. https://doi.org/10.1016/j.plipres.2005.12.002

Fevr, T., Robine, S., Louvard, D., & Huelsken, J. (2007). Wnt/beta-catenin is essential for intestinal homeostasis and maintenance of intestinal stem cells. *Molecular and Cellular Biology*, *27*(21), 7551–7559. https://doi.org/10.1128/MCB.01034-07

Finucane, M. M., Stevens, G. A., Cowan, M. J., Danaei, G., Lin, J. K., Paciorek, C. J., … Global Burden of Metabolic Risk Factors of Chronic Diseases Collaborating Group (Body Mass Index). (2011). National, regional, and global trends in body-mass index since 1980: systematic analysis of health examination surveys and epidemiological studies with 960 country-years and 9·1 million participants. *The Lancet*, *377*(9765), 557–567. https://doi.org/10.1016/S0140-6736(10)62037-5

Folmes, C. D. L., Dzeja, P. P., Nelson, T. J., & Terzic, A. (2012). Metabolic Plasticity in Stem Cell Homeostasis and Differentiation. *Cell Stem Cell*, *11*(5), 596–606. https://doi.org/10.1016/j.stem.2012.10.002

Font-Burgada, J., Sun, B., & Karin, M. (2016). Obesity and Cancer: The Oil that Feeds the Flame. *Cell Metabolism*, *23*(1), 48–62. https://doi.org/10.1016/j.cmet.2015.12.015

Foudi, A., Hochedlinger, K., Van Buren, D., Schindler, J. W., Jaenisch, R., Carey, V., & Hock, H. (2009). Analysis of histone 2B-GFP retention reveals slowly cycling hematopoietic stem cells. *Nature Biotechnology*, *27*(1), 84–90. https://doi.org/10.1038/nbt.1517

Fre, S., Huyghe, M., Mourikis, P., Robine, S., Louvard, D., & Artavanis-Tsakonas, S. (2005). Notch signals control the fate of immature progenitor cells in the intestine. *Nature*, *435*(7044), 964–968. https://doi.org/10.1038/nature03589

Friocourt, G., & Parnavelas, J. G. (2011). Identification of Arx targets unveils new candidates for controlling cortical interneuron migration and differentiation. *Frontiers in Cellular Neuroscience*, *5*, 28. https://doi.org/10.3389/fncel.2011.00028

Fukui, H., Xu, X., & Miwa, H. (2018). Role of Gut Microbiota-Gut Hormone Axis in the Pathophysiology of Functional Gastrointestinal Disorders. *Journal of Neurogastroenterology and Motility*, *24*(3), 367–386. https://doi.org/10.5056/jnm18071

Furness, J. B., Rivera, L. R., Cho, H.-J., Bravo, D. M., & Callaghan, B. (2013). The gut as a sensory organ.

Nature Reviews. Gastroenterology & Hepatology, *10*(12), 729–740. https://doi.org/10.1038/nrgastro.2013.180

Garg, S. K., Maurer, H., Reed, K., & Selagamsetty, R. (2014). Diabetes and cancer: two diseases with obesity as a common risk factor. *Diabetes, Obesity & Metabolism*, *16*(2), 97–110. https://doi.org/10.1111/dom.12124

Gegg, M., Böttcher, A., Burtscher, I., Hasenoeder, S., Van Campenhout, C., Aichler, M., … Lickert, H. (2014). Flattop regulates basal body docking and positioning in mono- and multiciliated cells. *ELife*, *3*. https://doi.org/10.7554/eLife.03842

Gelman, A., & Rubin, D. B. (1992). Inference from Iterative Simulation Using Multiple Sequences. *Statistical Science*, *7*(4), 457–472. https://doi.org/10.1214/ss/1177011136

Gerbe, F., & Jay, P. (2016). Intestinal tuft cells: epithelial sentinels linking luminal cues to the immune system. *Mucosal Immunology*, *9*(6), 1353–1359. https://doi.org/10.1038/mi.2016.68

Gerbe, F., van Es, J. H., Makrini, L., Brulin, B., Mellitzer, G., Robine, S., … Jay, P. (2011). Distinct ATOH1 and Neurog3 requirements define tuft cells as a new secretory cell type in the intestinal epithelium. *The Journal of Cell Biology*, *192*(5), 767–780. https://doi.org/10.1083/jcb.201010127

Ghaleb, A. M., McConnell, B. B., Kaestner, K. H., & Yang, V. W. (2011). Altered intestinal epithelial homeostasis in mice with intestine-specific deletion of the Krüppel-like factor 4 gene. *Developmental Biology*, *349*(2), 310–320. https://doi.org/10.1016/j.ydbio.2010.11.001

Gholkar, A. A., Cheung, K., Williams, K. J., Lo, Y.-C., Hamideh, S. A., Nnebe, C., … Torres, J. Z. (2016). Fatostatin Inhibits Cancer Cell Proliferation by Affecting Mitotic Microtubule Spindle Assembly and Cell Division. *The Journal of Biological Chemistry*, *291*(33), 17001–17008. https://doi.org/10.1074/jbc.C116.737346

Gierl, M. S., Karoulias, N., Wende, H., Strehle, M., & Birchmeier, C. (2006). The Zinc-finger factor Insm1 (IA-1) is essential for the development of pancreatic beta cells and intestinal endocrine cells. *Genes & Development*, *20*(17), 2465–2478. https://doi.org/10.1101/gad.381806

Glass, L. L., Calero-Nieto, F. J., Jawaid, W., Larraufie, P., Kay, R. G., Göttgens, B., … Gribble, F. M. (2017). Single-cell RNA-sequencing reveals a distinct population of proglucagon-expressing cells specific to the mouse upper small intestine. *Molecular Metabolism*, *6*(10), 1296–1303. https://doi.org/10.1016/j.molmet.2017.07.014

Goto, H., Inaba, H., & Inagaki, M. (2017). Mechanisms of ciliogenesis suppression in dividing cells. *Cellular and Molecular Life Sciences*, *74*(5), 881–890. https://doi.org/10.1007/s00018-016-2369-9

Gray, R. S., Abitua, P. B., Wlodarczyk, B. J., Szabo-Rogers, H. L., Blanchard, O., Lee, I., … Finnell, R. H. (2009). The planar cell polarity effector Fuz is essential for targeted membrane trafficking, ciliogenesis and mouse embryonic development. *Nature Cell Biology*, *11*(10), 1225–1232. https://doi.org/10.1038/ncb1966

GREGORIEFF, A., PINTO, D., BEGTHEL, H., DESTREE, O., KIELMAN, M., & CLEVERS, H. (2005). Expression Pattern of Wnt Signaling Components in the Adult Intestine. *Gastroenterology*, *129*(2), 626–638. https://doi.org/10.1016/j.gastro.2005.06.007

Gregorieff, A., Stange, D. E., Kujala, P., Begthel, H., van den Born, M., Korving, J., … Clevers, H. (2009). The Ets-Domain Transcription Factor Spdef Promotes Maturation of Goblet and Paneth Cells in the Intestinal Epithelium. *Gastroenterology*, *137*(4), 1333–1345.e3. https://doi.org/10.1053/j.gastro.2009.06.044

Grenier-Larouche, T., Carreau, A.-M., & Carpentier, A. C. (2017). Early Metabolic Improvement After Bariatric Surgery: The First Steps Toward Remission of Type 2 Diabetes. *Canadian Journal of Diabetes*, *41*(4), 418–425. https://doi.org/10.1016/j.jcjd.2016.10.013

Gribble, F. M., & Reimann, F. (2016). Enteroendocrine Cells: Chemosensors in the Intestinal Epithelium. *Annual Review of Physiology*, *78*(1), 277–299. https://doi.org/10.1146/annurev-physiol-021115-105439

Gribble, F. M., & Reimann, F. (2017). Signalling in the gut endocrine axis. *Physiology & Behavior*, *176*, 183–188. https://doi.org/10.1016/J.PHYSBEH.2017.02.039

Grün, D., Lyubimova, A., Kester, L., Wiebrands, K., Basak, O., Sasaki, N., … van Oudenaarden, A. (2015). Single-cell messenger RNA sequencing reveals rare intestinal cell types. *Nature*, *525*(7568), 251–255. https://doi.org/10.1038/nature14966

Grün, D., Muraro, M. J., Boisset, J.-C., Wiebrands, K., Lyubimova, A., Dharmadhikari, G., … van Oudenaarden, A. (2016). De Novo Prediction of Stem Cell Identity using Single-Cell Transcriptome Data. *Cell Stem Cell*, *19*(2), 266–277. https://doi.org/10.1016/j.stem.2016.05.010

Guo, D., Bell, E. H., Mischel, P., & Chakravarti, A. (2014). Targeting SREBP-1-driven lipid metabolism to treat cancer. *Current Pharmaceutical Design*, *20*(15), 2619–2626. Retrieved from http://www.ncbi.nlm.nih.gov/pubmed/23859617

Haas, S., Trumpp, A., & Milsom, M. D. (2018). Causes and Consequences of Hematopoietic Stem Cell Heterogeneity. *Cell Stem Cell*, *22*(5), 627–638. https://doi.org/10.1016/j.stem.2018.04.003

Haber, A. L., Biton, M., Rogel, N., Herbst, R. H., Shekhar, K., Smillie, C., … Regev, A. (2017). A single-cell survey of the small intestinal epithelium. *Nature*, *551*(7680), 333–339. https://doi.org/10.1038/nature24489

Habib, A. M., Richards, P., Cairns, L. S., Rogers, G. J., Bannon, C. A. M., Parker, H. E., … Gribble, F. M. (2012). Overlap of endocrine hormone expression in the mouse intestine revealed by transcriptional profiling and flow cytometry. *Endocrinology*, *153*(7), 3054–3065. https://doi.org/10.1210/en.2011-2170

Han, L., Shen, W.-J., Bittner, S., Kraemer, F. B., & Azhar, S. (2017). PPARs: regulators of metabolism and as therapeutic targets in cardiovascular disease. Part II: PPAR-β/δ and PPAR-γ. *Future Cardiology*, *13*(3), 279–296. https://doi.org/10.2217/fca-2017-0019

Hasegawa, H., & Nakamura, K. (2010). Tryptophan Hydroxylase and Serotonin Synthesis Regulation. *Handbook of Behavioral Neuroscience*, *21*, 183–202. https://doi.org/10.1016/S1569-7339(10)70078-3

HEATH, J. (1996). EPITHELIAL CELL MIGRATION IN THE INTESTINE. *Cell Biology International*, *20*(2), 139–146. https://doi.org/10.1006/cbir.1996.0018

Hellemans, J., Mortier, G., De Paepe, A., Speleman, F., & Vandesompele, J. (2007). qBase relative quantification framework and software for management and automated analysis of real-time quantitative PCR data. *Genome Biology*, *8*(2), R19. https://doi.org/10.1186/gb-2007-8-2-r19

Heuberger, J., Kosel, F., Qi, J., Grossmann, K. S., Rajewsky, K., & Birchmeier, W. (2014). Shp2/MAPK signaling controls goblet/paneth cell fate decisions in the intestine. *Proceedings of the National Academy of Sciences of the United States of America*, *111*(9), 3472–3477. https://doi.org/10.1073/pnas.1309342111

Hildebrandt, M. A., Hoffmann, C., Sherrill–Mix, S. A., Keilbaugh, S. A., Hamady, M., Chen, Y., … Wu, G. D. (2009). High-Fat Diet Determines the Composition of the Murine Gut Microbiome Independently of Obesity. *Gastroenterology*, *137*(5), 1716–1724.e2. https://doi.org/10.1053/j.gastro.2009.08.042

Hitz, C., Wurst, W., & Kuhn, R. (2007). Conditional brain-specific knockdown of MAPK using Cre/loxP regulated RNA interference. *Nucleic Acids Research*, *35*(12), e90–e90. https://doi.org/10.1093/nar/gkm475

Holst, J. J. (2013). Enteroendocrine secretion of gut hormones in diabetes, obesity and after bariatric surgery. *Current Opinion in Pharmacology*, *13*(6), 983–988. https://doi.org/10.1016/j.coph.2013.09.014

Horton, J. D., Goldstein, J. L., & Brown, M. S. (2002). SREBPs: activators of the complete program of cholesterol and fatty acid synthesis in the liver. *The Journal of Clinical Investigation*, *109*(9), 1125–1131. https://doi.org/10.1172/JCI15593

Hughes, K. R., Gândara, R. M. C., Javkar, T., Sablitzky, F., Hock, H., Potten, C. S., & Mahida, Y. R. (2012). Heterogeneity in histone 2B-green fluorescent protein-retaining putative small intestinal stem cells

at cell position 4 and their absence in the colon. *American Journal of Physiology-Gastrointestinal and Liver Physiology*, *303*(11), G1188–G1201. https://doi.org/10.1152/ajpgi.00080.2012

Hummel, K. P., Dickie, M. M., & Coleman, D. L. (1966). Diabetes, a new mutation in the mouse. *Science (New York, N.Y.)*, *153*(3740), 1127–1128. Retrieved from http://www.ncbi.nlm.nih.gov/pubmed/5918576

Hutch, C. R., & Sandoval, D. A. (2017). Physiological and molecular responses to bariatric surgery: markers or mechanisms underlying T2DM resolution? *Annals of the New York Academy of Sciences*, *1391*(1), 5–19. https://doi.org/10.1111/nyas.13194

Igal, R. A. (2010). Stearoyl-CoA desaturase-1: a novel key player in the mechanisms of cell proliferation, programmed cell death and transformation to cancer. *Carcinogenesis*, *31*(9), 1509–1515. https://doi.org/10.1093/carcin/bgq131

Imuta, Y., Kiyonari, H., Jang, C.-W., Behringer, R. R., & Sasaki, H. (2013). Generation of knock-in mice that express nuclear enhanced green fluorescent protein and tamoxifen-inducible Cre recombinase in the notochord from Foxa2 and T loci. *Genesis (New York, N.Y.: 2000)*, *51*(3), 210–218. https://doi.org/10.1002/dvg.22376

Ingalls, A. M., Dickie, M. M., & Snell, G. D. (1950). Obese, a new mutation in the house mouse. *The Journal of Heredity*, *41*(12), 317–318. Retrieved from http://www.ncbi.nlm.nih.gov/pubmed/14824537

Ireland, H., Houghton, C., Howard, L., & Winton, D. J. (2005). Cellular inheritance of a Cre-activated reporter gene to determine Paneth cell longevity in the murine small intestine. *Developmental Dynamics: An Official Publication of the American Association of Anatomists*, *233*(4), 1332–1336. https://doi.org/10.1002/dvdy.20446

Ito, K., Carracedo, A., Weiss, D., Arai, F., Ala, U., Avigan, D. E., … Pandolfi, P. P. (2012). A PML–PPAR-δ pathway for fatty acid oxidation regulates hematopoietic stem cell maintenance. *Nature Medicine*, *18*(9), 1350–1358. https://doi.org/10.1038/nm.2882

Ito, K., & Suda, T. (2014). Metabolic requirements for the maintenance of self-renewing stem cells. *Nature Reviews. Molecular Cell Biology*, *15*(4), 243–256. https://doi.org/10.1038/nrm3772

Itzkovitz, S., Lyubimova, A., Blat, I. C., Maynard, M., van Es, J., Lees, J., … van Oudenaarden, A. (2012). Single-molecule transcript counting of stem-cell markers in the mouse intestine. *Nature Cell Biology*, *14*(1), 106–114. https://doi.org/10.1038/ncb2384

Jackness, C., Karmally, W., Febres, G., Conwell, I. M., Ahmed, L., Bessler, M., … Korner, J. (2013). Very low-calorie diet mimics the early beneficial effect of Roux-en-Y gastric bypass on insulin sensitivity and β-cell Function in type 2 diabetic patients. *Diabetes*, *62*(9), 3027–3032. https://doi.org/10.2337/db12-1762

Jacobsen, S. H., Olesen, S. C., Dirksen, C., Jørgensen, N. B., Bojsen-Møller, K. N., Kielgast, U., … Madsbad, S. (2012). Changes in Gastrointestinal Hormone Responses, Insulin Sensitivity, and Beta-Cell Function Within 2 Weeks After Gastric Bypass in Non-diabetic Subjects. *Obesity Surgery*, *22*(7), 1084–1096. https://doi.org/10.1007/s11695-012-0621-4

Jamieson, P. M., Cleasby, M. E., Kuperman, Y., Morton, N. M., Kelly, P. A. T., Brownstein, D. G., … Vale, W. W. (2011). Urocortin 3 transgenic mice exhibit a metabolically favourable phenotype resisting obesity and hyperglycaemia on a high-fat diet. *Diabetologia*, *54*(9), 2392–2403. https://doi.org/10.1007/s00125-011-2205-6

Jenny, M., Uhl, C., Roche, C., Duluc, I., Guillermin, V., Guillemot, F., … Gradwohl, G. (2002). Neurogenin3 is differentially required for endocrine cell fate specification in the intestinal and gastric epithelium. *The EMBO Journal*, *21*(23), 6338–6347. Retrieved from http://www.ncbi.nlm.nih.gov/pubmed/12456641

Jensen, J., Pedersen, E. E., Galante, P., Hald, J., Heller, R. S., Ishibashi, M., … Madsen, O. D. (2000). Control of endodermal endocrine development by Hes-1. *Nature Genetics*, *24*(1), 36–44.

https://doi.org/10.1038/71657

Jeon, T.-I., & Osborne, T. F. (2012). SREBPs: metabolic integrators in physiology and metabolism. *Trends in Endocrinology & Metabolism*, *23*(2), 65–72. https://doi.org/10.1016/j.tem.2011.10.004

Johnson, W. E., Li, C., & Rabinovic, A. (2007). Adjusting batch effects in microarray expression data using empirical Bayes methods. *Biostatistics*, *8*(1), 118–127. https://doi.org/10.1093/biostatistics/kxj037

Jørgensen, N. B., Dirksen, C., Bojsen-Møller, K. N., Jacobsen, S. H., Worm, D., Hansen, D. L., … Holst, J. J. (2013). Exaggerated glucagon-like peptide 1 response is important for improved β-cell function and glucose tolerance after Roux-en-Y gastric bypass in patients with type 2 diabetes. *Diabetes*, *62*(9), 3044–3052. https://doi.org/10.2337/db13-0022

Kabiri, Z., Greicius, G., Madan, B., Biechele, S., Zhong, Z., Zaribafzadeh, H., … Virshup. (2014). Stroma provides an intestinal stem cell niche in the absence of epithelial Wnts. *Development*, *141*(11), 2206–2215. https://doi.org/10.1242/dev.104976

Kamisuki, S., Mao, Q., Abu-Elheiga, L., Gu, Z., Kugimiya, A., Kwon, Y., … Uesugi, M. (2009). A Small Molecule That Blocks Fat Synthesis By Inhibiting the Activation of SREBP. *Chemistry & Biology*, *16*(8), 882–892. https://doi.org/10.1016/J.CHEMBIOL.2009.07.007

Katz, J. P., Perreault, N., Goldstein, B. G., Lee, C. S., Labosky, P. A., Yang, V. W., & Kaestner, K. H. (2002). The zinc-finger transcription factor Klf4 is required for terminal differentiation of goblet cells in the colon. *Development (Cambridge, England)*, *129*(11), 2619–2628. Retrieved from http://www.ncbi.nlm.nih.gov/pubmed/12015290

Kim, D. Y., & Camilleri, M. (2000). Serotonin: a mediator of the brain-gut connection. *The American Journal of Gastroenterology*, *95*(10), 2698–2709. https://doi.org/10.1111/j.1572-0241.2000.03177.x

Kim, K.-S., Seeley, R. J., & Sandoval, D. A. (2018). Signalling from the periphery to the brain that regulates energy homeostasis. *Nature Reviews Neuroscience*, *19*(4), 185–196. https://doi.org/10.1038/nrn.2018.8

Kim, T.-H., Li, F., Ferreiro-Neira, I., Ho, L.-L., Luyten, A., Nalapareddy, K., … Shivdasani, R. A. (2014). Broadly permissive intestinal chromatin underlies lateral inhibition and cell plasticity. *Nature*, *506*(7489), 511–515. https://doi.org/10.1038/nature12903

Kim, T.-H., Saadatpour, A., Guo, G., Saxena, M., Cavazza, A., Desai, N., … Shivdasani, R. A. (2016). Single-Cell Transcript Profiles Reveal Multilineage Priming in Early Progenitors Derived from Lgr5 + Intestinal Stem Cells. *Cell Reports*, *16*(8), 2053–2060. https://doi.org/10.1016/j.celrep.2016.07.056

Kim, W., & Egan, J. M. (2008). The role of incretins in glucose homeostasis and diabetes treatment. *Pharmacological Reviews*, *60*(4), 470–512. https://doi.org/10.1124/pr.108.000604

Klein, A. M., & Simons, B. D. (2011). Universal patterns of stem cell fate in cycling adult tissues. *Development (Cambridge, England)*, *138*(15), 3103–3111. https://doi.org/10.1242/dev.060103

Klein, T. J., & Mlodzik, M. (2005). PLANAR CELL POLARIZATION: An Emerging Model Points in the Right Direction. *Annual Review of Cell and Developmental Biology*, *21*(1), 155–176. https://doi.org/10.1146/annurev.cellbio.21.012704.132806

Klil-Drori, A. J., Azoulay, L., & Pollak, M. N. (2017). Cancer, obesity, diabetes and antidiabetic drugs: is the fog clearing? *Nature Reviews Clinical Oncology*, *14*(2), 85–99. https://doi.org/10.1038/nrclinonc.2016.120

Knobloch, M., Braun, S. M. G., Zurkirchen, L., von Schoultz, C., Zamboni, N., Araúzo-Bravo, M. J., … Jessberger, S. (2013). Metabolic control of adult neural stem cell activity by Fasn-dependent lipogenesis. *Nature*, *493*(7431), 226–230. https://doi.org/10.1038/nature11689

Koh, A., De Vadder, F., Kovatcheva-Datchary, P., & Bäckhed, F. (2016). From Dietary Fiber to Host Physiology: Short-Chain Fatty Acids as Key Bacterial Metabolites. *Cell*, *165*(6), 1332–1345. https://doi.org/10.1016/j.cell.2016.05.041

Kojima, M., Hosoda, H., Date, Y., Nakazato, M., Matsuo, H., & Kangawa, K. (1999). Ghrelin is a growth-hormone-releasing acylated peptide from stomach. *Nature*, *402*(6762), 656–660. https://doi.org/10.1038/45230

Kondo, H., Minegishi, Y., Komine, Y., Mori, T., Matsumoto, I., Abe, K., … Murase, T. (2006). Differential regulation of intestinal lipid metabolism-related genes in obesity-resistant A/J vs. obesity-prone C57BL/6J mice. *American Journal of Physiology-Endocrinology and Metabolism*, *291*(5), E1092–E1099. https://doi.org/10.1152/ajpendo.00583.2005

Korinek, V., Barker, N., Moerer, P., van Donselaar, E., Huls, G., Peters, P. J., & Clevers, H. (1998). Depletion of epithelial stem-cell compartments in the small intestine of mice lacking Tcf-4. *Nature Genetics*, *19*(4), 379–383. https://doi.org/10.1038/1270

Korinek, V., Barker, N., Willert, K., Molenaar, M., Roose, J., Wagenaar, G., … Clevers, H. (1998). Two members of the Tcf family implicated in Wnt/beta-catenin signaling during embryogenesis in the mouse. *Molecular and Cellular Biology*, *18*(3), 1248–1256. Retrieved from http://www.ncbi.nlm.nih.gov/pubmed/9488439

Kosinski, C., Li, V. S. W., Chan, A. S. Y., Zhang, J., Ho, C., Tsui, W. Y., … Chen, X. (2007). Gene expression patterns of human colon tops and basal crypts and BMP antagonists as intestinal stem cell niche factors. *Proceedings of the National Academy of Sciences of the United States of America*, *104*(39), 15418–15423. https://doi.org/10.1073/pnas.0707210104

Kozak, M. (1984). Point mutations close to the AUG initiator codon affect the efficiency of translation of rat preproinsulin in vivo. *Nature*, *308*(5956), 241–246. https://doi.org/10.1038/308241a0

Kozak, M. (2002). Emerging links between initiation of translation and human diseases. *Mammalian Genome*, *13*(8), 401–410. https://doi.org/10.1007/s00335-002-4002-5

Kuleshov, M. V, Jones, M. R., Rouillard, A. D., Fernandez, N. F., Duan, Q., Wang, Z., … Ma'ayan, A. (2016). Enrichr: a comprehensive gene set enrichment analysis web server 2016 update. *Nucleic Acids Research*, *44*(W1), W90-7. https://doi.org/10.1093/nar/gkw377

Kuperman, Y., & Chen, A. (2008). Urocortins: emerging metabolic and energy homeostasis perspectives. *Trends in Endocrinology & Metabolism*, *19*(4), 122–129. https://doi.org/10.1016/j.tem.2007.12.002

Kuperman, Y., Issler, O., Regev, L., Musseri, I., Navon, I., Neufeld-Cohen, A., … Chen, A. (2010). Perifornical Urocortin-3 mediates the link between stress-induced anxiety and energy homeostasis. *Proceedings of the National Academy of Sciences*, *107*(18), 8393–8398. https://doi.org/10.1073/pnas.1003969107

Kurahashi, T., Furusawa, T., Ueda, T., & Bustin, M. (2009). The nucleosome binding protein HMGN3 is expressed in pancreatic α-cells and affects plasma glucagon levels in mice. *Journal of Cellular Biochemistry*, *109*(1), n/a-n/a. https://doi.org/10.1002/jcb.22377

La Manno, G., Soldatov, R., Zeisel, A., Braun, E., Hochgerner, H., Petukhov, V., … Kharchenko, P. V. (2018). RNA velocity of single cells. *Nature*, *560*(7719), 494–498. https://doi.org/10.1038/s41586-018-0414-6

Laferrere, B., Reilly, D., Arias, S., Swerdlow, N., Gorroochurn, P., Bawa, B., … Newgard, C. B. (2011). Differential Metabolic Impact of Gastric Bypass Surgery Versus Dietary Intervention in Obese Diabetic Subjects Despite Identical Weight Loss. *Science Translational Medicine*, *3*(80), 80re2-80re2. https://doi.org/10.1126/scitranslmed.3002043

Lan, X., Li, D., Zhong, B., Ren, J., Wang, X., Sun, Q., … Lu, S. (2015). Identification of differentially expressed genes related to metabolic syndrome induced with high-fat diet in E3 rats. *Experimental Biology and Medicine*, *240*(2), 235–241. https://doi.org/10.1177/1535370214554531

Lange, A., Gegg, M., Burtscher, I., Bengel, D., Kremmer, E., & Lickert, H. (2012). Fltp(T2AiCre): a new knock-in mouse line for conditional gene targeting in distinct mono- and multiciliated tissues. *Differentiation; Research in Biological Diversity*, *83*(2), S105-13. https://doi.org/10.1016/j.diff.2011.11.003

Larsson, L. I., St-Onge, L., Hougaard, D. M., Sosa-Pineda, B., & Gruss, P. (1998). Pax 4 and 6 regulate gastrointestinal endocrine cell development. *Mechanisms of Development*, *79*(1–2), 153–159. Retrieved from http://www.ncbi.nlm.nih.gov/pubmed/10349628

Law, C. W., Chen, Y., Shi, W., & Smyth, G. K. (2014). voom: precision weights unlock linear model analysis tools for RNA-seq read counts. *Genome Biology*, *15*(2), R29. https://doi.org/10.1186/gb-2014-15-2-r29

Lecarpentier, Y., Claes, V., Vallée, A., & Hébert, J.-L. (2017). Interactions between PPAR Gamma and the Canonical Wnt/Beta-Catenin Pathway in Type 2 Diabetes and Colon Cancer. *PPAR Research*, *2017*, 1–9. https://doi.org/10.1155/2017/5879090

Lee, C. S., Perreault, N., Brestelli, J. E., & Kaestner, K. H. (2002). Neurogenin 3 is essential for the proper specification of gastric enteroendocrine cells and the maintenance of gastric epithelial cell identity. *Genes & Development*, *16*(12), 1488–1497. https://doi.org/10.1101/gad.985002

Lee, E. C., Yu, D., Martinez de Velasco, J., Tessarollo, L., Swing, D. A., Court, D. L., … Copeland, N. G. (2001). A highly efficient Escherichia coli-based chromosome engineering system adapted for recombinogenic targeting and subcloning of BAC DNA. *Genomics*, *73*(1), 56–65. https://doi.org/10.1006/geno.2000.6451

Lee, G.-H., Proenca, R., Montez, J. M., Carroll, K. M., Darvishzadeh, J. G., Lee, J. I., & Friedman, J. M. (1996). Abnormal splicing of the leptin receptor in diabetic mice. *Nature*, *379*(6566), 632–635. https://doi.org/10.1038/379632a0

Lee, J.-H., Kang, H. S., Park, H. Y., Moon, Y.-A., Kang, Y. N., Oh, B.-C., … Im, S.-S. (2017). PPARα-dependent Insig2a overexpression inhibits SREBP-1c processing during fasting. *Scientific Reports*, *7*(1), 9958. https://doi.org/10.1038/s41598-017-10523-7

Lee, J.-M., Govindarajah, V., Goddard, B., Hinge, A., Muench, D. E., Filippi, M.-D., … Reynaud, D. (2018). Obesity alters the long-term fitness of the hematopoietic stem cell compartment through modulation of *Gfi1* expression. *The Journal of Experimental Medicine*, *215*(2), 627–644. https://doi.org/10.1084/jem.20170690

Lee, J. H., Jeon, Y. G., Lee, K.-H., Lee, H. W., Park, J., Jang, H., … Kim, J. B. (2017). RNF20 Suppresses Tumorigenesis by Inhibiting SREBP1c-PTTG1 Axis in Kidney Cancer. *Molecular and Cellular Biology*, *37*(22). https://doi.org/10.1128/MCB.00265-17

Leesnitzer, L. M., Parks, D. J., Bledsoe, R. K., Cobb, J. E., Collins, J. L., Consler, T. G., … Blanchard, S. G. (2002). Functional consequences of cysteine modification in the ligand binding sites of peroxisome proliferator activated receptors by GW9662. *Biochemistry*, *41*(21), 6640–6650. Retrieved from http://www.ncbi.nlm.nih.gov/pubmed/12022867

Li, F., He, J., Wei, J., Cho, W. C., & Liu, X. (2015). Diversity of epithelial stem cell types in adult lung. *Stem Cells International*, *2015*, 728307. https://doi.org/10.1155/2015/728307

Li, H. J., Ray, S. K., Singh, N. K., Johnston, B., & Leiter, A. B. (2011). Basic helix-loop-helix transcription factors and enteroendocrine cell differentiation. *Diabetes, Obesity and Metabolism*, *13*, 5–12. https://doi.org/10.1111/j.1463-1326.2011.01438.x

Li, N., Nakauka-Ddamba, A., Tobias, J., Jensen, S. T., & Lengner, C. J. (2016). Mouse Label-Retaining Cells Are Molecularly and Functionally Distinct From Reserve Intestinal Stem Cells. *Gastroenterology*, *151*(2), 298–310.e7. https://doi.org/10.1053/j.gastro.2016.04.049

Li, N., Yousefi, M., Nakauka-Ddamba, A., Jain, R., Tobias, J., Epstein, J. A., … Lengner, C. J. (2014). Single-cell analysis of proxy reporter allele-marked epithelial cells establishes intestinal stem cell hierarchy. *Stem Cell Reports*, *3*(5), 876–891. https://doi.org/10.1016/j.stemcr.2014.09.011

Li, X., Chen, Y.-T., Hu, P., & Huang, W.-C. (2014). Fatostatin displays high antitumor activity in prostate cancer by blocking SREBP-regulated metabolic pathways and androgen receptor signaling. *Molecular Cancer Therapeutics*, *13*(4), 855–866. https://doi.org/10.1158/1535-7163.MCT-13-0797

Li, Z., Chalazonitis, A., Huang, Y.-Y., Mann, J. J., Margolis, K. G., Yang, Q. M., … Gershon, M. D. (2011).

Essential roles of enteric neuronal serotonin in gastrointestinal motility and the development/survival of enteric dopaminergic neurons. *The Journal of Neuroscience : The Official Journal of the Society for Neuroscience*, *31*(24), 8998–9009. https://doi.org/10.1523/JNEUROSCI.6684-10.2011

Liu, P., Jenkins, N. A., & Copeland, N. G. (2003). A highly efficient recombineering-based method for generating conditional knockout mutations. *Genome Research*, *13*(3), 476–484. https://doi.org/10.1101/gr.749203

Lopez-Garcia, C., Klein, A. M., Simons, B. D., & Winton, D. J. (2010). Intestinal Stem Cell Replacement Follows a Pattern of Neutral Drift. *Science*, *330*(6005), 822–825. https://doi.org/10.1126/science.1196236

Ma, D. K., Jang, M.-H., Guo, J. U., Kitabatake, Y., Chang, M.-L., Pow-Anpongkul, N., … Song, H. (2009). Neuronal activity-induced Gadd45b promotes epigenetic DNA demethylation and adult neurogenesis. *Science (New York, N.Y.)*, *323*(5917), 1074–1077. https://doi.org/10.1126/science.1166859

Ma, K., Malhotra, P., Soni, V., Hedroug, O., Annaba, F., Dudeja, A., … Alrefai, W. A. (2014). Overactivation of Intestinal SREBP2 in Mice Increases Serum Cholesterol. *PLoS ONE*, *9*(1), e84221. https://doi.org/10.1371/journal.pone.0084221

Mabbott, N. A., Donaldson, D. S., Ohno, H., Williams, I. R., & Mahajan, A. (2013). Microfold (M) cells: important immunosurveillance posts in the intestinal epithelium. *Mucosal Immunology*, *6*(4), 666–677. https://doi.org/10.1038/mi.2013.30

Mah, A. T., Van Landeghem, L., Gavin, H. E., Magness, S. T., & Lund, P. K. (2014). Impact of diet-induced obesity on intestinal stem cells: hyperproliferation but impaired intrinsic function that requires insulin/IGF1. *Endocrinology*, *155*(9), 3302–3314. https://doi.org/10.1210/en.2014-1112

Makary, M. A., Clark, J. M., Shore, A. D., Magnuson, T. H., Richards, T., Bass, E. B., … Segal, J. B. (2010). Medication Utilization and Annual Health Care Costs in Patients With Type 2 Diabetes Mellitus Before and After Bariatric Surgery. *Archives of Surgery*, *145*(8), 726. https://doi.org/10.1001/archsurg.2010.150

Mana, M. D., Kuo, E. Y.-S., & Yilmaz, Ö. H. (2017). Dietary Regulation of Adult Stem Cells. *Current Stem Cell Reports*, *3*(1), 1–8. https://doi.org/10.1007/s40778-017-0072-x

Manning, B. D., & Toker, A. (2017). AKT/PKB Signaling: Navigating the Network. *Cell*, *169*(3), 381–405. https://doi.org/10.1016/j.cell.2017.04.001

Mao, J., Hu, X., Xiao, Y., Yang, C., Ding, Y., Hou, N., … Zhang, X. (2013). Overnutrition Stimulates Intestinal Epithelium Proliferation Through -Catenin Signaling in Obese Mice. *Diabetes*, *62*(11), 3736–3746. https://doi.org/10.2337/db13-0035

Marshman, E., Booth, C., & Potten, C. S. (2002). The intestinal epithelial stem cell. *BioEssays*, *24*(1), 91–98. https://doi.org/10.1002/bies.10028

Martinussen, C., Bojsen-Møller, K. N., Dirksen, C., Jacobsen, S. H., Jørgensen, N. B., Kristiansen, V. B., … Madsbad, S. (2015). Immediate enhancement of first-phase insulin secretion and unchanged glucose effectiveness in patients with type 2 diabetes after Roux-en-Y gastric bypass. *American Journal of Physiology-Endocrinology and Metabolism*, *308*(6), E535–E544. https://doi.org/10.1152/ajpendo.00506.2014

Matthews, D. R., Hosker, J. P., Rudenski, A. S., Naylor, B. A., Treacher, D. F., & Turner, R. C. (1985). Homeostasis model assessment: insulin resistance and beta-cell function from fasting plasma glucose and insulin concentrations in man. *Diabetologia*, *28*(7), 412–419. Retrieved from http://www.ncbi.nlm.nih.gov/pubmed/3899825

May, C. L., & Kaestner, K. H. (2010). Gut endocrine cell development. *Molecular and Cellular Endocrinology*, *323*(1), 70–75. https://doi.org/10.1016/j.mce.2009.12.009

McCole, D. F., & Barrett, K. E. (2007). Varied role of the gut epithelium in mucosal homeostasis. *Current*

Opinion in Gastroenterology, *23*(6), 647–654. https://doi.org/10.1097/MOG.0b013e3282f0153b

McFarlane, M. R., Cantoria, M. J., Linden, A. G., January, B. A., Liang, G., & Engelking, L. J. (2015). Scap is required for sterol synthesis and crypt growth in intestinal mucosa. *Journal of Lipid Research*, *56*(8), 1560–1571. https://doi.org/10.1194/jlr.M059709

McFarlane, M. R., Liang, G., & Engelking, L. J. (2014). Insig proteins mediate feedback inhibition of cholesterol synthesis in the intestine. *The Journal of Biological Chemistry*, *289*(4), 2148–2156. https://doi.org/10.1074/jbc.M113.524041

Meier, J. J., & Nauck, M. A. (2006). Incretins and the development of type 2 diabetes. *Current Diabetes Reports*, *6*(3), 194–201. Retrieved from http://www.ncbi.nlm.nih.gov/pubmed/16898571

Menendez, J. A., & Lupu, R. (2007). Fatty acid synthase and the lipogenic phenotype in cancer pathogenesis. *Nature Reviews Cancer*, *7*(10), 763–777. https://doi.org/10.1038/nrc2222

Middelhoff, M., Westphalen, C. B., Hayakawa, Y., Yan, K. S., Gershon, M. D., Wang, T. C., & Quante, M. (2017). Dclk1-expressing tuft cells: critical modulators of the intestinal niche? *American Journal of Physiology-Gastrointestinal and Liver Physiology*, *313*(4), G285–G299. https://doi.org/10.1152/ajpgi.00073.2017

Middendorp, S., Schneeberger, K., Wiegerinck, C. L., Mokry, M., Akkerman, R. D. L., van Wijngaarden, S., … Nieuwenhuis, E. E. S. (2014). Adult Stem Cells in the Small Intestine Are Intrinsically Programmed with Their Location-Specific Function. *STEM CELLS*, *32*(5), 1083–1091. https://doi.org/10.1002/stem.1655

Mihaylova, M. M., Cheng, C.-W., Cao, A. Q., Tripathi, S., Mana, M. D., Bauer-Rowe, K. E., … Yilmaz, Ö. H. (2018). Fasting Activates Fatty Acid Oxidation to Enhance Intestinal Stem Cell Function during Homeostasis and Aging. *Cell Stem Cell*, *22*(5), 769–778.e4. https://doi.org/10.1016/j.stem.2018.04.001

Mihaylova, M. M., Sabatini, D. M., & Yilmaz, Ö. H. (2014). Dietary and Metabolic Control of Stem Cell Function in Physiology and Cancer. *Cell Stem Cell*, *14*(3), 292–305. https://doi.org/10.1016/j.stem.2014.02.008

Milano, J., McKay, J., Dagenais, C., Foster-Brown, L., Pognan, F., Gadient, R., … Ciaccio, P. J. (2004). Modulation of notch processing by gamma-secretase inhibitors causes intestinal goblet cell metaplasia and induction of genes known to specify gut secretory lineage differentiation. *Toxicological Sciences: An Official Journal of the Society of Toxicology*, *82*(1), 341–358. https://doi.org/10.1093/toxsci/kfh254

Mingrone, G., Panunzi, S., De Gaetano, A., Guidone, C., Iaconelli, A., Nanni, G., … Rubino, F. (2015). Bariatric–metabolic surgery versus conventional medical treatment in obese patients with type 2 diabetes: 5 year follow-up of an open-label, single-centre, randomised controlled trial. *The Lancet*, *386*(9997), 964–973. https://doi.org/10.1016/S0140-6736(15)00075-6

Montgomery, R. K., Carlone, D. L., Richmond, C. A., Farilla, L., Kranendonk, M. E. G., Henderson, D. E., … Breault, D. T. (2011). Mouse telomerase reverse transcriptase (mTert) expression marks slowly cycling intestinal stem cells. *Proceedings of the National Academy of Sciences of the United States of America*, *108*(1), 179–184. https://doi.org/10.1073/pnas.1013004108

Moran, G. W., Leslie, F. C., Levison, S. E., Worthington, J., & McLaughlin, J. T. (2008). Enteroendocrine cells: neglected players in gastrointestinal disorders? *Therapeutic Advances in Gastroenterology*, *1*(1), 51–60. https://doi.org/10.1177/1756283X08093943

Motallebipour, M., Enroth, S., Punga, T., Ameur, A., Koch, C., Dunham, I., … Wadelius, C. (2009). Novel genes in cell cycle control and lipid metabolism with dynamically regulated binding sites for sterol regulatory element-binding protein 1 and RNA polymerase II in HepG2 cells detected by chromatin immunoprecipitation with microarray detection. *FEBS Journal*, *276*(7), 1878–1890. https://doi.org/10.1111/j.1742-4658.2009.06914.x

Mounier, C., Bouraoui, L., & Rassart, E. (2014). Lipogenesis in cancer progression (Review). *International Journal of Oncology*, *45*(2), 485–492. https://doi.org/10.3892/ijo.2014.2441

Müller, R. (2017). PPARβ/δ in human cancer. *Biochimie*, *136*, 90–99. https://doi.org/10.1016/j.biochi.2016.10.019

Muñoz, J., Stange, D. E., Schepers, A. G., van de Wetering, M., Koo, B.-K., Itzkovitz, S., … Clevers, H. (2012). The Lgr5 intestinal stem cell signature: robust expression of proposed quiescent '+4' cell markers. *The EMBO Journal*, *31*(14), 3079–3091. https://doi.org/10.1038/emboj.2012.166

Muzumdar, M. D., Tasic, B., Miyamichi, K., Li, L., & Luo, L. (2007). A global double-fluorescent Cre reporter mouse. *Genesis*, *45*(9), 593–605. https://doi.org/10.1002/dvg.20335

Nagai, T., Ibata, K., Park, E. S., Kubota, M., Mikoshiba, K., & Miyawaki, A. (2002). A variant of yellow fluorescent protein with fast and efficient maturation for cell-biological applications. *Nature Biotechnology*, *20*(1), 87–90. https://doi.org/10.1038/nbt0102-87

Nauck, M. A., & Meier, J. J. (2016). The incretin effect in healthy individuals and those with type 2 diabetes: physiology, pathophysiology, and response to therapeutic interventions. *The Lancet Diabetes & Endocrinology*, *4*(6), 525–536. https://doi.org/10.1016/S2213-8587(15)00482-9

Naya, F. J., Huang, H. P., Qiu, Y., Mutoh, H., DeMayo, F. J., Leiter, A. B., & Tsai, M. J. (1997). Diabetes, defective pancreatic morphogenesis, and abnormal enteroendocrine differentiation in BETA2/neuroD-deficient mice. *Genes & Development*, *11*(18), 2323–2334. Retrieved from http://www.ncbi.nlm.nih.gov/pubmed/9308961

Neuman, H., Debelius, J. W., Knight, R., & Koren, O. (2015). Microbial endocrinology: the interplay between the microbiota and the endocrine system. *FEMS Microbiology Reviews*, *39*(4), 509–521. https://doi.org/10.1093/femsre/fuu010

Noah, T. K., Donahue, B., & Shroyer, N. F. (2011). Intestinal development and differentiation. *Experimental Cell Research*, *317*(19), 2702–2710. https://doi.org/10.1016/J.YEXCR.2011.09.006

Noah, T. K., Kazanjian, A., Whitsett, J., & Shroyer, N. F. (2010). SAM pointed domain ETS factor (SPDEF) regulates terminal differentiation and maturation of intestinal goblet cells. *Experimental Cell Research*, *316*(3), 452–465. https://doi.org/10.1016/j.yexcr.2009.09.020

Norris, J. L., & Caprioli, R. M. (2013). Analysis of tissue specimens by matrix-assisted laser desorption/ionization imaging mass spectrometry in biological and clinical research. *Chemical Reviews*, *113*(4), 2309–2342. https://doi.org/10.1021/cr3004295

O'Brien, L. E., Soliman, S. S., Li, X., & Bilder, D. (2011). Altered Modes of Stem Cell Division Drive Adaptive Intestinal Growth. *Cell*, *147*(3), 603–614. https://doi.org/10.1016/j.cell.2011.08.048

Ochocki, J. D., & Simon, M. C. (2013). Nutrient-sensing pathways and metabolic regulation in stem cells. *The Journal of Cell Biology*, *203*(1), 23–33. https://doi.org/10.1083/jcb.201303110

Palmer, A., Phapale, P., Chernyavsky, I., Lavigne, R., Fay, D., Tarasov, A., … Alexandrov, T. (2017). FDR-controlled metabolite annotation for high-resolution imaging mass spectrometry. *Nature Methods*, *14*(1), 57–60. https://doi.org/10.1038/nmeth.4072

Palomer, X., Barroso, E., Pizarro-Delgado, J., Peña, L., Botteri, G., Zarei, M., … Vázquez-Carrera, M. (2018). PPARβ/δ: A Key Therapeutic Target in Metabolic Disorders. *International Journal of Molecular Sciences*, *19*(3). https://doi.org/10.3390/ijms19030913

Park, T. J., Mitchell, B. J., Abitua, P. B., Kintner, C., & Wallingford, J. B. (2008). Dishevelled controls apical docking and planar polarization of basal bodies in ciliated epithelial cells. *Nature Genetics*, *40*(7), 871–879. https://doi.org/10.1038/ng.104

Paulmann, N., Grohmann, M., Voigt, J.-P., Bert, B., Vowinckel, J., Bader, M., … Walther, D. J. (2009). Intracellular Serotonin Modulates Insulin Secretion from Pancreatic β-Cells by Protein Serotonylation. *PLoS Biology*, *7*(10), e1000229. https://doi.org/10.1371/journal.pbio.1000229

Pellegrinet, L., Rodilla, V., Liu, Z., Chen, S., Koch, U., Espinosa, L., … Radtke, F. (2011). Dll1- and dll4-mediated notch signaling are required for homeostasis of intestinal stem cells. *Gastroenterology*, *140*(4), 1230-1240.e1-7. https://doi.org/10.1053/j.gastro.2011.01.005

Peterli, R., Steinert, R. E., Woelnerhanssen, B., Peters, T., Christoffel-Courtin, C., Gass, M., … Beglinger,

C. (2012). Metabolic and Hormonal Changes After Laparoscopic Roux-en-Y Gastric Bypass and Sleeve Gastrectomy: a Randomized, Prospective Trial. *Obesity Surgery*, *22*(5), 740–748. https://doi.org/10.1007/s11695-012-0622-3

Pettersson, U. S., Waldén, T. B., Carlsson, P.-O., Jansson, L., & Phillipson, M. (2012). Female Mice are Protected against High-Fat Diet Induced Metabolic Syndrome and Increase the Regulatory T Cell Population in Adipose Tissue. *PLoS ONE*, *7*(9), e46057. https://doi.org/10.1371/journal.pone.0046057

Pinto, D., Gregorieff, A., Begthel, H., & Clevers, H. (2003). Canonical Wnt signals are essential for homeostasis of the intestinal epithelium. *Genes & Development*, *17*(14), 1709–1713. https://doi.org/10.1101/gad.267103

Pinto, D., Gregorieff, A., Begthel, H., & Clevers, H. (2003). Canonical Wnt signals are essential for homeostasis of the intestinal epithelium. *Genes & Development*, *17*(14), 1709–1713. https://doi.org/10.1101/gad.267103

Plourde, C.-É., Grenier-Larouche, T., Caron-Dorval, D., Biron, S., Marceau, S., Lebel, S., … Carpentier, A. C. (2014). Biliopancreatic diversion with duodenal switch improves insulin sensitivity and secretion through caloric restriction. *Obesity*, *22*(8), 1838–1846. https://doi.org/10.1002/oby.20771

Potten, C. S., Kovacs, L., & Hamilton, E. (1974). Continuous labelling studies on mouse skin and intestine. *Cell and Tissue Kinetics*, *7*(3), 271–283. Retrieved from http://www.ncbi.nlm.nih.gov/pubmed/4837676

Poulsen, P., Levin, K., Petersen, I., Christensen, K., Beck-Nielsen, H., & Vaag, A. (2005). Heritability of insulin secretion, peripheral and hepatic insulin action, and intracellular glucose partitioning in young and old Danish twins. *Diabetes*, *54*(1), 275–283. https://doi.org/10.2337/DIABETES.54.1.275

Povinelli, B. J., Rodriguez-Meira, A., & Mead, A. J. (2018). Single cell analysis of normal and leukemic hematopoiesis. *Molecular Aspects of Medicine*, *59*, 85–94. https://doi.org/10.1016/j.mam.2017.08.006

Powell, A. E., Vlacich, G., Zhao, Z.-Y., McKinley, E. T., Washington, M. K., Manning, H. C., & Coffey, R. J. (2014). Inducible loss of one Apc allele in Lrig1-expressing progenitor cells results in multiple distal colonic tumors with features of familial adenomatous polyposis. *American Journal of Physiology. Gastrointestinal and Liver Physiology*, *307*(1), G16-23. https://doi.org/10.1152/ajpgi.00358.2013

Purnell, J. Q., Selzer, F., Wahed, A. S., Pender, J., Pories, W., Pomp, A., … Wolfe, B. M. (2016). Type 2 Diabetes Remission Rates After Laparoscopic Gastric Bypass and Gastric Banding: Results of the Longitudinal Assessment of Bariatric Surgery Study. *Diabetes Care*, *39*(7), 1101–1107. https://doi.org/10.2337/dc15-2138

Rainer, J., Sanchez-Cabo, F., Stocker, G., Sturn, A., & Trajanoski, Z. (2006). CARMAweb: comprehensive R- and bioconductor-based web service for microarray data analysis. *Nucleic Acids Research*, *34*(Web Server), W498–W503. https://doi.org/10.1093/nar/gkl038

Rawlins, E. L., & Hogan, B. L. M. (2006). Epithelial stem cells of the lung: privileged few or opportunities for many? *Development*, *133*(13), 2455–2465. https://doi.org/10.1242/dev.02407

Renehan, A. G., Frystyk, J., & Flyvbjerg, A. (2006). Obesity and cancer risk: the role of the insulin-IGF axis. *Trends in Endocrinology and Metabolism: TEM*, *17*(8), 328–336. https://doi.org/10.1016/j.tem.2006.08.006

Reya, T., & Clevers, H. (2005). Wnt signalling in stem cells and cancer. *Nature*, *434*(7035), 843–850. https://doi.org/10.1038/nature03319

Riccio, O., van Gijn, M. E., Bezdek, A. C., Pellegrinet, L., van Es, J. H., Zimber-Strobl, U., … Radtke, F. (2008). Loss of intestinal crypt progenitor cells owing to inactivation of both Notch1 and Notch2 is accompanied by derepression of CDK inhibitors p27Kip1 and p57Kip2. *EMBO Reports*, *9*(4), 377–383. https://doi.org/10.1038/embor.2008.7

Richards, P., Pais, R., Habib, A. M., Brighton, C. A., Yeo, G. S. H., Reimann, F., & Gribble, F. M. (2016).

High fat diet impairs the function of glucagon-like peptide-1 producing L-cells. *Peptides*, *77*, 21–27. https://doi.org/10.1016/j.peptides.2015.06.006

Richmond, C. A., Shah, M. S., Deary, L. T., Trotier, D. C., Thomas, H., Ambruzs, D. M., … Breault, D. T. (2015). Dormant Intestinal Stem Cells Are Regulated by PTEN and Nutritional Status. *Cell Reports*, *13*(11), 2403–2411. https://doi.org/10.1016/j.celrep.2015.11.035

Ritsma, L., Ellenbroek, S. I. J., Zomer, A., Snippert, H. J., de Sauvage, F. J., Simons, B. D., … van Rheenen, J. (2014). Intestinal crypt homeostasis revealed at single-stem-cell level by in vivo live imaging. *Nature*, *507*(7492), 362–365. https://doi.org/10.1038/nature12972

Robinson, S. W., Dinulescu, D. M., & Cone, R. D. (2000). Genetic Models of Obesity and Energy Balance in the Mouse. *Annual Review of Genetics*, *34*(1), 687–745. https://doi.org/10.1146/annurev.genet.34.1.687

Roche, H. M., Phillips, C., & Gibney, M. J. (2005). The metabolic syndrome: the crossroads of diet and genetics. *The Proceedings of the Nutrition Society*, *64*(3), 371–377. Retrieved from http://www.ncbi.nlm.nih.gov/pubmed/16048671

Rock, J. R., & Hogan, B. L. M. (2011). Epithelial Progenitor Cells in Lung Development, Maintenance, Repair, and Disease. *Annual Review of Cell and Developmental Biology*, *27*(1), 493–512. https://doi.org/10.1146/annurev-cellbio-100109-104040

Rock, J. R., Onaitis, M. W., Rawlins, E. L., Lu, Y., Clark, C. P., Xue, Y., … Hogan, B. L. M. (2009). Basal cells as stem cells of the mouse trachea and human airway epithelium. *Proceedings of the National Academy of Sciences*, *106*(31), 12771–12775. https://doi.org/10.1073/pnas.0906850106

Rock, J. R., Randell, S. H., & Hogan, B. L. M. (2010). Airway basal stem cells: a perspective on their roles in epithelial homeostasis and remodeling. *Disease Models & Mechanisms*, *3*(9–10), 545–556. https://doi.org/10.1242/dmm.006031

Rodríguez-Colman, M. J., Schewe, M., Meerlo, M., Stigter, E., Gerrits, J., Pras-Raves, M., … Burgering, B. M. T. (2017). Interplay between metabolic identities in the intestinal crypt supports stem cell function. *Nature*, *543*(7645), 424–427. https://doi.org/10.1038/nature21673

Rossmeisl, M., Rim, J. S., Koza, R. A., & Kozak, L. P. (2003). Variation in type 2 diabetes--related traits in mouse strains susceptible to diet-induced obesity. *Diabetes*, *52*(8), 1958–1966. Retrieved from http://www.ncbi.nlm.nih.gov/pubmed/12882911

Rubino, F., & Marescaux, J. (2004). Effect of Duodenal???Jejunal Exclusion in a Non-obese Animal Model of Type 2 Diabetes. *Annals of Surgery*, *239*(1), 1–11. https://doi.org/10.1097/01.sla.0000102989.54824.fc

Rubino, F., Schauer, P. R., Kaplan, L. M., & Cummings, D. E. (2010). Metabolic Surgery to Treat Type 2 Diabetes: Clinical Outcomes and Mechanisms of Action. *Annual Review of Medicine*, *61*(1), 393–411. https://doi.org/10.1146/annurev.med.051308.105148

Salzman, N. H., Hung, K., Haribhai, D., Chu, H., Karlsson-Sjöberg, J., Amir, E., … Bos, N. A. (2010). Enteric defensins are essential regulators of intestinal microbial ecology. *Nature Immunology*, *11*(1), 76–83. https://doi.org/10.1038/ni.1825

Sánchez, I., & Dynlacht, B. D. (2016). Cilium assembly and disassembly. *Nature Cell Biology*, *18*(7), 711–717. https://doi.org/10.1038/ncb3370

Sangiorgi, E., & Capecchi, M. R. (2008). Bmi1 is expressed in vivo in intestinal stem cells. *Nature Genetics*, *40*(7), 915–920. https://doi.org/10.1038/ng.165

Sanyal, D. (2013). Diabetes is predominantly an intestinal disease. *Indian Journal of Endocrinology and Metabolism*, *17*(Suppl 1), S64-7. https://doi.org/10.4103/2230-8210.119508

Saruta, M., Takahashi, K., Suzuki, T., Fukuda, T., Torii, A., & Sasano, H. (2005). Urocortin 3/stresscopin in human colon: possible modulators of gastrointestinal function during stressful conditions. *Peptides*, *26*(7), 1196–1206. https://doi.org/10.1016/j.peptides.2005.01.014

Satija, R., Farrell, J. A., Gennert, D., Schier, A. F., & Regev, A. (2015). Spatial reconstruction of single-cell

gene expression data. *Nature Biotechnology*, *33*(5), 495–502. https://doi.org/10.1038/nbt.3192

Sato, T., van Es, J. H., Snippert, H. J., Stange, D. E., Vries, R. G., van den Born, M., … Clevers, H. (2011). Paneth cells constitute the niche for Lgr5 stem cells in intestinal crypts. *Nature*, *469*(7330), 415–418. https://doi.org/10.1038/nature09637

Sawada, M., Takahashi, K., Sawada, S., & Midorikawa, O. (1991). Selective killing of Paneth cells by intravenous administration of dithizone in rats. *International Journal of Experimental Pathology*, *72*(4), 407–421. Retrieved from http://www.ncbi.nlm.nih.gov/pubmed/1883741

Schauer, P. R., Bhatt, D. L., Kirwan, J. P., Wolski, K., Aminian, A., Brethauer, S. A., … STAMPEDE Investigators. (2017). Bariatric Surgery versus Intensive Medical Therapy for Diabetes — 5-Year Outcomes. *New England Journal of Medicine*, *376*(7), 641–651. https://doi.org/10.1056/NEJMoa1600869

Schuijers, J., van der Flier, L. G., van Es, J., & Clevers, H. (2014). Robust Cre-Mediated Recombination in Small Intestinal Stem Cells Utilizing the Olfm4 Locus. *Stem Cell Reports*, *3*(2), 234–241. https://doi.org/10.1016/j.stemcr.2014.05.018

Schulz, M. D., Atay, C., Heringer, J., Romrig, F. K., Schwitalla, S., Aydin, B., … Arkan, M. C. (2014). High-fat-diet-mediated dysbiosis promotes intestinal carcinogenesis independently of obesity. *Nature*, *514*(7523), 508–512. https://doi.org/10.1038/nature13398

Schulze, A., & Harris, A. L. (2012). How cancer metabolism is tuned for proliferation and vulnerable to disruption. *Nature*, *491*(7424), 364–373. https://doi.org/10.1038/nature11706

Schwabe, R. F., & Jobin, C. (2013). The microbiome and cancer. *Nature Reviews Cancer*, *13*(11), 800–812. https://doi.org/10.1038/nrc3610

Schwartz, M. W., Woods, S. C., Porte, D., Seeley, R. J., & Baskin, D. G. (2000). Central nervous system control of food intake. *Nature*, *404*(6778), 661–671. https://doi.org/10.1038/35007534

Seeley, R. J., Chambers, A. P., & Sandoval, D. A. (2015). The role of gut adaptation in the potent effects of multiple bariatric surgeries on obesity and diabetes. *Cell Metabolism*, *21*(3), 369–378. https://doi.org/10.1016/j.cmet.2015.01.001

Sethi, J. K., & Vidal-Puig, A. (2010). Wnt signalling and the control of cellular metabolism. *The Biochemical Journal*, *427*(1), 1–17. https://doi.org/10.1042/BJ20091866

Shao, W., & Espenshade, P. J. (2012). Expanding Roles for SREBP in Metabolism. *Cell Metabolism*, *16*(4), 414–419. https://doi.org/10.1016/J.CMET.2012.09.002

Shi, H., & Clegg, D. J. (2009). Sex differences in the regulation of body weight. *Physiology & Behavior*, *97*(2), 199–204. https://doi.org/10.1016/j.physbeh.2009.02.017

Shroyer, N. F., Helmrath, M. A., Wang, V. Y.-C., Antalffy, B., Henning, S. J., & Zoghbi, H. Y. (2007). Intestine-specific ablation of mouse atonal homolog 1 (Math1) reveals a role in cellular homeostasis. *Gastroenterology*, *132*(7), 2478–2488. https://doi.org/10.1053/j.gastro.2007.03.047

Shroyer, N. F., Wallis, D., Venken, K. J. T., Bellen, H. J., & Zoghbi, H. Y. (2005). Gfi1 functions downstream of Math1 to control intestinal secretory cell subtype allocation and differentiation. *Genes & Development*, *19*(20), 2412–2417. https://doi.org/10.1101/gad.1353905

Siddle, K. (2011). Signalling by insulin and IGF receptors: supporting acts and new players. *Journal of Molecular Endocrinology*, *47*(1), R1–R10. https://doi.org/10.1530/JME-11-0022

Silberg, D. G., Swain, G. P., Suh, E. R., & Traber, P. G. (2000). Cdx1 and cdx2 expression during intestinal development. *Gastroenterology*, *119*(4), 961–971. Retrieved from http://www.ncbi.nlm.nih.gov/pubmed/11040183

Singer, K., DelProposto, J., Lee Morris, D., Zamarron, B., Mergian, T., Maley, N., … Nien-Kai Lumeng, C. (2014). Diet-induced obesity promotes myelopoiesis in hematopoietic stem cells. *Molecular Metabolism*, *3*(6), 664–675. https://doi.org/10.1016/j.molmet.2014.06.005

Singh, A. K., Singh, R., & Kota, S. K. (2015). Bariatric surgery and diabetes remission: Who would have thought it? *Indian Journal of Endocrinology and Metabolism*, *19*(5), 563–576.

https://doi.org/10.4103/2230-8210.163113

Snippert, H. J., van der Flier, L. G., Sato, T., van Es, J. H., van den Born, M., Kroon-Veenboer, C., … Clevers, H. (2010). Intestinal Crypt Homeostasis Results from Neutral Competition between Symmetrically Dividing Lgr5 Stem Cells. *Cell*, *143*(1), 134–144. https://doi.org/10.1016/J.CELL.2010.09.016

Sommer, F., & Bäckhed, F. (2013). The gut microbiota — masters of host development and physiology. *Nature Reviews Microbiology*, *11*(4), 227–238. https://doi.org/10.1038/nrmicro2974

Soneson, C., & Robinson, M. D. (2018). Bias, robustness and scalability in single-cell differential expression analysis. *Nature Methods*, *15*(4), 255–261. https://doi.org/10.1038/nmeth.4612

Soriano, P. (1999). Generalized lacZ expression with the ROSA26 Cre reporter strain. *Nature Genetics*, *21*(1), 70–71. https://doi.org/10.1038/5007

Soyal, S. M., Nofziger, C., Dossena, S., Paulmichl, M., & Patsch, W. (2015). Targeting SREBPs for treatment of the metabolic syndrome. *Trends in Pharmacological Sciences*, *36*(6), 406–416. https://doi.org/10.1016/J.TIPS.2015.04.010

Stange, D. E., & Clevers, H. (2013). Concise review: The Yin and Yang of intestinal (cancer) stem cells and their progenitors. *STEM CELLS*, *31*(11), 2287–2295. https://doi.org/10.1002/stem.1475

Steinbach, G., Heymsfield, S., Olansen, N. E., Tighe, A., & Holt, P. R. (1994). Effect of caloric restriction on colonic proliferation in obese persons: implications for colon cancer prevention. *Cancer Research*, *54*(5), 1194–1197. Retrieved from http://www.ncbi.nlm.nih.gov/pubmed/8118805

Steinert, R. E., Feinle-Bisset, C., Asarian, L., Horowitz, M., Beglinger, C., & Geary, N. (2017). Ghrelin, CCK, GLP-1, and PYY(3–36): Secretory Controls and Physiological Roles in Eating and Glycemia in Health, Obesity, and After RYGB. *Physiological Reviews*, *97*(1), 411–463. https://doi.org/10.1152/physrev.00031.2014

Sternini, C., Anselmi, L., & Rozengurt, E. (2008). Enteroendocrine cells: a site of "taste" in gastrointestinal chemosensing. *Current Opinion in Endocrinology, Diabetes, and Obesity*, *15*(1), 73–78. https://doi.org/10.1097/MED.0b013e3282f43a73

Stone, T. W., McPherson, M., & Gail Darlington, L. (2018). Obesity and Cancer: Existing and New Hypotheses for a Causal Connection. *EBioMedicine*, *30*, 14–28. https://doi.org/10.1016/j.ebiom.2018.02.022

Stringari, C., Edwards, R. A., Pate, K. T., Waterman, M. L., Donovan, P. J., & Gratton, E. (2012). Metabolic trajectory of cellular differentiation in small intestine by Phasor Fluorescence Lifetime Microscopy of NADH. *Scientific Reports*, *2*(1), 568. https://doi.org/10.1038/srep00568

SUGIMOTO, Y., KIMURA, I., YAMADA, J., WATANABE, Y., TAKEUCHI, N., & HORISAKA, K. (1990). Effects of serotonin on blood glucose and insulin levels of glucose- and streptozotocin-treated mice. *The Japanese Journal of Pharmacology*, *54*(1), 93–96. https://doi.org/10.1254/jjp.54.93

Sun, N., Ly, A., Meding, S., Witting, M., Hauck, S. M., Ueffing, M., … Walch, A. (2014). High-resolution metabolite imaging of light and dark treated retina using MALDI-FTICR mass spectrometry. *PROTEOMICS*, *14*(7–8), 913–923. https://doi.org/10.1002/pmic.201300407

Svendsen, B., Pedersen, J., Albrechtsen, N. J. W., Hartmann, B., Toräng, S., Rehfeld, J. F., … Holst, J. J. (2015). An Analysis of Cosecretion and Coexpression of Gut Hormones From Male Rat Proximal and Distal Small Intestine. *Endocrinology*, *156*(3), 847–857. https://doi.org/10.1210/en.2014-1710

Swinburn, B., Sacks, G., & Ravussin, E. (2009). Increased food energy supply is more than sufficient to explain the US epidemic of obesity. *The American Journal of Clinical Nutrition*, *90*(6), 1453–1456. https://doi.org/10.3945/ajcn.2009.28595

Takeda, N., Jain, R., LeBoeuf, M. R., Wang, Q., Lu, M. M., & Epstein, J. A. (2011). Interconversion Between Intestinal Stem Cell Populations in Distinct Niches. *Science*, *334*(6061), 1420–1424. https://doi.org/10.1126/science.1213214

Tamplin, O. J., Kinzel, D., Cox, B. J., Bell, C. E., Rossant, J., & Lickert, H. (2008). Microarray analysis of

Foxa2 mutant mouse embryos reveals novel gene expression and inductive roles for the gastrula organizer and its derivatives. *BMC Genomics*, *9*(1), 511. https://doi.org/10.1186/1471-2164-9-511

Tanaka, C., Asakawa, A., Ushikai, M., Sakoguchi, T., Amitani, H., Terashi, M., … Inui, A. (2009). Comparison of the anorexigenic activity of CRF family peptides. *Biochemical and Biophysical Research Communications*, *390*(3), 887–891. https://doi.org/10.1016/j.bbrc.2009.10.069

Tetteh, P. W., Basak, O., Farin, H. F., Wiebrands, K., Kretzschmar, K., Begthel, H., … Clevers, H. (2016). Replacement of Lost Lgr5-Positive Stem Cells through Plasticity of Their Enterocyte-Lineage Daughters. *Cell Stem Cell*, *18*(2), 203–213. https://doi.org/10.1016/j.stem.2016.01.001

Tiano, J. P., & Mauvais-Jarvis, F. (2012). Importance of oestrogen receptors to preserve functional β-cell mass in diabetes. *Nature Reviews Endocrinology*, *8*(6), 342–351. https://doi.org/10.1038/nrendo.2011.242

Tirosh, I., Izar, B., Prakadan, S. M., Wadsworth, M. H., Treacy, D., Trombetta, J. J., … Garraway, L. A. (2016). Dissecting the multicellular ecosystem of metastatic melanoma by single-cell RNA-seq. *Science (New York, N.Y.)*, *352*(6282), 189–196. https://doi.org/10.1126/science.aad0501

Tobin, J. F., & Freedman, L. P. (2006). Nuclear receptors as drug targets in metabolic diseases: new approaches to therapy. *Trends in Endocrinology & Metabolism*, *17*(7), 284–290. https://doi.org/10.1016/j.tem.2006.07.004

Tolhurst, G., Heffron, H., Lam, Y. S., Parker, H. E., Habib, A. M., Diakogiannaki, E., … Gribble, F. M. (2012). Short-Chain Fatty Acids Stimulate Glucagon-Like Peptide-1 Secretion via the G-Protein-Coupled Receptor FFAR2. *Diabetes*, *61*(2), 364–371. https://doi.org/10.2337/db11-1019

Tschöp, M., Weyer, C., Tataranni, P. A., Devanarayan, V., Ravussin, E., & Heiman, M. L. (2001). Circulating ghrelin levels are decreased in human obesity. *Diabetes*, *50*(4), 707–709. Retrieved from http://www.ncbi.nlm.nih.gov/pubmed/11289032

Tsoli, M., Chronaiou, A., Kehagias, I., Kalfarentzos, F., & Alexandrides, T. K. (2013). Hormone changes and diabetes resolution after biliopancreatic diversion and laparoscopic sleeve gastrectomy: a comparative prospective study. *Surgery for Obesity and Related Diseases*, *9*(5), 667–677. https://doi.org/10.1016/J.SOARD.2012.12.006

Turnbaugh, P. J., Ley, R. E., Mahowald, M. A., Magrini, V., Mardis, E. R., & Gordon, J. I. (2006). An obesity-associated gut microbiome with increased capacity for energy harvest. *Nature*, *444*(7122), 1027–1031. https://doi.org/10.1038/nature05414

Ueda, T., Furusawa, T., Kurahashi, T., Tessarollo, L., & Bustin, M. (2009). The Nucleosome Binding Protein HMGN3 Modulates the Transcription Profile of Pancreatic Cells and Affects Insulin Secretion. *Molecular and Cellular Biology*, *29*(19), 5264–5276. https://doi.org/10.1128/MCB.00526-09

Ueo, T., Imayoshi, I., Kobayashi, T., Ohtsuka, T., Seno, H., Nakase, H., … Kageyama, R. (2012). The role of Hes genes in intestinal development, homeostasis and tumor formation. *Development*, *139*(6), 1071–1082. https://doi.org/10.1242/dev.069070

Ushikai, M., Asakawa, A., Sakoguchi, T., Tanaka, C., & Inui, A. (2011). Centrally administered urocortin 3 inhibits food intake and gastric emptying in mice. *Endocrine*, *39*(2), 113–117. https://doi.org/10.1007/s12020-010-9420-7

Valenta, T., Degirmenci, B., Moor, A. E., Herr, P., Zimmerli, D., Moor, M. B., … Basler, K. (2016). Wnt Ligands Secreted by Subepithelial Mesenchymal Cells Are Essential for the Survival of Intestinal Stem Cells and Gut Homeostasis. *Cell Reports*, *15*(5), 911–918. https://doi.org/10.1016/j.celrep.2016.03.088

van de Wetering, M., Sancho, E., Verweij, C., de Lau, W., Oving, I., Hurlstone, A., … Clevers, H. (2002). The β-Catenin/TCF-4 Complex Imposes a Crypt Progenitor Phenotype on Colorectal Cancer Cells. *Cell*, *111*(2), 241–250. https://doi.org/10.1016/S0092-8674(02)01014-0

van den Berg, S. M., Seijkens, T. T. P., Kusters, P. J. H., Beckers, L., den Toom, M., Smeets, E., … Lutgens, E. (2016). Diet-induced obesity in mice diminishes hematopoietic stem and progenitor cells in the

bone marrow. *The FASEB Journal*, *30*(5), 1779–1788. https://doi.org/10.1096/fj.201500175

van der Flier, L. G., & Clevers, H. (2009). Stem Cells, Self-Renewal, and Differentiation in the Intestinal Epithelium. *Annual Review of Physiology*, *71*(1), 241–260. https://doi.org/10.1146/annurev.physiol.010908.163145

van der Flier, L. G., Haegebarth, A., Stange, D. E., van de Wetering, M., & Clevers, H. (2009). OLFM4 Is a Robust Marker for Stem Cells in Human Intestine and Marks a Subset of Colorectal Cancer Cells. *Gastroenterology*, *137*(1), 15–17. https://doi.org/10.1053/j.gastro.2009.05.035

van der Meulen, T., & Huising, M. O. (2014). Maturation of Stem Cell-Derived Beta-cells Guided by the Expression of Urocortin 3. *The Review of Diabetic Studies*, *11*(1), 115–132. https://doi.org/10.1900/RDS.2014.11.115

van Es, J. H., de Geest, N., van de Born, M., Clevers, H., & Hassan, B. A. (2010). Intestinal stem cells lacking the Math1 tumour suppressor are refractory to Notch inhibitors. *Nature Communications*, *1*(2), 18. https://doi.org/10.1038/ncomms1017

van Es, J. H., Haegebarth, A., Kujala, P., Itzkovitz, S., Koo, B.-K., Boj, S. F., … Clevers, H. (2012). A Critical Role for the Wnt Effector Tcf4 in Adult Intestinal Homeostatic Self-Renewal. *Molecular and Cellular Biology*, *32*(10), 1918–1927. https://doi.org/10.1128/MCB.06288-11

van Es, J. H., Jay, P., Gregorieff, A., van Gijn, M. E., Jonkheer, S., Hatzis, P., … Clevers, H. (2005). Wnt signalling induces maturation of Paneth cells in intestinal crypts. *Nature Cell Biology*, *7*(4), 381–386. https://doi.org/10.1038/ncb1240

van Es, J. H., Sato, T., van de Wetering, M., Lyubimova, A., Yee Nee, A. N., Gregorieff, A., … Clevers, H. (2012). Dll1+ secretory progenitor cells revert to stem cells upon crypt damage. *Nature Cell Biology*, *14*(10), 1099–1104. https://doi.org/10.1038/ncb2581

van Es, J. H., van Gijn, M. E., Riccio, O., van den Born, M., Vooijs, M., Begthel, H., … Clevers, H. (2005). Notch/gamma-secretase inhibition turns proliferative cells in intestinal crypts and adenomas into goblet cells. *Nature*, *435*(7044), 959–963. https://doi.org/10.1038/nature03659

Van Landeghem, L., Santoro, M. A., Krebs, A. E., Mah, A. T., Dehmer, J. J., Gracz, A. D., … Lund, P. K. (2012). Activation of two distinct Sox9-EGFP-expressing intestinal stem cell populations during crypt regeneration after irradiation. *American Journal of Physiology. Gastrointestinal and Liver Physiology*, *302*(10), G1111-32. https://doi.org/10.1152/ajpgi.00519.2011

Van Landeghem, L., Santoro, M. A., Mah, A. T., Krebs, A. E., Dehmer, J. J., McNaughton, K. K., … Lund, P. K. (2015). IGF1 stimulates crypt expansion *via* differential activation of 2 intestinal stem cell populations. *The FASEB Journal*, *29*(7), 2828–2842. https://doi.org/10.1096/fj.14-264010

Varnat, F., Heggeler, B. B.-T., Grisel, P., Boucard, N., Corthésy-Theulaz, I., Wahli, W., & Desvergne, B. (2006). PPARbeta/delta regulates paneth cell differentiation via controlling the hedgehog signaling pathway. *Gastroenterology*, *131*(2), 538–553. https://doi.org/10.1053/j.gastro.2006.05.004

Vázquez-Carrera, M. (2016). Unraveling the Effects of PPARβ/δ on Insulin Resistance and Cardiovascular Disease. *Trends in Endocrinology & Metabolism*, *27*(5), 319–334. https://doi.org/10.1016/J.TEM.2016.02.008

Vilsbøll, T., Christensen, M., Junker, A. E., Knop, F. K., & Gluud, L. L. (2012). Effects of glucagon-like peptide-1 receptor agonists on weight loss: systematic review and meta-analyses of randomised controlled trials. *BMJ (Clinical Research Ed.)*, *344*, d7771. https://doi.org/10.1136/BMJ.D7771

Vladar, E. K., Bayly, R. D., Sangoram, A. M., Scott, M. P., & Axelrod, J. D. (2012). Microtubules Enable the Planar Cell Polarity of Airway Cilia. *Current Biology*, *22*(23), 2203–2212. https://doi.org/10.1016/J.CUB.2012.09.046

Vladar, E. K., & Stearns, T. (2007). Molecular characterization of centriole assembly in ciliated epithelial cells. *The Journal of Cell Biology*, *178*(1), 31–42. https://doi.org/10.1083/jcb.200703064

Vooijs, M., Ong, C.-T., Hadland, B., Huppert, S., Liu, Z., Korving, J., … Kopan, R. (2007). Mapping the consequence of Notch1 proteolysis in vivo with NIP-CRE. *Development (Cambridge, England)*,

134(3), 535–544. https://doi.org/10.1242/dev.02733

Wallingford, J. B. (2012). Planar Cell Polarity and the Developmental Control of Cell Behavior in Vertebrate Embryos. *Annual Review of Cell and Developmental Biology*, *28*(1), 627–653. https://doi.org/10.1146/annurev-cellbio-092910-154208

Wang, C.-Y., & Liao, J. K. (2012). A mouse model of diet-induced obesity and insulin resistance. *Methods in Molecular Biology (Clifton, N.J.)*, *821*, 421–433. https://doi.org/10.1007/978-1-61779-430-8_27

Wang, X., Yamamoto, Y., Wilson, L. H., Zhang, T., Howitt, B. E., Farrow, M. A., … Xian, W. (2015). Cloning and variation of ground state intestinal stem cells. *Nature*, *522*(7555), 173–178. https://doi.org/10.1038/nature14484

Wang, Y.-X. (2010). PPARs: diverse regulators in energy metabolism and metabolic diseases. *Cell Research*, *20*(2), 124–137. https://doi.org/10.1038/cr.2010.13

Wang, Y. C., McPherson, K., Marsh, T., Gortmaker, S. L., & Brown, M. (2011). Health and economic burden of the projected obesity trends in the USA and the UK. *The Lancet*, *378*(9793), 815–825. https://doi.org/10.1016/S0140-6736(11)60814-3

Wang, Y., & Nathans, J. (2007). Tissue/planar cell polarity in vertebrates: new insights and new questions. *Development (Cambridge, England)*, *134*(4), 647–658. https://doi.org/10.1242/dev.02772

Warming, S., Costantino, N., Court, D. L., Jenkins, N. A., & Copeland, N. G. (2005). Simple and highly efficient BAC recombineering using galK selection. *Nucleic Acids Research*, *33*(4), e36. https://doi.org/10.1093/nar/gni035

Watanabe, H., Akasaka, D., Ogasawara, H., Sato, K., Miyake, M., Saito, K., … Aso, H. (2010). Peripheral Serotonin Enhances Lipid Metabolism by Accelerating Bile Acid Turnover. *Endocrinology*, *151*(10), 4776–4786. https://doi.org/10.1210/en.2009-1349

Weir, G. C., & Bonner-Weir, S. (2004). Five stages of evolving beta-cell dysfunction during progression to diabetes. *Diabetes*, *53 Suppl 3*, S16-21. Retrieved from http://www.ncbi.nlm.nih.gov/pubmed/15561905

Weiss, L., Hoffmann, G. E., Schreiber, R., Andres, H., Fuchs, E., Körber, E., & Kolb, H. J. (1986). Fatty-acid biosynthesis in man, a pathway of minor importance. Purification, optimal assay conditions, and organ distribution of fatty-acid synthase. *Biological Chemistry Hoppe-Seyler*, *367*(9), 905–912. Retrieved from http://www.ncbi.nlm.nih.gov/pubmed/3790257

WHO | Definition and diagnosis of diabetes mellitus and intermediate hyperglycaemia. (2013). *WHO*.

WHO | *Global report on diabetes*. (2017). *WHO*.

Winzell, M. S., & Ahrén, B. (2004). The high-fat diet-fed mouse: a model for studying mechanisms and treatment of impaired glucose tolerance and type 2 diabetes. *Diabetes*, *53 Suppl 3*, S215-9. Retrieved from http://www.ncbi.nlm.nih.gov/pubmed/15561913

Wishart, D. S., Tzur, D., Knox, C., Eisner, R., Guo, A. C., Young, N., … Querengesser, L. (2007). HMDB: the Human Metabolome Database. *Nucleic Acids Research*, *35*(Database), D521–D526. https://doi.org/10.1093/nar/gkl923

Wolf, F. A., Angerer, P., & Theis, F. J. (2018). SCANPY: large-scale single-cell gene expression data analysis. *Genome Biology*, *19*(1), 15. https://doi.org/10.1186/s13059-017-1382-0

Wolf, F. A., Hamey, F., Plass, M., Solana, J., Dahlin, J. S., Gottgens, B., … Theis, F. J. (2018). Graph abstraction reconciles clustering with trajectory inference through a topology preserving map of single cells. *BioRxiv*, 208819. https://doi.org/10.1101/208819

Wölnerhanssen, B. K., Moran, A. W., Burdyga, G., Meyer-Gerspach, A. C., Peterli, R., Manz, M., … Shirazi-Beechey, S. P. (2017). Deregulation of transcription factors controlling intestinal epithelial cell differentiation; a predisposing factor for reduced enteroendocrine cell number in morbidly obese individuals. *Scientific Reports*, *7*(1), 8174. https://doi.org/10.1038/s41598-017-08487-9

Wong, R. H. F., & Sul, H. S. (2010). Insulin signaling in fatty acid and fat synthesis: a transcriptional perspective. *Current Opinion in Pharmacology*, *10*(6), 684–691.

https://doi.org/10.1016/j.coph.2010.08.004

Worthington, J. J., Reimann, F., & Gribble, F. M. (2018). Enteroendocrine cells-sensory sentinels of the intestinal environment and orchestrators of mucosal immunity. *Mucosal Immunology*, *11*(1), 3–20. https://doi.org/10.1038/mi.2017.73

Wu, L., Zhu, J., Prokop, L. J., & Murad, M. H. (2015). Pharmacologic Therapy of Diabetes and Overall Cancer Risk and Mortality: A Meta-Analysis of 265 Studies. *Scientific Reports*, *5*(1), 10147. https://doi.org/10.1038/srep10147

Xia, J., & Wishart, D. S. (2010). MetPA: a web-based metabolomics tool for pathway analysis and visualization. *Bioinformatics*, *26*(18), 2342–2344. https://doi.org/10.1093/bioinformatics/btq418

Xu, H. E., Stanley, T. B., Montana, V. G., Lambert, M. H., Shearer, B. G., Cobb, J. E., … Stimmel, J. B. (2002). Structural basis for antagonist-mediated recruitment of nuclear co-repressors by PPARα. *Nature*, *415*(6873), 813–817. https://doi.org/10.1038/415813a

Yamada, J., Sugimoto, Y., Kimura, I., Takeuchi, N., & Horisaka, K. (1989). Serotonin-induced hypoglycemia and increased serum insulin levels in mice. *Life Sciences*, *45*(20), 1931–1936. Retrieved from http://www.ncbi.nlm.nih.gov/pubmed/2689822

Yan, K. S., Chia, L. A., Li, X., Ootani, A., Su, J., Lee, J. Y., … Kuo, C. J. (2012). The intestinal stem cell markers Bmi1 and Lgr5 identify two functionally distinct populations. *Proceedings of the National Academy of Sciences of the United States of America*, *109*(2), 466–471. https://doi.org/10.1073/pnas.1118857109

Yan, K. S., Gevaert, O., Zheng, G. X. Y., Anchang, B., Probert, C. S., Larkin, K. A., … Kuo, C. J. (2017). Intestinal Enteroendocrine Lineage Cells Possess Homeostatic and Injury-Inducible Stem Cell Activity. *Cell Stem Cell*, *21*(1), 78–90.e6. https://doi.org/10.1016/j.stem.2017.06.014

Yan, K. S., Janda, C. Y., Chang, J., Zheng, G. X. Y., Larkin, K. A., Luca, V. C., … Kuo, C. J. (2017). Non-equivalence of Wnt and R-spondin ligands during Lgr5+ intestinal stem-cell self-renewal. *Nature*, *545*(7653), 238–242. https://doi.org/10.1038/nature22313

Yang, H., Wang, X., Xiong, X., & Yin, Y. (2016). Energy metabolism in intestinal epithelial cells during maturation along the crypt-villus axis. *Scientific Reports*, *6*(1), 31917. https://doi.org/10.1038/srep31917

Yang, Q., Bermingham, N. A., Finegold, M. J., & Zoghbi, H. Y. (2001). Requirement of Math1 for secretory cell lineage commitment in the mouse intestine. *Science (New York, N.Y.)*, *294*(5549), 2155–2158. https://doi.org/10.1126/science.1065718

Yang, W., Bancroft, L., Nicholas, C., Lozonschi, I., & Augenlicht, L. H. (2003). Targeted Inactivation of p27kip1 Is Sufficient for Large and Small Intestinal Tumorigenesis in the Mouse, Which Can Be Augmented by a Western-Style High-Risk Diet. *Cancer Research*, *63*(16).

Yates, L. L., Schnatwinkel, C., Murdoch, J. N., Bogani, D., Formstone, C. J., Townsend, S., … Dean, C. H. (2010). The PCP genes Celsr1 and Vangl2 are required for normal lung branching morphogenesis. *Human Molecular Genetics*, *19*(11), 2251–2267. https://doi.org/10.1093/hmg/ddq104

Ye, D. Z., & Kaestner, K. H. (2009). Foxa1 and Foxa2 control the differentiation of goblet and enteroendocrine L- and D-cells in mice. *Gastroenterology*, *137*(6), 2052–2062. https://doi.org/10.1053/j.gastro.2009.08.059

Yecies, J. L., Zhang, H. H., Menon, S., Liu, S., Yecies, D., Lipovsky, A. I., … Manning, B. D. (2011). Akt stimulates hepatic SREBP1c and lipogenesis through parallel mTORC1-dependent and independent pathways. *Cell Metabolism*, *14*(1), 21–32. https://doi.org/10.1016/j.cmet.2011.06.002

Yilmaz, Ö. H., Katajisto, P., Lamming, D. W., Gültekin, Y., Bauer-Rowe, K. E., Sengupta, S., … Sabatini, D. M. (2012). mTORC1 in the Paneth cell niche couples intestinal stem-cell function to calorie intake. *Nature*, *486*(7404), 490–495. https://doi.org/10.1038/nature11163

You, Y., Richer, E. J., Huang, T., & Brody, S. L. (2002). Growth and differentiation of mouse tracheal epithelial cells: selection of a proliferative population. *American Journal of Physiology. Lung Cellular*

and Molecular Physiology, *283*(6), L1315-21. https://doi.org/10.1152/ajplung.00169.2002

Yu, X., Ng, C. P., Habacher, H., & Roy, S. (2008). Foxj1 transcription factors are master regulators of the motile ciliogenic program. *Nature Genetics*, *40*(12), 1445–1453. https://doi.org/10.1038/ng.263

Zecchini, V., Domaschenz, R., Winton, D., & Jones, P. (2005). Notch signaling regulates the differentiation of post-mitotic intestinal epithelial cells. *Genes & Development*, *19*(14), 1686–1691. https://doi.org/10.1101/gad.341705

Zhang, C.-S., Wang, L.-X., Wang, R., Liu, Y., Song, L.-M., Yuan, J.-H., … Dong, J. (2018). The Correlation Between Circulating Ghrelin and Insulin Resistance in Obesity: A Meta-Analysis. *Frontiers in Physiology*, *9*, 1308. https://doi.org/10.3389/fphys.2018.01308

Zhou, W., Davis, E. A., Li, K., Nowak, R. A., & Dailey, M. J. (2018). Sex differences influence intestinal epithelial stem cell proliferation independent of obesity. *Physiological Reports*, *6*(13), e13746. https://doi.org/10.14814/phy2.13746

10 Acknowledgements

First of all, I want to thank my doctorate superviser, Prof. Dr. Heiko Lickert, who made this research work possible. I highly appriciate his immense expertise and enthusiasm, which inspired and motivated me all along during my doctorate. I am gratefull to him for the scientific support and creation of an excellent scientific environment and a pleasant working atmosphere.

I also wish to present my special thanks to the members of my thesis committee, Prof. Dr. Thomas Floss, Dr. Jantje Gerdes, Dr. Kerstin Stemmer and Dr. Anika Böttcher, for their encouragement and valuable comments on my project.

My heartfelt thanks goes to Dr. Anika Böttcher, my direct supervisor, mentor and friend. Thank you, for the motivation, for your constant guidance and support - in all scientific and non-scientific questions, for your dedication and time, and for the opportunity to learn from your knowledge. Moreover, I want to thank the other members of the "gut group", Michael Sterr, Felizitas von Hahn and Lena Oppenländer. Thank you for your support and help and for all the fun we have had in the last five years. Feli and Michi, I appreciate our close friendship very much.

Additionally, I would like to thank Kerstin Diemer, Jürgen Schultheiss, Anne Theis, Bianca Vogel and Heide Oller for the help with the experimental work and, especially, the animal care takers for the great support with the mouse work. I would also like to acknowledge Dr. Aurelia Raducanu for the assistance with the FACS, and Dr. Ingo Burtscher for the support with the cloning strategy for the generation of the Fltp-Venus fusion mouse. Moreover, my sencere thanks goes to my bachelor and master students, Saphira Baumgarten, Sandra Straub and Julia Hinterdobler for their valuable contribution to this work. Many thanks to all my fellow labmates for the scientific and non-scientific support and for the great time I have had with you.

My special thanks goes to our collaborators, Prof. Dr. Dr. Fabian Theis and Sophie Tritschler at the Institute of Computational Biology. Thank you, Sophie, for the indispensable contribution to this work, for our stimulating discussions and a very fruitful and pleasant teamwork on the single-cell analysis. Without your great effort, this project would be less exciting. I also want to thank our collaborators, Prof. Dr. med. Axel Walch and Dr. Na Sun as well as Dr. Martin Irmler, for the valuable contribution to this work. In addition, I would like to acknowledge Dr. Kerstin Stemmer and Dr. Carola Meyer, who introduced me to the methods for metabolic assessment in mice.

I also want to pay my regards to Dr. Andrzej Malinowski, Dr. Chirag Jain, Dr. Pallavi Mahaddalkar, Dr. Anika Böttcher, Dr. Ingo Burtscher, Michael Sterr and Dr. Felizitas von Hahn for the critical reading of my thesis.

Finally, I want to express my warmest gratitude to my family – my parents for their unconditional love and support, for their sacrifices to give their children a better future. I am also sencerely thankful to my parents in law for the constant support, especially during my PhD time. My deepest gratitude goes to my husband for his endless patience, wise advice, encouragement, love and continual support, and to my lovely son, who gives meaning to my life and makes me happy every day.

11 Publications

Data in chapter 4.1 and related methods provided in this thesis are the principal basis for the paper manuscript with the working title "*Obesity and pre-diabetes alters intestinal stem cell turnover and lineage allocation*", which is currently in preparation and to which the PhD candidate contributed as the first-author:

Aliluev A.*, **Tritschler S.***, Sterr M., Oppenländer L., Hinterdobler J., Irmler M., Beckers J., Sun N., Walch A.K., Stemmer K., Tschöp M.H., Theis F.J., Lickert H., Boettcher A. *Obesity and pre-diabetes alters intestinal stem cell turnover and lineage allocation*. Manuscript in preparation for Nature Metabolism.

* These authors contributed equally to this work.

Furhter author contributions:

Böttcher A., Büttner M., Tritschler S., Sterr M., **Aliluev A.**, Burtscher I., Sass S., Irmler M., Beckers J., Ziegenhain C., Enard W., Schamberger AC., Verhamme F.M., Eickelberg O., Theis F.J., and Lickert H.. *Wnt/PCP-primed intestinal stem cells directly differentiate into enteroendocrine or Paneth cells*. In revision, Nat. Cell Biol.

Ivanovska, J., **Tregubova, A**., Mahadevan, V., Chakilam, S., Gandesiri, M., Benderska, N., … Schneider-Stock, R. (2013). Identification of DAPK as a scaffold protein for the LIMK/cofilin complex in TNF-induced apoptosis. *The International Journal of Biochemistry & Cell Biology*, *45*(8), 1720–1729. https://doi.org/10.1016/j.biocel.2013.05.013